Exploring Two-dimensional van der Waals Supramolecular Networks: A Scanning Tunnelling Microscopy Approach

by

Haoxuan Ding

A thesis submitted to The University of Birmingham for the degree of Doctor of Philosophy

Nanoscale Physics Research Laboratory

School of Physics and Astronomy

University of Birmingham

March 2024

Abstract

Supramolecular self-assembly has emerged as a strategic avenue for engineering chemically bespoke surfaces. Over the preceding three decades, research focused on a variety of key parameters, such as temperature, solute concentration, and molecular architecture, has led to the successful fabrication of self-assembled molecular networks (SAMNs). Various types of intermolecular interactions have been explored in the construction of SAMNs. The study of self-assembly on surfaces began with early investigations of hydrogen-bonded assemblies and has since expanded to include other non-covalent interactions, such as coordination bonds and weaker van der Waals (vdW) interactions.

Among the many techniques in characterising molecular assembly on surfaces, scanning tunnelling microscopy (STM) has become the most popular choice due to its ability to provide real space images with atomic resolution. One of the useful properties of the STM is that it can provide information on structures not having long range-order as well as single atom level defects.

This thesis presents a study on the role of vdW interaction in molecular assembly, exploring how this non-directional and relatively weak force influences molecular self-assembly patterns with a large number of molecules. The study examines the chemisorbed alkanethiol molecules on the Au(111) surfaces and the formation of two-dimensional (2D) vdW supramolecular structures via the self-assembled co-crystallisation of alkanethiol and fullerene molecules. The absence of specific functional groups on the molecules used in this study leads to much more complex self-assembled structures and structural diversity. The fullerene/alkanethiol co-assembly exhibits different phases on the Au(111) substrate, as investigated using high-resolution STM at room temperature. The results show how collective interactions among many molecules dictate the stable structure transition.

Publications

1. **Ding, H.**; Zhang, X.; Li, B.; Wang, Y.; Xia, C.; Zhao, H.; Yang, H.; Gao, Y.; Chen, X.; Gao, J.; Pan, M.; Guo, Q. Orientational Growth of Flexible van Der Waals Supramolecular Networks. *Small Struct.* 2024, 5 (1). https://doi.org/10.1002/sstr.202300230.

2. **Ding, H.**; Gao, J.; Zhao, H.; Xia, C.; Grose, M.; Li, F.-S.; Guo, Q. Perturbational Imaging of Molecules with the Scanning Tunneling Microscope. *J. Phys. Chem. C* 2020, 124 (47), 25892–25897. https://doi.org/10.1021/acs.jpcc.0c08521.

3. Zhang, X.; **Ding, H.**; Yang, S.; Yang, H.; Yang, X.; Li, B.; Xing, X.; Sun, Y.; Gu, G.; Chen, X.; Gao, J.; Pan, M.; Chi, L.; Guo, Q. Kinetic Controlled Chirality Transfer and Induction in 2D Hydrogen-Bonding Assemblies of Glycylglycine on Au(111). *Small* 2023, *19* (17), e2207111. https://doi.org/10.1002/smll.202207111.

4. Zhang, X.; **Ding, H.**; Chen, X.; Lin, H.; Li, Q.; Gao, J.; Pan, M.; Guo, Q. Complex Supramolecular Tessellations with On-Surface Self-Synthesized C_{60} Tiles through van Der Waals Interaction. *Nanoscale* 2022, 14 (4), 1333–1339. https://doi.org/10.1039/d1nr05589e.

5. Zhang, X.; Shen, Q.; **Ding, H.**; Chen, X.; Yang, H.; Li, B.; Liu, X.; Lin, H.; Li, Q.; Gao, J.; Li, G.; Pan, M.; Guo, Q. On-Surface Synthesis of Thiophene-Containing Large-Sized Organometallic Macrocycles on the Ag(111) Surface. *J. Phys. Chem. C* 2021, 125 (21), 11454–11461. https://doi.org/10.1021/acs.jpcc.1c01540.

6. Pan, M.; Zhang, X.; Zhou, Y.; Wang, P.; Bian, Q.; Liu, H.; Wang, X.; Li, X.; Chen, A.; Lei, X.; Li, S.; Cheng, Z.; Shao, Z.; **Ding, H.**; Gao, J.; Li, F.; Liu, F. Growth of Mesoscale Ordered Two-Dimensional Hydrogen-Bond Organic Framework with the Observation of Flat Band. *Phys. Rev. Lett.* 2023, 130 (3), 036203. https://doi.org/10.1103/physrevlett.130.036203.

7. Lin, H.; Wang, Z.; Wang, H.; Gao, J.; **Ding, H.**; Xu, Y.; Li, Q.; Guo, Q.; Ma, Z.; Yang, X.; Pan, M. In Situ Observation of Stepwise C–H Bond Scission: Deciphering the Catalytic Selectivity of Ethylbenzene-to-Styrene Conversion on TiO2. *J. Phys. Chem. Lett.* 2020, 11 (22), 9850–9855. https://doi.org/10.1021/acs.jpclett.0c02729.

8. Zhang, X.; Fan, X.; Zhu, G.; Wang, Y.; **Ding, H.**; Lin, H.; Li, Y.; Li, Q.; Gao, J.; Pan, M.; Guo, Q. Two-Dimensional van Der Waals Supramolecular Frameworks from Co-Hosted Molecular Assembly and C_{60} Dimerization. *J. Phys. Chem. C* 2020, 124 (23), 12589–12595. https://doi.org/10.1021/acs.jpcc.0c03167.

9. Zhang, X.; Gao, J.; Fan, X.; Wang, Y.; **Ding, H.**; Qin, X.; Jiang, S.; Zhao, T.; Zhu, G.; Lu, H.; Yang, Z.; Lin, H.; Li, Q.; Chi, L.; Pan, M.; Guo, Q. Orientation-Selective Growth of Single-Atomic-Layer Gold Nanosheets via van Der Waals Interlocking and Octanethiolate-Confined Molecular Channels. *J. Phys. Chem. C* 2019, 123 (41), 25228–25235. https://doi.org/10.1021/acs.jpcc.9b07149.

10. Gao, J.; Lin, H.; Qin, X.; Zhang, X.; **Ding, H.**; Wang, Y.; Fard, M. R.; Kaya, D.; Zhu, G.; Li, Q.; Li, Y.; Pan, M.; Guo, Q. Probing Phase Evolutions of Au-Methyl-Propyl-Thiolate Self-Assembled Monolayers on Au(111) at the Molecular Level. *J. Phys. Chem. B* 2018, 122 (25), 6666–6672. https://doi.org/10.1021/acs.jpcb.8b03390.

Abbreviation

AAD	Au Adatom Dithiolate
AFM	Atomic Force Microscopy
CCI	Constant Current Imaging
CFM	Chemical Force Microscopy
CPC	Connector Plate Cryostat
DFT	Density Functional Theory
DLs	Discommensuration Lines
DT	Decanethiol
FCC	Face Centred Cubic
FEL	Fast Entry Lock
FWHM	Full Width at Half Maximum
HCP	Hexagonal Closed Packed
HOMO	Highest Occupied Molecular Orbitals
HOPG	Highly Oriented Pyrolytic Graphite
K-cell	Knudsen Cells
LDOS	Local Density of State
LEED	Low Energy Electron Diffraction
LT	Low Temperature
LUMO	Lowest Unoccupied Molecular Orbitals
MBE	Molecular Beam Epitaxy
MD	Molecular Dynamics
MoS_2	Molybdenum Disulfide
NND	Nearest Neighbour Distances

NMR	Nuclear Magnetic Resonance
OMBE	Organic Molecular Beam Epitaxy
OT	Octanethiol
PBN	Pyrolytic Boron Nitride
PVD	Physics Vapor Deposition
RT	Room Temperature
SAMs	Self-assembled Monolayers
SAMNs	Self-assembled Molecular Networks
SC	Simple Cubic
SEM	Scanning Electron Microscopy
STM	Scanning Tunnelling Microscopy
STS	Scanning Tunnelling Spectroscopy
TEM	Transmission Electron Microscopy
TEAS	Thermal Energy Atom Scattering
TP	Turbo Pump
TSP	Titanium Sublimation Pump
UHV	Ultra-high Vacuum
VT	Variable Temperature
vdW	van der Waals
XPS	X-ray Photoelectron Spectroscopy
XRD	X-ray Diffraction
1D	One Dimensional
2D	Two Dimensional
3D	Three Dimensional

Acknowledgement

I'm immensely grateful to a distinguished group of individuals and organisations whose support and contributions have been crucial in the successful completion of this research:

My principal supervisor, Dr Quanmin Guo, whose dedication to our project, constant encouragement, and patience have been central to my progress.

My co-supervisors, Dr Wolfgang Theis and Dr Ziyou Li, whose professional advice and knowledge significantly improved the calibre of my work.

Professor Leigh Canham, Dr Andrey Kaplan, Ms Hualin Yang, Mr Bosheng Li and group members at the Nanoscale Physics Research Laboratory (NPRL), thanks for their ongoing assistance and encouragement throughout my doctoral studies.

I owe a deep debt of gratitude for the collaborations from:

Dr Xin Zhang, Professor Jianzhi Gao and Professor Minghu Pan from Shaanxi Normal University, China. Dr Fangsen Li from Chinese Academy of Sciences.

My heartfelt thanks go to the kind hearted colleges of Birmingham and Xi'an, whose readiness to give their time has been a fundamental element of my research.

I would like to express my appreciation to my friends and family:

Mr Yepeng Yang, Dr Fangzhou Shi, Mr Tong Pan, Mr Wei Li and Dr Xiaoyu Qin for their constant belief and support.

Thanks to Dr Shu Yang and Dr Huan Lu for their selfless assistance over the years, which has lifted me over hurdles.

To my parents, who have guided me towards this PhD journey from its inception, your wisdom and love have illuminated my path.

Table of Contents

1. Introduction

Supramolecular chemistry emerges as a pivotal domain within the contemporary chemical sciences landscape, bridging the conventional disciplines of chemistry, materials science, and physics[1]. This subject paves the way for creating innovative molecular structures and materials, signalling substantial promise for a wide range of applications across various domains[2,3]. These include fields from biology[4] and medicine[5] to development of new materials[6].

The association of supramolecular chemistry with two Nobel Prizes in 1987[7] and 2016[8] underscores the field's significance and highlights its standing as an independent discipline and a fundamental theme across various chemical research areas. At its core, supramolecular chemistry leverages non-covalent interactions to engineer and manage self-assembled patterns through a broad spectrum of interaction types, such as hydrogen bonds[9,10], halogen bonds[11,12], π-interactions[13] and coordination bonds[14]. These interactions are instrumental in designing and forming complex architectures.

The field of molecular self-assembly draws significant inspiration from biological self-assembly[15], where molecular units spontaneously organise into stable complexes, crucial for the functionality and reproduction of living organisms[16]. Adopting self-assembly in supramolecular chemistry has become a central theme, signifying an essential strategy for the non-covalent synthesis of intricate systems through molecular recognition[17].

Supramolecular self-assembly is constituted by molecules bonded through non-covalent forces, ranging from simple dyads like DNA double helices to vast complexes forming spherical, rod-like, or sheet-like structures[18]. It originated in solution-based systems and now spans various phases[19]. In addition to solid-state systems, this field now includes liquid crystals[20], ionic liquids[21], and gas-phase[22] applications.

The self-assembly process involves distinct or connected components spontaneously organising into structured aggregates through targeted local interactions[23]. While this approach may seem simple, it typically relies on a trial-and-error methodology. Artificial molecular systems seldom reach the intricate complexity found in nature. Despite these challenges, there is a growing fascination with crafting bicomponent self-assembled structures. In these systems, molecular building blocks of different chemical natures are arranged within an orderly framework. These bicomponent assemblies are anticipated to display functionalities not achievable by systems composed of a single component[24].

Supramolecular systems composed of two components have been explored across various settings, including in solution[25] and the solid/liquid as well as solid/air(vacuum) interfaces[19,26]. Achieving successful two-component networks on surfaces typically demands a thorough comprehension and control over the interactions between molecules and at interfaces. A multi-component crystalline network is often formed by mixing two or more building blocks at a solid interface[17]. There are three possible scenarios to consider when introducing multiple building blocks at a vacuum-solid or liquid-solid interface:

(i) Phase separation: Both building blocks adhere to the surface, but each forms a distinct domain, adopting a structure similar to a single-component system[27].

(ii) Random mixing: One molecular component is randomly incorporated into a crystalline framework of the other without substantially altering the latter's unit cell. This type of mixing usually happens when the components share similar unit cell dimensions, except for the rare occurrence of 2D solid solutions[28].

(iii) Co-crystallisation: The different molecular building blocks together create a crystalline framework with specific surface stoichiometry, resulting in a novel two-component 2D network. Co-crystallisation typically stems from relatively strong intermolecular forces,

such as hydrogen bonding or the need to fill space efficiently, which is often seen in host-guest systems[29].

Host-guest systems are an example of two-component systems, where one component constructs the host framework while the other fills the spaces within this framework as the guest[30]. Typically, the host-forming molecule is adept at creating an open, porous structure through self-assembly, facilitated by strategic design features like hydrogen bonding groups or lengthy alkyl chains on its molecular structure. Alternatively, the host framework can be formed from inherently porous materials, where the porosity is a direct attribute of the chemical structure, leading to building blocks that naturally contain permanent covalent gaps. These host molecules often consist of covalent macrocycles that can form host-guest complexes both in solution and on solid surfaces. A notable category of host frameworks with covalent openings includes two-dimensional surface covalent organic frameworks (2D-sCOFs)[31], which have been increasingly utilised for trapping guest components[32].

However, not all bicomponent molecular networks can be classified as host-guest systems, as neither component can independently form an open, porous network under any experimental conditions[33]. The components co-crystallise on the substrate's surface in these instances due to specific intermolecular forces[34,35]. This co-crystallisation process might produce a periodic pattern of the two components, characterised by a distinct unit cell, or lead to their random distribution[36,37]. Alternatively, the components might co-crystallise in a layered, sandwich-type structure, where one component layers over the monolayer created by the other component[38,39]. Bicomponent networks that do not exhibit host-guest characteristics are commonly found on surfaces in ultra-high vacuum (UHV)[40] and under ambient conditions[41]. Similar to the single-component host systems mentioned earlier, these networks can be categorised by the primary intermolecular forces that contribute to their stability, including hydrogen bonding[34], halogen bonding[37], or metal-ligand coordination[38].

Characterisation of supramolecular systems, particularly those bound to surfaces, requires distinct techniques compared to solution or solid-state systems. Scanning probe microscopies (SPM), including scanning tunnelling microscopy (STM)[42] and atomic force microscopy (AFM)[43], are the principal methods for analysing surface-bound supramolecular systems, offering unparalleled insight into the molecular arrangements and providing detailed structural and electronic information at the molecular or sub-molecular level. Since its inception over 40 years ago, the advancement of STM has been instrumental in enabling atomistic real-space visualisation and manipulation of adsorbed species on surfaces, facilitating the exploration of single molecules and the application of molecular manipulation, chemical modification, and spectroscopic measurement[44,45].

Supramolecular self-assembly encounters unique challenges and opportunities due to the non-covalent designing strategy of molecular architectures[46]. Engineering supramolecular self-assembly in two dimensions provides new pathways for creating nanostructured materials with distinctive functional properties. This approach is in line with the ongoing miniaturisation trend, demanding innovative nanofabrication technologies[47].

In conclusion, supramolecular chemistry, particularly in the context of two-dimensional surface self-assembly, is at a pivotal juncture, with its foundations in synthesis and characterisation methodologies. There is a growing emphasis on harnessing these 2D materials for specific applications and their integration into devices, suggesting a promising future for this area of research.

In this thesis, the modification of metal and metal oxide surfaces can be achieved by applying a single layer of organic molecules. One of the most common methods for creating such a layer is to form self-assembled monolayers (SAMs)[48–50]. This thesis begins with examining the earliest and most extensively studied example of SAMs on metal surfaces: chemisorbed alkanethiol on gold[50–52]. It introduces the latest developments in understanding

the interfacial structure of alkanethiol SAMs on gold, presenting a comprehensive structural model to account for the close-packed and striped phases observed in alkanethiol SAMs. Additionally, the thesis explores the phase transitions occurring in long-chain molecular monolayers, specifically octanethiol (OT)[53] and decanethiol (DT)[54] SAMs. It introduces a novel striped phase as a molecular template for depositing C_{60} molecules.

We have developed a two-dimensional van der Waals supramolecular network between C_{60} and alkanethiol molecules on an Au(111) substrate. The absence of specific functional groups on both the C_{60} and alkanethiol molecules means that this particular pairing is less than ideal for creating ordered molecular frameworks using traditional design methods. Our prior research on this combination revealed phase separation between C_{60} and the thiols on Au(111)[27], highlighting that the coverage of thiols plays a crucial role in the structural formation of these binary molecular networks. Nevertheless, by correctly adjusting the ratio of C_{60} to OT, we can form a regular, porous structure where the nanopores are filled with thiols, inverting the typical approach of constructing a porous framework from host molecules and filling it with guest molecules. This porous framework emerges through a cooperative self-organisation process, with the C_{60} molecules and thiols acting as co-hosts.

Additionally, when we switch the molecular template to DT SAMs, the C_{60} molecules tend to form extensive nanochain structures on the Au(111) surface at room temperature. This method significantly advances our understanding of van der Waals (vdW) co-assembly on surfaces and presents a promising avenue for crafting complex functional nanostructures. These results are poised to profoundly impact the future design and synthesis of molecular nanostructures and nanomaterials, offering enhanced control over their structures and properties.

Chapter 2 offers a detailed review of relevant literature, covering the properties of the Au(111) substrate, SAMs, and fullerene (C_{60}) molecules. It also introduces the operational principles of STM and discusses two deposition methods.

Chapter 3 fully describes the experimental setup and sample preparation techniques used in this project. It includes the Fermi-STM setup, *in-situ* evaporators for depositing molecules, and sample cleaning methods completed in the UHV chamber.

Chapter 4 marks the beginning of the data analysis in this thesis, highlighting key experimental outcomes in forming alkanethiol SAMs on Au(111). It details the characterisation of long-chain (octanethiol and decanethiol) molecules on the Au(111) surface. After annealing, we observed several distinct phases and intermediate molecular surface coverages, including well-resolved striped phases and mesh-like structures in STM images.

Chapter 5 discusses the experimental creation of a two-dimensional vdW supramolecular network through the self-assembled co-crystallisation of C_{60} and OT molecules on Au(111) surfaces. This network features a two-dimensional C_{60} lattice interspersed with RS-Au-SR ($R=CH_3(CH_2)_9S$) units.

Chapter 6 describes the fabrication of C_{60}-based 2D supramolecular tessellations on an Au(111) surface, facilitated by cooperative vdW interactions without the need for specific functional groups for bonding.

Chapter 7 outlines the engineering of a 2D C_{60}/DT porous molecular framework and the formation of extensive nanochain structures on the Au(111) surface at room temperature. We achieve flexible bicomponent molecular structures that exhibit orientational growth by adjusting the molecular coverage and annealing temperature. A synthesis strategy is also concluded.

Finally, chapter 8 will summarise the findings of this study and offer recommendations for future research.

References

1. Barth, J. V., Costantini, G. & Kern, K. Engineering atomic and molecular nanostructures at surfaces. *Nature* 437, 671–679 (2005).

2. Slater, A. G., Beton, P. H. & Champness, N. R. Two-dimensional supramolecular chemistry on surfaces. *Chem. Sci.* 2, 1440–1448 (2011).

3. Champness, N. R. *Supramolecular Chemistry on Surfaces: 2D Networks and 2D Structures*. (Wiley-VCH, 2022). doi:10.1002/9783527816699.ch1.

4. Peng, H.-Q. *et al.* Biological Applications of Supramolecular Assemblies Designed for Excitation Energy Transfer. *Chem. Rev.* 115, 7502–7542 (2015).

5. Smith, D. K. From fundamental supramolecular chemistry to self-assembled nanomaterials and medicines and back again – how Sam inspired SAMul. *Chem. Commun.* 54, 4743–4760 (2018).

6. Stupp, S. I. & Palmer, L. C. Supramolecular Chemistry and Self-Assembly in Organic Materials Design. *Chem. Mater.* 26, 507–518 (2014).

7. Lehn, J. Supramolecular Chemistry—Scope and Perspectives Molecules, Supermolecules, and Molecular Devices (Nobel Lecture). *Angew. Chem. Int. Ed. Engl.* 27, 89–112 (1988).

8. Stoddart, J. F. Mechanically Interlocked Molecules (MIMs)—Molecular Shuttles, Switches, and Machines (Nobel Lecture). *Angew. Chem. Int. Ed.* 56, 11094–11125 (2017).

9. Prins, L. J., Reinhoudt, D. N. & Timmerman, P. Noncovalent Synthesis Using Hydrogen Bonding. *Angew. Chem. Int. Ed.* 40, 2382–2426 (2001).

10. González-Rodríguez, D. & Schenning, A. P. H. J. Hydrogen-bonded Supramolecular π-Functional Materials. *Chem. Mater.* 23, 310–325 (2011).

11. Metrangolo, P., Meyer, F., Pilati, T., Resnati, G. & Terraneo, G. Halogen Bonding in Supramolecular Chemistry. *Angew. Chem. Int. Ed.* 47, 6114–6127 (2008).

12. Gilday, L. C. *et al.* Halogen Bonding in Supramolecular Chemistry. *Chem. Rev.* 115, 7118–7195 (2015).

13. Hunter, C. A. & Sanders, J. K. M. The nature of .pi.-.pi. interactions. *J. Am. Chem. Soc.* 112, 5525–5534 (1990).

14. Chakrabarty, R., Mukherjee, P. S. & Stang, P. J. Supramolecular Coordination: Self-Assembly of Finite Two- and Three-Dimensional Ensembles. *Chem. Rev.* 111, 6810–6918 (2011).

15. Grzybowski, B. A., Wilmer, C. E., Kim, J., Browne, K. P. & Bishop, K. J. M. Self-assembly : from crystals to cells. *Soft Matter* 5, 1110–1128 (2009).

16. Stephanopoulos, N., Ortony, J. H. & Stupp, S. I. Self-assembly for the synthesis of functional biomaterials. *Acta Mater.* 61, 912–930 (2013).

17. Mali, K. S., Pearce, N., Feyter, S. D. & Champness, N. R. Frontiers of supramolecular chemistry at solid surfaces. *Chem. Soc. Rev.* 46, 2520–2542 (2017).

18. Williams, G. T. *et al.* Advances in applied supramolecular technologies. *Chem. Soc. Rev.* 50, 2737–2763 (2021).

19. Desiraju, G. R. Crystal Engineering: From Molecule to Crystal. *J. Am. Chem. Soc.* 135, 9952–9967 (2013).

20. Saez, I. M. & Goodby, J. W. Supermolecular liquid crystals. *J. Mater. Chem.* 15, 26–40 (2004).

21. Hayes, R., Warr, G. G. & Atkin, R. Structure and Nanostructure in Ionic Liquids. *Chem. Rev.* 115, 6357–6426 (2015).

22. Schalley, C. A. Supramolecular chemistry goes gas phase: the mass spectrometric examination of noncovalent interactions in host–guest chemistry and molecular recognition. *Int. J. Mass Spectrom.* 194, 11–39 (2000).

23. Whitesides, G. M. & Grzybowski, B. Self-Assembly at All Scales. *Science* 295, 2418–2421 (2002).

24. Okesola, B. O. & Mata, A. Multicomponent self-assembly as a tool to harness new properties from peptides and proteins in material design. *Chem. Soc. Rev.* 47, 3721–3736 (2018).

25. Greef, T. F. A. D. *et al.* Supramolecular Polymerization. *Chem. Rev.* 109, 5687–5754 (2009).

26. Elemans, J. A. A. W., Lei, S. & Feyter, S. D. Molecular and Supramolecular Networks on Surfaces: From Two-Dimensional Crystal Engineering to Reactivity. *Angew. Chem. Int. Ed.* 48, 7298–7332 (2009).

27. Li, F., Tang, L., Zhou, W. & Guo, Q. Formation of Confined C_{60} Islands within Octanethiol Self-Assembled Monolayers on Au(111). *J. Phys. Chem. C* 113, 17899–17903 (2009).

28. MacLeod, J. M. *et al.* A 2D Substitutional Solid Solution through Hydrogen Bonding of Molecular Building Blocks. *ACS Nano* 11, 8901–8909 (2017).

29. Theobald, J. A., Oxtoby, N. S., Phillips, M. A., Champness, N. R. & Beton, P. H. Controlling molecular deposition and layer structure with supramolecular surface assemblies. *Nature* 424, 1029–1031 (2003).

30. Teyssandier, J., Feyter, S. D. & Mali, K. S. Host–guest chemistry in two-dimensional supramolecular networks. *Chem. Commun.* 52, 11465–11487 (2016).

31. Liang, R.-R., Jiang, S.-Y., A, R.-H. & Zhao, X. Two-dimensional covalent organic frameworks with hierarchical porosity. *Chem. Soc. Rev.* 49, 3920–3951 (2020).

32. Blunt, M. O., Russell, J. C., Champness, N. R. & Beton, P. H. Templating molecular adsorption using a covalent organic framework. *Chem. Commun.* 46, 7157–7159 (2010).

33. Ciesielski, A., Palma, C., Bonini, M. & Samorì, P. Towards Supramolecular Engineering of Functional Nanomaterials: Pre-Programming Multi-Component 2D Self-Assembly at Solid-Liquid Interfaces. *Adv. Mater.* 22, 3506–3520 (2010).

34. Ding, Y., Wang, X., Xie, L., Yao, X. & Xu, W. Two-dimensional self-assembled nanostructures of nucleobases and their related derivatives on Au(111). *Chem. Commun.* 54, 9259–9269 (2018).

35. Bouju, X., Mattioli, C., Franc, G., Pujol, A. & Gourdon, A. Bicomponent Supramolecular Architectures at the Vacuum–Solid Interface. *Chem. Rev.* 117, 1407–1444 (2017).

36. Zheng, Q.-N. *et al.* Formation of Halogen Bond-Based 2D Supramolecular Assemblies by Electric Manipulation. *J. Am. Chem. Soc.* 137, 6128–6131 (2015).

37. Mukherjee, A., Teyssandier, J., Hennrich, G., Feyter, S. D. & Mali, K. S. Two-dimensional crystal engineering using halogen and hydrogen bonds: towards structural landscapes. *Chem. Sci.* 8, 3759–3769 (2017).

38. Schlickum, U. *et al.* Metal−Organic Honeycomb Nanomeshes with Tunable Cavity Size. *Nano Lett.* 7, 3813–3817 (2007).

39. Écija, D. *et al.* Five-vertex Archimedean surface tessellation by lanthanide-directed molecular self-assembly. *Proc. Natl. Acad. Sci.* 110, 6678–6681 (2013).

40. Xiao, W. *et al.* C_{60}/Corannulene on Cu(110): A Surface-Supported Bistable Buckybowl−Buckyball Host−Guest System. *J. Am. Chem. Soc.* 130, 4767–4771 (2008).

41. Qiu, X. *et al.* Alkane-Assisted Adsorption and Assembly of Phthalocyanines and Porphyrins. *J. Am. Chem. Soc.* 122, 5550–5556 (2000).

42. Binnig, G., Rohrer, H., Gerber, C. & Weibel, E. Tunneling through a controllable vacuum gap. *Appl. Phys. Lett.* 40, 178–180 (1982).

43. Binnig, G., Quate, C. F. & Gerber, Ch. Atomic Force Microscope. *Phys. Rev. Lett.* 56, 930–933 (1986).

44. Guo, J. & Jiang, Y. Submolecular Insights into Interfacial Water by Hydrogen-Sensitive Scanning Probe Microscopy. *Acc. Chem. Res.* 55, 1680–1692 (2022).

45. Gross, L., Mohn, F., Moll, N., Liljeroth, P. & Meyer, G. The Chemical Structure of a Molecule Resolved by Atomic Force Microscopy. *Science* 325, 1110–1114 (2009).

46. Song, W., Martsinovich, N., Heckl, W. M. & Lackinger, M. Born–Haber Cycle for Monolayer Self-Assembly at the Liquid–Solid Interface: Assessing the Enthalpic Driving Force. *J. Am. Chem. Soc.* 135, 14854–14862 (2013).

47. Saywell, A. *et al.* Self-assembled aggregates formed by single-molecule magnets on a gold surface. *Nat. Commun.* 1, 75 (2010).

48. Guo, Q. & Li, F. Self-assembled alkanethiol monolayers on gold surfaces: resolving the complex structure at the interface by STM. *Phys. Chem. Chem. Phys.* 16, 19074–19090 (2014).

49. Poirier, G. E. & Pylant, E. D. The Self-Assembly Mechanism of Alkanethiols on Au(111). *Science* 272, 1145–1148 (1996).

50. Maksymovych, P., Sorescu, D. C. & Yates, J. T. Gold-Adatom-Mediated Bonding in Self-Assembled Short-Chain Alkanethiolate Species on the Au(111) Surface. *Phys. Rev. Lett.* 97, 146103 (2006).

51. Maksymovych, P., Voznyy, O., Dougherty, D. B., Sorescu, D. C. & Yates, J. T. Gold adatom as a key structural component in self-assembled monolayers of organosulfur molecules on Au(111). *Prog. Surf. Sci.* 85, 206–240 (2010).

52. Maksymovych, P. & Dougherty, D. B. Molecular self-assembly guided by surface reconstruction: CH3SH monolayer on the Au(111) surface. *Surf. Sci.* 602, 2017–2024 (2008).

53. Li, F., Tang, L., Zhou, W. & Guo, Q. Resolving the Au-Adatom-Alkanethiolate Bonding Site on Au(111) with Domain Boundary Imaging Using High-Resolution Scanning Tunneling Microscopy. *J. Am. Chem. Soc.* 132, 13059–13063 (2010).

54. Poirier, G. E. Coverage-Dependent Phases and Phase Stability of Decanethiol on Au(111). *Langmuir* 15, 1167–1175 (1999).

2. Literature Review

This literature review explores the complex topic of supramolecular self-assembly on the Au(111) surface, from the basic concepts to the fine details of molecular interactions and structures. It highlights the structural characteristics of the Au(111) surface, such as its geometric features and monoatomic step edges, which play crucial roles in the self-assembly processes. The discussion extends to the self-assembly mechanisms of alkanethiol molecules, emphasising the influence of molecular coverage on forming self-assembled monolayers (SAMs). The intriguing properties and assembly behaviours of C_{60} molecules on Au(111) are explored, showcasing their potential in forming complex two-dimensional structures and bridging the gap between molecular self-assembly and electronic functionality.

Moreover, the review acknowledges the pivotal role of STM in providing deep insights into molecular self-assembly and surface interactions. STM's application in surface science highlights its importance in elucidating the complex molecular structures on surfaces. By concentrating on these key areas, the review aims to offer a succinct yet rich overview of the self-assembly of organic molecules on the Au(111) surface.

2.1 Supramolecular Self-Assembly

Surface-assisted supramolecular self-assembly opens avenues for crafting interfaces with tailored chemical properties. In the past thirty years, the exploration of crucial factors like temperature, concentration of the solute, and molecular architecture has gradually enhanced our ability to construct complex SAMNs[1–4]. The initial nucleation and growth phases significantly influence these networks' formation and eventual structure. Investigating and steering the self-assembly at this critical size range becomes possible through confined molecules within precisely patterned surface areas, showcasing nanoscale dimensions[5]. This

approach presents promising opportunities for understanding and directing the assembly process.

Materials confined in small spaces often exhibit physical and chemical properties that differ significantly from those in their bulk form[6]. These changes become evident as the size of the material gets close to that of its components and can continue to be observed even at much larger scales. In the realm of supramolecular chemistry, spatial confinement can lead to significant alterations in how molecules assemble due to restricted movement, constraints related to size and shape, and unique interactions with the surrounding environment. Understanding these effects could lead to the development of precise templates for better control over material creation at the nanoscale.

Research into how confinement influences material behaviour has primarily focused on crystal formation from solutions[7,8]. Crystals confined in small spaces are typically produced by limiting their growth within a porous medium, like porous glass, polymer networks, or anodised aluminium oxide. This confinement, which creates a high surface-to-volume ratio, affects the thermodynamic stability of the crystals, mainly when they are near the critical nucleus size[9,10]. It can result in size-dependent polymorphism, where less stable crystal forms are preferred under nanoscale confinement and can also influence how crystals nucleate and their eventual orientation[11].

Besides solutions, confinement can also affect the assembly of supramolecular structures on solid surfaces. Here, molecules can form two-dimensional networks on a crystal surface, with their arrangement determined by the forces between molecules and the surface. However, this review focuses on surface-based assembly, where molecules are confined to a 2D space. This self-assembly can be formed naturally through surface features like step edges or artificially using methods like selective oxidation[12], etching[13], or chemical modification[14].

Also, different growth patterns can be achieved by controlling the deposition rate and surface temperature to produce other nanostructures[15]. It is experimentally crucial in preparing molecularly self-assembled films, as nucleation depends on these factors. The deposition rate influences the type of nucleation, whether heterogeneous or homogeneous. Furthermore, high-quality films can be produced by controlling the surface temperature of the sample and by introducing surface activators[16].

The study of self-assembly on surfaces necessitates detailed characterisation at the molecular level. A range of approaches have been employed to elucidate the precise arrangement of molecules in self-assembled arrays. Among these, SPM techniques, particularly STM[17], have proven exceptionally effective in providing detailed insights into the structure of supramolecular systems, often at the molecular scale. However, to gain a comprehensive understanding, it is beneficial to complement STM with other techniques that can analyse chemical speciation and structural features beyond the reach of STM. For instance, X-ray photoelectron spectroscopy (XPS)[18,19] enables the examination of the chemical composition of molecules within supramolecular arrays, while X-ray standing wave (XSW)[20] analysis can provide information about the adsorption site. On single crystal surfaces, typical high symmetry sites are three-fold of four-fold hollow, bridging site and atop site.

Despite the availability of various techniques, STM and atomic force microscopy (AFM)[21] remain the predominant tools for studying surface-based supramolecular structures. These SPM techniques are invaluable for characterising individual molecules and molecular assemblies confined to a substrate, providing molecular or even sub-molecular insights. The hallmark of all SPM techniques is the use of a probe to measure specific probe-sample interactions across a grid of points, which is then used to generate an ‘image’ of a defined spatial region of the surface. This often results in resolution at the sub-Ångström level, enabling detailed visualisation and analysis of the surface structures.

A significant consideration in utilising STM for characterisation is that the molecules must be studied on a supporting substrate, thus precluding the examination of solvent-confined systems. The operational mechanics of STM are well-suited for investigating systems confined to a two-dimensional substrate, providing an invaluable technique for studying chemical reactions on potentially reactive and/or catalytic surfaces [22–24]. The requirement for a substrate for these systems precludes the use of transmission electron microscopy (TEM)[25], which, although capable of providing atomic-level resolution, is less suitable for molecule-substrate systems due to the requirement for very thin substrates and beam damage to molecules.

The study of supramolecular self-assembly on surfaces likely commenced with early investigations of hydrogen-bonded assemblies[26–28]. However, it has since expanded to include other non-covalent interactions, such as coordination bonds[29–31] and weaker van der Waals interactions[32–34]. The application of STM facilitates the ready identification of defects within supramolecular arrays and, intriguingly, enables the study of extended structures that lack long-range order. This methodology has been applied to the examination of random, entropically stabilised rhombus tilings[35–37], a molecular Penrose tile[38], quasicrystalline structures[39], and assemblies exhibiting the structure of Sierpiński triangles[40]. These studies have now progressed to the creation of covalently linked structures, including nanographene[41] and covalent-organic frameworks (COFs)[42].

Although the van der Waals interaction is relatively weak, it is critical to self-assemble organic molecules such as fullerenes on the Au(111) surface[43–45]. It can form reversibly, facilitating the formation of well-organized and relatively defect-free supramolecular structures over comparatively large areas. The organic molecules can be used as self-assembly building blocks. Organic molecules are much more advantageous due to their extensive range of potential bonding strengths and a high degree of control and flexibility in their synthesis.

2.2 Surface Structure of Au(111)

Gold stands out as one of the most chemically inert metals in nature. Among many metal substrates available to us, gold is one of the preferred candidates in both vacuum and ambient conditions[46]. It can be treated as a physical support, and it does not break the molecules down. Beyond its remarkable inertness, an astonishing attribute of gold, specifically its Au(111) surface, is its unique surface structure. Conventionally, gold's bulk structure is identified as face-centred cubic (FCC), a configuration known for its efficiency in atomic packing alongside the close-packed hexagonal (HCP) structure. Before the advent of STM, surface orientations like (100)[47] and (111)[48] were examined through techniques such as Reflection High-energy Electron Diffraction (RHEED)[48], High-resolution Helium Atom Scattering (HRHAS)[49], Low Energy Electron Diffraction (LEED)[50,51], and TEM[48,52–54]. TEM first revealed a long-range surface with a reconstruction period of 6.3 nm on the reconstructed (111) gold surface, markedly distinct from the smooth, unreconstructed (111) surface. The use of STM to investigate the Au(111) surface has yielded images with atomic resolution, providing direct visual insight into the atomic structure of the surface[55,56].

2.2.1 The Features of the Au(111) Surface

The Au(111) surface, renowned for its chemical inertness and distinctive surface reconstruction, ranks among the most extensively studied metal substrates[46,47]. Figure 2.1 provides fundamental structural details of gold through a ball-and-stick model. Figure 2.1 (a) showcases a typical face-centred cubic (FCC) unit cell, where blue balls symbolise the atoms at the unit cell's corners, and red balls depict the atoms located on the faces of the unit cell. The grey triangle illustrates the (111) plane situated within the unit cell, offering a clear visual representation of its atomic arrangement[57].

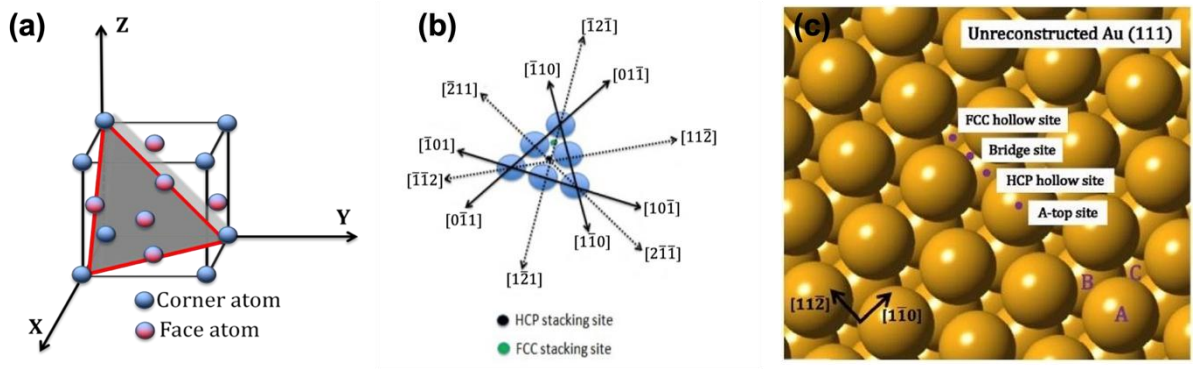

Figure 2.1 Schematic showing (a) Ball-and-stick model of the unit FCC cell in gold's bulk lattice structure; the grey-coloured plane represents the (111) plane. (b) Top view of the grey plane in (a), highlighting the primary crystallographic axes. (c) Ball model illustrating the surface of (1 × 1) Au(111). Purple circles indicate an FCC hollow site, an HCP hollow site, a bridge site, and a top site on the unreconstructed gold surface. Gold atoms in the crystal can be classified into three categories: A, B, and C. Figures are reproduced from Ref [58].

Figure 2.1 (a) shows a ball model of the unreconstructed Au(111) surface, with the four primary adsorption sites denoted by purple spheres. FCC hollow sites are slightly deeper than HCP hollow sites on the gold surface. A top site is directly above each densely packed gold atom in the topmost layer. The purple sphere in Figure 2.1 (c) shows one of the most often encountered bridge locations on the surface. Bridge sites are any sites placed between the other three types of adsorption sites.

2.2.2 The (22× √ 3) Unit Cell

The topography of the reconstructed Au(111) surface is seen in Figure 2.2 (a), with periodic fluctuations discernible as zigzag patterns. On the Au(111) surface, Figure 2.2 (c) depicts a unit cell represented by the Frenkel-Kontorova model[49,59], the ground state determined by F. C. Frank *et al*. This model describes a one-dimensional chain of particles connected by springs in the presence of a periodic potential. It captures the competition between the elastic energy of the springs, which favours uniform particle spacing, and the periodic potential energy, which favours particles sitting in potential minima. This model is used to study phenomena such as

dislocations in crystals, charge density waves, and surface adsorption, and it predicts the existence of commensurate and incommensurate states, as well as kink (soliton) solutions. The lower section illustrates the corrugation of the gold surface in the z-direction. The HCP and FCC zones are designated with identical heights. Gold atoms bind to the layer's bridge sites between the two zones, forming the incommensurate regions. These atoms appear taller in the STM images than those on hollow sites[56].

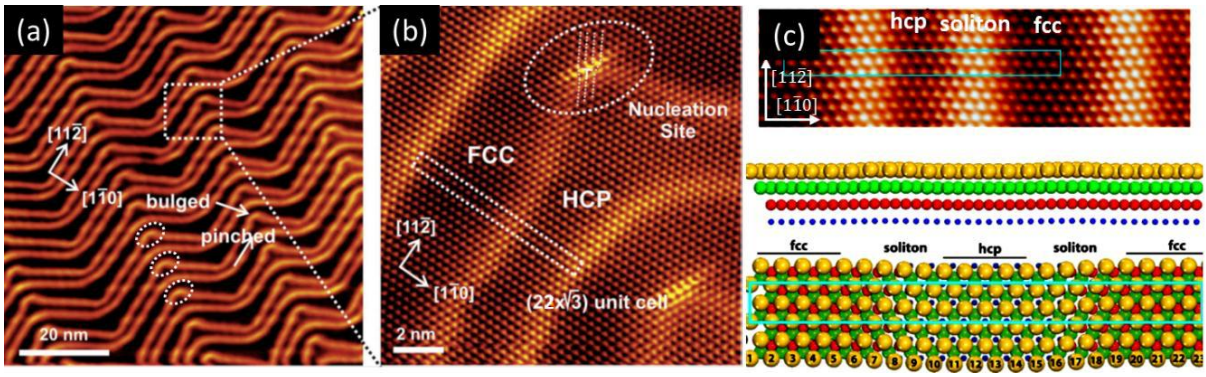

Figure 2.2 STM picture of the reconstructed Au(111) surface in (a). Arrows point to bulged and squeezed elbows. (b) STM image of a herringbone structure on the surface of Au(111). (c) STM image and model of the Au(111)-$(22 \times \sqrt{3})$ reconstruction unit-cell with atomic resolution. Figures are reproduced from Ref [55,60].

The schematic figure in the lower portion of Figure 2.2 (c) represents the gold atoms in the first and second layers, corresponding to the sequential wrinkles in the upper part. Gold atoms in the region HCP stack according to the ABABA model[61]. The gold atoms in the region FCC stack according to the ABCABC model are consistent with the stacking-fault model proposed by Hove *et al*. in 1981[47]. One FCC region, one HCP region and two transition regions are included within a unit cell denoted by a green rectangle. Twenty-three gold atoms occupy each of the 22 bulk lattice locations in the unit cell. This causes a 4.55% uniaxial contraction of gold atoms in one of the [110] directions.

Figure 2.2 (b) illustrates that a unit cell is highlighted in a blue box. The nearest neighbour distance (NND) of the surface gold atoms is measured between 2.70 Å to 2.90 Å. It

agrees with the previous theoretical simulations, which showed a value of 2.7744 Å. Following the close-packing directions, the lateral displacement of atoms is measured as 0.90 Å $\pm$ 0.01Å. It achieves a good agreement with the theoretical result of 0.83 Å. Due to the difference in the occupation sites, gold atoms in the transition regions are brighter than the ones in the FCC or HCP regions. The bright patterns formed by these atoms on the Au(111) are known as the well-known herringbone reconstruction, also called dis-commensuration lines (DLs). The majority of the DLs run in the direction of $[11\bar{2}]$ and are perpendicular to the close-packing directions of the gold atoms [62].

Each $\left(22 \times \sqrt{3}\right)$ unit cell, denoted by the green box in Figure 2.2 (b), contains two DLs split in one HCP area from two half FCC regions. The HCP and FCC sections on both sides of the DLs are 22 and 44 Å wide, respectively. The difference in width indicates that the binding energies of the two locations are different[63]. On the Au(111) surface, the stressed domains are caused by the long-range elastic contact force. The gold atoms at the top layer of Au(111) have a lower coordination number than those in bulk and become unstable. Due to the relatively soft potential energy curve on the repulsive side, surface gold atoms can reduce atomic spacing by shifting a small distance from their original places without too much energy cost. This type of reconstruction does not occur on other (111) metal surfaces, presumably due to a harder repulsive potential. Meanwhile, these surface atoms continue to inhibit the triangular hollow spots preferentially. As a result, most atoms are found in the three-fold hollow sites (FCC and HCP hollow sites), but others are located in the transition areas[64]. Due to bending to relieve stress, the DLs are not always perpendicular to the close-packed directions, causing the gold surface to become anisotropic. When atoms or molecules are deposited on the gold surface, the interaction between the adsorbate and substrate can alter the surface elastic force and lift the herringbone reconstruction[65,66].

2.2.3 Monoatomic Step Edges on Au(111)

The A and B steps are two distinct monoatomic steps composed of closely packed Au atoms on the Au(111) surface. These processes affect the local surface strain and alter the patterns of DLs. The steps of type A ascend along the [11$\bar{2}$] azimuth (or the comparable [$\bar{2}$11] or [1$\bar{2}$1] azimuths) and include a {100} microfacet. As for the B steps, they descend along the [11$\bar{2}$] azimuth and include a {111} microfacet.

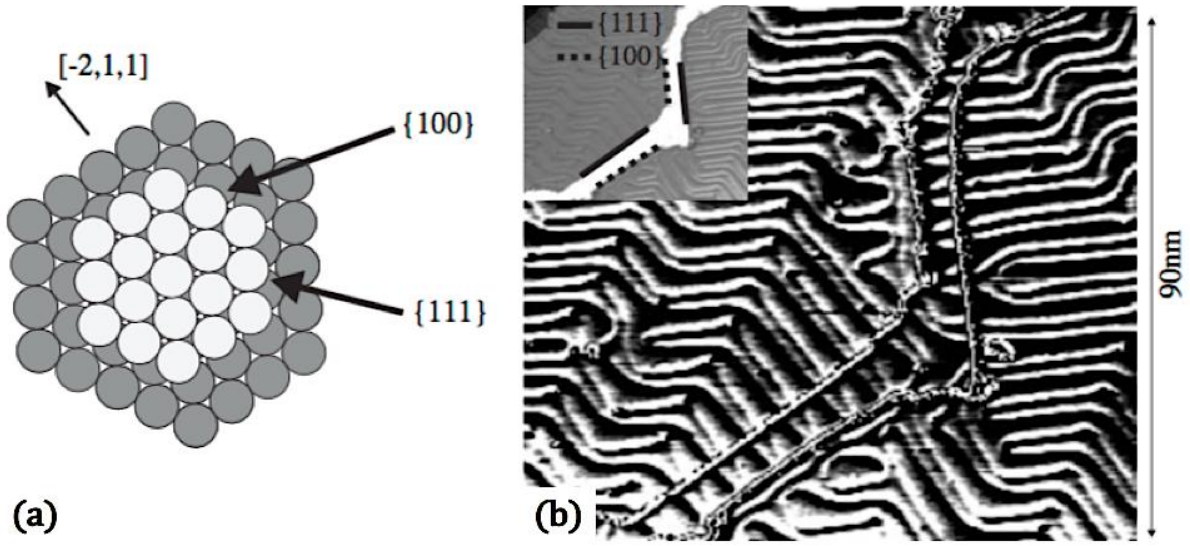

Figure 2.3 (a) Schematic top view of two types of close-packed gold steps: A step with {100} microfacets and another B step with 111 microfacets. The B step descends with the [$\bar{2}$11] azimuth, while the A step ascends. (b) The STM image illustrates the two distinct step edges on Au (111). A lengthy plateau runs from the image's lower left to the upper right corner. The dashed and dashed lines in the inset indicate the {100} and {111} type of steps, respectively. Close to the two stairs, the herringbone restoration has a distinct shape. Figures and captions are reproduced from Ref [67].

Figure 2.3 (a) shows the micro facets of the {111} and {100} type steps, respectively. At a {100} step edge, gold atoms are positioned on the layer's bridge sites, while those at a {111} step edge are placed on the layer's hollow sites. Compared to the {100} facet step, the {111} facet step has a greater atomic density, resulting in lower step energy[65–67].

As illustrated in Figure 2.3 (b), the patterns generated by the DLs on the Au(111) surface surrounding the two types of step edges are different. The DLs can run unassisted across a {111}-step distance. Atoms beneath the plateau have an unreconstructed FCC structure, enabling the atoms at the step edges of the two layers to compress synchronously. When the DLs approach the step edge, the transition area atoms typically flip to FCC stacking. Globally, it results in an expansion of FCC regions and a contraction of HCP regions. As a result, the DLs travel over the {111} step's upper terrace rather than interrupt. On the other hand, when the DLs approach a {100} step point, they reverse direction with a "U" shaped terminus. The FCC regions on the bottom terrace of the {100} steps are sealed by an additional DL growing parallel to the step, ensuring all gold atoms near the step edges have FCC stacking.

2.2.4 Elbow Sites and Rotational Domains

Figure 2.4 (a) illustrates a typical topography of the reconstructed Au(111) surface under our STM. A pair of DLs on either side of a commensuration (FCC or HCP) remain parallel between two adjacent bending points, as indicated by the white dashed lines. Several earlier studies have determined the heights of DLs to be between 0.02 nm and 0.08 nm[68].

The line profile of Figure 2.4 (b) illustrates the surface fluctuation along the black solid line AB. This suggests that the DLs are 0.2 nm taller than the unreconstructed sections, consistent with earlier findings. The DLs on the Au(111) surface regularly bend with a period of 25 nm, and the zigzag patterns are well-known as herringbone reconstructions.

Figure 2.4 (a) illustrates the bending points of domain lines (DLs) on the Au(111) surface. These DLs are categorised into type x or type y based on the number of elbow sites they encompass, with type x DLs featuring sharp elbow sites, while those of type y DLs are more rounded. Specifically, the sharp elbow sites on type x DL can bend towards the nearby face-centred cubic (FCC) or hexagonal close-packed (HCP) regions.

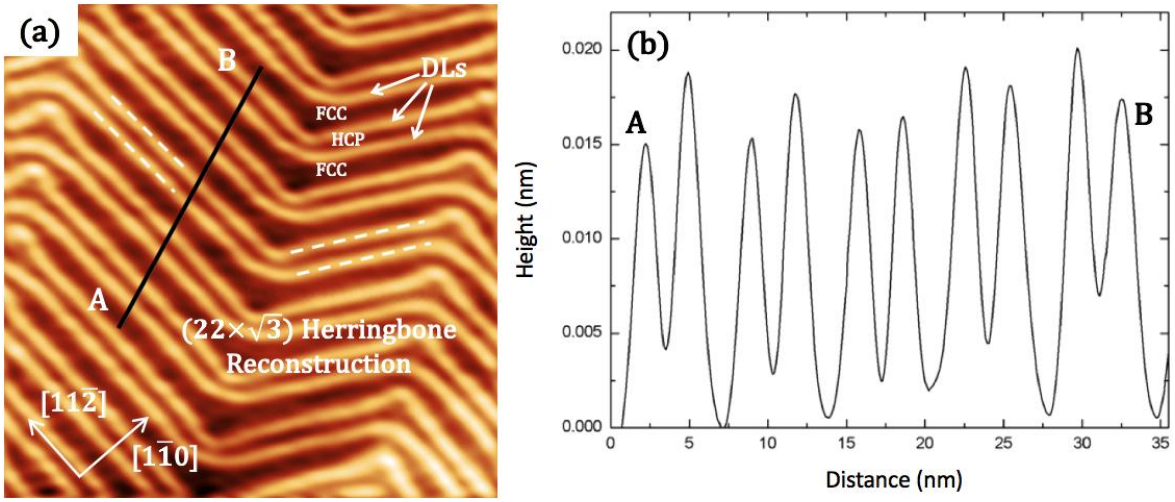

Figure 2.4 (a) STM picture of the DLs on the surface of Au(111) under Room Temperature (RT) (-1.61 V, 0.04 nA. 60 nm × 60 nm). These DLs denote the broad FCC and narrow HCP regions on the gold surface. (b) A line profile along AB demonstrates the height disparities between the FCC, HCP, and DL zones on the Au(111) surface. Figures are reproduced from Ref [69].

In Figure 2.5 (a), a sequence of sharp elbow sites is shown bending into adjacent FCC commensuration zones on the Au(111) surface, resulting in bulged elbow formations. The green boxes highlight areas where the elbow sites appear pinched. These specific sites tend to align with neighbouring HCP regions[65,66]. Along the directions indicated by yellow or green arrows, clusters of bulged or pinched elbows form linear arrays on the surface of Au(111).

Figure 2.5 (b) provides a closer look at the atomic configurations of these sharp and rounded elbow sites. It reiterates that the gold atoms within the DLs are situated in bridge positions, detailing the intricate structural nuances of the Au(111) surface at the atomic scale. There is a row of gold atoms terminating at the elbow site, where the defect is formed. In material science, it can be described as the Burgers vector. To encompass the dislocation while computing the Burgers vector, create a rectangular counterclockwise circuit from a starting point (Figure 2.5 (b)). The Burgers vector will be used to complete the circuit, that is, from the end to the beginning.

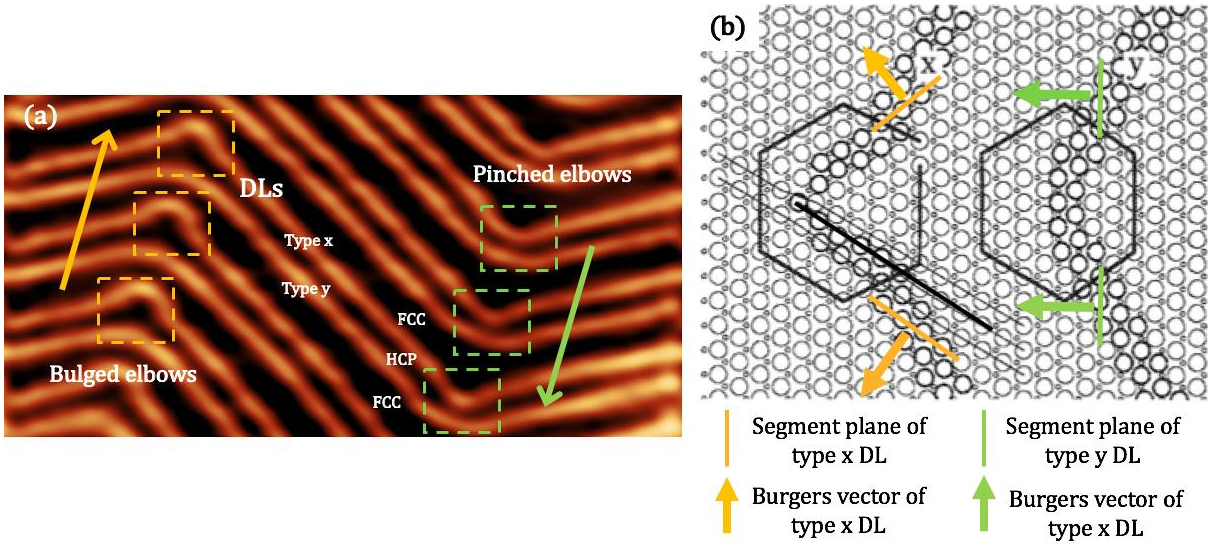

Figure 2.5 (a) High-resolution STM image of the DLs on the Au(111) surface under RT. DLs have either sharp or rounded bending points. Orange and green dashed boxes indicate the bulged and pinched elbow sites with pointed shapes, respectively (-2.0 V, 0.05 nA, 30 nm × 60 nm). (b) Schematic representation of a hypothetical atomic lattice for the pointed and rounded elbow locations. Gold atoms on both sides of the type x DLs occupy distinct orientations of bridge sites. In contrast, gold atoms in the type y DLs occupy identical directions to bridge sites. Figures are reproduced from Ref [65,66].

The dislocation plane determines the vector's direction and is generally one of the closest-packed crystallographic planes. For BCC and FCC lattices exclusively, the magnitude is commonly expressed using the equation:

$$\|b\| = \left(\frac{a}{2}\right)\sqrt{h^2 + k^2 + l^2} \tag{1.1}$$

where a is the unit cell edge length, $\|b\|$is the magnitude of Burgers vector and h, k, and l are the components of the vector. $\boldsymbol{b} = \left(\frac{a}{2}\right)\langle hkl\rangle$.

2.3 Self-assembled Monolayer of Alkanethiol Molecules

As the most straightforward two-dimensional molecular self-assembly system, the self-assembly of alkanethiol molecules on Au(111) surfaces has been studied since 1983[70] and has been extensively explored for more than three decades[71–78]. Alkanethiol molecules are a class

of non-aromatic compounds containing a mercaptan functional group (-SH), which is vital to their chemical properties and can be seen structurally as the replacement of oxygen by sulphur in ordinary alcohols[60,70,79,80]. Figure 2.6 (a) shows a model of a long chain alkanethiol molecular monomer with the S atom in red, which forms a mercaptide group (-SH) with the H atom in white and the C atom in blue in the middle.

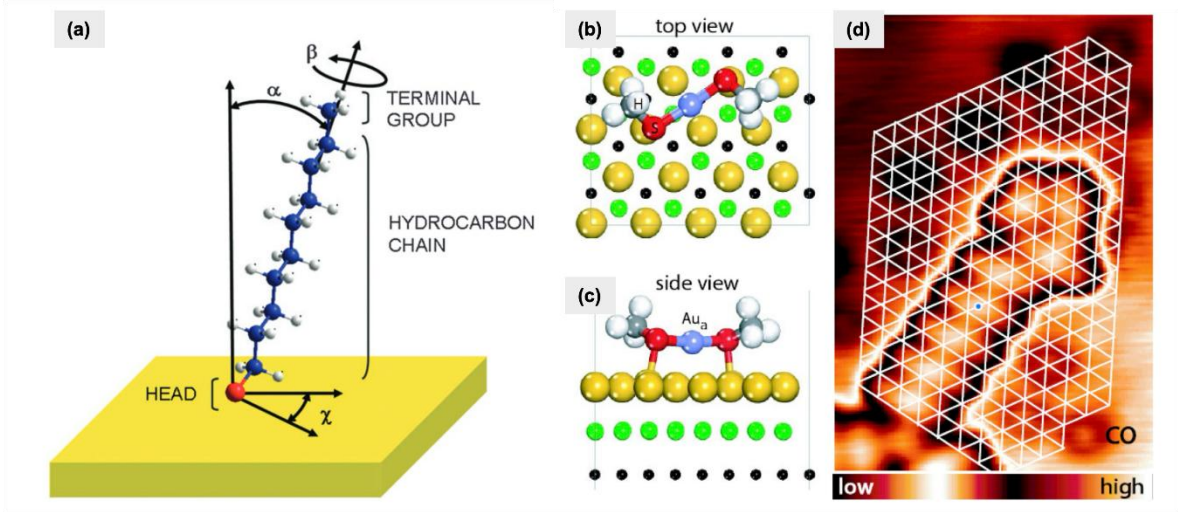

Figure 2.6 A standing-up molecule adsorbed on Au(111) during saturation coverage phases. Typical angles are α=30°, β= 55°, and χ= 14°. Sulfur atoms are red; carbon atoms are blue; hydrogen atoms are white. (b) and (c) Calculated structure of the adatom-bonded complex, which serves as the building block of the CH_3S striped phase. (d) Triangulation of the CH_3S striped phase relative to the underlying lattice, using CO molecules as markers for the Au lattice atoms. The off-hollow position of the Au adatom (indicated by the blue circle) corresponds well with theoretical predictions. Figures and captions are reproduced from Ref [73] and Ref [81].

When a thiol molecule comes into contact with an Au(111) surface at room temperature, a specific reaction occurs. The S-H bond, a key component of the thiol molecule, breaks, leading to the release of H atoms. These H atoms then combine to form hydrogen gas (H_2). The resulting alkyl thiol group (RS-) forms a chemical bond with the gold atoms on the surface. The structure of the alkyl thiol molecular layer that forms results from the interplay between the S-Au bond strength and the van der Waals (vdW) forces among the alkyl chains[79,82].

Figures 2.6 (b) and (c) illustrate the adatom-based structural model for the striped phase unit, suggesting that the released Au adatoms are incorporated into the RS–Au–SR complexes. This hypothesis is directly supported by a quantitative correlation between the coverage of the adatom complexes and the residual coverage of the herringbone reconstruction, as derived from the STM images. A single Au adatom at the threefold hollow site was assumed to bind two CH_3S species. DFT calculations of this model have yielded this structure where the Au adatom is positioned above a twofold bridge site rather than a hollow site. In this configuration, each sulfur headgroup forms one bond with the Au adatom and another bond with the underlying lattice atom, with bond lengths of r(S-Au-adatom)= 2.33 ± 0.01 Å and r(S-Au-lattice)= 2.49 ± 0.01 Å. The symmetry of the calculated structure is in excellent agreement with that observed in the STM image[60]. The central part of the molecule is the alkyl chain, which plays a role in applications such as electron conduction or the electron/photon-induced cross-linking polymerisation of molecules[83–86].

The structure of the self-assembled monomolecular layer of alkanethiol varies with the length of the alkyl chain, indicated by the number of carbon (C) atoms in the thiol molecule, denoted as 'n'. This variability demonstrates the structural differences between the self-assembled molecular layers of short-chain and long-chain alkyl thiol molecules. This review categorises thiol molecules with less than four carbon atoms (n<4) as short-chain thiol molecules. Specifically, discussions will focus on three short-chain molecules: methylthiol (CH_3SH)[87–89], ethylthiol (CH_3CH_2SH)[90–92], and propanethiol ($CH_3(CH_2)_2SH$)[93,94], highlighting the distinct characteristics of short-chain thiol molecule self-assembled layers compared to their long-chain counterparts.

As seen in Figure 2.6 (b), the structure of alkanethiol/Au(111) is well-characterised. The primary bonding structural motif of the alkanethiol on Au(111) is structurally consistent with Au-adatom-dithiolate(AAD)[60,81,82], with the Au adatom occupying the bridge site and the

two S atoms occupying roughly the same site. Although this structural motif is referred to as the staple motif, the AAD is three-legged and bonds to the Au(111) surface through the Au adatom. On the one hand, the bond between S and the Au adatom is strong enough that AAD may move as a single molecule unit on the surface. On the other hand, the link between S and Au is sufficiently weak to enable the S-Au bond to be broken at room temperature (RT). The mobile alkyl chains suggest that the S-Au bond plays a prominent role and that the van der Waals contact between the alkyl chains is less than optimal[85,86].

2.3.1 Short-chain Alkanethiol Molecules on Au(111) Surface

Methylthiolate is a colourless gas at room temperature and pressure, and self-assembled films of methyl mercaptan salts have been experimentally prepared on Au(111) surfaces using a vapour phase method[87,89,92]. The structures of the self-assembled molecular films were characterised using different instruments, and several models for the adsorption of the methylthiolate molecular monolayer on the Au(111) surface have been proposed[88,95–97]. In the first models, it was assumed that the S-atoms of the methylthiolate molecules were adsorbed on the FCC (face-centred cubic) sites or bridge sites on the Au(111) surface, and later on, it was proposed that the Au additional atoms were an essential component of the self-assembled monolayer in this process. On this basis, Voznyy *et al*. proposed a structural model of CH_3S-Au-SCH_3, which fits well with experimental data and is the most accepted model for the self-assembly of methyl mercaptan molecules[60,97].

Q. Guo *et al*. used STM to systematically investigate the molecular self-assembly of methyl mercaptan molecules on Au(111) surfaces[92]. Using high-resolution STM images, they analysed the phase transitions and the corresponding molecular structure models of methylthiolate molecules at different coverage levels. They found that the molecular monolayer was a (3×4) structural phase when all the methylthiolate molecules were absorbed

on the Au(111) surface at saturation coverage. This structural phase was discovered in 1997[98] and researchers were not aware of this (3×4) structure at that time [99].

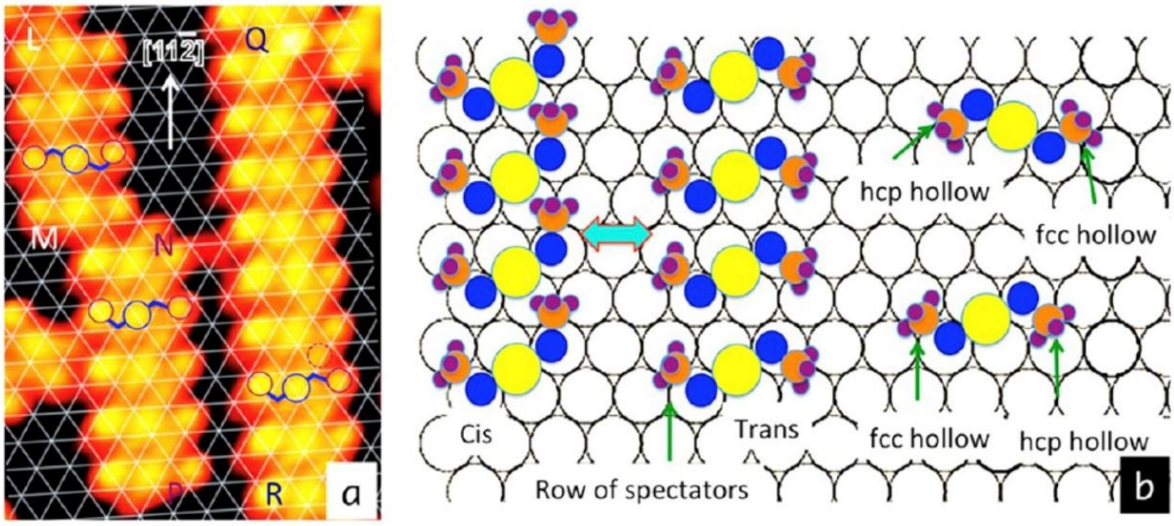

Figure 2.7 (a) The triangulation method determines the relative orientation of AAD units inside the stripes. AAD within stripes NP and QR have the same direction in the image. AAD inside stripe LM adopts a different orientation. (b) Ball model of the local structure surrounding solitary AAD and AAD stripes. Figures and captions are reproduced from Ref [92].

Meanwhile, Q. Guo *et al*. showed that as the molecular coverage of methylthiolate decreases, the molecular SAMs change from a (3×4) phase structure at saturation coverage (1/3 ML) (1 ML means one thiol molecule should be adsorbed on each Au atom) to $\left(7 \times \sqrt{3}\right)$rect and (3×4) phases coexisted at 0.286 ML coverage[89,91]. A striped phase structure appears at molecular coverage less than 0.28 ML, while at molecular coverage less than 0.25 ML, more AAD units appear on the Au(111) surface. As shown in Figure 2.7, Au-adatoms occupy the bridge sites on the Au(111) surface with the bond length between the S-atoms and Au-adatoms (0.25±0.01 nm). The bond length between the S-atoms and the Au-atoms is smaller than the distance between the top site and the bridge site so that the two S-atoms do not occupy the top site Au-atoms near the FCC vacancy and the HCP vacancy but deviate from the top site.

The previous study using normal incidence X-ray standing wave (NIXSW) analysis also shows that the sulphur head group occupies the atop site for methythiolates on Au(111), with an Au–S distance of 0.25±0.01 nm, and not the hollow or bridging sites favoured by theoretical calculations[100].

Three stripes are depicted in Figure 2.7 (a): LM, NP, and QR. AAD units in stripe NP are oriented similarly to those in stripe QR. AAD units take on an alternate orientation in stripe LM. Although the two directions appear identical, they differ in minor ways, as illustrated schematically in Figure 2.7 (b). Regardless of the orientation of the AAD, the Au adatom occupies the bridge location. S atoms are located above, but not immediately above, surface Au atoms. From the STM image, the bond distance between sulfur (S) and gold (Au) adatoms measures 0.23±0.01 nm, shorter than the 0.25±0.01 nm distance between an atop site and its nearest bridge site. The location between the S atom and the Au adatom features mixed coordination: face-centred cubic (FCC) on one side and hexagonal close-packed (HCP) on the opposite side.

Consequently, this arrangement results in asymmetry between two methyl groups attached to the sulfur; one group is oriented towards an HCP site, and the other towards an FCC site, leading to different energy barriers for the cis-trans transition between these two methyl groups[89,91,92]. An AAD unit that has the same orientation as the CH_3 group can be defined as cis, and with an opposite orientation is the trans. Although this energy difference might be insignificant, as both methyl groups can undergo cis-trans transition when the alkylthiolate is isolated, the dynamics change in a collective environment. As illustrated in Figure 2.7 (b), methyl groups on one side of a molecular stripe may not participate actively in the alkylthiolate adsorption dynamics and are considered spectators, with the cis-trans transition primarily occurring on one side. It remains unclear whether the methyl group next to an HCP site or the one next to an FCC site acts as the spectator. However, it is suggested that the cis-trans

transition predominantly occurs within a single molecular stripe, involving the bulk of the groups.

The self-assembled molecular monolayer structure of ethylthiolate molecules on Au(111) is similar to that of methylthiolate[89,91,101,102]. D. M. Kolb *et al.* prepared an ethylthiolate molecular monolayer on Au(111) using a liquid phase method and observed a (3×4) densely packed structure and a $\left(7.5 \times \sqrt{3}\right)$ striped phase structure by STM at room temperature[103]. However, no specific molecular adsorption sites or structural models could be given.

Q. Guo *et al*. used the vapour phase method to deposit ethylthiolate molecules onto the Au(111) surface placed in a UHV system[89,91,101,102]. A densely packed(3×4) structure of ethylthiolate molecules at a coverage of 1/3 ML is produced. The long-range ordered $\left(5\sqrt{3} \times \sqrt{3}\right)R30°$ and $\left(6\sqrt{3} \times \sqrt{3}\right)R30°$ striped phase structures were observed at 0.27 ML and 0.23 ML coverage, respectively, and the STM image showed that these striped phase structures were composed of AAD units as well, in which the adsorption sites of the Au-atom and the two S-atoms were consistent with the adsorption sites of the methylthiolate on the Au(111) surface of the striped phase.

In Figure 2.8 (a), propylthiolate molecules have longer alkyl chains (3 C atoms) than methyl and ethylthiolate molecules[79,104]. As the alkyl chain grows, the STM image shows that the (3×4) structure will disappear, and a $c(4 \times 2)$ structure will emerge. However, the structure of the propylthiolate molecular monolayer at saturation coverage of the Au(111) surface still appears as a (3×4) phase. Unlike the (3×4) phase in the methylthiolate and ethylthiolate molecular monolayer, the propylthiolate SAMs have narrower molecular domains of (3×4) structure and relatively concentrated domains of (3×4) structure.

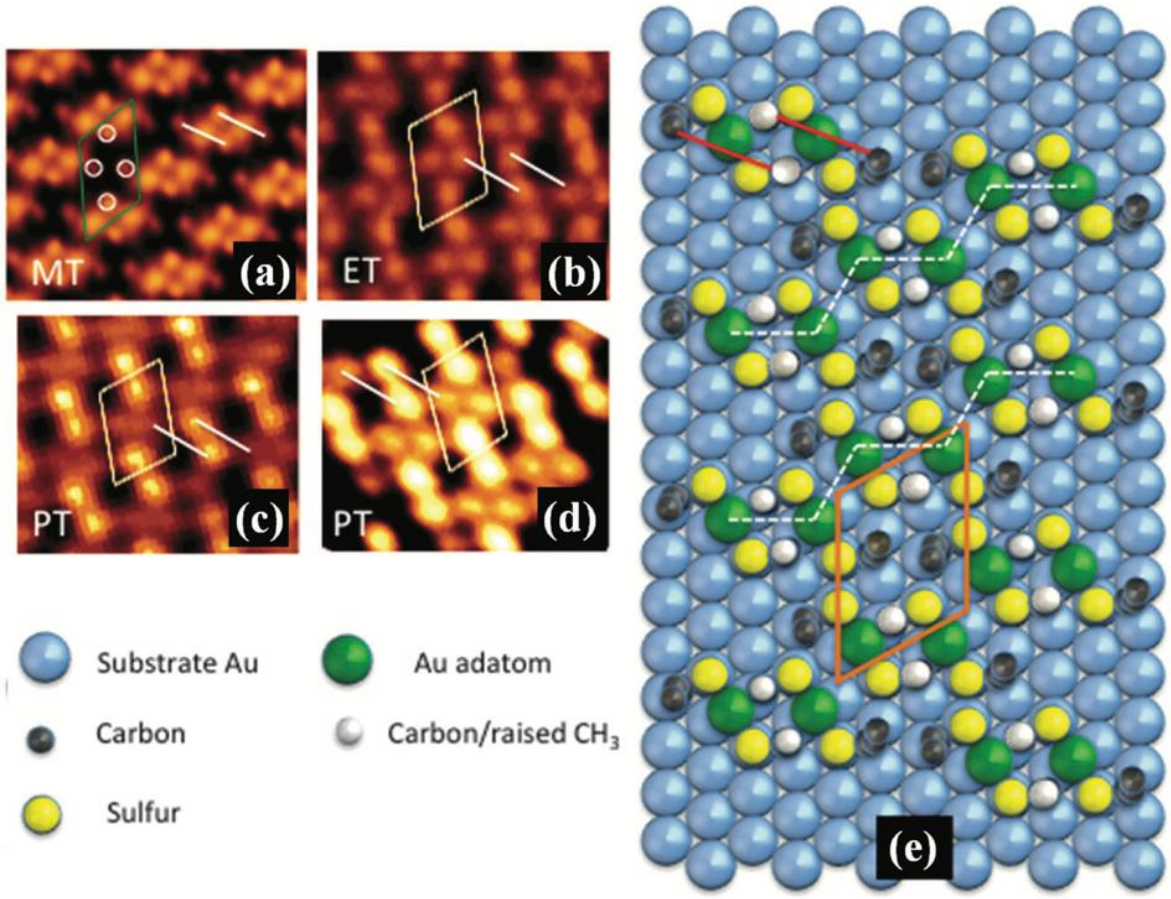

Figure 2.8 STM images of methylthiolate (a), ethylthiolate (b), and propylthiolate (c)/(d) monolayers are shown in Figure 2.8 (a–d). Each image contains white bars to emphasise the Au-adatom-dithiolate unit. Circles denote the locations of the methyl groups within the unit cell in (a). (e) Ball model of a monolayer of propylthiolate on Au (111). White dots denote the zigzag arrangement of the $CH_3(CH_2)_2S–Au–S(CH_2)_2CH_3$ rows. Figures and captions are reproduced from Ref [106].

The structural model in Figure 2.8 (b) is based on propylthiolate, and hydrogen atoms are omitted for clarity. Based on this model, it is evident that each RS–Au–SR has a distinct environment for its two propyl chains. Propyl chains adjacent to Au atoms of RS–Au–SRs are represented by light grey spheres. It appears taller because it is less slanted than the others (black spheres). The end group is CH_3. It is more likely that the differences are caused by geometric effects, where it can tilt up taller under STM, but electronically, they are quite similar. This results in half of the propyl chains in the SAM being twice as tall. A similar phenomenon occurs with methyl- and ethylthiolate monolayers, although with a lower contrast in height[105].

Even SAMs of mixed species can produce the (3×4) phase. This phase has been shown to form in a mixed methyl- and propylthiolate monolayer[79].

The presence of these domains makes the propylthiolate SAMs' saturation coverage only 0.325 ML, less than 1/3 ML of the methylthiolate and ethylthiolate SAMs. Q. Guo *et al*. suggested that this may be due to the energy barrier inherent to the propylthiolate SAMs preventing the molecules from forming larger (3×4) structures. At the same time, the increase in alkyl chain length may introduce more significant stress, which is released at the domain boundaries by the formation of narrower (3×4) structured molecular domains in monolayer[87,91,92,104,106,107].

Through the study of SAMs of methylthiolate[89,91,92], ethylthiolate[91,101,102,108] and propylthiolate[109], a model for the adsorption of short-chain (n<4) alkanethiol molecules on Au(111) surfaces and the phase transition processes at different molecular coverages has been determined. On this basis, the adsorption mechanism of long-chain (n>3) thiol molecules in self-assembled molecular films on the Au(111) surface will be discussed.

2.3.2 Long-chain Alkanethiol Molecules on Au(111) Surface

The influence of longer alkyl rows makes visualising the adsorption pattern of long-chain alkanethiol molecules on the Au(111) surface challenging[110,111]. In early experiments on the adsorption of alkanethiol molecules on the Au(111) surface to form molecular films, a model shown in Figure 2.9 (a) was proposed[110]. Each thiol molecule is shown as a separate unit adsorbed on the Au(111) surface and self-assembles to form SAMs. The dark blue atom represents the S atom, the green part represents the methyl group, which appears as the end group and the middle grey part of the alkyl chain represents the C chain.

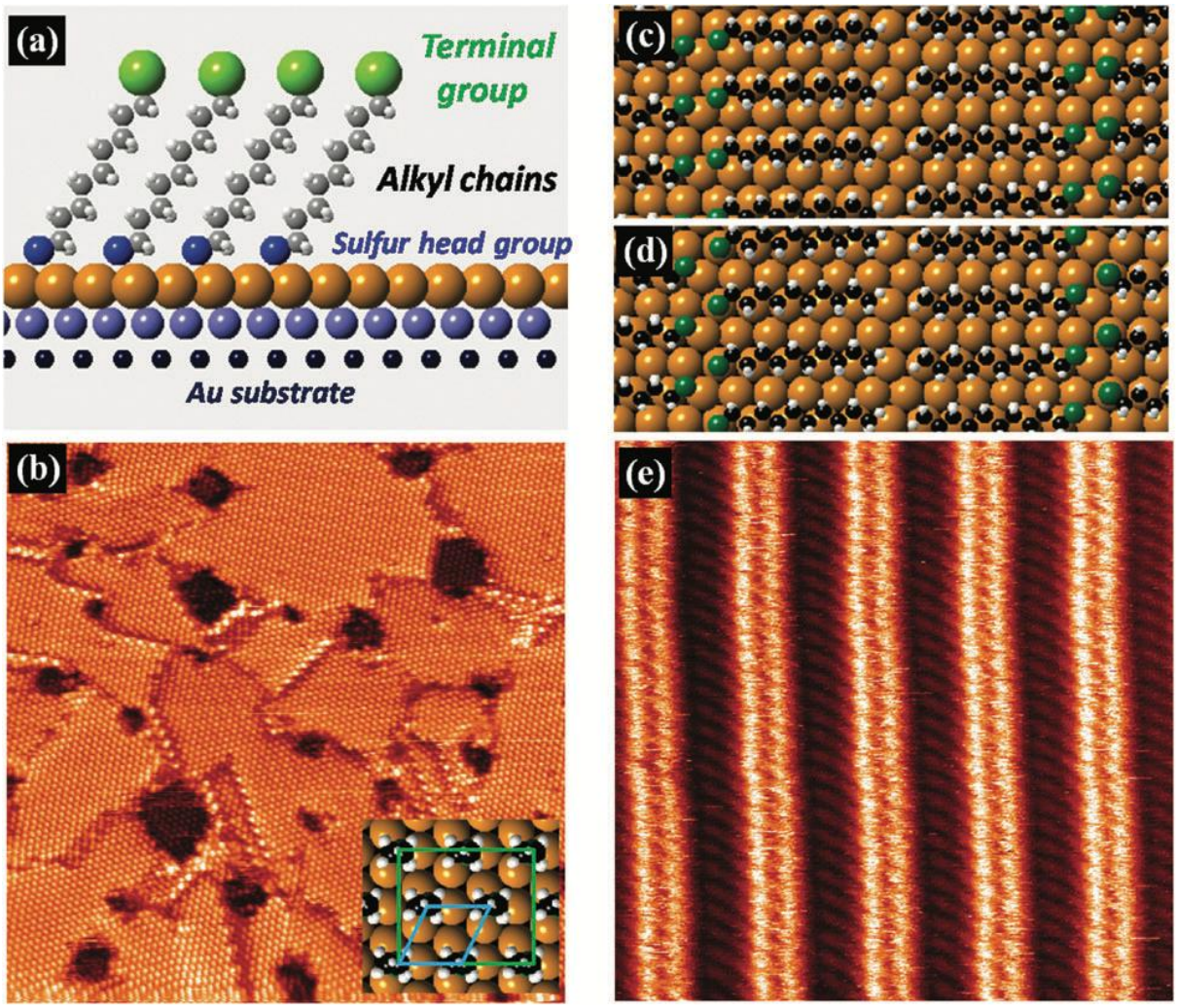

Figure 2.9 (a) A simplified representation of alkanethiol monolayers, assuming the –SR group attaches directly to a uniform, high-symmetry location on an ideal Au(111) surface. (b) STM image of an octanethiol monolayer at full coverage, measuring 40 nm by 40 nm. The inset illustrates a previously accepted structural theory before identifying the RS–Au–SR arrangement, which shows its structural phase $(\sqrt{3} \times \sqrt{3})R30°$. (c) and (d) depict structural concepts of the striped phase, characterised by thiol molecules oriented horizontally. (e) An STM image of a striped phase with dimensions of 15 nm by 15 nm. Figures and captions are reproduced from Ref [79].

However, by considering the presence of Au-S bonds on the molecular surface, recent experiments have shown that this model of adsorption of alkyl thiol molecules on the Au(111) surface does not correspond to the STM image. Subsequently, the Au-S-R structure was proposed based on the plausible presence of Au adatoms[60,81]. This new structural model is widely accepted, a large number of Au atoms are inevitably involved in the formation of

alkanethiol SAMs on the Au(111) surface, and theoretical calculations predict that the involvement of additional Au atoms reduces the energy of the whole system of alkanethiol SAMs on the substrate. This also provides theoretical evidence for the existence of the Au-S-R structure[111].

Figure 2.9 (b) shows a $(\sqrt{3} \times \sqrt{3})R30°$ densely packed phase structure formed by the self-assembly of molecules on the Au(111) surface, which has a molecular coverage of 1/3 layer. The $(\sqrt{3} \times \sqrt{3})R30°$ phase has also been observed by LEED[112] and HAS[113] techniques. Infrared spectroscopy showed that the alkyl chains of the alkanethiol molecules in the $(\sqrt{3} \times \sqrt{3})R30°$ phase are at an angle of 30° to the surface of the substrate[114,115].

As shown in Figure 2.9 (b), the edge of each domain boundary shows the etching pits of varying sizes, and the structure of the alkanethiol molecules in these pits is also a densely packed phase structure[82]. It was found that the dehydrogenation of the long-chain thiol molecules formed these etching pits[82]. This is due to the formation of S-Au bonds between the S atoms and the Au atoms on the surface of the samples, which then results in the absence of some Au atoms on the relatively flat Au(111) surface. That also provides indirect evidence for involvement of Au atoms in forming alkanethiol SAMs[116]. Also, Au atoms at the steps of the Au(111) surface are involved in constructing alkanethiol SAMs. Etching pits are not usually seen if alkanethiol SAMs are prepared under UHV condition using the vapour phase method. Since the molecular beam flow is often minimal in the vapour phase process, there are enough Au atoms at the steps and terraces to form SAMs[101,107].

Considering the participation of Au atoms, two models for the unitary structure of thiol molecular films can be created. One is a single thiol model in the form of Au-adatoms, the Au-S-R structural unit model, and a double thiol model with Au atoms as linking atoms. The other is the RS-Au-SR structural unit model. Since involving Au atoms structural form in molecular

self-assembly is the key, the AAD unitary model (RS-Au-SR) has gained increasing experimental and theoretical support[60,79,81,97,117].

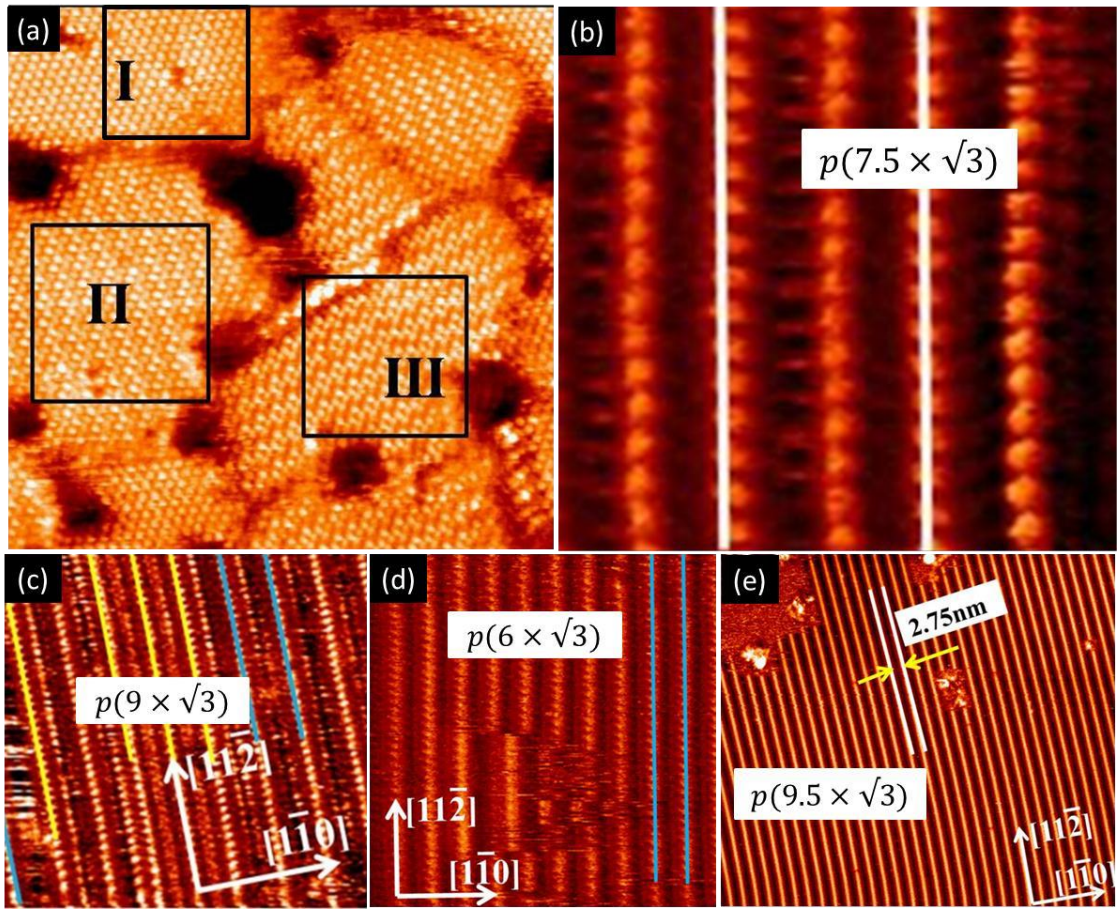

Figure 2.10 STM image of alkanethiol molecules on Au(111) surface with different molecular coverage (a) STM image of octanethiol molecules saturated on the Au(111) surface. (b)–(e) Several low-coverage striped phases with different periods. Figures are reproduced from Ref [79].

This RS-Au-SR dual thiol unitary structure model has been demonstrated for short-chain (n< 4) alkanethiol SAMs. In contrast, long-chain (n>3) alkanethiol SAMs have only been directly observed for butylthiolate[109]. However, in recent studies, the RS-Au-SR model has been consistently identified as the most fundamental structural unit for both SAMs formed on flat Au surfaces and Au nanoparticle surfaces by using NIXSW[100] and XPS[118]. Therefore, although the structural units of alkanethiol molecules with longer alkyl chains (n≥4) self-

assembled on Au(111) surfaces are not directly observed experimentally, this RS-Au-SR structure model is gaining acceptance[119–122].

Figure 2.10 (a) shows an STM image of octanethiol (OT) molecules saturated on the Au(111) surface. The OT molecule is stably adsorbed on the Au(111) surface by forming a chemical bond with the Au atom on the surface. At the same time, the vdW forces between the alkyl chains ensure the stability of the surface structure. Each bright spot in the image corresponds to a molecule. Previous studies have favoured the hollow position of the Au additional atom at FCC on the Au(111) surface, which has threefold symmetry[60,81]. Recent studies suggest that based on the RS-Au-SR unit structure model, it is more reasonable for the Au-adatom to fall at the Au(111) surface bridge position and for the two S-atoms bonded to the Au-atom to fall near the top position of the Au-atom on the surface. This ensures sufficient space between the alkyl chains to form the $(\sqrt{3} \times \sqrt{3})R30°$ structure. A $c(4 \times 2)$ STM also observed a superlattice structure with light and dark differences on the surface of the molecular layer.

Black rectangles mark the three regions with different molecular self-assembly structures. In region I, the surface molecules are uniformly bright and dark, with a $(\sqrt{3} \times \sqrt{3})R30°$ phase. In Regions II and III, the molecules are both bright and dark, and the molecules show a regular periodic arrangement of brightness and darkness, with a $c(4 \times 2)$ phase. This $c(4 \times 2)$phase is due to a phase transition following a lateral displacement of the molecule in the $(\sqrt{3} \times \sqrt{3})R30°$ structural phase along the $[11\bar{2}]$ direction. The experimental results prefer to consider that the bright spots represent information on the electronic state of the head group (S-Au) of the alkyl chain. As the gap between the highest occupied molecular orbitals (HOMO) and the lowest unoccupied molecular orbitals (LUMO) of the methyl group (-CH3) is greater than 5 eV. This results the energy of the terminated group of the alkyl chain

exceeds the energy that electrons can tunnel at the STM tip or within the molecule during STM scanning. In addition, LEED experiments revealed that the head group (S-Au) is ordered while the end group (-CH_3) is disordered at room temperature[112], which indirectly confirms this claim experimentally. Heating and annealing the sample surface further obtained the structure of the molecule in the striped phase at low coverage. It was shown that after annealing at different temperatures, the surface molecules showed different coverages, which led to the appearance of a striated phase structure in the form of $(p \times \sqrt{3})$ (p is the ratio of the intermolecular width of the striated phase to the distance between the nearest neighbouring atoms on the Au(111) surface. For example, $(7.5 \times \sqrt{3})$ striated phase structures appeared when the sample was heated at 353 K for 1 hour, and $(9 \times \sqrt{3})$ standing structures appeared when the sample was heated at 373 K for 30 minutes. Figure 2.10 (c) (d) (e) illustrates the STM images at different molecular coverage levels. In addition to their different periods, these striped phases have some common features: all the molecules in the stripe chain preferentially grow in the $[11\bar{2}]$ direction, where the molecular spacing is $\sqrt{3}a$ (a is the nearest neighbour spacing in the Au(111) plane.

The self-assembly mechanism of long-chain (n≥4) alkanethiol molecules on Au(111) surfaces has been investigated by different experimental techniques and theoretical simulations[82,116,123–126], and the monolayer of alkanethiol molecules is determined to form a molecular membrane in the AAD (RS-Au-SR) model as a unitary structure. The adsorption positions of the Au additional atom and the two S atoms were further demonstrated. On this basis, the influence of molecular coverage on the molecular adsorption structure was further investigated in chapter 4. The self-assembly of alkanethiol molecules on Au(111) surfaces is an essential branch of the molecular self-assembly monolayer. More theoretical calculations and experimental data are needed to support this mechanism.

2.4 C_{60} Molecule

The fullerene family of carbon allotropes comprises those having cage-like and tube-like structures[127]. Hollow closed-cage molecules are frequently abbreviated as C_n, where n denotes a molecule's total number of carbon atoms. Krätschmer and Diederlich *et al.*[128] acquired macroscopic amounts of the well-known carbon isomers C_{20}, C_{28}, C_{36}, C_{60}, C_{70}, C_{76}, and C_{84} from benzene-soluble compounds generated by resistive heating graphite using the gravity chromatography approach in an inert environment. The atoms within these molecules donate covalent single or double bonds, forming entirely or partly closed meshes with five, six, or seven atom rings[129].

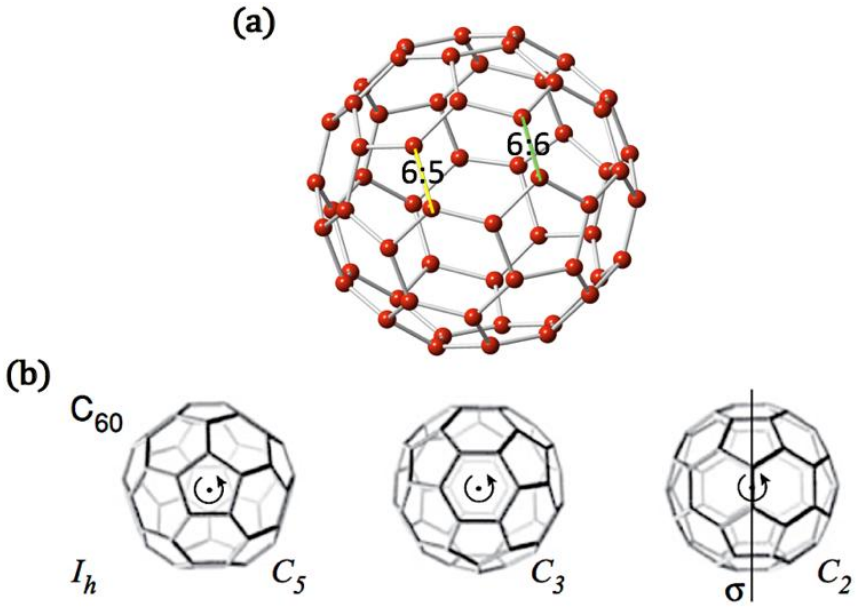

Figure 2.11 (a) Schematic representation of the structure of a C_{60} molecule. (b) DFT simulations illustrate the three symmetry types of a C_{60} molecule: C5, C3, and C2. Figures are reproduced from Ref [130].

C_{60} has the fewest carbon atoms and exhibits the highest symmetry of all completely closed fullerene molecules. Apart from the properties described above, Howard *et al.* effectively synthesised these two molecules using hydrocarbon combustion[131]. C_{60} molecules have a physical diameter of ~ 7.1 Å, which is measured from the centre of the C_{60} molecule to

the centre of the carbon atom. The vdW diameter (~ 10.3 Å) is affected by the outer electrons of the carbon atoms. It is determined by XRD [135] in the C_{60} crystal[132] and the gas phase[128,133,134], which measures the distance from the centre of one C_{60} molecule to the centre of the other nearest C_{60} molecule.

A C_{60} cage is composed of 60 carbon atoms. Figure 2.11 (a) depicts a schematic representation of the C_{60}, which is composed of 20 hexagons (six-atom rings) and 12 pentagons (five-atom rings). Only two forms of covalent bonding bind the carbon atoms in hexagons and pentagons. Between two adjacent hexagons, a carbon-carbon double bond (referred to as 6:6 bonds) occurs that is electron-deficient and has an average bond length of 1.450 ± 0.015 Å. There is a single electron-rich carbon bond between a pentagon and a hexagon ring (designated as a 6:5 bond)[136,137]. A single carbon bond is on average 0.5 Å larger in length than a double bond[138].

In group theory, symmetries such as C_2, C_3, and C_5 refer to cyclic groups of rotations that leave an object invariant. These symmetries are common in the study of molecular and crystallographic structures. Basically, C_2, C_3, and C_5 symmetries are cyclic groups of rotations by 180°, 120°/240°, and 72°/144°/216°/288° respectively, each defining a specific set of symmetrical rotations for objects like molecules and geometric shapes.

As seen in Figure 2.11 (b), the structure of a C_{60} molecule belongs to the three-dimensional complete icosahedral point group denoted by the symbol I_h. It has an order of 120 and comprises a succession of subgroups of symmetries, all occurring on a sphere. It is symmetrical in the I_h direction, with five, three, and twofold axes. One hexagon and one pentagon ring are detected along the rotation axis of a C_{60} molecule's C_5 and C_3 symmetries. While the C_{60} molecule rotates by a mirror plane perpendicular to the three-fold axis, the C_{60} molecule with C_2 symmetry rotates by a mirror plane that divides the molecule into two equal

pieces. At room temperature, C_{60} molecules can assume a variety of orientations when placed on a flat substrate such as Au(111) surface, and the height change associated with rotation can be ignored[139–141].

2.4.1 Self-assembled C_{60} Molecules on Au(111) Surface

Due to their high electron affinity, free C_{60} molecules can gain electrons from the surface atoms of the metal[140]. Under the combined influence of both molecule-substrate and molecule-molecule interactions, C_{60} molecules can easily absorb and form some self-assembled structures on the metal surface. At room temperature, C_{60} molecules exist in a solid state, but these solid C_{60} molecules gain energy upon heating. They are deposited as gaseous molecules on the metal surface, where the molecules diffuse around the surface[142]. When the molecules are trapped by the potential well on the metal surface, the C_{60} molecules will adsorb to a particular site and thus combine with numerous other molecules by vdW forces. Then, a specific assembly structure is formed on the metal surface. The interaction of C_{60} molecules with different metal surfaces takes various forms, and the adsorption configurations of C_{60} molecules on the Au(111) surface are discussed below.

C_{60} molecules can move across the Au(111) surface at room temperature, eventually halting their diffusion at the edge of a surface step, which serves as a nucleation site. As depicted in Figure 2.12 (a), subsequent C_{60} molecules will attach near the initial C_{60} molecule on the Au(111) surface, forming a monolayer structure. At reduced temperatures (approximately 80 K), C_{60} molecules lack the necessary energy to surpass the potential barriers at the curves of the "herringbone" pattern created by the mismatch in lattice structures on the substrate surface.

The molecules are bound to the elbow site for nucleation. As the molecules are gradually deposited, smaller islands of two-dimensional C_{60} molecules are formed at the bend

of the 'herringbone' structure, as shown in Figure 2.12 (b). At lower molecular coverage, the molecules are initially deposited only in the FCC portion of the structure near the step edge due to the different affinity of the FCC and HCP portions for C_{60} molecules. As the amount of molecules deposited increases, the densely packed C_{60} molecular island is formed in a layered fashion[132].

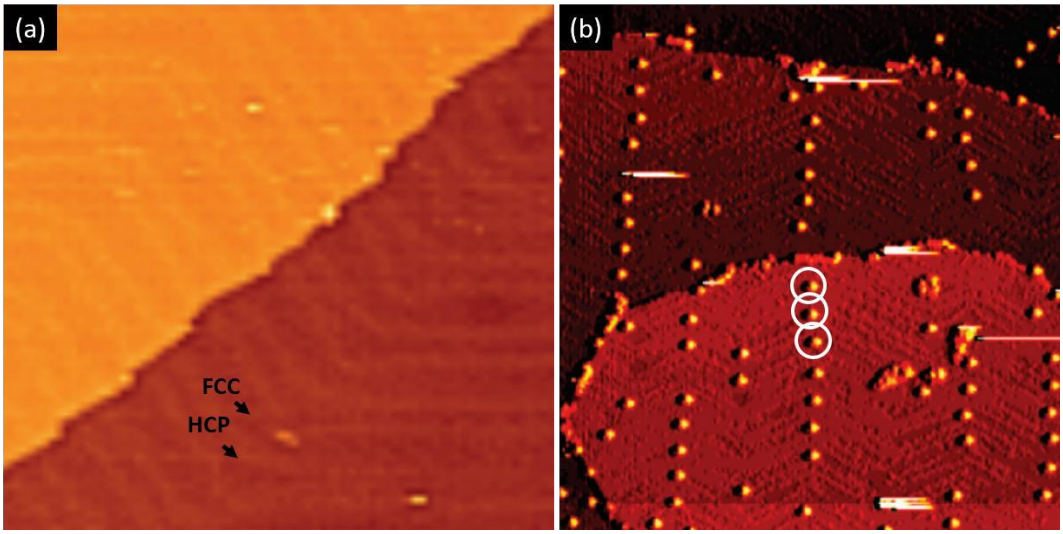

Figure 2.12 Absorption Site of C_{60} on Au(111). (a) STM image of herringbone structure on Au(111) surface. (b) STM image of C_{60} molecular adsorption on Au(111) surface at low temperature. Figures and captions are reproduced from Ref [69].

Compared to the first layer, the C_{60} molecules in the second layer have a weaker interaction with the substrate and are more likely to be desorbed on the surface. Due to this nature, clean C_{60} molecular monolayers can be obtained experimentally by annealing the C_{60} molecular layer in the temperature range 300 °C < 7 < 500 °C (where 300 °C is the desorption temperature of the second layer and 500 °C is the desorption temperature of the first layer[142]. The crystallographic orientation of the densely packed phase C_{60} molecule cover layer on the Au(111) surface is not identical. Furthermore, the relative orientation of the densely packed phase C_{60} molecule cover layer can be obtained using the $[11\bar{2}]$ direction on the Au(111) surface as a reference.

2.4.2 Close-packing Structures of C_{60} on Au(111) Surface

Many densely packed structures can develop when a thin layer of C_{60} molecules is placed on the Au(111) substrate at room temperature[68]. Each C_{60} molecule is simultaneously impacted and stabilised by vdW forces from neighbouring molecules and the chemical contact with the gold substrate[143,144]. When the gold substrate is heated to a sufficient temperature C_{60} molecules diffuse freely across the smooth sample surface before adhering to step edges or defects[145]. Then, these molecules coalesce into dense islands. The vdW force assembles C_{60} molecules into multilayer thin films at large coverages[146].

R0° Structure and (2√3×2√3)R30° Structure

At room temperature, the majority of C_{60} molecules form an R0° or In-phase structure on the Au(111) surface[147]. In-phase means the closed-packed direction of the C_{60} molecules is the same as the closed-packed direction of gold atoms. C_{60} molecules form long chains with the {111} steps and form as large-sized domains. Assuming that the substrate is free of defects, the orientations of the C_{60} domains are frequently defined by the gold step types[43].

In Figure 2.13 (a), all C_{60} molecules occupy comparable FCC or HCP hollow sites on the Au(111) substrate, forming a greater connection between C_{60} layers and gold atoms. The close-packed directions of the C_{60} make an angle of 30° to the gold atoms below, and the nearest neighbour distance (NND) of the molecules is $2\sqrt{3}$ times the spacing of the surface gold atoms. The *R*30° lattice is thus thermodynamically more favourable for C_{60} molecules than the *R*0° configuration. Since the R30° lattice matches the substrate gold distance, and the R0° lattice is in random absorption sites. Therefore, the R30° structure is more stable on the surface. The C_{60} molecules on the Au(111) surface, on the other hand, can alter the gold surface. Certain C_{60} molecules seem brighter than others in the *R*30° phase. These brighter molecules interact with the gold substrate more weakly.

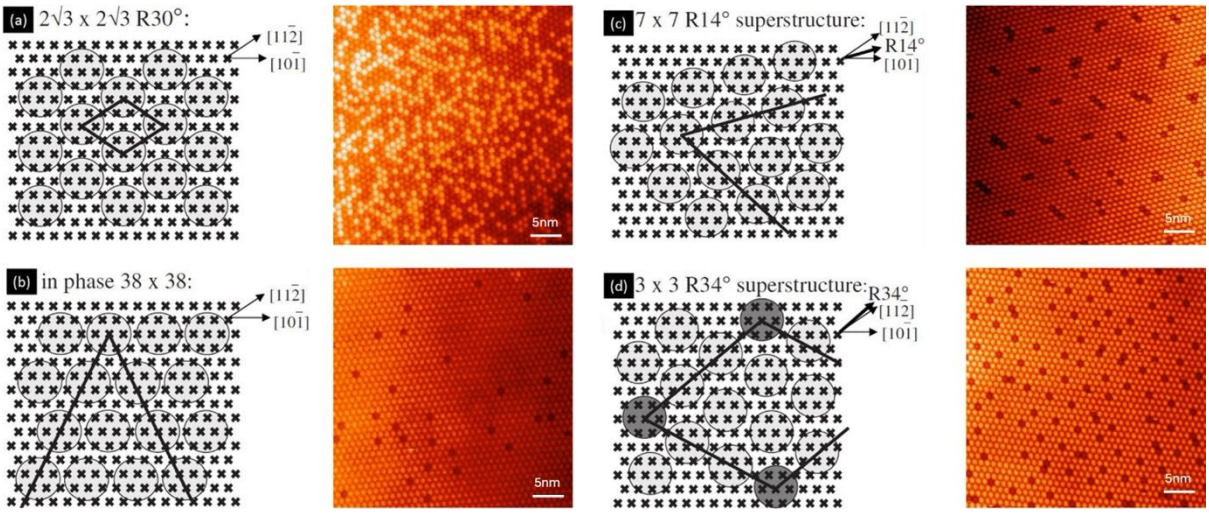

Figure 2.13 Schematic depicting the four superstructures of C_{60} molecules on the unreconstructed surface of Au(111) and their corresponding STM images: (a) the $R30°$ phase, (b) the R0°, (c) $(7 \times 7)\, R14°$ and (d)$(3 \times 3)\ R34°$ phases. (a) A solid black parallelogram denotes the unit cell of R30°, and (b) a rhombus denotes half of the intact unit cell of $R0°$. The crosses on the substrate represent gold atoms, while the light and dark spheres represent C_{60} molecules. The thick black arrows indicate the orientations of close packing of the molecules in the two types of formations. Figures are reproduced from Ref [148,149].

Figure 2.13 (b) illustrates this packing configuration. A black triangle denotes half of a supercell containing (38×38) gold atoms or (11×11) C_{60} molecules. This dense packing is also observed when C_{60} is placed on metal surfaces such as Cu(110) or Ni(110)[143]. The NND of C_{60} molecules in the R0° phase is 0.98±0.01 nm, which is not an integral multiple of the distance between gold atoms on the surface. Due to the mismatch in the lattice, some C_{60} molecules are trapped in three-fold hollow sites, while others are trapped in bridge or A-top sites. The C_{60} molecules on the Au(111) surface prefer to cluster evenly in the three-fold hollow spots at higher temperatures[147]. This results in a phase transition from R0° to $\left(2\sqrt{3} \times 2\sqrt{3}\right) R30°$.

(7×7)R14° Structure and (3×3)R34° Structure

On occasion, the $(7 \times 7)\ R14°$and $(3 \times 3)\ R34°$ phases are also seen on the gold substrate[150]. Figure 2.13 (c) and (d) show the structure of each phase, with black crosses representing the

surface gold atoms and bright and dark spheres representing the adsorbed C_{60} molecules. The thick black arrows indicate the close packing directions of the C_{60} molecules in the diagrams.

R. Berndt *et al*. discovered the *R*14° superstructure first, in which the close-packing orientation of the C_{60} molecules rotates 14 degrees relative to the Au(111) surface[151]. As the solid black lines indicate, this structure has a relatively large unit cell of 49 molecules. The unit cell's molecules are arranged in a (7×7) array on the Au(111) surface at random locations. In comparison to R14°, the R34° superstructure is less visible. Figure 2.13 (d) shows that this structure consists of a unit cell of (3×3) molecules, with every third C_{60} molecule occupying the same gold surface sites[152–154].

2.4.3 Electronic Properties of C_{60} Molecules

The electronic characteristics of C_{60} were investigated using XPS and inverse photoemission spectroscopy (IPES)[142]. The difference in energy between the highest occupied molecular orbitals (HOMO) and the lowest unoccupied molecular orbitals (LUMO) of a C_{60} crystal is 3.7 eV[151]. The C_{60} molecules deposited onto specific noble metal substrates, e.g. Au(111) or Ag(111) can work as electron acceptors. It thus leads to a shrink of the molecules' HOMO-LUMO gap. As Modesti *et al*. show, the transition from metallic to semiconducting behaviour depends strongly on the substrate on which the C_{60} layer is grown[139,155].

As previously stated, the LUMO state localises in the 6:5 single bonds (sp^2 bonds) of one C_{60}, shown in Figure 2.14 (a) as a doughnut-like structure. When a pentagonal ring, a carbon atom, or a hexagonal ring of a C_{60} molecule is oriented downward toward the surface of Au(111), patterns with one, two, or three-fold symmetry are seen in the STM image at low temperatures[153,156].

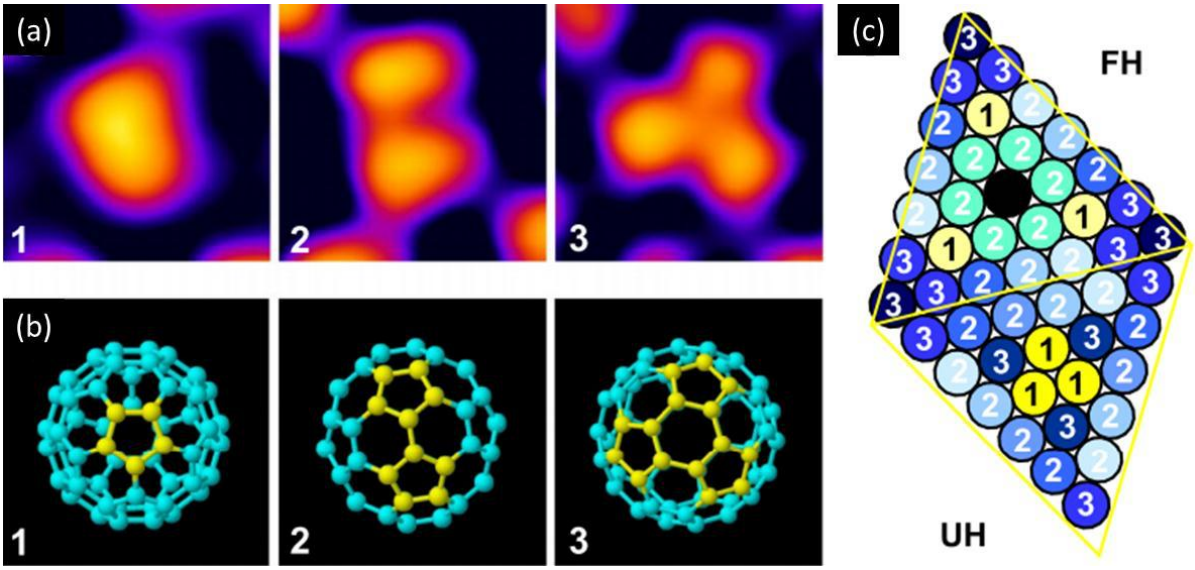

Figure 2.14 (a) STM images of adsorbed C_{60} with one, two, or threefold symmetry axis. (b) Corresponding top view models of (a). (c) Model arrangement of C_{60} in the superlattice. Figures and captions are reproduced from Ref [151].

Schull and Berndt investigated the tendencies of C_{60} molecules in this superlattice structure by using STM. The 5.7K low temperature "froze out" molecular rotation[151]. They saw three orientations of C_{60} molecules at low temperatures, as shown in Figure 2.14 (a). Each of the three C_{60} molecules in the $(3 \times 3)R34°$ phase occupies the same point on the Au(111) surface, and the orientation of the C_{60} molecules is at an angle of 34° to the Au(111) surface $[10\bar{1}]$direction. The height difference of C_{60} molecules varies between 0.35 Å and 1.2 Å depending on the scanning bias, which they attribute to the difference between the LUMO of C_{60} molecules at different energy levels. They also investigated the kinetics of the dark-to-light and light-to-dark transitions at room temperature.

If C_{60} molecules are placed on a more active metal substrate with a lower work function, charge transfer from substrate to C_{60} is enhanced, making the bond slightly dipolar[157]. Apart from surface energy, the intermolecular Coulomb force significantly affects the electronic characteristics of the adsorbed C_{60}. Due to the schematic structure and link type differences,

the electronic states of the two hexagons in the C_{60} molecules differ. At the same time, the bias voltage and tunnelling current are kept constant.

2.4.4 Van der Waals Interaction

The most common interactions are included in Table 2.1, along with their energy range, bonding lengths, and other characteristics utilised to examine the various molecular configurations on metal surfaces[158]. Intermolecular interactions include hydrogen bonding, dipole-dipole force, and vdW dispersion force. The vdW forces between uncharged molecules are frequently less energetic, resulting in longer bonding lengths than the other two interactions. Metal-ligand interactions exist between the interface atoms and a single molecule or a group of molecules, and charge transfer is directed. Compared to vdW forces, these interactions are more energetic and have shorter bonding lengths.

Interaction type	Energy range	Bonding length	Nature
van der Waals	$\sim 0.02 - 0.1$ eV	< 1 nm	Non-selective
Hydrogen bonding	$\sim 0.05 - 0.7$ eV	≈ 0.15 nm $- 0.35$ nm	Selective and directed
Ionic	$\sim 0.05 - 2.5$ eV	Up to several nm	Non-selective
Dipole-dipole	$\sim 0.1 - 0.5$ eV	≈ 0.2 nm $- 0.3$ nm	Directed
Metal-ligand interactions	$\sim 0.5 - 2.0$ eV	≈ 0.15 nm $- 0.35$ nm	Selective and directed
Reconstruction mediated	≈ 1 eV	System dependent	Covalent

Table 2.1 Typical interactions with various interaction energy, bonding lengths, and bonding characteristics. The table is reproduced from Ref [136,158].

When two atoms or molecules are separated by a significant distance, they experience an attraction known as vdW forces, alternatively referred to as fluctuating dipole forces or molecular bonding. These forces arise because both atoms or molecules have dipole moments, which, although averaging to zero, can fluctuate momentarily due to quantum mechanical effects. When the first atom or molecule acquires a temporary dipole moment, it induces

polarisation in the second one, leading it to obtain a dipole moment to reduce its energy. Consequently, the two atoms or molecules now become dipoles momentarily and attract each other.

This type of interaction is characteristic of inert atoms, such as noble gases (helium, neon, krypton, argon, xenon), whose electrons do not engage in covalent or ionic bonds. Similarly, it is typical in bonding between inert molecules like nitrogen (N_2), where the electrons are unable to form covalent or ionic bonds between molecules. Although this bonding is weaker than covalent or ionic bonds, it is longer ranged since electron transfer between atoms is not required.

Consider two atoms separated by a distance r along the $\hat{x}$ direction. Suppose one atom momentarily possesses a dipole moment $\boldsymbol{p_1}$ oriented in the $\hat{z}$ direction. Consequently, the second atom experiences an electric field given by

$$E = \frac{p_1}{4\pi\epsilon_0 r^3} \tag{1.2}$$

in the negative $\hat{z}$ direction. Due to its polarizability, the second atom develops a dipole moment $\boldsymbol{p_2} = \chi \boldsymbol{E}$, resulting in an attraction between the two atoms. The potential energy between these two dipoles can be expressed as:

$$U = \frac{|p_1||p_2|}{4\pi\epsilon_0 r^3} = \frac{|p_1|\chi|p_1|}{(4\pi\epsilon_0)^2 r^6} = \frac{|p_1|^2\chi}{(4\pi\epsilon_0)^2 r^6} \tag{1.3}$$

The force between the two atoms, which is given by $-\frac{dU}{dr}$, is attractive and proportional to $\frac{1}{r^7}$. If we use R=r, A is a constant for identical atoms or molecules, it can be written as

$$\Delta U = -\frac{A}{R^6} \tag{1.4}$$

This interaction is known as the vdW interaction, also called the London interaction or the induced dipole-dipole interaction. It is the primary attractive force in crystals of inert gases and crystals of many organic molecules.

As two atoms approach each other, their charge distributions gradually begin to overlap, leading to changes in the system's electrostatic energy. The overlap energy becomes repulsive at sufficiently close separations, largely due to the Pauli exclusion principle. This principle states that no two electrons can have identical quantum numbers. When the charge distributions of two atoms overlap, electrons from atom B may partially occupy states already filled by electrons from atom A, and vice versa. The Pauli exclusion principle prevents such multiple occupancy, allowing electron distributions of atoms with closed shells to overlap only if accompanied by the partial promotion of electrons to unoccupied high-energy states. This electron overlap increases the total energy of the system, resulting in a repulsive contribution to the interaction.

experimental data on inert gases can be well-fitted using an empirical repulsive potential of the form $\frac{B}{R^{12}}$, where B is a positive constant combined with a long-range attractive potential as described in equation (1.3). The potential can be written as:

$$U(R) = \frac{A}{R^{12}} - \frac{B}{R^6} \tag{1.5}$$

The constants A and B are empirical parameters determined from independent measurements in the gas phase, including data on virial coefficients and viscosity. The total potential energy of two atoms at separation R is typically written as:

$$U(R) = 4\epsilon\left[\left(\frac{\sigma}{R}\right)^{12} - \left(\frac{\sigma}{R}\right)^{6}\right] \tag{1.6}$$

where ϵ and σ are parameters derived from gas-phase data, ensuring that calculations on the properties of the solid do not involve adjustable parameters. The ϵ is related to the depth of the energy well, and σ is related to the equilibrium distance between the pair of atoms. This potential form is known as the Lennard-Jones potential. It describes the essential features of interactions between simple atoms and molecules.

2.4.5 Two-dimensional C_{60}-based Complex Structures

Supramolecular self-assembly emerges as an advanced methodology for probing interactions between C_{60} molecules and substrates, facilitating the development of C_{60}-based nanostructures[159]. The strategic harnessing of selective noncovalent forces—including hydrogen bonding, dipole-dipole interactions, donor-acceptor (D–A) relationships, and van der Waals (vdW) forces—is pivotal in the construction of extensive supramolecular architectures spanning one, two, or three dimensions. Despite significant investigations into the interactions of C_{60} molecules with diverse metallic surfaces, the fabrication of a high degree of order C_{60} nanostructures remains a formidable challenge[160].

Precise positioning of C_{60} molecules on substrates to engender two-dimensional (2D) nanoarrays is realisable through chemical or physical methodologies. This investigation capitalised on Langmuir-Blodgett technology, a novel approach introduced by Metzger, to form a monolayer of C_{60}[161]. Furthermore, STM was employed to characterise C_{60} nanoscale structures, which are markedly influenced by the proximal molecular layer on the substrate[162–164]. The interaction dynamics between C_{60} and metallic surfaces often reflect the extent to which the metal modulates the electronic structure of the fullerene entities. The direct bonding of C_{60} onto a metallic surface, or its concurrent adsorption with a buffer layer on a substrate, can stem from electronic charge transfer[165]. Given the distinctive and rigid spherical configuration of fullerene molecules, it is critical to identify an apt host capable of efficaciously interacting with fullerenes to fabricate C_{60}-based supramolecular self-assembly systems.

The bottom-up approach holds considerable promise for creating supramolecular assemblies. Achieving high-quality thin films through this method necessitates thoroughly comprehending vertical interactions on the nanoscale. This process involves molecular adsorption to the surface, diffusion across it, assembly, and vertical growth to construct a

surface-assisted molecular assembly from the bottom up. C_{60} molecules often undergo phase separation, resulting in the formation of randomly mixed domains. These domains can either merge into an intermixed phase or trigger a local reorganisation of the layers previously deposited, significantly affecting the structural configuration of C_{60} arrays[166]. Using proper templates, strengthened by robust and directional hydrogen bonds and metal coordination interactions, stabilises guest fullerene molecules through noncovalent bonding[167,168].

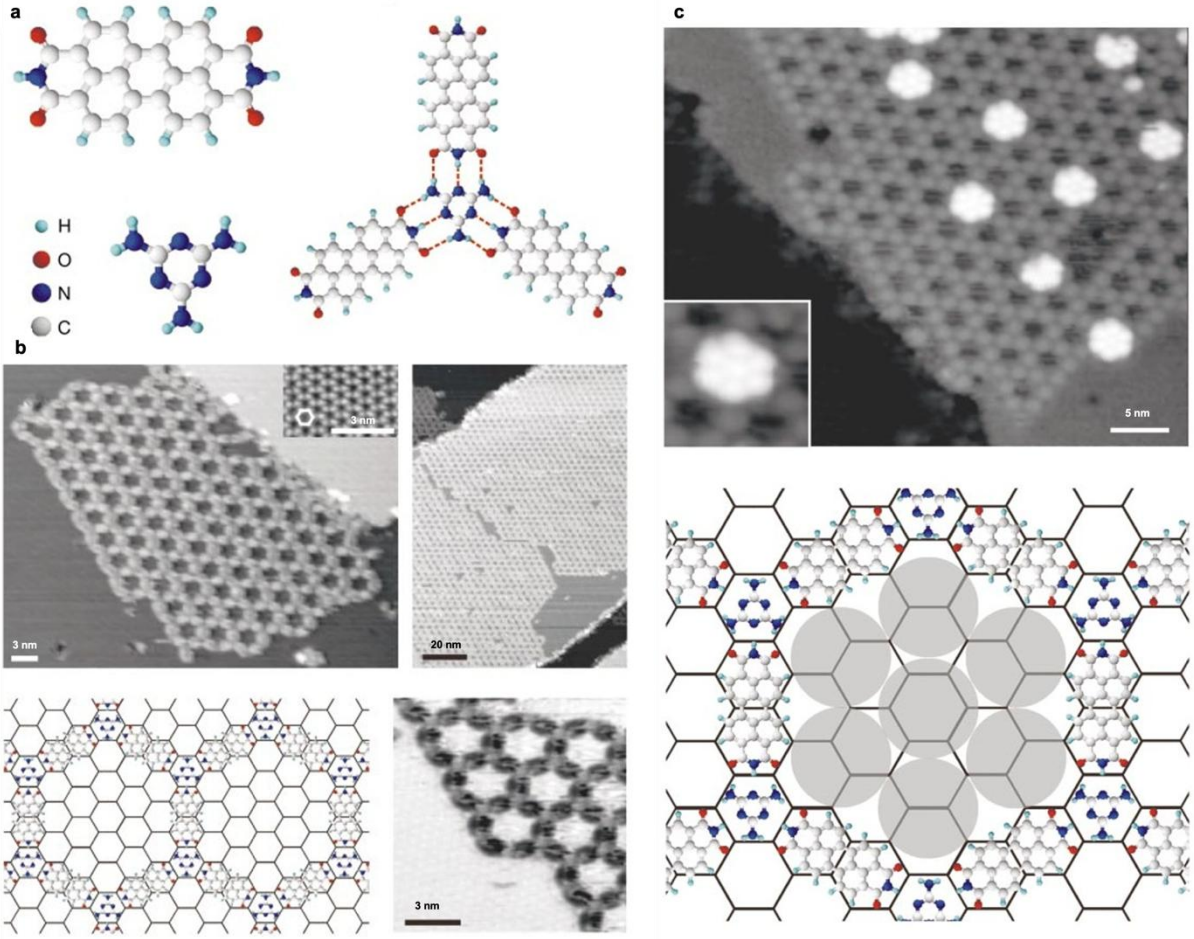

Figure 2.15 Supramolecular self-assembly of a PTCDI–melamine supramolecular network. (a) The chemical structures of PTCDI and melamine, respectively, are presented. A schematic of a PTCDI-melamine junction is shown, where dotted lines indicate the hydrogen bonds that stabilise the molecules' interaction. STM images display a PTCDI-melamine network and a schematic diagram illustrating how the network aligns with the surface. (c) The STM image shows C_{60} clusters on a PTCDI-melamine network, with an inset providing a high-resolution glimpse of a single heptamer. Additionally, a schematic representation of a C_{60} cluster is provided. Figures and captions are reproduced from Ref [28].

For example, C_{60} molecules can be encapsulated within nanoscale porous frameworks through the self-assembly of functional molecules on substrates pre-coated with 2D networks[169,170]. By layering additional C_{60} molecules atop these networks, highly ordered binary molecular systems are formed[28,171]. Within this framework, the organic networks dictate the placement of C_{60} molecules, with directional bonding mechanisms, such as hydrogen bonding, playing a crucial role in forming two-dimensional networks[172].

Theobald *et al.* showcased the simultaneous deposition of melamine and PTCDI on a Ag:Si(111) substrate[28]. In this arrangement, melamine serves as a tripartite connector, and PTCDI establishes the periphery, as depicted in Figure 2.15. This combination forms tripartite junctions through hydrogen bonding, creating a honeycomb pattern with the nearest melamine molecules being 9.98 Å apart. Figure 2.15 (b) schematic displays the hexagonal pore architecture arising from these interconnected junctions. Subsequent C_{60} deposition captures heptameric C_{60} clusters within the network's pores. The seamless integration of C_{60} into the PTCDI+melamine network leads to the formation of C_{60} heptamers, as illustrated in Figure 2.15 (c). Nevertheless, these C_{60} heptamers are less firmly fixed within the cavities than their interaction with the PTCDI+melamine matrix. Remarkably, the deposition of melamine onto the initially established dense-packed and hexagonal structures on a clean AgSi surface resulted in the formation of hexagonal networks that reflect the PTCDI+melamine bimolecular arrangement.

2.5 Scanning Tunnelling Microscopy

Since its development in 1980s, the STM has been investigated and refined to permit the measurement of material surfaces in extreme environments such as electrolyte solutions, ultra-high vacuum, and low-temperature[173]. It is a critical instrument for characterising the physicochemical structure, electronic characteristics, and optical properties of solid surfaces

and surface nanomaterials and has also advanced the field of surface research[174–177]. In 1981, G. Binnig *et al*. developed the world's first STM at the IBM Zürich Research Laboratory[17]. It shows the topography of material surfaces with atomic resolution in real-time[178]. Binnig and Rohrer shared the 1986 Nobel Prize in Physics for their work[179].

Initially, STM was used to determine the topography and electronic structure of the conducting materials[175,176,179,180]. The scanning tunnelling spectroscopy (STS) method was then used to investigate the information in the surface's local electronic structure[181,182]. Following STM, many additional microscopy methods, including Atomic Force Microscopy (AFM)[21,183–188] and Q-plus AFM[189–195] were developed and used for surface investigation in succession[196,197]

2.5.1 STM Theory

STM is a technique that detects the tunnelling current between two electrodes (sample and tip). It operates based on a quantum mechanics process known as electron tunnelling[198]. A one-dimensional model illustrates the notion of electron tunnelling[199]. The mathematical description of the tip-barrier-sample junction is derived in the Appendix as a one-dimensional energy model[173,200,201].

The tip and sample in STM act as the two electrodes, with the Fermi levels denoted by $\mathrm{E_{Ft}}$ and $\mathrm{E_{Fs}}$. The vacuum between the apex of the tip and the sample surface acts as the barrier. To simplify the equation, E_{Ft} and E_{Fs} are equal to each other before the application of a bias voltage. When the STM tip is approached highly close to the sample surface($\sim$10 Å). The bias voltage applied on the sample or tip substantially influences the total number of electrons going through the barrier. A negative bias voltage V is applied to the sample, making its Fermi level an upward shift of eV, where e represents the charge of electrons. Electrons with energies

ranging from between E_{Ft} to $E_{Ft} + eV$ tunnel through the potential barrier and generate tunnelling current. The tunnelling current is determined as follows[173]:

$$I \propto \int_{E_{Ft}}^{E_{Ft}+eV} |\Psi(z)|^2 e^{-2z\sqrt{\frac{2m}{\hbar^2}\left(\Phi - \frac{e|V|}{2}\right)}}) \tag{1.7}$$

By taking into consideration the sample surface's local density of states (LDOS) $\rho_s(\mathrm{E_{Fs}})$, it can be written as:

$$\rho_s(E_{Fs}) \propto \frac{1}{eV} \int_{E_{Ft}}^{E_{Ft}+eV} |\Psi(z)|^2 \tag{1.8}$$

Then, an exponential relationship between the tunnelling current *I* and the barrier width *z* (the distance between the tip apex and the corresponding atoms on the sample surface during scanning) can be derived.

$$I \propto V\rho_s(E_{Fs}) e^{\left(-2z\sqrt{\frac{2m}{\hbar^2}\left(\Phi - \frac{e|V|}{2}\right)}\right)} \tag{1.9}$$

where z denotes the gap between the tip apex and the sample's surface atoms. The $\hbar$ denotes the reduced Plank constant and equals $\frac{h}{2\pi}$. Moreover, *m* represents the free electron mass in the simple model, and Φ is the sample's work function.

The tip-sample distance can be determined sensitively by measuring the tunnelling current, and vice versa. 1 Å difference in tip-sample distance can result in a difference of the tunnelling current by a factor of 10. The maximum scanning resolution achievable with an STM in a UHV condition is 0.1 Å in the depth direction and 1 Å in the lateral direction. Thus, when STM continually records the tunnelling current, the surface topography in real space can be directly acquired with atomic resolution. It enhanced the surface science to get an atomic or molecular level understanding of their study objects[173].

STM can also measure the target sample's electronic contour. STS is used for this purpose. Equation (1.9) is represented by calculating the derivative on both sides of the expression with regard to the bias voltage V.

$$\frac{dI}{dV} \propto \rho_s(E_{Fs}) \tag{2.0}$$

To investigate the occupied and unoccupied electron density states on the sample surface, an I-V curve can be generated by sweeping the bias voltage from a negative to a positive value while simultaneously recording the corresponding current. The Fermi-level local density of states (LDOS) is then obtained by differentiating the recorded I-V curve[199].

2.5.2 STM in Surface Science

STM provides many benefits as a potent tool for surface science research. It is frequently used to investigate three-dimensional contours and the locations of surface reconstructions and defects[180,181,202,203]. STM was used to characterise a clean Si(111) surface with complete information on the 7×7 reconstruction directly[179]. Each unit cell was discovered to contain 12 adatoms and a hybrid of two triangles. Therefore, the unit cell of Si(111) has a three-fold symmetry. Additionally, compared to the unreconstructed surface, the initial 49 dangling bonds in a unit cell are reduced to 12 after the surface reconstruction is visible.

The STM are adaptable and can be utilised in UHV, air, or liquids[174,177,202–209]. The sample of interest is scanned at various temperatures without causing damage[201,210–214]. The variable temperature operated in the microscope stage of the LT-STM at our laboratory ranges from 5 K to 400 K. Additionally, the STM is an effective instrument for analysing surface dynamic processes. Earlier investigations investigated the surface diffusion of Si(111) surfaces that were both clean and oxygen-free. During scanning, the feedback loop of the STM was paused while the tip remained stationary over a designated location[175]. Then, the continuous tunnelling current was recorded and analysed using a power spectrum analyser. The current fluctuation induced by adatom diffusion across the tunnelling region was utilised to derive diffusion coefficients.

However, STM does have certain drawbacks. STM operates on the quantum tunnelling principle and requires conductivity in the testing sample and the scanning tip. STM has difficulty immediately achieving high-resolution of the sample surface regarding semiconductors or insulators. Techniques developed latterly, such as atomic force microscopy (AFM)[183,185,186], successfully compensate for this deficit. Additionally, the variation depicted in the STM images does not always correspond to the actual physical height difference. This is because STM simultaneously captures electronic and geometric data while scanning.

On the other hand, the STM is highly sensitive to the experimental environment. The tunnelling current is generated between the tips and surfaces on the picoampere and nanoampere scales. The UHV environment with a pressure of 10^{-10} mbar is often required to get the most significant resolution STM pictures of atomic structures. As a result, STM is complicated in its design and costly to construct. Another downside of STM is the scan area limitation. The highest scanning magnifications in the x, y, and z axes are typically in micrometres, and identify just local surface characteristics[173].

This review highlighted the experimental challenges and limitations of performing such measurements. It is important to recognise that STM, along with other SPM techniques, probes molecules adsorbed on a substrate, and the interaction between the molecule of interest and the substrate significantly influences the observed properties.

References

1. Verstraete, L. & Feyter, S. D. 2D Self-assembled molecular networks and on-surface reactivity under nanoscale lateral confinement. *Chem. Soc. Rev.* 50, 5884–5897 (2021).

2. Barth, J. V. Molecular Architectonic on Metal Surfaces. *Annu. Rev. Phys. Chem.* 58, 375–407 (2007).

3. Kuhnke, K., Große, C., Merino, P. & Kern, K. Atomic-Scale Imaging and Spectroscopy of Electroluminescence at Molecular Interfaces. *Chem. Rev.* 117, 5174–5222 (2017).

4. Geagea, E., Palmino, F. & Cherioux, F. On-Surface Chemistry on Low-Reactive Surfaces. *Chemistry* 4, 796–810 (2022).

5. Rengarajan, G. T., Enke, D., Steinhart, M. & Beiner, M. Size-dependent growth of polymorphs in nanopores and Ostwald's step rule of stages. *Phys. Chem. Chem. Phys.* 13, 21367–21374 (2011).

6. Philip Moriarty. Nanostructured materials. *Rep. Prog. Phys.* 64, 297 (2001).

7. Diao, Y., Harada, T., Myerson, A. S., Hatton, T. A. & Trout, B. L. The role of nanopore shape in surface-induced crystallization. *Nat. Mater.* 10, 867–871 (2011).

8. Hamilton, B. D., Weissbuch, I., Lahav, M., Hillmyer, M. A. & Ward, M. D. Manipulating Crystal Orientation in Nanoscale Cylindrical Pores by Stereochemical Inhibition. *J. Am. Chem. Soc.* 131, 2588–2596 (2009).

9. Hamilton, B. D., Ha, J.-M., Hillmyer, M. A. & Ward, M. D. Manipulating Crystal Growth and Polymorphism by Confinement in Nanoscale Crystallization Chambers. *Acc. Chem. Res.* 45, 414–423 (2012).

10. Jiang, Q. & Ward, M. D. Crystallization under nanoscale confinement. *Chem. Soc. Rev.* 43, 2066–2079 (2013).

11. Meldrum, F. C. & O'Shaughnessy, C. Crystallization in Confinement. *Adv. Mater.* 32, e2001068 (2020).

12. Otero, R. *et al.* One-Dimensional Assembly and Selective Orientation of Lander Molecules on an O–Cu Template. *Angew. Chem. Int. Ed.* 43, 2092–2095 (2004).

13. Patrick, D. L., Cee, V. J. & Jr., T. P. B. 'Molecule Corrals' for Studies of Monolayer Organic Films. *Science* 265, 231–234 (1994).

14. Greenwood, J. *et al.* Covalent Modification of Graphene and Graphite Using Diazonium Chemistry: Tunable Grafting and Nanomanipulation. *ACS Nano* 9, 5520–5535 (2015).

15. Chen, J. *et al.* Building two-dimensional materials one row at a time: Avoiding the nucleation barrier. *Science* 362, 1135–1139 (2018).

16. Sleutel, M., Lutsko, J., Driessche, A. E. S. V., Durán-Olivencia, M. A. & Maes, D. Observing classical nucleation theory at work by monitoring phase transitions with molecular precision. *Nat. Commun.* 5, 5598 (2014).

17. Binnig, G., Rohrer, H., Gerber, C. & Weibel, E. Tunneling through a controllable vacuum gap. *Appl. Phys. Lett.* 40, 178–180 (1982).

18. Yang, B. *et al.* Synthesis of Surface Covalent Organic Frameworks via Dimerization and Cyclotrimerization of Acetyls. *J Am Chem Soc* 137, 4904–4907 (2015).

19. She, Z. *et al.* Coordination controlled electrodeposition and patterning of layers of palladium/copper nanoparticles on top of a self-assembled monolayer. *Nanoscale* 11, 13773–13782 (2019).

20. Judd, C. J. *et al.* Structural characterisation of molecular conformation and the incorporation of adatoms in an on-surface Ullmann-type reaction. *Commun. Chem.* 3, 166 (2020).

21. Binnig, G., Quate, C. F. & Gerber, Ch. Atomic Force Microscope. *Phys. Rev. Lett.* 56, 930–933 (1986).

22. Vang, R. T., Lauritsen, J. V., Lægsgaard, E. & Besenbacher, F. Scanning tunneling microscopy as a tool to study catalytically relevant model systems. *Chem. Soc. Rev.* 37, 2191–2203 (2008).

23. Lindner, R. & Kühnle, A. On-Surface Reactions. *ChemPhysChem* 16, 1582–1592 (2015).

24. Shen, Q., Gao, H.-Y. & Fuchs, H. Frontiers of on-surface synthesis: From principles to applications. *Nano Today* 13, 77–96 (2017).

25. Wiktor, C., Meledina, M., Turner, S., Lebedev, O. I. & Fischer, R. A. Transmission electron microscopy on metal–organic frameworks – a review. *J. Mater. Chem. A* 5, 14969–14989 (2017).

26. Barth, J. V. *et al.* Building Supramolecular Nanostructures at Surfaces by Hydrogen Bonding. *Angew. Chem. Int. Ed.* 39, 1230–1234 (2000).

27. Griessl, S., Lackinger, M., Edelwirth, M., Hietschold, M. & Heckl, W. M. Self-Assembled Two-Dimensional Molecular Host-Guest Architectures From Trimesic Acid. *Single Mol.* 3, 25–31 (2002).

28. Theobald, J. A., Oxtoby, N. S., Phillips, M. A., Champness, N. R. & Beton, P. H. Controlling molecular deposition and layer structure with supramolecular surface assemblies. *Nature* 424, 1029–1031 (2003).

29. Stepanow, S. *et al.* Steering molecular organization and host–guest interactions using two-dimensional nanoporous coordination systems. *Nat. Mater.* 3, 229–233 (2004).

30. Dong, L., Gao, Z. & Lin, N. Self-assembly of metal–organic coordination structures on surfaces. *Prog. Surf. Sci.* 91, 101–135 (2016).

31. Zhang, X. *et al.* On-Surface Synthesis of Thiophene-Containing Large-Sized Organometallic Macrocycles on the Ag(111) Surface. *J Phys Chem C* 125, 11454–11461 (2021).

32. Elemans, J. A. A. W., Lei, S. & Feyter, S. D. Molecular and Supramolecular Networks on Surfaces: From Two-Dimensional Crystal Engineering to Reactivity. *Angew. Chem. Int. Ed.* 48, 7298–7332 (2009).

33. Elemans, J. A. A. W., Cat, I. D., Xu, H. & Feyter, S. D. Two-dimensional chirality at liquid–solid interfaces. *Chem. Soc. Rev.* 38, 722–736 (2009).

34. Tobe, Y., Tahara, K. & Feyter, S. D. Chirality in porous self-assembled monolayer networks at liquid/solid interfaces: induction, reversion, recognition and transfer. *Chem. Commun.* 57, 962–977 (2020).

35. Blunt, M. O. *et al.* Random Tiling and Topological Defects in a Two-Dimensional Molecular Network. *Science* 322, 1077–1081 (2008).

36. Steeno, R. *et al.* Molecular dopant determines the structure of a physisorbed self-assembled molecular network. *Chem. Commun.* 57, 1454–1457 (2021).

37. Stannard, A. *et al.* Broken symmetry and the variation of critical properties in the phase behaviour of supramolecular rhombus tilings. *Nat. Chem.* 4, 112–117 (2012).

38. Wasio, N. A. *et al.* Self-assembly of hydrogen-bonded two-dimensional quasicrystals. *Nature* 507, 86–89 (2014).

39. Urgel, J. I. *et al.* Quasicrystallinity expressed in two-dimensional coordination networks. *Nat. Chem.* 8, 657–662 (2016).

40. Shang, J. *et al.* Assembling molecular Sierpiński triangle fractals. *Nat. Chem.* 7, 389–393 (2015).

41. Narita, A., Wang, X.-Y., Feng, X. & Müllen, K. New advances in nanographene chemistry. *Chem. Soc. Rev.* 44, 6616–6643 (2015).

42. Jin, Y. *et al.* Confined growth of ordered organic frameworks at an interface. *Chem. Soc. Rev.* 49, 4637–4666 (2020).

43. Tang, L., Xie, Y. & Guo, Q. Complex orientational ordering of C_{60} molecules on Au(111). *J Chem Phys* 135, 114702 (2011).

44. Tang, L., Zhang, X. & Guo, Q. Organizing C_{60} molecules on a nanostructured Au(111) surface. *Surf Sci* 604, 1310–1314 (2010).

45. Tang, L. & Guo, Q. Orientational ordering of the second layer of C_{60} molecules on Au(111). *Phys Chem Chem Phys* 14, 3323–3328 (2012).

46. Haiss, W., Lackey, D., Sass, J. K. & Besocke, K. H. Atomic resolution scanning tunneling microscopy images of Au(111) surfaces in air and polar organic solvents. *J. Chem. Phys.* 95, 2193–2196 (1991).

47. Hove, M. A. V. *et al.* The surface reconstructions of the (100) crystal faces of iridium, platinum and gold I. Experimental observations and possible structural models. *Surf. Sci.* 103, 189–217 (1981).

48. Heyraud, J. C. & Métois, J. J. Anomalous 13 422 diffraction spots from {111} flat gold crystallites: (111) surface reconstruction and moiré fringes between the surface and the bulk. *Surf. Sci.* 100, 519–528 (1980).

49. Harten, U., Lahee, A. M., Toennies, J. P. & Wöll, Ch. Observation of a Soliton Reconstruction of Au(111) by High-Resolution Helium-Atom Diffraction. *Phys. Rev. Lett.* 54, 2619–2622 (1985).

50. Perdereau, J., Biberian, J. P. & Rhead, G. E. Adsorption and surface alloying of lead monolayers on (111) and (110) faces of gold. *J. Phys. F: Met. Phys.* 4, 798 (2001).

51. Nakai, Y., Zei, M. S., Kolb, D. M. & Lehmpfuhl, G. A LEED and RHEED Investigation of Cu on Au(111) in the Underpotential Region. *Berichte Bunsenges. für Phys. Chem.* 88, 340–345 (1984).

52. Frank, F. C. & Merwe, J. H. van der. One-dimensional dislocations. I. Static theory. *Proc. R. Soc. Lond. Ser. A Math. Phys. Sci.* 198, 205–216 (1949).

53. Yagi, K. *et al.* Surface study by an UHV electron microscope. *Surf. Sci.* 86, 174–181 (1979).

54. Tanishiro, Y., Kanamori, H., Takayanagi, K., Yagi, K. & Honjo, G. UHV transmission electron microscopy on the reconstructed surface of (111) gold I. General features. *Surf. Sci.* 111, 395–413 (1981).

55. Wöll, Ch., Chiang, S., Wilson, R. J. & Lippel, P. H. Determination of atom positions at stacking-fault dislocations on Au(111) by scanning tunneling microscopy. *Phys. Rev. B* 39, 7988–7991 (1988).

56. Barth, J. V., Brune, H., Ertl, G. & Behm, R. J. Scanning tunneling microscopy observations on the reconstructed Au(111) surface: Atomic structure, long-range superstructure, rotational domains, and surface defects. *Phys. Rev. B* 42, 9307–9318 (1990).

57. Hallmark, V. M., Chiang, S., Rabolt, J. F., Swalen, J. D. & Wilson, R. J. Observation of Atomic Corrugation on Au(111) by Scanning Tunneling Microscopy. *Phys. Rev. Lett.* 59, 2879–2882 (1987).

58. Gao, J. Structural analysis of self-assembled monolayers on Au(111) and point defects on HOPG. (University of Birmingham, 2013).

59. Lin, B. & Hu, B. Frenkel-Kontorova model with toda interactions. *J. Stat. Phys.* 69, 1047–1068 (1992).

60. Maksymovych, P., Voznyy, O., Dougherty, D. B., Sorescu, D. C. & Yates, J. T. Gold adatom as a key structural component in self-assembled monolayers of organosulfur molecules on Au(111). *Prog. Surf. Sci.* 85, 206–240 (2010).

61. Takeuchi, N., Chan, C. T. & Ho, K. M. Au(111): A theoretical study of the surface reconstruction and the surface electronic structure. *Phys. Rev. B* 43, 13899–13906 (1990).

62. Narasimhan, S. & Vanderbilt, D. Elastic stress domains and the herringbone reconstruction on Au(111). *Phys. Rev. Lett.* 69, 1564–1567 (1992).

63. Alerhand, O. L., Vanderbilt, D., Meade, R. D. & Joannopoulos, J. D. Spontaneous Formation of Stress Domains on Crystal Surfaces. *Phys. Rev. Lett.* 61, 1973–1976 (1988).

64. Needs, R. J. & Mansfield, M. Calculations of the surface stress tensor and surface energy of the (111) surfaces of iridium, platinum and gold. *J. Phys.: Condens. Matter* 1, 7555 (1989).

65. Chambliss, D. D., Wilson, R. J. & Chiang, S. Nucleation of ordered Ni island arrays on Au(111) by surface-lattice dislocations. *Phys. Rev. Lett.* 66, 1721–1724 (1991).

66. Chambliss, D. D., Wilson, R. J. & Chiang, S. Ordered nucleation of Ni and Au islands on Au(111) studied by scanning tunneling microscopy. *J. Vac. Sci. Technol. B: Microelectron. Nanometer Struct. Process., Meas., Phenom.* 9, 933–937 (1991).

67. Rousset, S., Repain, V., Baudot, G., Garreau, Y. & Lecoeur, J. Self-ordering of Au(111) vicinal surfaces and application to nanostructure organized growth. *J. Phys.: Condens. Matter* 15, S3363 (2003).

68. Altman, E. I. & Colton, R. J. Nucleation, growth, and structure of fullerene films on Au(111). *Surf. Sci.* 279, 49–67 (1992).

69. Wang, Yi. Heterostructures of C_{60}/C_{70} and rotation of C_{70}-Au magic number clusters on Au(111) and highly oriented pyrolytic graphite. (University of Birmingham, 2020).

70. Nuzzo, R. G. & Allara, D. L. Adsorption of bifunctional organic disulfides on gold surfaces. *J Am Chem Soc* 105, 4481–4483 (1983).

71. Schreiber, F. Structure and growth of self-assembling monolayers. *Prog. Surf. Sci.* 65, 151–257 (2000).

72. Love, J. C., Estroff, L. A., Kriebel, J. K., Nuzzo, R. G. & Whitesides, G. M. Self-Assembled Monolayers of Thiolates on Metals as a Form of Nanotechnology. *Chem Rev* 105, 1103–1170 (2005).

73. Vericat, C., Vela, M. E., Benitez, G., Carro, P. & Salvarezza, R. C. Self-assembled monolayers of thiols and dithiols on gold : new challenges for a well-known system. *Chem. Soc. Rev.* 39, 1805–1834 (2010).

74. Schwartz, D. K. Mechanisms and kinetics of self-assembled monolayer formation. *Annu. Rev. Phys. Chem.* 52, 107–137 (2001).

75. Smith, R. K., Lewis, P. A. & Weiss, P. S. Patterning self-assembled monolayers. *Prog Surf Sci* 75, 1–68 (2004).

76. Vericat, C., Vela, M. E. & Salvarezza, R. C. Self-assembled monolayers of alkanethiols on Au(111): surface structures, defects and dynamics. *Phys Chem Chem Phys* 7, 3258–3268 (2005).

77. Vericat, C. *et al.* Surface characterization of sulfur and alkanethiol self-assembled monolayers on Au(111). *J Phys Condens Matter* 18, R867 (2006).

78. Kind, M. & Wöll, C. Organic surfaces exposed by self-assembled organothiol monolayers: Preparation, characterization, and application. *Prog Surf Sci* 84, 230–278 (2009).

79. Guo, Q. & Li, F. Self-assembled alkanethiol monolayers on gold surfaces: resolving the complex structure at the interface by STM. *Phys. Chem. Chem. Phys.* 16, 19074–19090 (2014).

80. Ulman, A. Formation and Structure of Self-Assembled Monolayers. *Chem Rev* 96, 1533–1554 (1996).

81. Maksymovych, P., Sorescu, D. C. & Yates, J. T. Gold-Adatom-Mediated Bonding in Self-Assembled Short-Chain Alkanethiolate Species on the Au(111) Surface. *Phys. Rev. Lett.* 97, 146103 (2006).

82. Li, F., Tang, L., Zhou, W. & Guo, Q. Resolving the Au-Adatom-Alkanethiolate Bonding Site on Au(111) with Domain Boundary Imaging Using High-Resolution Scanning Tunneling Microscopy. *J. Am. Chem. Soc.* 132, 13059–13063 (2010).

83. Haick, H. & Cahen, D. Making contact: Connecting molecules electrically to the macroscopic world. *Prog. Surf. Sci.* 83, 217–261 (2008).

84. Samanta, D. & Sarkar, A. Immobilization of bio-macromolecules on self-assembled monolayers: methods and sensor applications. *Chem. Soc. Rev.* 40, 2567–2592 (2011).

85. Häkkinen, H. The gold–sulfur interface at the nanoscale. *Nat Chem* 4, 443–455 (2012).

86. Pensa, E. *et al.* The Chemistry of the Sulfur–Gold Interface: In Search of a Unified Model. *Acc. Chem. Res.* 45, 1183–1192 (2012).

87. Holmes, S. *et al.* Bridge-bonded methylthiolate on Au(111) observed with the scanning tunneling microscope. *Phys Chem Chem Phys* 20, 19486–19491 (2018).

88. Mazzarello, R. *et al.* Structure of a CH3S Monolayer on Au(111) Solved by the Interplay between Molecular Dynamics Calculations and Diffraction Measurements. *Phys Rev Lett* 98, 016102 (2007).

89. Tang, L., Li, F., Zhou, W. & Guo, Q. The structure of methylthiolate and ethylthiolate monolayers on Au(111): Absence of the $(\sqrt{3}\times\sqrt{3})R30°$ phase. *Surf Sci* 606, L31–L35 (2012).

90. Ding, H. *et al.* Perturbational Imaging of Molecules with the Scanning Tunneling Microscope. *J. Phys. Chem. C* 124, 25892–25897 (2020).

91. Li, F., Tang, L., Voznyy, O., Gao, J. & Guo, Q. The striped phases of ethylthiolate monolayers on the Au(111) surface: A scanning tunneling microscopy study. *J Chem Phys* 138, 194707 (2013).

92. Tang, L., Li, F. S. & Guo, Q. Complete Structural Phases for Self-Assembled Methylthiolate Monolayers on Au(111). *J Phys Chem C* 117, 21234–21244 (2013).

93. Rzeźnicka, I. I., Lee, J., Maksymovych, P. & Yates, J. T. Nondissociative Chemisorption of Short Chain Alkanethiols on Au(111). *J Phys Chem B* 109, 15992–15996 (2005).

94. Wang, Y. *et al.* Gold Mining by Alkanethiol Radicals: Vacancies and Pits in the Self-Assembled Monolayers of 1-Propanethiol and 1-Butanethiol on Au(111). *J Phys Chem C* 115, 10630–10639 (2011).

95. Chaudhuri, A., Lerotholi, T. J., Jackson, D. C., Woodruff, D. P. & Dhanak, V. Local Methylthiolate Adsorption Geometry on Au(111) from Photoemission Core-Level Shifts. *Phys Rev Lett* 102, 126101 (2009).

96. Kondoh, H. *et al.* Adsorption of Thiolates to Singly Coordinated Sites on Au(111) Evidenced by Photoelectron Diffraction. *Phys Rev Lett* 90, 066102 (2003).

97. Voznyy, O., Dubowski, J. J., Yates, J. T. & Maksymovych, P. The Role of Gold Adatoms and Stereochemistry in Self-Assembly of Methylthiolate on Au(111). *J. Am. Chem. Soc.* 131, 12989–12993 (2009).

98. Mom, R. V. *et al.* The Pressure Gap for Thiols: Methanethiol Self-Assembly on Au(111) from Vacuum to 1 bar. *J. Phys. Chem. C* 123, 12382–12389 (2019).

99. Renzi, V. D. *et al.* Ordered (3 × 4) High-Density Phase of Methylthiolate on Au(111). *J. Phys. Chem. B* 108, 16–20 (2004).

100. Roper, M. G. *et al.* Atop adsorption site of sulphur head groups in gold-thiolate self-assembled monolayers. *Chem Phys Lett* 389, 87–91 (2004).

101. Li, F., Tang, L., Gao, J., Zhou, W. & Guo, Q. Adsorption and Electron-Induced Dissociation of Ethanethiol on Au(111). *Langmuir* 28, 11115–11120 (2012).

102. Gao, J. *et al.* Spontaneous Breaking and Remaking of the RS–Au–SR Staple in Self-assembled Ethylthiolate/Au(111) Interface. *J Phys Chem C* 122, 19473–19480 (2018).

103. Hagenström, H., Schneeweiss, M. A. & Kolb, D. M. Modification of a Au(111) Electrode with Ethanethiol. 1. Adlayer Structure and Electrochemistry. *Langmuir* 15, 2435–2443 (1999).

104. Gao, J. *et al.* Growth of Two-Dimensional C_{60} Nanoclusters within a Propylthiolate Matrix. *J Phys Chem C* 120, 25481–25488 (2016).

105. Gao, J. *et al.* Probing Phase Evolutions of Au-Methyl-Propyl-Thiolate Self-Assembled Monolayers on Au(111) at the Molecular Level. *J Phys Chem B* 122, 6666–6672 (2018).

106. Gao, J., Li, F. & Guo, Q. Balance of Forces in Self-Assembled Monolayers. *J Phys Chem C* 117, 24985–24990 (2013).

107. Gao, J., Li, F. & Guo, Q. Mixed Methyl- and Propyl-Thiolate Monolayers on a Au(111) Surface. *Langmuir* 29, 11082–11086 (2013).

108. Clair, S., Kim, Y. & Kawai, M. Coverage-Dependent Formation of Chiral Ethylthiolate-Au Complexes on Au(111). *Langmuir* 27, 627–629 (2011).

109. Chaudhuri, A. *et al.* Structural investigation of Au(111) / butylthiolate adsorption phases. *Phys. Chem. Chem. Phys.* 12, 3229–3238 (2010).

110. Yu, M. *et al.* True Nature of an Archetypal Self-Assembly System: Mobile Au-Thiolate Species on Au(111). *Phys. Rev. Lett.* 97, 166102 (2006).

111. Grönbeck, H., Häkkinen, H. & Whetten, R. L. Gold−Thiolate Complexes Form a Unique c(4 × 2) Structure on Au(111). *J. Phys. Chem. C* 112, 15940–15942 (2008).

112. Chaudhuri, A., Lerotholi, T. J., Jackson, D. C., Woodruff, D. P. & Jones, R. G. (2√3×3)rect. phase of alkylthiolate self-assembled monolayers on Au(111): A symmetry-constrained structural solution. *Phys. Rev. B* 79, 195439 (2009).

113. Chidsey, C. E. D., Liu, G.-Y., Rowntree, P. & Scoles, G. Molecular order at the surface of an organic monolayer studied by low energy helium diffraction. *J. Chem. Phys.* 91, 4421–4423 (1989).

114. Nuzzo, R. G., Dubois, L. H. & Allara, D. L. Fundamental studies of microscopic wetting on organic surfaces. 1. Formation and structural characterization of a self-consistent series of polyfunctional organic monolayers. *J. Am. Chem. Soc.* 112, 558–569 (1990).

115. Nuzzo, R. G., Korenic, E. M. & Dubois, L. H. Studies of the temperature-dependent phase behavior of long chain n -alkyl thiol monolayers on gold. *J Chem Phys* 93, 767–773 (1990).

116. Poirier, G. E. Coverage-Dependent Phases and Phase Stability of Decanethiol on Au(111). *Langmuir* 15, 1167–1175 (1999).

117. Maksymovych, P. & Yates, J. T. Au Adatoms in Self-Assembly of Benzenethiol on the Au(111) Surface. *J Am Chem Soc* 130, 7518–7519 (2008).

118. Woodruff, D. P. & Bradshaw, A. M. Adsorbate structure determination on surfaces using photoelectron diffraction. *Rep. Prog. Phys.* 57, 1029 (1994).

119. Jadzinsky, P. D., Calero, G., Ackerson, C. J., Bushnell, D. A. & Kornberg, R. D. Structure of a Thiol Monolayer-Protected Gold Nanoparticle at 1.1 Å Resolution. *Science* 318, 430–433 (2007).

120. Häkkinen, H. Atomic and electronic structure of gold clusters : understanding flakes, cages and superatoms from simple concepts. *Chem. Soc. Rev.* 37, 1847–1859 (2008).

121. Sardar, R., Funston, A. M., Mulvaney, P. & Murray, R. W. Gold Nanoparticles: Past, Present, and Future. *Langmuir* 25, 13840–13851 (2009).

122. Jin, R. Quantum sized, thiolate -protected gold nanoclusters. *Nanoscale* 2, 343–362 (2009).

123. Taylor, R., Torr, N., Huang, Z., Li, F. & Guo, Q. A scanning tunnelling microscopy investigation of gold island formation from an octanethiol self-assembled monolayer on Au(111). *Surf Sci* 604, 165–170 (2010).

124. Fitts, W. P., White, J. M. & Poirier, G. E. Low-Coverage Decanethiolate Structure on Au(111): Substrate Effects. *Langmuir* 18, 1561–1566 (2002).

125. Qian, Y., Yang, G., Yu, J., Jung, T. A. & Liu, G. Structures of Annealed Decanethiol Self-Assembled Monolayers on Au(111): an Ultrahigh Vacuum Scanning Tunneling Microscopy Study. *Langmuir* 19, 6056–6065 (2003).

126. Poirier, G. E., Fitts, W. P. & White, J. M. Two-Dimensional Phase Diagram of Decanethiol on Au(111). *Langmuir* 17, 1176–1183 (2001).

127. Kroto, H. W., Heath, J. R., O'Brien, S. C., Curl, R. F. & Smalley, R. E. C_{60}: Buckminsterfullerene. *Nature* 318, 162–163 (1985).

128. Krätschmer, W., Lamb, L. D., Fostiropoulos, K. & Huffman, D. R. Solid C_{60}: a new form of carbon. *Nature* 347, 354–358 (1990).

129. McClure, D. S. Mathematics and Chemistry: Chemical Applications of Group Theory. F. Albert Cotton. Interscience(Wiley), New York, 1963. x + 295 pp. Illus. $12.50. *Science* 142, 1562–1563 (1963).

130. Tamai, A. *et al.* Electronic structure at the C_{60}/metal interface: An angle-resolved photoemission and first-principles study. *Phys. Rev. B* 77, 075134 (2007).

131. Howard, J. B., McKinnon, J. T., Makarovsky, Y., Lafleur, A. L. & Johnson, M. E. Fullerenes C_{60} and C_{70} in flames. *Nature* 352, 139–141 (1991).

132. Hedberg, K. *et al.* Bond Lengths in Free Molecules of Buckminsterfullerene, C_{60}, from Gas-Phase Electron Diffraction. *Science* 254, 410–412 (1991).

133. Yannoni, C. S., Johnson, R. D., Meijer, G., Bethune, D. S. & Salem, J. R. Carbon-13 NMR study of the C_{60} cluster in the solid state: molecular motion and carbon chemical shift anisotropy. *J. Phys. Chem.* 95, 9–10 (1991).

134. Yannoni, C. S., Bernier, P. P., Bethune, D. S., Meijer, G. & Salem, J. R. NMR determination of the bond lengths in C_{60}. *J. Am. Chem. Soc.* 113, 3190–3192 (1991).

135. Heiney, P. A. *et al.* Orientational ordering transition in solid C_{60}. *Phys Rev Lett* 66, 2911–2914 (1991).

136. Rossel, F. *et al.* Growth and characterization of fullerene nanocrystals on NaCl/Au(111). *Phys. Rev. B* 84, 075426 (2011).

137. Schneider, W.-D. A local view of the Kondo effect: Scanning tunneling spectroscopy. *Pramana* 52, 537–552 (1999).

138. Weaver, J. H. Fullerenes and fullerides: photoemission and scanning tunneling microscopy studies. *Acc. Chem. Res.* 25, 143–149 (1992).

139. Hunt, M. R. C., Modesti, S., Rudolf, P. & Palmer, R. E. Charge transfer and structure in C_{60} adsorption on metal surfaces. *Phys. Rev. B* 51, 10039–10047 (1995).

140. Haddon, R. C., Brus, L. E. & Raghavachari, K. Electronic structure and bonding in icosahedral C_{60}. *Chem. Phys. Lett.* 125, 459–464 (1986).

141. Saito, S. & Oshiyama, A. Cohesive mechanism and energy bands of solid C_{60}. *Phys. Rev. Lett.* 66, 2637–2640 (1991).

142. David, W. I. F., Ibberson, R. M., Dennis, T. J. S., Hare, J. P. & Prassides, K. Structural Phase Transitions in the Fullerene C_{60}. *Epl Europhys Lett* 18, 219–225 (1992).

143. Murray, P. W., Pedersen, M. Ø., Lægsgaard, E., Stensgaard, I. & Besenbacher, F. Growth of C_{60} on Cu(110) and Ni(110) surfaces: C_{60}-induced interfacial roughening. *Phys. Rev. B* 55, 9360–9363 (1997).

144. Hamada, I. & Tsukada, M. Adsorption of C_{60} on Au(111) revisited: A van der Waals density functional study. *Phys. Rev. B* 83, 245437 (2011).

145. Tzeng, C.-T., Lo, W.-S., Yuh, J.-Y., Chu, R.-Y. & Tsuei, K.-D. Photoemission, near-edge x-ray-absorption spectroscopy, and low-energy electron-diffraction study of C_{60} on Au(111) surfaces. *Phys. Rev. B* 61, 2263–2272 (1999).

146. Fartash, A. In-plane orientational order across C_{60}(111)/Au(111) interfaces. *Thin Solid Films* 323, 296–303 (1998).

147. Gardener, J. A., Briggs, G. A. D. & Castell, M. R. Scanning tunneling microscopy studies of C_{60} monolayers on Au(111). *Phys. Rev. B* 80, 235434 (2009).

148. Gardener, J. A., Briggs, G. A. D. & Castell, M. R. Scanning tunneling microscopy studies of C_{60} monolayers on Au(111). *Phys Rev B* 80, 235434 (2009).

149. Xie, Y. An STM Study of C_{60} Molecule on Au(111): Close-Packed Single Layer and Magic Number Clusters. (University of Birmingham, 2013).

150. Zhang, X., Tang, L. & Guo, Q. Low-Temperature Growth of C_{60} Monolayers on Au(111): Island Orientation Control with Site-Selective Nucleation. *J Phys Chem C* 114, 6433–6439 (2010).

151. Schull, G. & Berndt, R. Orientationally Ordered (7×7) Superstructure of C_{60} on Au(111). *Phys Rev Lett* 99, 226105 (2007).

152. Fujita, D., Yakabe, T., Nejoh, H., Sato, T. & Iwatsuki, M. Scanning tunneling microscopy study on the initial adsorption behavior of C_{60} molecules on a reconstructed Au(111)-(23 × √3) surface at various temperatures. *Surf. Sci.* 366, 93–98 (1996).

153. Sakurai, T. *et al.* Scanning tunneling microscopy study of fullerenes. *Prog. Surf. Sci.* 51, 263–408 (1996).

154. Johansson, M. K.-J., Maxwell, A. J., Gray, S. M., Brühwiler, P. A. & Johansson, L. S. O. Adsorption of C_{60} on Al(111) studied with scanning tunnelling microscopy. *Surf. Sci.* 397, 314–321 (1998).

155. Modesti, S., Cerasari, S. & Rudolf, P. Determination of charge states of C_{60} adsorbed on metal surfaces. *Phys. Rev. Lett.* 71, 2469–2472 (1993).

156. Hashizume, T. *et al.* Intramolecular structures of C_{60} molecules adsorbed on the Cu(111)-(1×1) surface. *Phys Rev Lett* 71, 2959–2962 (1993).

157. Lu, X., Grobis, M., Khoo, K. H., Louie, S. G. & Crommie, M. F. Charge transfer and screening in individual C_{60} molecules on metal substrates: A scanning tunneling spectroscopy and theoretical study. *Phys Rev B* 70, 115418 (2004).

158. Hunter, C. A. Quantifying Intermolecular Interactions: Guidelines for the Molecular Recognition Toolbox. *Angew. Chem. Int. Ed.* 43, 5310–5324 (2004).

159. Diederich, F. & Gómez-López, M. Supramolecular fullerene chemistry. *Chem. Soc. Rev.* 28, 263–277 (1999).

160. Mali, K. S., Pearce, N., Feyter, S. D. & Champness, N. R. Frontiers of supramolecular chemistry at solid surfaces. *Chem. Soc. Rev.* 46, 2520–2542 (2017).

161. Wang, P., Metzger, R. M. & Chen, B. Stable monolayers of fullerene derivatives. *Thin Solid Films* 327, 96–99 (1998).

162. Kuzume, A., Herrero, E., Feliu, J. M., Nichols, R. J. & Schiffrin, D. J. Fullerene monolayers adsorbed on high index gold single crystal surfaces. *Phys. Chem. Chem. Phys.* 6, 619–625 (2004).

163. Leigh, D. F. *et al.* Self-assembly of trimetallic nitride template fullerenes on surfaces studied by STM. *Surf. Sci.* 601, 2750–2755 (2007).

164. Uemura, S., Sakata, M., Hirayama, C. & Kunitake, M. Fullerene Adlayers on Various Single-Crystal Metal Surfaces Prepared by Transfer from L Films. *Langmuir* 20, 9198–9201 (2004).

165. Hands, I. D., Dunn, J. L. & Bates, C. A. Visualization of static Jahn-Teller effects in the fullerene anion C_{60}. *Phys. Rev. B* 82, 155425 (2010).

166. Hung, K.-T., Huang, K.-T., Hsiao, C.-Y. & Shih, C.-F. Improving efficiency of pentacene/C_{60} based solar cells with mixed interlayers. *Thin Solid Films* 519, 5270–5273 (2011).

167. Zhang, X., Zeng, Q. & Wang, C. Molecular templates and nano-reactors: two-dimensional hydrogen bonded supramolecular networks on solid/liquid interfaces. *RSC Adv.* 3, 11351–11366 (2013).

168. Liang, H. *et al.* Two-dimensional molecular porous networks constructed by surface assembling. *Coord. Chem. Rev.* 253, 2959–2979 (2009).

169. Boyd, P. D. W. *et al.* Selective Supramolecular Porphyrin/Fullerene Interactions1. *J Am Chem Soc* 121, 10487–10495 (1999).

170. Zhang, H. L., Chen, W., Huang, H., Chen, L. & Wee, A. T. S. Preferential Trapping of C_{60} in Nanomesh Voids. *J. Am. Chem. Soc.* 130, 2720–2721 (2008).

171. Xu, W. *et al.* Construction and photophysics study of supramolecular complexes composed of three-point binding fullerene -trispyridylporphyrin dyads and zinc porphyrin. *Phys. Chem. Chem. Phys.* 13, 428–433 (2010).

172. Sygula, A., Fronczek, F. R., Sygula, R., Rabideau, P. W. & Olmstead, M. M. A Double Concave Hydrocarbon Buckycatcher. *J. Am. Chem. Soc.* 129, 3842–3843 (2007).

173. Chen, C. J. *Introduction to Scanning Tunneling Microscopy*. (Oxford University Press, Oxford, 2008).

174. Binnig, G. & Rohrer, H. Scanning tunneling microscopy—from birth to adolescence. *Rev. Mod. Phys.* 59, 615–625 (1987).

175. Besocke, K. An easily operable scanning tunneling microscope. *Surf. Sci.* 181, 145–153 (1987).

176. Okumura, A., Miyamura, K. & Gohshi, Y. The STM system constructed for analytical application. *J. Microsc.* 152, 631–635 (1988).

177. Feenstra, R. M. Cross-sectional scanning tunnelling microscopy of III-V semiconductor structures. *Semicond. Sci. Technol.* 9, 2157 (1994).

178. Binnig, G. & Rohrer, H. Scanning tunneling microscope. 55, (1982).

179. Binnig, G., Rohrer, H., Gerber, Ch. & Weibel, E. 7 × 7 Reconstruction on Si(111) Resolved in Real Space. *Phys Rev Lett* 50, 120–123 (1983).

180. Binnig, G., Rohrer, H., Gerber, Ch. & Weibel, E. Surface Studies by Scanning Tunneling Microscopy. *Phys. Rev. Lett.* 49, 57–61 (1982).

181. Lang, N. D. Spectroscopy of single atoms in the scanning tunneling microscope. *Phys. Rev. B* 34, 5947–5950 (1986).

182. Gimzewski, J. K., Reihl, B., Coombs, J. H. & Schlittler, R. R. Photon emission with the scanning tunneling microscope. *Z. für Phys. B Condens. Matter* 72, 497–501 (1988).

183. Giessibl, F. J. Atomic Resolution of the Silicon (111)-(7×7) Surface by Atomic Force Microscopy. *Science* 267, 68–71 (1995).

184. Giessibl, F. J., Hembacher, S., Bielefeldt, H. & Mannhart, J. Subatomic Features on the Silicon (111)-(7×7) Surface Observed by Atomic Force Microscopy. *Science* 289, 422–425 (2000).

185. Giessibl, F. J. Advances in atomic force microscopy. *Rev Mod Phys* 75, 949–983 (2003).

186. Hembacher, S., Giessibl, F. J. & Mannhart, J. Force Microscopy with Light-Atom Probes. *Science* 305, 380–383 (2004).

187. Ternes, M., Lutz, C. P., Hirjibehedin, C. F., Giessibl, F. J. & Heinrich, A. J. The Force Needed to Move an Atom on a Surface. *Science* 319, 1066–1069 (2008).

188. Gross, L. *et al.* Measuring the Charge State of an Adatom with Noncontact Atomic Force Microscopy. *Science* 324, 1428–1431 (2009).

189. Ternes, M. *et al.* Interplay of Conductance, Force, and Structural Change in Metallic Point Contacts. *Phys Rev Lett* 106, 016802 (2011).

190. Welker, J. & Giessibl, F. J. Revealing the Angular Symmetry of Chemical Bonds by Atomic Force Microscopy. *Science* 336, 444–449 (2012).

191. Pielmeier, F. & Giessibl, F. J. Spin Resolution and Evidence for Superexchange on NiO(001) Observed by Force Microscopy. *Phys Rev Lett* 110, 266101 (2013).

192. Emmrich, M. *et al.* Subatomic resolution force microscopy reveals internal structure and adsorption sites of small iron clusters. *Science* 348, 308–311 (2015).

193. Huber, F. *et al.* Chemical bond formation showing a transition from physisorption to chemisorption. *Science* 366, 235–238 (2019).

194. Giessibl, F. J. The qPlus sensor, a powerful core for the atomic force microscope. *Rev Sci Instrum* 90, 011101 (2019).

195. Stilp, F. *et al.* Very weak bonds to artificial atoms formed by quantum corrals. *Science* 372, 1196–1200 (2021).

196. Voigtländer, B. *Scanning Probe Microscopy: Atomic Force Microscopy and Scanning Tunneling Microscopy*. (Springer, 2015).

197. Wiesendanger, R. *Scanning Probe Microscopy and Spectroscopy: Methods and Applications*. (Cambridge University Press, 1994).

198. Gottlieb, A. D. & Wesoloski, L. Bardeen's tunnelling theory as applied to scanning tunnelling microscopy: a technical guide to the traditional interpretation. *Nanotechnology* 17, R57 (2006).

199. Bardeen, J. Tunnelling from a Many-Particle Point of View. *Phys. Rev. Lett.* 6, 57–59 (1961).

200. Landau, L. D. & Lifshitz, E. M. *Quantum Mechanics: Non-Relativistic Theory*. (Pergamon Press, Oxford, 1977).

201. Wiesendanger, R. Spin mapping at the nanoscale and atomic scale. *Rev. Mod. Phys.* 81, 1495–1550 (2009).

202. Eigler, D. M. & Schweizer, E. K. Positioning single atoms with a scanning tunnelling microscope. *Nature* 344, 524–526 (1990).

203. Crommie, M. F., Lutz, C. P. & Eigler, D. M. Confinement of Electrons to Quantum Corrals on a Metal Surface. *Science* 262, 218–220 (1993).

204. Avouris, P. Manipulation of Matter at the Atomic and Molecular Levels. *Acc. Chem. Res.* 28, 95–102 (1995).

205. Moresco, F. *et al.* Conformational Changes of Single Molecules Induced by Scanning Tunneling Microscopy Manipulation: A Route to Molecular Switching. *Phys. Rev. Lett.* 86, 672–675 (2001).

206. Pan, S. H., Hudson, E. W. & Davis, J. C. 3He refrigerator based very low temperature scanning tunneling microscope. *Rev. Sci. Instrum.* 70, 1459–1463 (1999).

207. Bartels, L. *et al.* Dynamics of Electron-Induced Manipulation of Individual CO Molecules on Cu(111). *Phys. Rev. Lett.* 80, 2004–2007 (1998).

208. Petersen, L. *et al.* A fast-scanning, low- and variable-temperature scanning tunneling microscope. *Rev. Sci. Instrum.* 72, 1438–1444 (2001).

209. Laegsgaard, E. *et al.* A high-pressure scanning tunneling microscope. *Rev. Sci. Instrum.* 72, 3537–3542 (2001).

210. Weiss, C. *et al.* Imaging Pauli Repulsion in Scanning Tunneling Microscopy. *Phys. Rev. Lett.* 105, 086103 (2010).

211. Rost, M. J. *et al.* Scanning probe microscopes go video rate and beyond. *Rev. Sci. Instrum.* 76, 053710 (2005).

212. Repp, J., Meyer, G., Stojković, S. M., Gourdon, A. & Joachim, C. Molecules on Insulating Films: Scanning-Tunneling Microscopy Imaging of Individual Molecular Orbitals. *Phys. Rev. Lett.* 94, 026803 (2005).

213. Sainoo, Y. *et al.* Excitation of Molecular Vibrational Modes with Inelastic Scanning Tunneling Microscopy Processes: Examination through Action Spectra of cis-2-Butene on Pd(110). *Phys. Rev. Lett.* 95, 246102 (2005).

214. Davis, J. J. Molecular bioelectronics. *Philos. Trans. R. Soc. Lond. Ser. A: Math., Phys. Eng. Sci.* 361, 2807–2825 (2003).

3. Experimental Apparatus

3.1 Introduction

The data presented in this thesis are based on the use of an Omicron ultra-high vacuum (UHV) Fermi Scanning Tunnelling Microscope (Fermi-STM)[1], a UHV high-temperature evaporator, an argon ion gun, and an electrochemical etching tip device. The high vacuum electron beam evaporator is mainly used to prepare Au films on highly oriented pyrolytic graphite (HOPG) or mica, which uses vacuum vapour deposition to create a gold thin film of ~ 200 nm thickness with high purity. Impurities in the Au(111) sample can be removed by using an argon ion gun. A high-voltage electric field ionizes argon gas, producing a large quantity of argon ions. These ions are then accelerated by electric and magnetic fields and directed to bombard the surface, effectively cleaning the Au(111) surface by removing contaminants[2]. UHV high-temperature evaporator based on the molecular beam epitaxy technique (MBE) can produce ideal molecular monolayers, metal films, and other nanomaterials on the surface of Au(111). The resolution of the STM images is directly governed by the tungsten tip, which can be obtained using an electrochemical etching technique[3–5].

3.2 Omicron Fermi-STM

Fermi-STM is contained within a UHV chamber known as the main chamber, with a pressure of 2×10^{-10} mbar. The tips and samples are transferred into the main chamber via a fast entry lock (FEL) attached to the main chamber in Figure 3.1. FEL must be pumped down to $\sim 10^{-9}$ mbar prior to opening the valve between the two chambers in order to maintain the vacuum in the main chamber within the 10^{-9} mbar range during sample transfer[1].

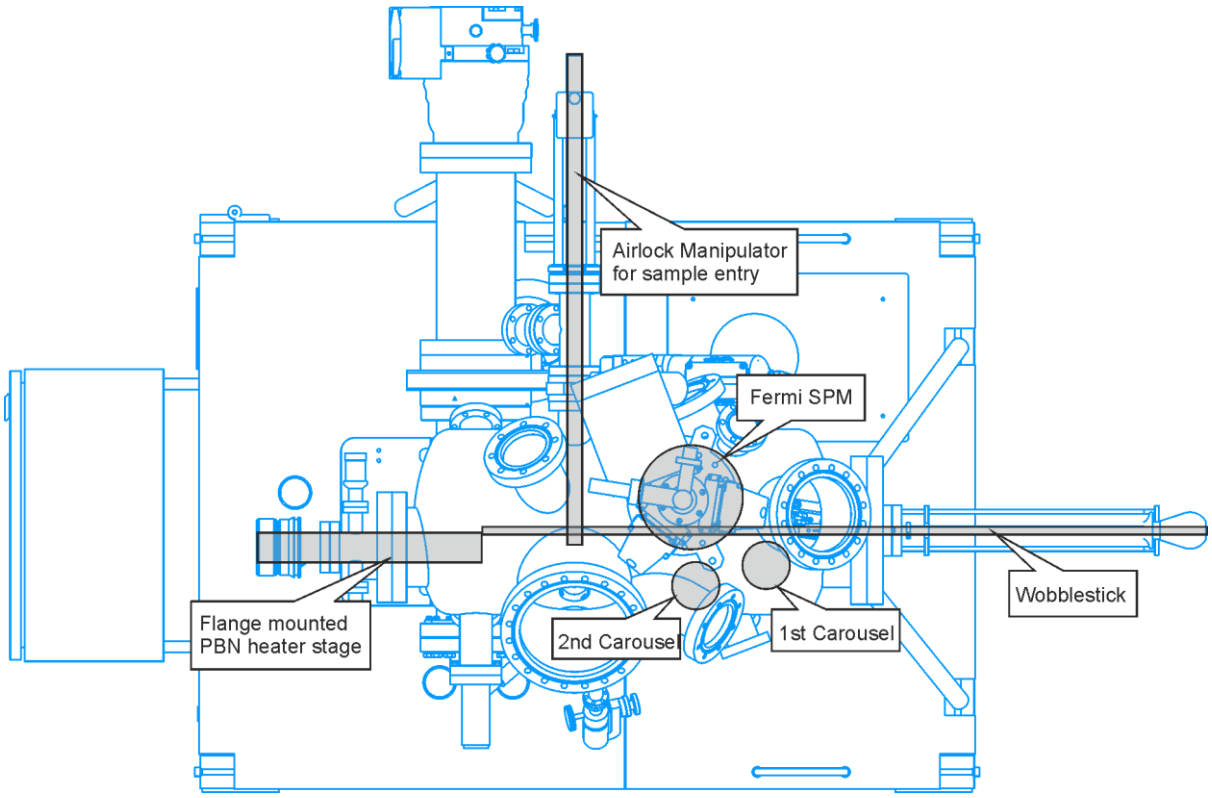

Figure 3.1 Omicron Fermi-STM schematic diagram. The flange mounted PBN heater stage (manipulator) is located on the left side of the main chamber, which is connected on its left side to the FEL. A carousel stage for storing the samples and tips is between the STM and the manipulator. An STM stage is installed on the right side of the main chamber. Figure is reproduced from Ref [1].

Both the carousels and manipulator are situated in the UHV main chamber of a Fermi-STM. It facilitates sample transfer. The chamber's cryostat system can adjust the temperature of the samples. The manipulator's samples can be heated to 750 K using resistive heating or 1500 K using direct heating. The chamber is equipped with an Ar^+ ion sputtering system for Ion bombardment to clean noble samples such as gold, silver, and platinum. This sputtering method can also manufacture atomic defects of specific sizes on substances such as graphite and silicon by adjusting the beam energy.

A wobble stick is half-inserted into the UHV main chamber on the right side of Figure 3.1 It features can be used to transfer samples between the Fermi STM stage, the manipulator, and the FEL transfer rod. Additionally, it is utilised to store samples on the carousel stage.

3.2.1 Stage Design

During operation, the STM is particularly sensitive to external vibrations. As a result, the STM features an internal spring suspension and eddy current damping for vibration isolation, both of which are located around the scanning stage. As seen in Fig. 3.2 (a), the scanner is secured to the eddy current damping stage via soft springs. The magnets around the STM stage can damp the movement of the copper plates, therefore increasing the stability of the working system. In combination with the eddy current damping stage, the springs can significantly reduce the amount of external vibration that enters the STM stage[1]. For a typical 20-bit digital-to-analog converter (DAC) with a range of ±10 V and a speed of up to 10^6 samples per second, the output voltage has a noise floor of approximately 50 $nV/Hz^{-1/2}$.

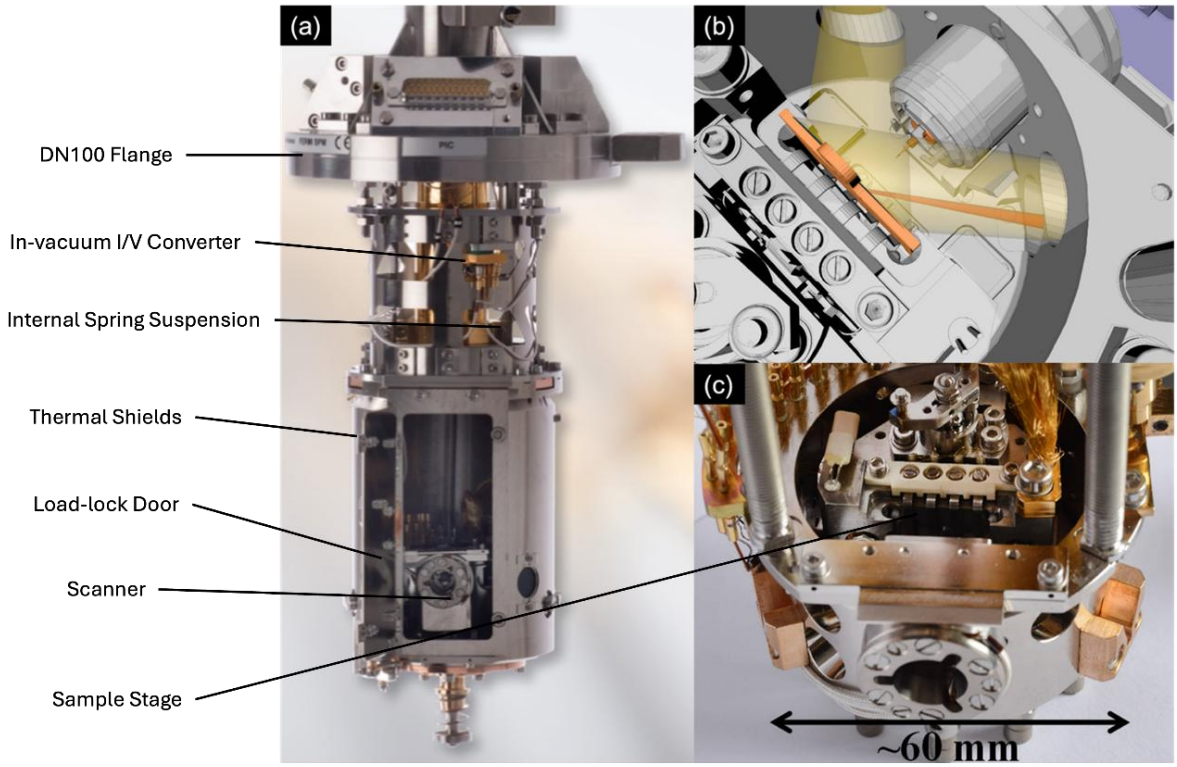

Figure 3.2 (a) The instrument (Fermi-STM) mounted on a CF150-108 flange. (b) Optical access of Fermi-STM. (c) Details of the eddy current vibration isolation system. Figures are reproduced from Ref [1].

3.2.2 Ultra-High Vacuum Condition

To analyse the qualities of a surface, it is critical to maintain stable operation throughout the experiment. The rate at which reactive species from surrounding gases reach the surface should be low. The optimal environment for such studies is a vacuum, which confines a finite amount of gas in a particular space. UHV is defined as pressure greater than or equal to 10^{-9} mbar[4].

The ion pumps (IP) and titanium sublimation pumps (TSP) are used to pump the chamber. The IP constantly functions while the chamber is at $\sim 10^{-9}$ mbar, while the TSP operates for one minute every eight hours. The UHV condition may be maintained for an extended time using these pumps. Initially, a rotary pump is operated for roughly 30 minutes to lower the atmospheric pressure to higher than $\sim 10^{-3}$ mbar to attain UHV. For the turbomolecular pump, it functions as an additional pump. As a result, the turbopump is triggered when the vacuum drops below $\sim 10^{-3}$ mbar. The chamber is sealed with heat shields after the pressure drops to a level of $\sim 10^{-6}$ mbar or less. A heater raises the temperature of the whole Fermi-STM to 140°C for 24 to 48 hours. Then, to degas IP and TSP, the main chamber temperature must rise to about 80°C. A valve may be closed between the turbopump and the chamber, enabling the rotary and turbopumps to be vented. At the same time, IP and TSP maintain a chamber pressure of $\sim 10^{-10}$mbar after complete degassing. This valve can then be closed. The system will maintain $\sim 10^{-10}$ mbar during STM scanning[6].

3.2.3 Cooling Down and Temperature Stability

As demonstrated in Figure 3.2, the new compact STM scanner with an *in-situ* tip exchange system for maximum stability is directly affixed to the Fermi-STM scanning stage. The sample receiving system is situated on an *r*, φ slider that allows coarse *z* or *x*-direction movement. Mechanical springs secure the sample, triggered with the wobbling stick once transferred to the sample stage. This prevents placing strain on the clamping mechanism during sample

insertion, which might eventually result in sample clamping loosening. Two sealed ports with glass windows for optical access and one port for *in-situ* evaporators are provided on the Fermi-STM stage in Figure 3.2 (b). The stage is only 60mm in diameter. The scanning range area (x, y, z) is $(2.9\mu m \times 2.9\mu m \times 0.9\mu m)$ at RT. And the scanning range area is limited to $(0.8\mu m \times 0.8\mu m \times 0.3\mu m)$ at LT (15K)[1].

The cooling system of Fermi-STM consists of an STM scanner system and an optimised heat control system. A flow cryostat system is applied, which can operate by using liquid helium or liquid nitrogen. The Fermi-STM realises a novel scanning tip design, in which a compact STM scanner is directly installed to the stage. The sample and STM stage are linked individually to the flow cryostat's cold finger through flexible cooling connectors. Temperature control is accomplished by the employment of heater components and temperature sensors. An exterior thermal shield of the whole STM is pre-cooled through a flow cryostat's exhaust gas line. Each heating element equipped with temperature sensors is separately programmable through a controller. The x/y/z drift $< 0.5\text{Å/h}$, and z-stability $< 2\text{pm}$.

A flexible transfer tube transports cooling liquid from a dewar to the flow cryostat. It is feasible to function without mechanical pumps by employing slight overpressure in the Dewar. This eliminates the possibility of mechanical pumps affecting the vibration isolation. The Dewar's overpressure is continuously maintained at one psi for liquid helium and two psi for liquid nitrogen. A needle valve maintains a steady flow of helium or nitrogen. When the scanner temperature is kept higher than the sample temperature, Thermal drift is minimised in STM measurements. The temperature of the scanner is regulated by a heating component and temperature-detecting sensor located on the STM scanner head. For convenience, this temperature can be referred to as "scanner" temperature in the following experiment. The temperature variation from the tip to the base is around 5K. At the sample stage, the sample temperature is determined near the sample. It takes approximately 2.5 hours to obtain steady

drift values for STM experiments during the cooling-down operation. The lowest temperature of the sample is ~7K. The temperature of the scanner can be maintained at ~25K. Also, the sample can be swapped three hours later. Using an active temperature management system, the temperature stability of 0.1mK/min was attained at the STM head (scanner)[1].

3.2.4 *In-situ* Tip & Sample Exchange

An *in-situ* tip exchange system is required for essential experimental methods in ultra-high vacuum and rapid transitions between STM and AFM modes without venting the whole chamber. A novel method for inserting a tip via the scanner tube's backside is applied in Fermi-STM. As shown in Figure 3.3 (a), a tip-loading device controlled by a rotating wobbling stick can pick up a tip from a tip carrier plate and insert it into the scanner. The tip is secured on top of the scanner using a bayonet-like mechanism. The sample will be retained in the sample stage during tip exchange by applying this method. The rotating wobbling stick is utilised to transmit sample plates and tip carrier plates from the carousel to the STM stage (Figure 3.3 (b)). And it can control the door shield of the STM stage as well[1].

The sample plate in Figure 3.3 (b) was designed for radiative heating to a range of temperatures. Additionally, it features a ceramic plate that serves as a fixation for testing samples during scanning. The ceramic plate is covered with metal on only one side to prevent it from charging. This enables the sample holder to be utilised in electron spectroscopy applications. A tiny PBN plate is placed beneath the sample inside the metal groove-like radiation barrier. To avoid localised overheating, the contact brushes attached to the sample holder and the STM stage are constructed of the same material[1].

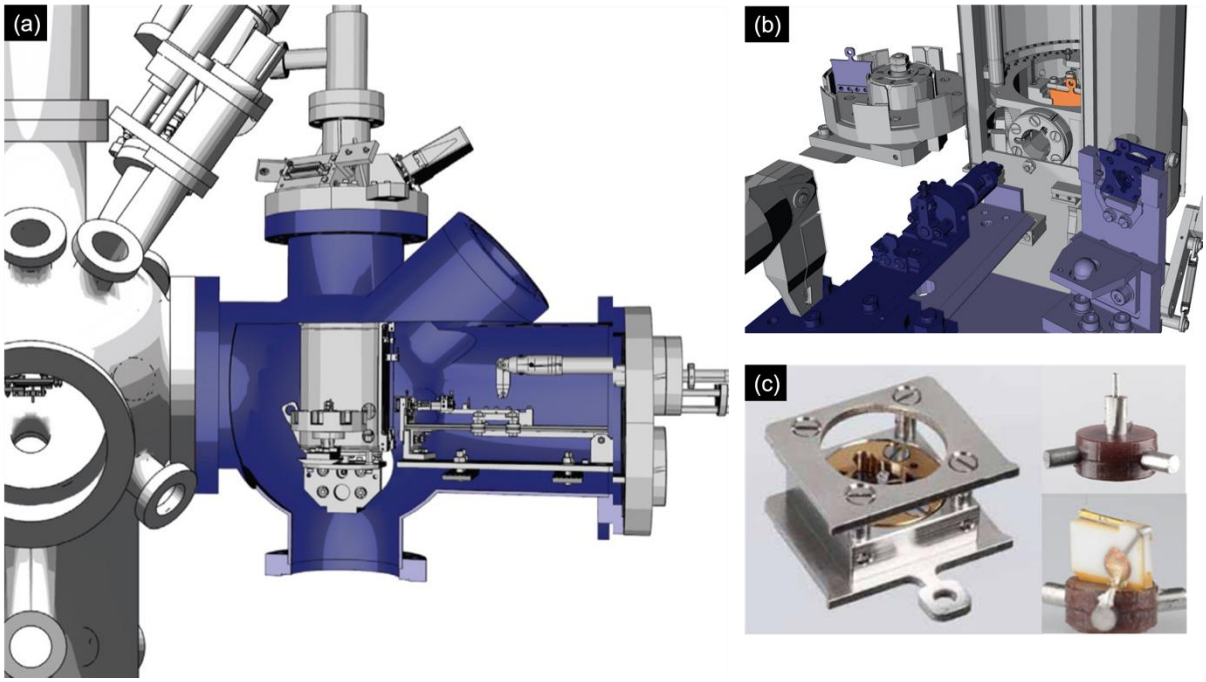

Figure 3.3 (a) Integration to a UHV system. (b) *In-situ* tip exchange system. A tip-loading system operated by a wobble stick. It can pick up a tip from a carrier plate and insert it into the scanner. (c) The tip transfer plate and tip holders for STM and Q-Plus AFM. Figures are reproduced from Ref [7].

3.2.5 Radiative Heating and Direct Current Heating

The Omicron Fermi-STM is equipped with two different heating systems in the manipulator. The first is radiative heating, whereas the second is direct current heating. As illustrated in Figure 3.4, radiative heating is primarily accomplished using the PBN plate incorporated into the metal shield. When a sample is placed on the sample stage, the contact brushes on the sample holder and stage make a robust closed-loop circuit between the sample and the heater. The current flows through and warms both PBN and the sample above. The sample temperature can be raised to 750 K in this mode. Direct current heating is suitable for samples with adequate electrical conductivity. This option allows for sample heating up to 1500 K[1].

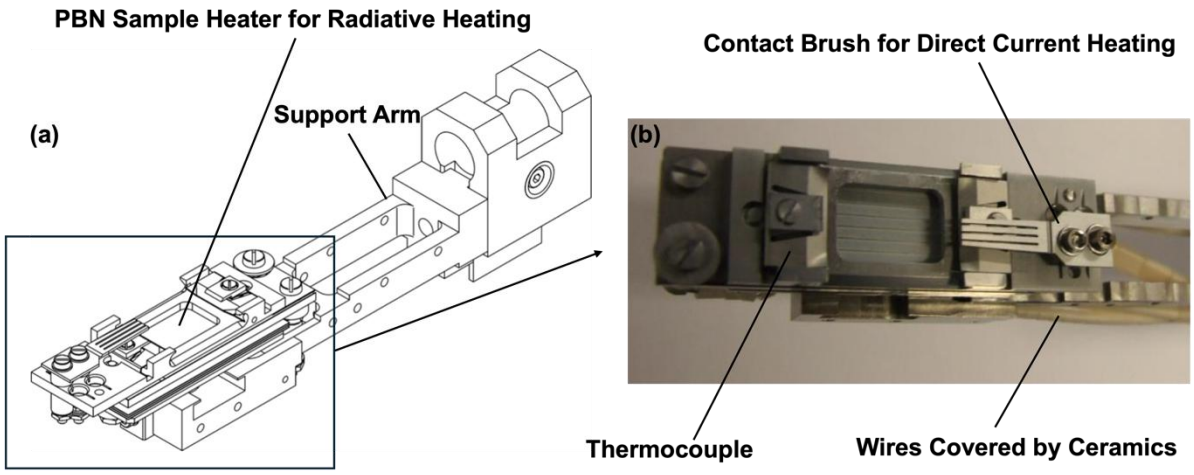

Figure 3.4 Schematic diagram (a) of Manipulator's head for primary (polar) rotation, with current resistive sample heater (b). Figures are reproduced from Ref [1].

3.3 ISE 5 Ion Gun

The ISE 5 ion gun is used to sputter and clean the sample surface, with argon ions being the most often employed sputtering ions in surface science. During the ion bombardment process, the optimal working pressure in the chamber for the ISE 5 ion gun is between 5×10^{-6} and 8×10^{-5} mbar. It can generate a beam energy range of 250 eV to 5 keV and a maximum discharge current of 1 mA at the working pressure. Figure 3.5 (a), (b), and (c) illustrate the external view, inner view, and operating principle of an ISE 5 ion gun, respectively[7].

The exterior and internal views of an ISE 5 sputtering ion gun are depicted in Figure 3.5 (a) and (b), where a magnet covers the gas cell. The cathode potential of the ion flight tube is higher than the earth potential of the metal cover outside. Argon gas is introduced into the ion cannon through a leaky valve. The discharge applied between the cathode and anode then ionises and confines the Argon atoms in the gas cell. The magnet that surrounds the cell generates a magnetic field. A pair of focus plates can be used to regulate and limit the flux of the ion beam.

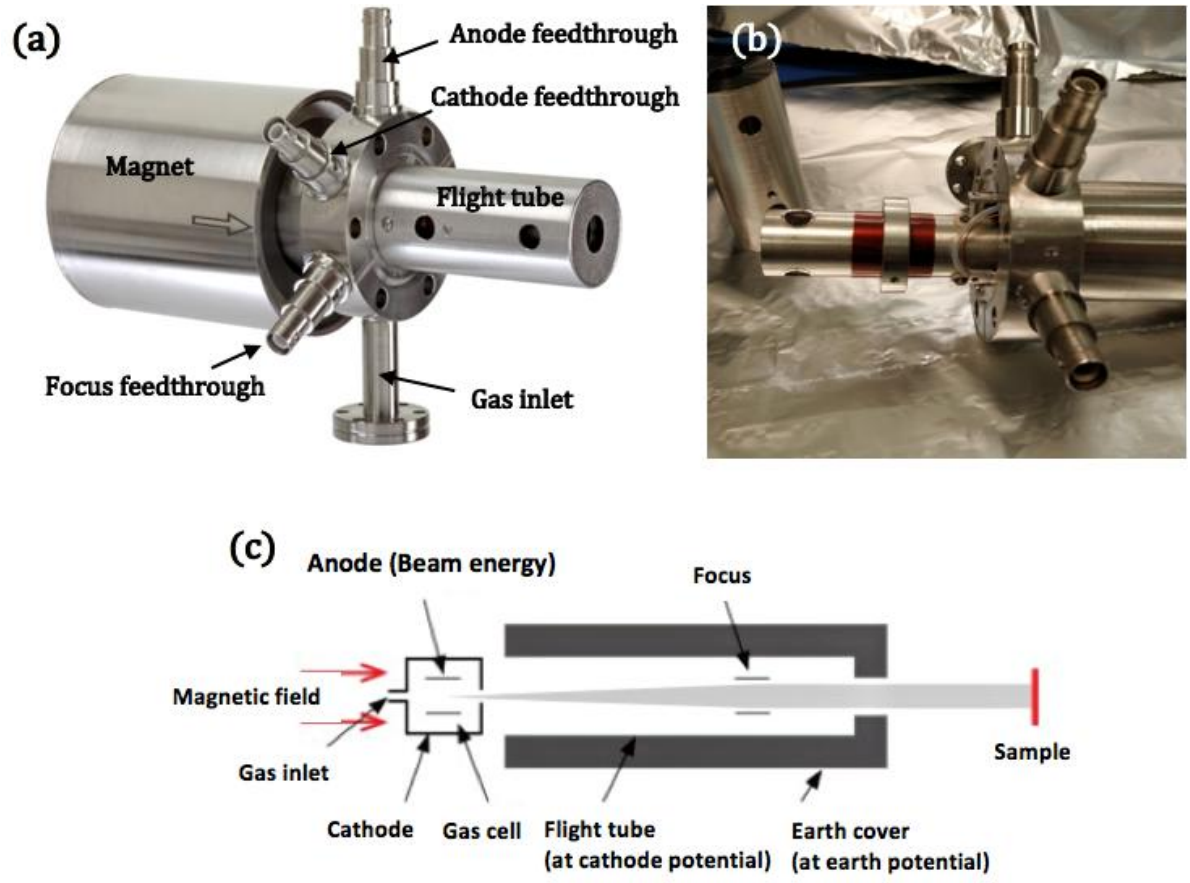

Figure 3.5 External view of an ISE 5 cold cathode sputter ion gun in Figure 3.5 (a). It illustrates the significant components, including a permanent magnet covering the gas cell, feedthrough for the high voltage anode, cathode, beam focus, and gas input. (b) The ion gun's internal construction. Argon gas enters the gas cell through the white tube inside the earth metal cover. (c) Schematic illustrating the operation of a cold cathode source ion gun. The cathode potential of the ion flight tube is greater than that of the earth cover outside. Figures are reproduced from Ref [7].

3.4 Tip Preparation

The quality of the STM tip directly affects the ability to get high-resolution STM images. Typically, the optimal tip contains just one or a few atoms at its terminal. The tip is manufactured by electrochemical etching 0.4 mm diameter tungsten wire that is 99.9% pure. It is formed by electrochemical corrosion with a solution of 2M NaOH. The solution in this concentration can be prepared by dissolving 40 g NaOH pellets in 500 ml distilled water[8].

Figure 3.6 (a) and (b), a tip etching mount and its fundamental schematic design. The etching system is coupled to a limited electronic control that supplies and regulates the etching voltage and threshold current. A piece of clean tungsten wire bent in a circle and attached to the cathode power source is inserted into the solution. Following that, another part of the tungsten wire around 3 cm to 4 cm in length is cleaned multiple times in distilled water before being put into the tip holder and trapped using clamps on the etching stage. Connect the tip and tip holder to the power supply's anode. Before etching, we must ensure that the tungsten wire is positioned precisely above the solution surface and points straight toward the centre of the platinum ring. The handwheel on top of the etching stage is used to modify the vertical position.

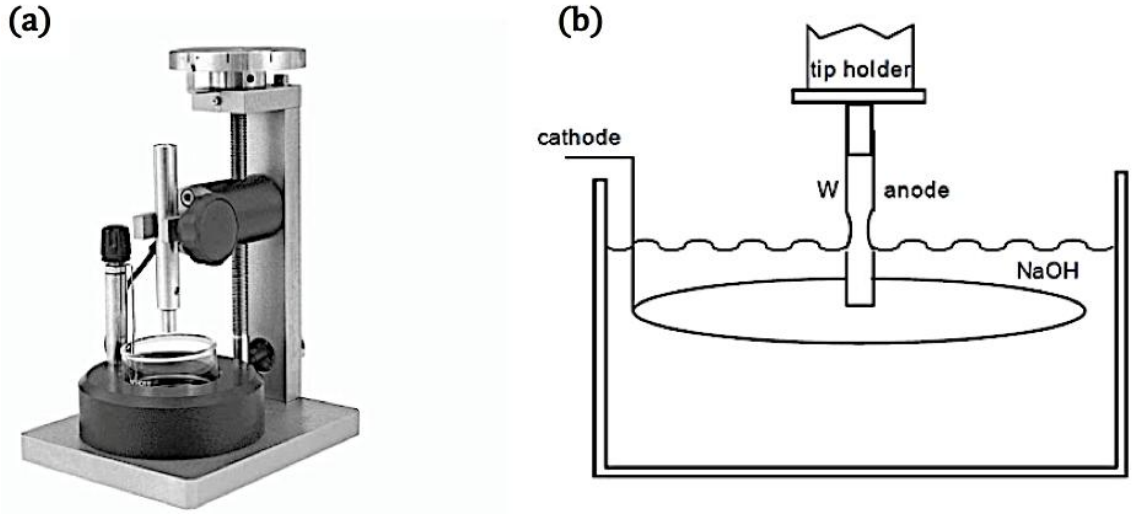

Figure 3.6 (a) Omicron adjustable-height tip etching mount with adjustable etching voltage and threshold curren. (b) Schematic of STM tip etching in a sodium hydroxide solution. Tungsten wire is linked to the anode of the power supply through the tip holder. A platinum wire connecting the cathode of the power supply is placed into a solution with its termination twisted into a circle. Figures are reproduced from Ref [9].

When the etching begins, tungsten wire is progressively incorporated into the NaOH solution through the handwheel until a gap of 2 to 3 mm between the solution surface and the tip holder is left. Then, a voltage of 10 V is delivered straight to the tungsten wire to initiate the electrochemical etching reaction. At the anode, the chemical reaction is expressed as:

$$W(s) + 8OH^- \rightarrow WO_4{}^{2-} + 4H_2O + 6e^-$$

Tungsten interacts with OH^- and forms $WO_4{}^{2-}$ throughout the reaction. At the contact between the tungsten wire and the NaOH solution, the solution surface creates a meniscus. It generates a gradient of concentrated OH- at this location. As a result, after the etching is complete, the tungsten wire terminal remaining on the tip holder is sharp and forms a quasi-circular cone. H_2 bubbles are generated around the cathode. The chemical reaction is as follows:

$$6H_2O + 6e^- \rightarrow 3H_{2(g)} + 6OH^-$$

Thus, the total electrochemical reaction process for tip etching is as follows:

$$W_{(s)} + 2OH^- + 2H_2O \rightarrow WO_4{}^{2-} + 3H_{2(g)}$$

When the first etching is done, the power supply needs to be switched off immediately[10]. Then, the tip is taken out of the solution and cleaned with distilled water again. The new prepared tip is commonly checked with an optical microscope before being put into the UHV chamber. The STM tip with a very long terminal produces strong vibrations during scanning. However, its terminal would be thick when the tip is too short. It leads to a low resolution of the scanning images. In most cases, for achieving a tip with perfect shapes and symmetric apex, twice or more times of etching is required.

3.5 Liquid-phase Method

The liquid phase method to create SAMs involves immersing a clean substrate, typically made of metals like gold or silver, into a solution containing the desired molecules. These molecules, which have functional groups with a strong affinity for the substrate, adsorb onto the surface through their head groups. Over time, they organise into a tightly packed, ordered monolayer due to intermolecular forces like van der Waals interactions and hydrogen bonding. After sufficient assembly time, the substrate is removed, rinsed with a clean solvent to remove any excess molecules, and dried. The formation and quality of the SAMs are then characterised

using techniques such as ellipsometry, contact angle measurements, and STM or AFM. This method is favoured for its simplicity and effectiveness in creating uniform and well-ordered monolayers.

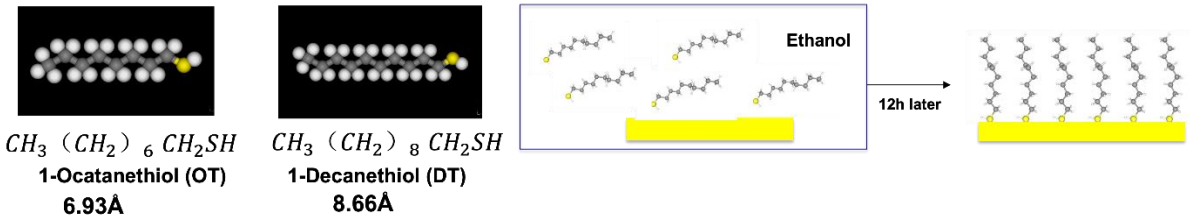

Figure 3.7 Schematic diagram of liquid-phase method to create alkanethiol/Au SAMs.

In our case, as shown in Figure 3.7. Self-assembled monolayers of alkanethiol molecules on Au(111) surfaces are prepared by liquid-phase methods. The surface structure formed depends on the molecular coverage. The treated Au(111) samples were immersed in an ethanol solution of OT or DT molecules at a concentration of 0.1 mol/L and a purity of ≥98.5% for 12 hours to prepare an OT/Au(111) or DT/Au(111) SAMs with densely packed phase structure in saturation coverage. Then the sample is transferred to UHV chamber to deposit C_{60} molecules.

3.6 Fullerene Evaporator

In-situ deposition within the UHV-STM system is facilitated by a Knudsen cell (K cell), which serves as an effusion evaporator for generating a low-pressure particle source during crystal deposition. A careful selection of materials for the thermal evaporator in Figure 3.8. The controlled operating temperature is 50 to 700 °C, permits evaporation in the UHV chamber and eliminates cross-talk between consecutively evaporated substances[11].

A standard Knudsen cell comprises a crucible, heat shields, a water-cooling system, an orifice shutter, and tantalum heating filaments, as illustrated in Figure 3.7(a). For the deposition of C_{60}, the C_{60} powder is contained within a ceramic crucible. As depicted in Figure 3.7(b),

The deposition temperature for C_{60} molecules ranges from 300 °C to 400 °C, at which additional cooling water is not required. The experiment employs a thermocouple to monitor the heating temperature. Initially introducing the C_{60} source into the UHV necessitates an extended degassing period to eliminate impurities. The crucible is heated to 400°C for 5 minutes, causing the pressure to rise to 1×10^{-7} mbar initially. After several degassing cycles, a chamber pressure below 5×10^{-8} mbar at 400 °C indicates the C_{60} source is sufficiently purified for deposition. Prior to each deposition, the C_{60} source undergoes degassing at 400 °C for 10 minutes, followed by deposition starting at a K cell temperature of 395°C. At this temperature, C_{60} molecules sublimate directly from solid to gas, allowing for precise control over the quantity of molecules deposited by adjusting the duration of evaporation[8].

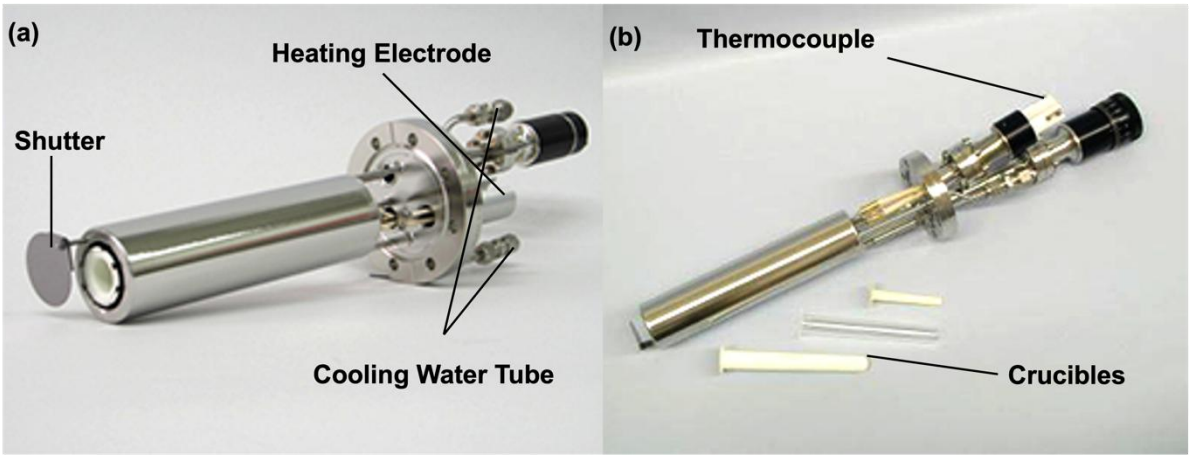

Figure 3.8 Knudsen cell Thermal evaporators for Thin Film Growth. (a) It contains pure C_{60} powders inside the crucible. There is a shutter on the terminal, which enables C_{60} gas to be evaporated out or not. (b) The feedthrough of the thermocouple attached is the bottom for measuring temperature. Figures are reproduced from Ref [11].

3.7 Au(111) Sample Preparation

The Au(111) substrate utilised is generated using the physical vapour deposition (PVD) approach by depositing gold atoms on HOPG. Prior to being moved into a UHV chamber, the HOPG sample used to support gold films is cleaned by cleaving several layers away. Then a

vaporising boat with gold wires is positioned just under HOPG in the evaporator chamber. The temperature of the molybdenum boat is progressively increased to 1273 K by e-beam, which melts the gold wire and initiates evaporation. Also, the thickness and rate of gold deposition are determined using an embedded quartz crystal oscillator installed inside the evaporator chamber[9].

Ion sputtering can clean the surface after transferring the prepared Au(111) sample to the STM UHV chamber. Argon gas is ionised and accelerated within ISE 5 ion gun, where it collides with the Au(111) surface with great force. This ion bombardment method allows the removal of the adsorbed impurities, metal oxide, and a few layers of gold on the sample surface. The Au(111) surface is somewhat damaged due to ion bombardment. To eliminate any leftover contaminants from the surface, the sample will be heated to 873 K. Also, high-temperature annealing treatment increases the diffusing of surface gold atoms, which contributes to the Au(111) sample surface's self-healing and smoothing[10].

3.8 STM Data Analysis

In STM, the sample is scanned by a very fine metallic tip connected to an XYZ positioning device made of piezoelectric materials. As shown in Figure 3.9, the sample is positively or negatively biased, allowing a small tunnelling current to flow when the tip is near the sample. If the tunnelling current exceeds a preset value, the distance between the tip and the sample is increased; if it falls below this value, the feedback system decreases the distance. The tip scans line by line over the sample surface, following its topography. The tunnelling current flows across the small gap between the tip and the sample, and even tiny changes in this separation cause large changes in the tunnelling current, enabling precise control of the tip-sample distance.

There are two primary modes are used to obtain surface images: constant height mode and constant current mode. In constant height mode, the tip maintains a fixed height above the sample surface, and variations in the tunnelling current are measured to create the topographical image, providing rapid imaging but requiring a very flat surface. In contrast, constant current mode adjusts the tip height to maintain a constant tunnelling current as it scans the sample, allowing it to follow the surface contours more accurately and produce detailed topographical images, albeit at a slower scanning speed.

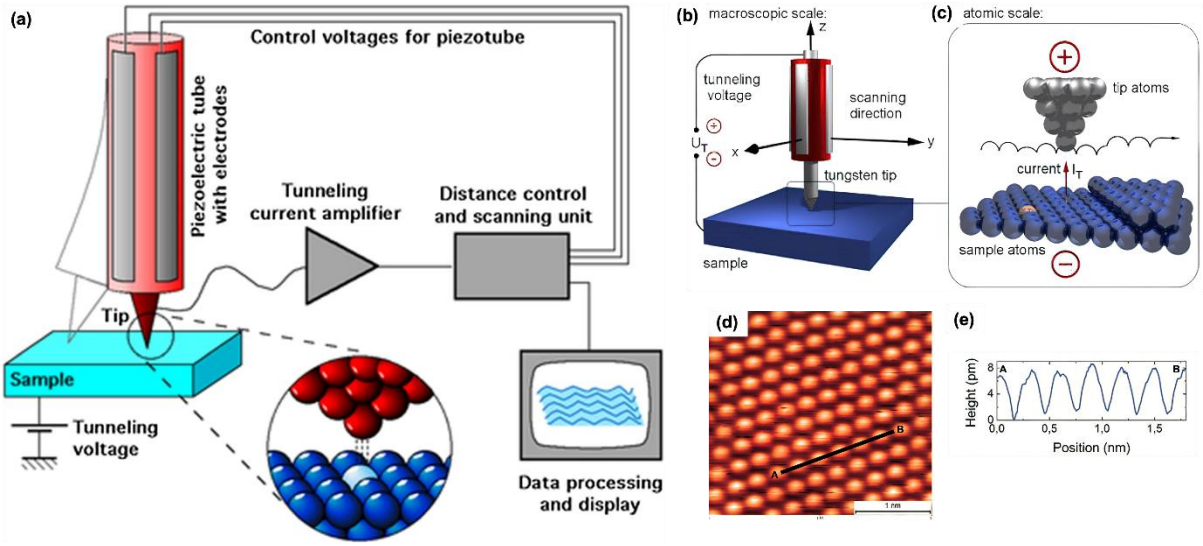

Figure 3.8 The schematic diagram of STM. (a) Working principle of STM system. (b) and (c) A schematic diagram of the STM piezo tube in different scales. (c) Typical STM image in constant current mode for Au(111) sample. (d) Line profile of A-B in STM image. Figures are reproduced from Ref [3–5].

Our system operates in constant current mode because it is more convenient, and the accidental tip crash can be avoided. During the stable scanning, the drift rates will be less than 0.5 pm/min, as high-resolution imaging can take up to 30 minutes, causing a 30 pm variation in tip-sample separation. To accomplish this, the microscope must be at thermal equilibrium with no temperature or air pressure fluctuations, and residual piezoelectric creep must be eliminated by positioning the tip and waiting for an extended period, sometimes up to 12 hours, for stable imaging.

In STM measurement, uncertainty in imaging arises from thermal drift, piezoelectric creep, electronic noise, vibrations, and tip conditions. To minimise these uncertainties, it is essential to ensure the STM system is at thermal equilibrium before imaging, use vibration isolation techniques, and employ high-quality electrical grounding and shielding. Allowing time for piezoelectric elements to stabilise can mitigate creep, while regular calibration with known standards, such as close-packed C_{60} structure and alkanethiol striped phase in our case, helps correct discrepancies. Optimising feedback control parameters ensures stable operation and monitoring or replacing the tip maintains high resolution and accuracy. Uncertainty in STM measurements comes from systematic errors, like calibration issues and environmental factors, and random errors, such as electronic noise and short-term fluctuations. Systematic errors can be identified and corrected through regular calibration, thermal equilibrium, vibration isolation, and feedback control adjustment. Random errors can be reduced by grounding, shielding, and averaging multiple measurements. To combine these errors into a single uncertainty measure, quantify the systematic and random errors (typically the standard deviation), then use the root-mean-square method. This approach provides a comprehensive measure of total uncertainty in STM measurements, which is around $0.02 - 0.05$ nm level.

Also, Fourier transformation in STM images is a mathematical process that converts spatial data from STM images into frequency space using the Fast Fourier Transform (FFT). FFT analysis is employed in STM images to identify periodic structures and repetitive patterns, filter out high-frequency noise to enhance image clarity, and determine the surface symmetry, aiding in material characterisation. It also allows for studying surface modulations such as superstructures or charge density waves, highlights periodic features not immediately apparent in real-space images, and quantifies spatial frequencies related to atomic spacings and structural parameters. This comprehensive analysis enhances our ability to accurately interpret and characterise the sample surface.

When we analyse the STM data, the basic filters tool allows the application of several simple filters to STM images, which can be highly effective for data denoising. However, it is crucial to exercise caution, as the real measured data may be altered in the process, potentially obscuring important features of the image. All filters modify the data based on the values in the neighbourhood of the filtered pixel. For some filters, the size and shape of this neighbourhood are fixed. However, the size can be adjusted for most filters using the size parameter. For non-Gaussian filters, the size parameter determines the diameter of the neighbourhood in pixels. It is advisable to use filters of odd sizes to ensure a symmetric effect.

The Gaussian filter is a smoothing filter where the size parameter determines the full width at half maximum (FWHM) of the Gaussian function. The relationship between FWHM and the standard deviation (σ) is $\mathrm{FWHM} = 2\sqrt{(2\ln 2)} \cdot \sigma \approx 2.35482\sigma$. Careful consideration of these parameters is essential to preserve the integrity of the original data while effectively reducing noise.

References

1. Omicron. Omicron's product introduction (Electronics Technical Reference Manual). https://www.scientaomicron.com/en.

2. Oura, K., Lifshits, V., Saranin, A., Zotov, A. & Katayama, M. *Surface Science: An Introduction*. (Springer Science & Business Media).

3. Wiesendanger, R. *Scanning Probe Microscopy and Spectroscopy: Methods and Applications*. (Cambridge University Press, 1994).

4. Voigtländer, B. *Scanning Probe Microscopy: Atomic Force Microscopy and Scanning Tunneling Microscopy*. (Springer, 2015).

5. Chen, C. J. *Introduction to Scanning Tunneling Microscopy*. (Oxford University Press, Oxford, 2008).

6. Binnig, G. & Rohrer, H. Scanning tunneling microscope. 55, (1982).

7. Omicron. Omicron's product introduction (Ion Sources Manual). https://www.scientaomicron.com/en/products-solutions.

8. Xie, Y. An STM Study of C_{60} Molecule on Au(111): Close-Packed Single Layer and Magic Number Clusters. (University of Birmingham, 2013).

9. Wang, Yi. Heterostructures of C_{60}/C_{70} and rotation of C_{70}-Au magic number clusters on Au(111) and highly oriented pyrolytic graphite. (University of Birmingham, 2020).

10. Gao, J. Structural analysis of self-assembled monolayers on Au(111) and point defects on HOPG. (University of Birmingham, 2013).

11. Createc. Createc's product introduction (High-Temperature Cell Manual). https://www.createc.de/Home/.

4. Coverage-Dependent Phases of Octanethiol or Decanethiol Molecules on Au(111)

Portions of the figures presented in this chapter include reproduced data from previously published works, in which I have had the privilege of contributing as both a co-author[1] and the first author[2]. These figures are based on re-executed experimental results originally found in the Supporting Information of the following publications:

- Zhang, X.; Gao, J.; Fan, X.; Wang, Y.; **Ding, H.**; Qin, X.; Jiang, S.; Zhao, T.; Zhu, G.; Lu, H.; Yang, Z.; Lin, H.; Li, Q.; Chi, L.; Pan, M.; Guo, Q. Orientation-Selective Growth of Single-Atomic-Layer Gold Nanosheets via van Der Waals Interlocking and Octanethiolate-Confined Molecular Channels. *J. Phys. Chem. C* 2019, 123 (41), 25228–25235. (Roles: Formal analysis, Validation, Visualisation.)
- **Ding, H.**; Zhang, X.; Li, B.; Wang, Y.; Xia, C.; Zhao, H.; Yang, H.; Gao, Y.; Chen, X.; Gao, J.; Pan, M.; Guo, Q. Orientational Growth of Flexible van Der Waals Supramolecular Networks. *Small Struct.* 2024, 5. (Roles: Conceptualisation, Data curation, Formal analysis, Investigation, Methodology, Resources, Software, Validation, Visualisation, Writing-original draft, and Writing-review and editing.)

4.1 Introduction

Molecular self-assembly depends on molecule-substrate interactions and van der Waals forces between molecules[3]. Molecules can form self-assembled membrane systems on different substrates[4,5]. The classification of self-assembled systems is based on the chemical interaction of the molecule's head with the substrate, such as the S-Au bond interaction of alkanethiol/Au(111) SAMs[6–8]. In contrast, the rest of the molecule can be arbitrarily selected. The alkanethiol/Au(111) SAMs have received the most attention and have been well studied

over three decades. Despite the extensive research on alkanethiols over the years[9–11], Our renewed interest in studying alkanethiols stems from advancements in experimental and theoretical techniques that open up new avenues for exploration beyond what was previously possible. This research aims to uncover novel properties and applications of alkanethiols, addressing contemporary scientific and technological challenges in nanotechnology, materials science, and surface chemistry[12–15].

In this chapter, the structural features of self-assembled monolayers are characterised by alkanethiol molecules: the two-dimensional crystal structure of the surface, defects, structural features of the molecular chains, and the structure of the Au-S internal interface. At lower coverage, alkanethiol self-assembled monolayers (SAMs) exhibit a variety of structural phases, which can be induced by selectively removing molecules through partial thermal desorption. The configuration of these phases can be described by the notation $p(r \times \sqrt{3})a$, where "ra" represents the vertical distance between adjacent stripes and a denotes the NND of gold. The alkanethiol coverage ranges from 0.1 to 0.315 monolayers (ML)[16–18]. One monolayer is defined as one alkanethiol molecule per surface Au atom. Incrementally heating the sample from a fully covered layer allows molecules to be desorbed in ultra-high vacuum (UHV) conditions without breaking apart, offering a simple yet effective method for adjusting the surface coverage[4,19–22]. After thermal desorption, STM is deployed to assess the molecular coverage and elucidate the molecular monolayer's structure[22,23].

The relationship between the structure of OT molecules on Au(111) with different molecular coverage of the surface has been investigated[22]. At saturation coverage, the OT/Au(111) SAMs are close-packed structure. As the annealing temperature increases, the molecules adsorbed on the Au(111) surface partially desorb and spontaneously form different molecular structures at low coverage[22–24]. The structural phases of molecules at low coverage

have been well studied and reported. The $p(6.5 \times \sqrt{3})$ striped phase with a surface molecular coverage of 0.23 ML and a period of *6.5a* by heating /Au(111) samples at saturation coverage for three hours at 393 K using different annealing conditions. The STM images reveal that the striped phase molecular structure experiences periodic dislocation fractures in the $[11\bar{2}]$ direction, which is presumed to be due to stress release on the molecular chain's on Au(111) surface. This phenomenon can be explained by the Frenkel-Kontorova model. The Frenkel-Kontorova model describes how a chain of atoms or molecules interacts with a periodic potential, such as a substrate surface, leading to dislocations and stress relief in the chain. In this context, the periodic dislocation fractures observed in the STM images align with the model's predictions, where the interaction between the molecular chain and the Au(111) surface induces stress that is periodically relieved through dislocations. There is also revealed a transfer from the $p(6.5 \times \sqrt{3})$ to the $p(11.5 \times \sqrt{3})$ striped phase during the STM scanning, which the tip-sample electric field may induce. In addition, a mesh-like molecular structure consisting of a short *6.5a* striped phase is observed. It is found that this transition from $p(6.5 \times \sqrt{3})$ to mesh-like structures was caused by a reduction in molecular coverage.

Similarly, the same approach has investigated the structural configurations of DT molecules on Au(111) surfaces[25–32]. Given that DT molecules possess a structure analogous to OT, but with alkyl chains extended by two additional carbon atoms, they exhibit comparable phase transitions as molecular coverage decreases. Notably, a close-packed structure alongside a $p(7.5 \times \sqrt{3})$ striped phase has been identified, illustrating the consistent behaviour across these thiol-based molecular systems on gold surfaces.

The striped phase of alkanethiol SAMs on Au(111) can serve as an effective molecular template for depositing C_{60} molecules, enabling controlled placement and periodic pattern formation at the nanoscale. This template enhances the interaction between the Au(111) surface

and C_{60} molecules, resulting in more stable and uniform deposition. Functionalisation of the striped phase allows for versatile surface engineering, which is crucial for the fabrication of nanodevices such as organic photovoltaics, transistors, and sensors. Additionally, this approach provides a model system to study vdW interactions and optimise the electronic and structural properties of C_{60} molecules, offering significant benefits for nanotechnology and materials science applications.

4.2 Experimental Procedure

To obtain a clean Au(111) surface, the Au(111) surface was treated by ion bombardment with 1 keV energy argon ions under 1×10^{-5} mbar, then annealing the sample at 500°C for 30 minutes. This ion bombardment and annealing treatment cycle can be repeated several times inside the STM chamber until a clean Au(111) surface is obtained. Self-assembled monolayers of alkanethiol molecules on Au(111) surfaces are prepared by liquid-phase methods. The treated Au(111) samples were immersed in an ethanol solution of OT or DT molecules at a concentration of 0.1 mol/L and a purity of ≥98.5% for 12 hours to prepare an OT/Au(111) or DT/Au(111) SAMs with densely packed phase structure in saturation coverage.

4.3 Results and Discussion

4.3.1 The $(3 \times 2\sqrt{3})$R30° Phase

For long-chain alkanethiol molecules, a $\left(3 \times 2\sqrt{3}\right)$ phase is observed at saturation coverage, the most common and simplest two-dimensional structure in OT SAMs[22,23]. The STM image in Figure 4.1 (a) shows freshly prepared OT/Au(111) SAMs' structure on the Au(111) surface. Multiple molecular domains can be observed, with molecular domain boundaries formed

between adjacent molecular domains, and within each molecular domain, the molecules are arranged in $(3 \times 2\sqrt{3})$.

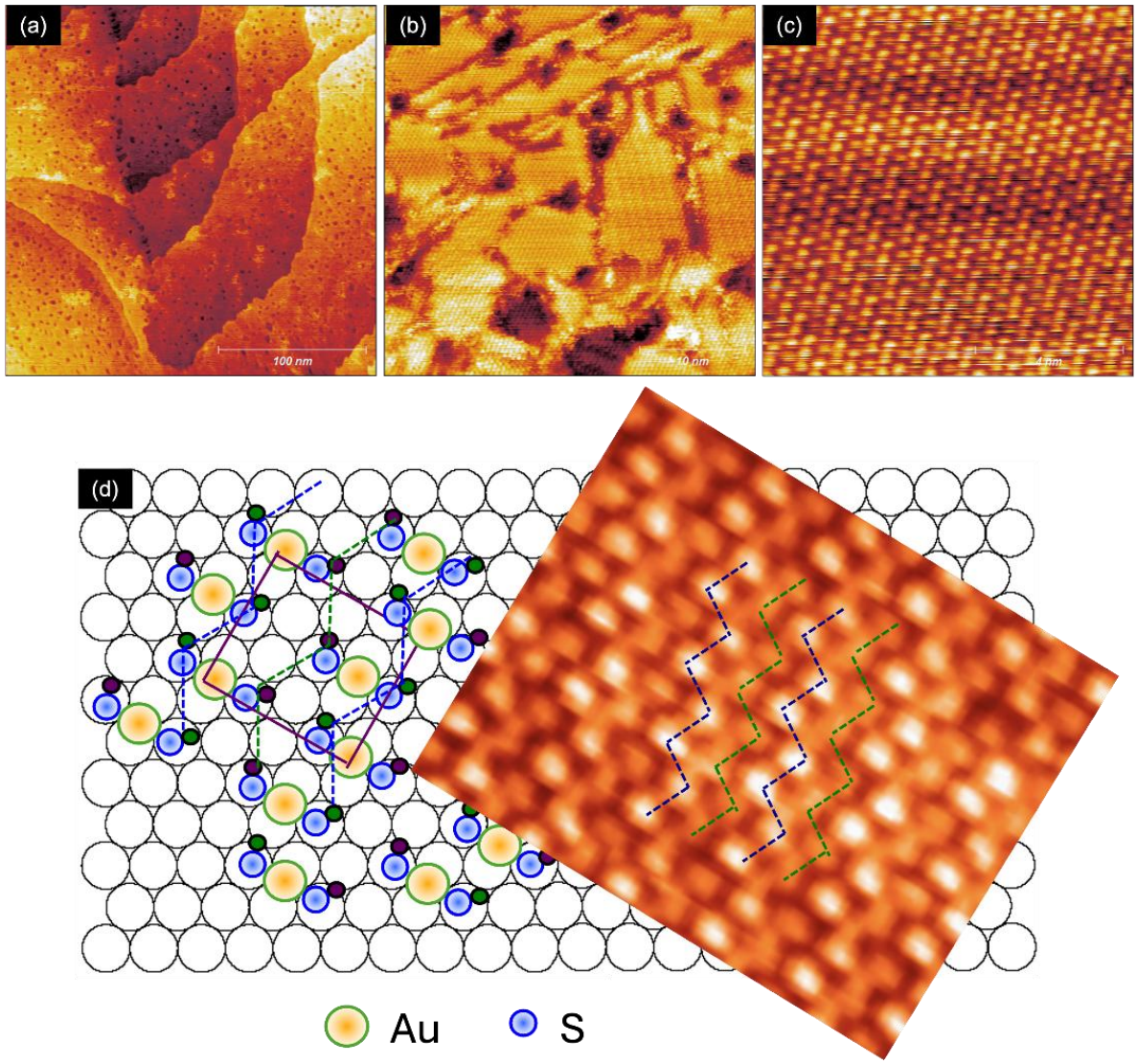

Figure 4.1 STM image of a freshly prepared monolayer on Au(111). The densely packed $(3 \times 2\sqrt{3})$ molecular domains separated by single atomic layer depth corrosion pits and molecular domain boundaries are shown. STM imaging parameters: (a) 300 pA, -1.5 V; 250 nm, RT. (b) 300 pA, -2.2 V; 35 nm, RT. (c) 300 pA, -2.0 V; 10 nm, RT. (d) Ball model for $(3 \times 2\sqrt{3})$ structure.

Figure 4.1 (d) gives a $(3 \times 2\sqrt{3})$ structure model relative to the (1×1) Au(111) substrate, where only the relative positions of the molecules are shown. Although the exact adsorption position of the molecule on the surface and the adsorption structure of the inner

interface are still in debate, a bright spot within a molecular domain in the STM image represents a molecule. Thus, In the $(3 \times 2\sqrt{3})$ structure, the S atom in the alkanethiol molecule is attached to the Au substrate and is fixed in a certain adsorption position, with the vdW forces between the molecular chains serving to stabilise the structure[20,33,34]. The unit cell of the OT molecules in the $(3 \times 2\sqrt{3})$ structure is confirmed.

In STM images of Figure 4 (d), the dashed zig-zag lines represent the positions of alkyl chains. These lines appear in different colours due to bright and dim variations, which means the different LDOS at the surface. This reflects the different orientations of the alkyl chain. Although the alkyl chains of the alkanethiol molecules are not directly visible in the STM image, only the CH_3 group can be visible. They extend upwards from the sulfur atoms, forming a densely packed, ordered layer above the gold surface that is tilted to balance vdW interactions between neighbouring chains. This arrangement creates a well-organized, crystalline-like structure on the gold substrate.

The STM image reveals some large etch pits and regular molecular arrangements within these pits. The depth of these pits is ~0.207 nm using the STM measurement, which is approximately equal to the height of an Au atomic monolayer on the Au(111) surface (~0.24 nm). The mechanism for forming these pits has been highly debated since the discovery of Au adatoms. Their formation is primarily believed to be due to the need to extract a certain amount of Au atoms from the (1×1) Au(111) substrate during self-assembly. This has been discussed in detail in the literature review. There is no consensus on how many Au atoms have been extracted. The "Au-adatom-monothiolate" model suggests that 0.33 ML Au-atoms are required in the $(3 \times 2\sqrt{3})$ structure, while the AAD model indicates that only 0.167 ML Au-atoms are necessary.

4.3.2 The p(6.5× √ 3) Striped Phase

Based on the closed-packed structure of the molecule, the OT/Au(111) SAMs were annealed to 393 K for three hours to partially desorb the OT molecules. The STM characterisation shows this treatment, resulting in the coexistence of the δ-striped phase and the close-packed phase in Figure 4.2 (a). The STM image of the disconnected δ-striped phase is in Figure 4.2 (b). The following data analysis will focus on the disconnected δ-striped phase structure[28].

The two structural phases (Φ, δ) in Figure 4.2 (a) are set according to the nomenclature of Poirier[28,35] for the different structural phases in the DT monolayer on the Au(111) surface.

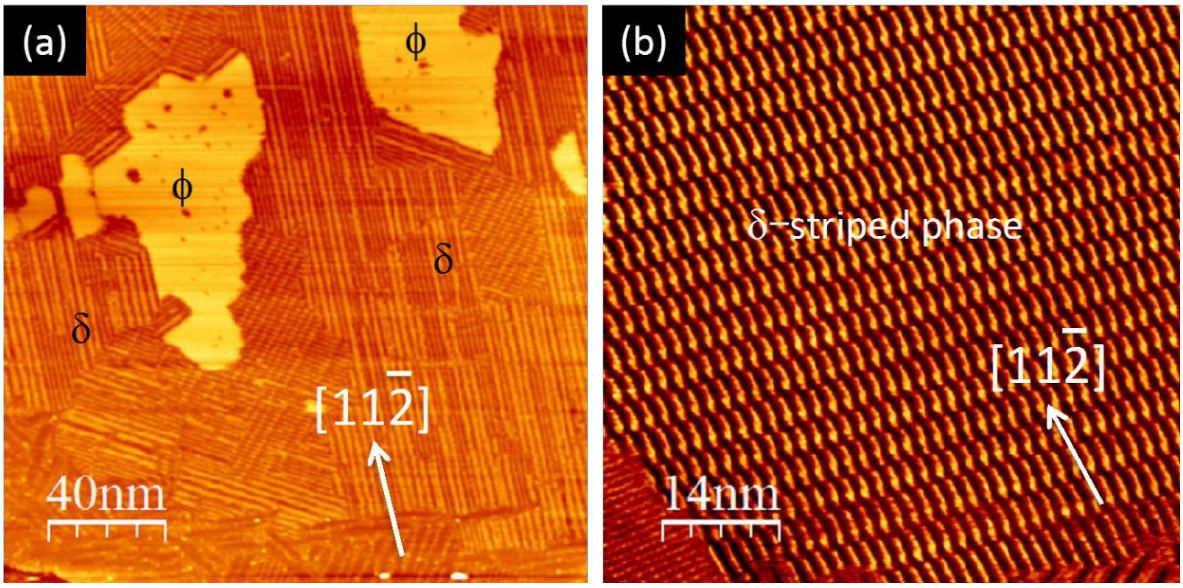

Figure 4.2 STM images of the OT/Au(111) on Au(111). (a) STM image of coexistence of the δ-striped phase and the Φ-phase. (b) STM image of δ-striped phase. STM imaging parameters: (a) 300 pA, 1.2 V; 200 nm, RT. (b) 300 pA, 1.2 V; 70 nm, RT. Figures and caption are reproduced from Supplementary Information of Ref [1].

As shown in Figure 4.2 (a), the annealed sample has a small proportion of close-packed OT molecules on the surface, with the majority being striped phases. Figure 4.2 (b) shows an STM image of a large area of disconnected strips on the sample's surface, which shows that the strips are disconnected at almost the same length along the [11$\bar{2}$] direction. The length of each short segment is between 4 and 6 nm. This regular dislocation may be due to stress release on

the surface as the sample cools to room temperature. In this chapter, we have only suggested one possible reason for forming this striped phase structure, but the deeper formation mechanism needs further investigation.

Figure 4.3 (a) shows a high-resolution STM image of a disconnected δ-stripe phase, where the STM characterisation revealed they were arranged in pairs along the $[11\bar{2}]$ direction[23,36,37]. Two paired OT chains are not equivalent positions, one higher than the other. By varying the scanning parameters and tip condition appropriately, we obtained STM images of the same region, as shown in the inset image of Figure 4.3 (a). As shown in the inset image, there is another molecular chain between the two pairs of OT molecules, which means the disconnected δ-stripe phase of the OT molecule consists of three chains.

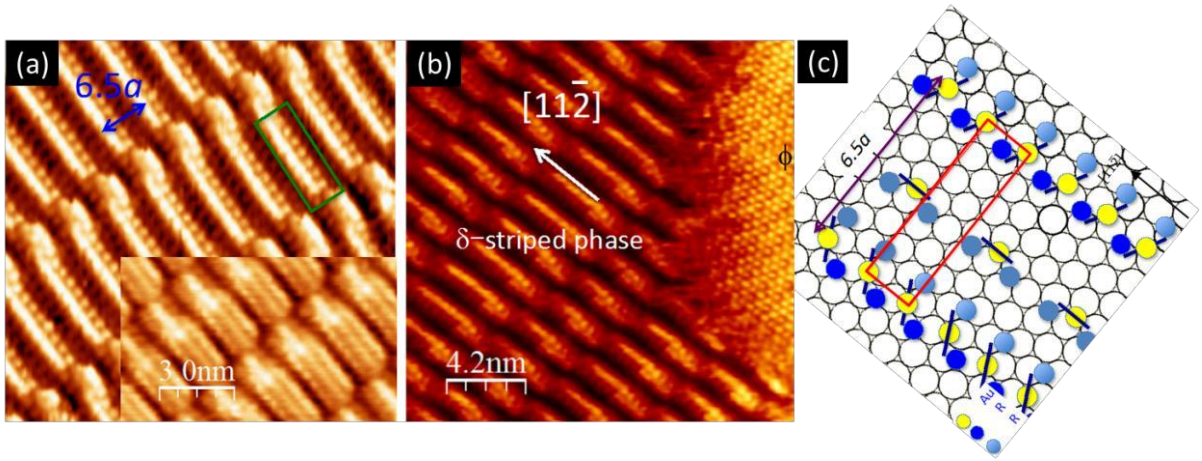

Figure 4.3 (a) High-resolution of the short segment δ-striped phase, which has a repeating distance of 6.5a. Inset shows the appearance of an "extra row". (b) The δ-phase is used as an accurate calibration standard to determine the repeating distance in the short segment δ-striped phase. (c) Structural model for the short segment δ-striped phase. STM imaging parameters: (a) 300 pA, -1.0 V; 15 nm, RT. (b) 300 pA, 1.5 V; 21 nm, RT. Figures and caption are reproduced from Supplementary Information of Ref [1].

Figure 4.3 (b) shows a high-resolution STM image of the coexistence of the disconnected δ-stripe phase and the close-packed phase, where the distance between molecules in the closed-pack phase is approximately 0.50±0.02 nm. This length can be used as a reference to minimise the thermal drift of surface molecules during scanning and calibrate the

measurement of the piezoelectric ceramic STM scanning tube[24,37–39]. So, the δ-phase with a period of *6.5a* is confirmed. A schematic diagram of the disconnected δ-striped phase with a period of *6.5a*, as shown in Figure. 4.3 (c) can be proposed using the AAD model.

The AAD model has been confirmed for OT/Au(111) SAMs on Au(111) surfaces[22,23]. Additionally, the apparent heights of the two alkyl chains in each structural unit (RS-Au-SR) are different, represented by dark blue and light blue circles, respectively. However, the actual heights of the alkyl rows paired between the two chains in the striped phase are the same and relatively lower heights, represented by light blue circles. In this diagram, the Au adatoms occupy the bridge sites, and the two S atoms occupy the top site, forming the δ strip phase structure along the $[11\bar{2}]$ direction[28–30,35].

Evidence for dislocations in STM images of OT SAMs on Au(111) includes irregularities such as mismatched AAD rows that disrupt the periodic pattern, indicative of stress or defects in the molecular layer. These dislocations manifest as observable disruptions or shifts in the regular zig-zag arrangement of AAD units and variations in image contrast due to changes in electronic density. The "extra row" refers to an additional row of molecules misaligned with the regular grid, which is not visible under STM. The proposed molecular model aligns well with the observed STM image.

4.3.3 The p(11.5×√3) Striped Phase

The $p\left(6.5 \times \sqrt{3}\right)$ striped structure of OT molecules is relatively stable at room temperature on Au(111) and under specific scanning parameters (low tunnelling currents). This structure is not affected by the tip of the STM. However, when the molecular surface is scanned with higher tunnelling currents, the $p\left(6.5 \times \sqrt{3}\right)$ structure is susceptible to the influence of the tip and thus induces a phase change. A transition structure of the $p\left(6.5 \times \sqrt{3}\right)$ to $p\left(11.5 \times \sqrt{3}\right)$ was found by increasing the tunnelling current during the STM scan. That means the $p\left(6.5 \times \sqrt{3}\right)$ striped

phase structure can be transferred due to the STM tip perturbation, and its molecular coverage (0.23 ML) does not change, which facilitates the proposal of models with different molecular structures at the same molecular coverage.

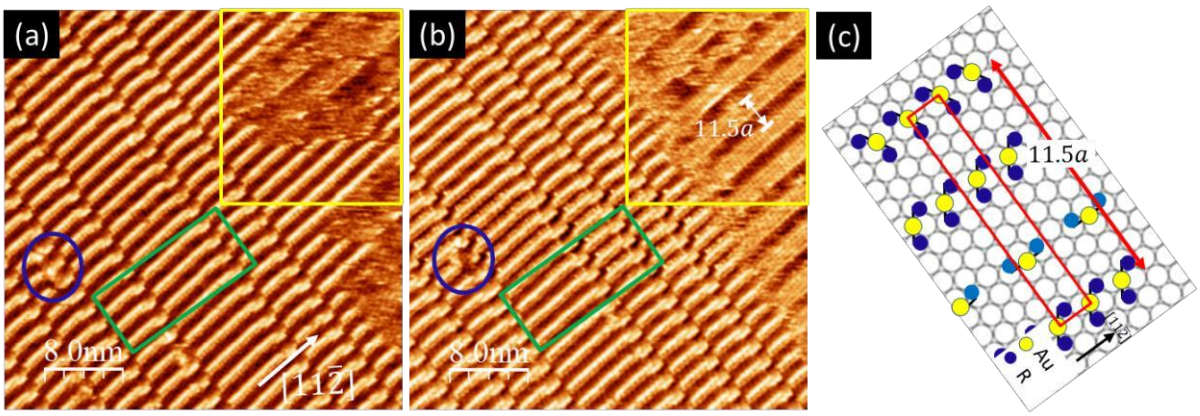

Figure 4.4 (a) STM image of $p(6.5 \times \sqrt{3})$ striped phase. (b) STM image of coexistence of the $p(6.5 \times \sqrt{3})$ striped phase and $p(11.5 \times \sqrt{3})$ striped phase. (c) schematic diagram of $p(6.5 \times \sqrt{3})$. STM imaging parameters: (a) 100 pA, 1.5 V; 40 nm, RT. (b) 500 pA, 1.5 V; 40 nm, RT.

Figure 4.4 (a) and (b) show the STM image of the change in the self-assembled structure of the OT molecule induced by the tip. Figure 4.4 (a) shows the image under 100 pA tunnelling current. The phase transition process can be determined using the blue highlight region as a reference point. Comparing the locations of the green rectangles in Figure 4.4 (a) and (b), the location of the break in the striped phase of the OT molecule has changed, but it still appears as an $p(6.5 \times \sqrt{3})$ striped phase structure. This may be because the tip perturbed some structural units (RS-Au-SR) in the molecular chain of the striped phase on the sample's surface when the scan was carried out with a high tunnelling current (500 pA)[22,23,36]. The molecules are not closely aligned under the low coverage (0.23 ML), so they may move back and forth within a reasonable range[15,38,39].

Moreover, changing the scanning parameters may cause the dislocation of one or several structural units in the striped phase. The domain marked by the yellow rectangle shows

the phase transition from the $p(6.5 \times \sqrt{3})$ to the $p(11.5 \times \sqrt{3})$ striped phase structure. Figure 4.4 (b) shows that the brighter part of the $p(11.5 \times \sqrt{3})$ striped phase consists of four molecular chains at the same height. This further justifies the proposed model of the $p(6.5 \times \sqrt{3})$ striped structure presented in Figure 4.3 (c). The darker part of the $p(11.5 \times \sqrt{3})$ striped structure is also filled with OT molecules, and the model of this phase is in Figure 4.4 (c). It was obtained based on the known molecular coverage (0.23 ML), where the dark blue and light blue circles indicate the different high and low-height molecular chains in the striped phase.

4.3.4 The Mesh-Like Phase

The STM image in Figure 4.5 (a) contains three molecular assembly structures of the OT molecule $p(11.5 \times \sqrt{3})$ in striped phase δ, melt phase ε and mesh-like phase δ' consisting of a short chain-like structure. The STM high-resolution image combined with the accurate molecular coverage estimation can help us model the different assembly structures of the molecules on the Au(111) surface[40]. In general, low-coverage molecules can form melt phase structures on the Au(111) surface. It can be considered similar to a 2D gas. In this phase, the molecules on the surface exhibit a high degree of mobility and disorder. This contrasts with more ordered phases, where the molecules are fixed in specific patterns or arrangements. The presence of a large area of liquid phase ε structure around the mesh-like molecule structure δ' can also indicate that its molecular coverage should be slightly lower than that of the $p(6.5 \times \sqrt{3})$ striped phase (0.23 ML).

Figure 4.5 (b) shows a high-resolution STM image of an OT molecule composed of short-chain mesh-like structures. Every 3-5 molecules assemble to form a structure where two parallel short-chain molecular structures are regularly interlaced. These chains are misaligned

by about one molecule, creating a mesh-like pattern. The distance between the two short chains along the $[1\bar{1}0]$ direction is approximately 2.34±0.02 nm, which corresponds to the distance (*8a*) of eight Au atoms in the $[1\bar{1}0]$direction. Using the $[11\bar{2}]$ direction as the densely packed OT molecules, we obtained the mesh-like structure shown in Figure 4.5 (c), where the dark blue and light blue circles indicate the different heights of OT molecules. The number of Au atoms and OT molecules in the diagram gives a molecular coverage of about 0.19 ML, consistent with our previous assumptions.

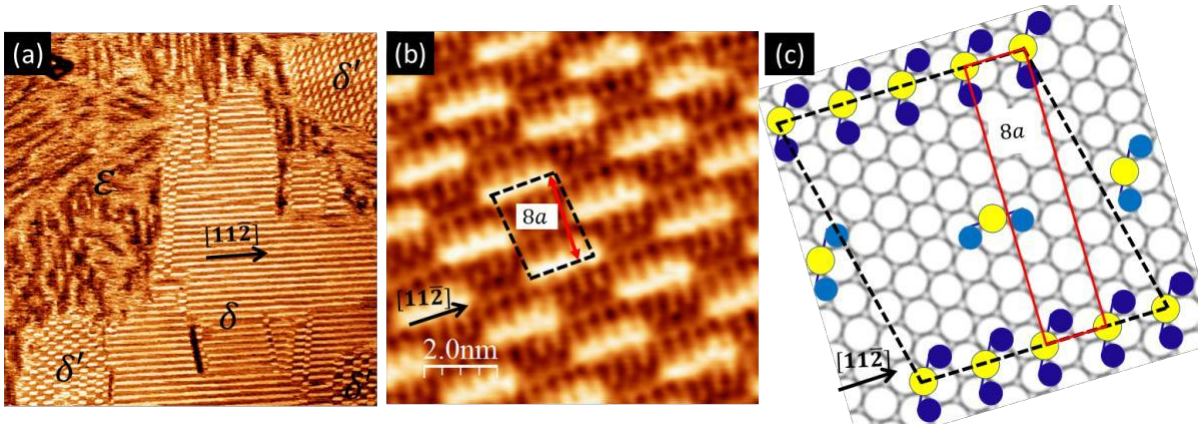

Figure 4.5 (a) STM image of the coexistence of the $p(6.5 \times \sqrt{3})$ striped phase, melt phase, and mesh-like structure, consisting of short segment staple rows. (b) High-resolution STM image of the mesh-like structure. (c) Proposed real space model of mesh-like short segment staple rows. STM imaging parameters: (a) 500 pA, 1.5 V; 40 nm, RT. (b) 300 pA, -1.0 V; 10 nm, RT.

In Figure 4.5 (c), the mesh-like molecular assembly model shows that the OT molecules are still arranged in a standing pattern on the Au(111) surface with the AAD unit (RS-Au-SR). However, the alkyl chains may be tilted at an angle as the coverage decreases, which does not affect the structural modelling of the molecular assembly pattern. In addition to the standing arrangement of OT molecules on Au(111), we have also attempted to have them adsorbed in a flat-lying position on the Au(111) surface. The molecular coverage of the OT molecules lying flat was about 0.12 ML, which is significantly lower than the reasonable range of molecular coverage with the annealing parameters in this experiment.

4.3.5 The Structural Phases of Decanethiol on Au(111)

We adopted the same preparation method to create the DT/Au(111) sample, which was then annealed at 390 K for 90 minutes. This annealing process leads to the partial desorption of the molecules[27,28,30]. The resulting structure of the DT monolayer post-annealing is depicted in Figure 4.6 (a), where most of the surface exhibits the δ-striped phase, with remnants of the densely packed phase still visible. The striped phase displays variability, particularly in the longer length of the β-phase. The close-packed directions on a Au(111) surface are along the $[1\bar{1}0]$ directions, which have the highest atomic density and lowest step energy, making them stable and common orientations for step edges. However, after adsorption of alkanethiol molecules to the step edges, the steps shift to the $[11\bar{2}]$ direction, resulting in significant movement. This is evident because the $[11\bar{2}]$ direction is parallel to the rows of AAD units, a well-known characteristic of alkanethiol/Au(111) SAMs. In some areas of the step edges, the alignment remains along the close-packed $[1\bar{1}0]$ direction of Au(111), as not all of the original structure is eliminated.

Figure 4.6 (c) shows a regular pattern of long striped rows commonly observed. Under most scanning conditions, the β-phase appears to consist of one row aligned along the $[11\bar{2}]$ direction. A high-resolution STM image of these short segment δ-striped phases is presented in Figure 4.6 (d), revealing a stripe periodicity of 7.5a. This periodicity is determined with high precision using the densely-packed phase $\left(3 \times 2\sqrt{3}\right)$ (Figure 4.6 (b)) as a calibration benchmark[22,24], eliminating uncertainties related to scanner non-linearity and thermal effects. It is seen to consist of paired rows along the $[11\bar{2}]$ direction. Within each pair, the two rows are not equivalent; one row appears taller than the other. There is also evidence suggesting that thiolates occupy the space between pairs[23].

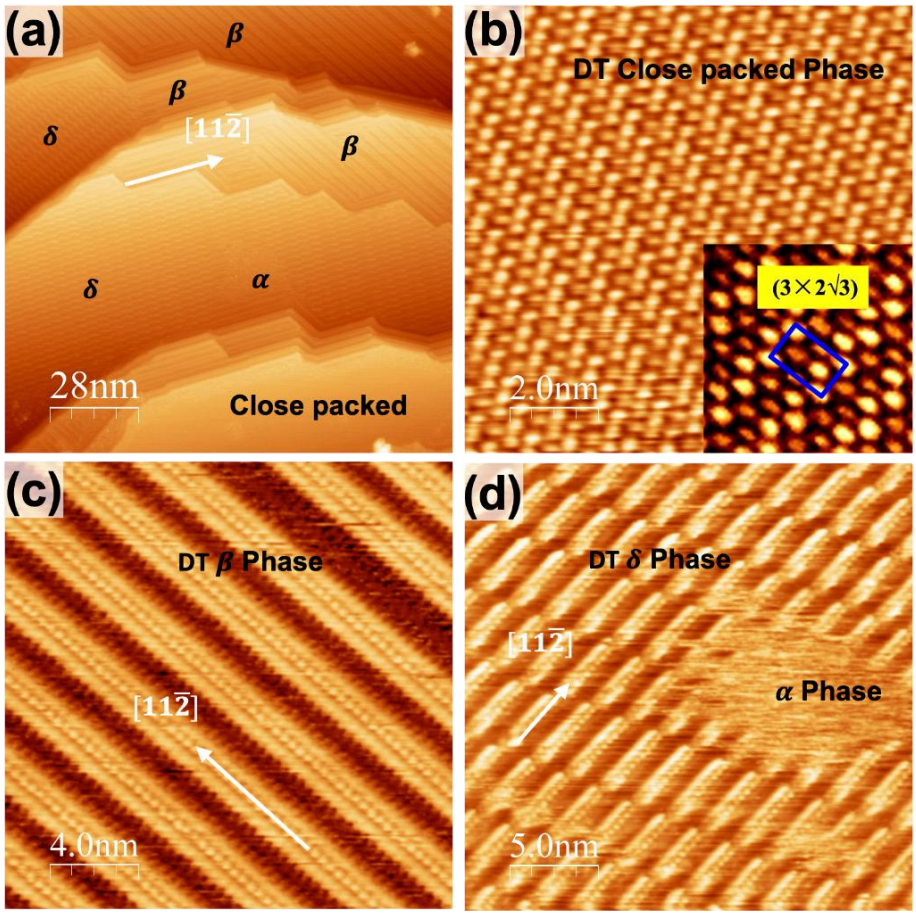

Figure 4.6 (a) STM images of DT/Au(111) Self-assembled Monolayer(SAMs) after annealing at 393 K for 120 min in the ultra-high vacuum chamber. (a) Coexistence of several phases of DT/Au(111) SAMs (140 nm × 140 nm; Vb = 1.8 V; It = 0.3 nA). (b) Close packed phase (10 nm × 10 nm; Vb = -2.0 V; It = 0.3 nA). The inset is $(3 \times 2\sqrt{3})$ unit cell. (c) Striped phase in relatively high coverage (20 nm × 20 nm; Vb = -0.5 V; It = 0.3 nA). (d) Striped phase low coverage. The δ phase will be further used to deposit C_{60}. The distance between each DT is 0.5 nm. Figures and caption are reproduced from Supplementary Information of Ref [2].

As depicted in Figure 4.6 (d), the DT/Au(111) SAMs acts as a molecular template. The interaction of DT with the Au(111) surface leads to the forming of a gold-adatom-dithiolate structure[18,20,33,41], referred to as the AAD unit. These RS–Au–SR motifs are arranged into long-range, ordered crystalline domains at full coverage, maintaining a nearest neighbour distance of 0.50±0.02 nm. At high coverages, the alkyl chains exhibit a tilt of approximately 30° from the surface, while at lower coverages, they tend to lay almost flat on the surface[17,23,41,42].

4.4 Summary

Compared to the $(3 \times 2\sqrt{3})$ densely packed alkanethiol molecules at saturated coverage, the striped phase structure is more interesting and has potential applications[17,43–45]. This chapter focuses on three structures of OT molecules at low coverage: the $p(6.5 \times \sqrt{3})$, the $p(11.5 \times \sqrt{3})$ striped phases, and the mesh-like phase formed by the regular arrangement of short strip rows. The $p(7.5 \times \sqrt{3})$ striped phase for DT molecules is reproduced. These periodic molecular strip structures have not been discussed in previous studies. They can be used as a functionalised molecular template to control the formation of C_{60} molecular and atomic structures deposited on their surfaces[1,2,46,47].

However, this study has some unresolved problems: firstly, the plausibility of stress release in explaining the regular dislocation of the striped phase; secondly, the validity of the mesh-like structure modelled in terms of molecular standing on the surface. They will be further investigated in future experiments. All the discussions in this thesis are based on the AAD unit, and all the proposed real space models of alkanethiol/Au(111) SAMs regarding this AAD unit have been confirmed and supported by relevant experimental data and theoretical analysis.

References

1. Zhang, X. *et al.* Orientation-Selective Growth of Single-Atomic-Layer Gold Nanosheets via van der Waals Interlocking and Octanethiolate-Confined Molecular Channels. *J. Phys. Chem. C* 123, 25228–25235 (2019).

2. Ding, H. *et al.* Orientational Growth of Flexible van der Waals Supramolecular Networks. *Small Struct.* 5, (2024).

3. Love, J. C., Estroff, L. A., Kriebel, J. K., Nuzzo, R. G. & Whitesides, G. M. Self-Assembled Monolayers of Thiolates on Metals as a Form of Nanotechnology. *Chem Rev* 105, 1103–1170 (2005).

4. Vericat, C. *et al.* Surface characterization of sulfur and alkanethiol self-assembled monolayers on Au(111). *J Phys Condens Matter* 18, R867 (2006).

5. CAMILLONE, N. I. *et al.* ChemInform Abstract: New Monolayer Phases of n-Alkane Thiols Self-Assembled on Au(111): Preparation, Surface Characterization, and Imaging. *ChemInform* 26, no-no (1995).

6. Schreiber, F. Self-assembled monolayers: from 'simple' model systems to biofunctionalized interfaces. *J. Phys.: Condens. Matter* 16, R881 (2004).

7. Picraux, L. B., Zangmeister, C. D. & Batteas, J. D. Preparation and Structure of a Low-Density, Flat-Lying Decanethiol Monolayer from the Densely Packed, Upright Monolayer on Gold. *Langmuir* 22, 174–180 (2006).

8. Guo, Q., Sun, X. & Palmer, R. E. Structural dynamics induced by self-assembled monolayers on Au(111). *Phys Rev B* 71, 035406 (2005).

9. Chaudhuri, A., Lerotholi, T. J., Jackson, D. C., Woodruff, D. P. & Jones, R. G. $(2\sqrt{3}\times3)$rect. phase of alkylthiolate self-assembled monolayers on Au(111): A symmetry-constrained structural solution. *Phys. Rev. B* 79, 195439 (2009).

10. Poirier, G. E. & Pylant, E. D. The Self-Assembly Mechanism of Alkanethiols on Au(111). *Science* 272, 1145–1148 (1996).

11. Vericat, C., Vela, M. E. & Salvarezza, R. C. Self-assembled monolayers of alkanethiols on Au(111): surface structures, defects and dynamics. *Phys Chem Chem Phys* 7, 3258–3268 (2005).

12. Clair, S., Kim, Y. & Kawai, M. Coverage-Dependent Formation of Chiral Ethylthiolate-Au Complexes on Au(111). *Langmuir* 27, 627–629 (2011).

13. Saito, S. & Oshiyama, A. Cohesive mechanism and energy bands of solid C_{60}. *Phys. Rev. Lett.* 66, 2637–2640 (1991).

14. Shaheen, A. *et al.* Characterization of Self-Assembled Monolayers on a Ruthenium Surface. *Langmuir* 33, 6419–6426 (2017).

15. Gao, J., Li, F. & Guo, Q. Balance of Forces in Self-Assembled Monolayers. *J Phys Chem C* 117, 24985–24990 (2013).

16. Smith, R. K., Lewis, P. A. & Weiss, P. S. Patterning self-assembled monolayers. *Prog Surf Sci* 75, 1–68 (2004).

17. Kind, M. & Wöll, C. Organic surfaces exposed by self-assembled organothiol monolayers: Preparation, characterization, and application. *Prog Surf Sci* 84, 230–278 (2009).

18. Maksymovych, P., Voznyy, O., Dougherty, D. B., Sorescu, D. C. & Yates, J. T. Gold adatom as a key structural component in self-assembled monolayers of organosulfur molecules on Au(111). *Prog. Surf. Sci.* 85, 206–240 (2010).

19. Ulman, A. Formation and Structure of Self-Assembled Monolayers. *Chem Rev* 96, 1533–1554 (1996).

20. Maksymovych, P. & Yates, J. T. Au Adatoms in Self-Assembly of Benzenethiol on the Au(111) Surface. *J Am Chem Soc* 130, 7518–7519 (2008).

21. Li, F., Zhou, W., Tang, L. & Guo, Q. Surface melting and recrystallization of a self-assembled octanethiol monolayer on Au(111)a). *J Vac Sci Technology Vac Surfaces Films* 29, 021011 (2011).

22. Li, F., Tang, L., Zhou, W. & Guo, Q. Resolving the Au-Adatom-Alkanethiolate Bonding Site on Au(111) with Domain Boundary Imaging Using High-Resolution Scanning Tunneling Microscopy. *J. Am. Chem. Soc.* 132, 13059–13063 (2010).

23. Guo, Q. & Li, F. Self-assembled alkanethiol monolayers on gold surfaces: resolving the complex structure at the interface by STM. *Phys. Chem. Chem. Phys.* 16, 19074–19090 (2014).

24. Li, F., Tang, L., Zhou, W. & Guo, Q. Relationship between the c(4×2) and the (√3×√3)R30° phases in alkanethiol self-assembled monolayers on Au(111). *Phys Chem Chem Phys* 13, 11958–11964 (2011).

25. Kano, S., Tada, T. & Majima, Y. Nanoparticle characterization based on STM and STS. *Chem Soc Rev* 44, 970–987 (2014).

26. Yamada, R., Wano, H. & Uosaki, K. Effect of Temperature on Structure of the Self-Assembled Monolayer of Decanethiol on Au(111) Surface. *Langmuir* 16, 5523–5525 (2000).

27. Gojzewski, H., Kappl, M. & Ptak, A. Effect of the Chain Length and Temperature on the Adhesive Properties of Alkanethiol Self-Assembled Monolayers. *Langmuir* 33, 11862–11868 (2017).

28. Fitts, W. P., White, J. M. & Poirier, G. E. Low-Coverage Decanethiolate Structure on Au(111): Substrate Effects. *Langmuir* 18, 1561–1566 (2002).

29. Qian, Y., Yang, G., Yu, J., Jung, T. A. & Liu, G. Structures of Annealed Decanethiol Self-Assembled Monolayers on Au(111): an Ultrahigh Vacuum Scanning Tunneling Microscopy Study. *Langmuir* 19, 6056–6065 (2003).

30. Poirier, G. E., Fitts, W. P. & White, J. M. Two-Dimensional Phase Diagram of Decanethiol on Au(111). *Langmuir* 17, 1176–1183 (2001).

31. Toerker, M. *et al.* Annealed decanethiol monolayers on Au(111) – intermediate phases between structures with high and low molecular surface density. *Surf Sci* 445, 100–108 (2000).

32. Kap, O. *et al.* Structural Stability of Physisorbed Air-Oxidized Decanethiols on Au(111). *J. Phys. Chem. C* 124, 11977–11984 (2020).

33. Maksymovych, P. & Yates, J. T. Au Adatoms in Self-Assembly of Benzenethiol on the Au(111) Surface. *J. Am. Chem. Soc.* 130, 7518–7519 (2008).

34. Maksymovych, P., Sorescu, D. C., Jordan, K. D. & Jr., J. T. Y. Collective Reactivity of Molecular Chains Self-Assembled on a Surface. *Science* 322, 1664–1667 (2008).

35. Poirier, G. E. Coverage-Dependent Phases and Phase Stability of Decanethiol on Au(111). *Langmuir* 15, 1167–1175 (1999).

36. Ding, H. *et al.* Perturbational Imaging of Molecules with the Scanning Tunneling Microscope. *J. Phys. Chem. C* 124, 25892–25897 (2020).

37. Gao, J. *et al.* Spontaneous Breaking and Remaking of the RS–Au–SR Staple in Self-assembled Ethylthiolate/Au(111) Interface. *J Phys Chem C* 122, 19473–19480 (2018).

38. Gao, J. *et al.* Probing Phase Evolutions of Au-Methyl-Propyl-Thiolate Self-Assembled Monolayers on Au(111) at the Molecular Level. *J. Phys. Chem. B* 122, 6666–6672 (2018).

39. Tang, L., Li, F., Zhou, W. & Guo, Q. The structure of methylthiolate and ethylthiolate monolayers on Au(111): Absence of the (√3×√3)R30° phase. *Surf Sci* 606, L31–L35 (2012).

40. Celestin, M., Krishnan, S., Bhansali, S., Stefanakos, E. & Goswami, D. Y. A review of self-assembled monolayers as potential terahertz frequency tunnel diodes. *Nano Res* 7, 589–625 (2014).

41. Maksymovych, P., Sorescu, D. C. & Yates, J. T. Gold-Adatom-Mediated Bonding in Self-Assembled Short-Chain Alkanethiolate Species on the Au(111) Surface. *Phys. Rev. Lett.* 97, 146103 (2006).

42. Yu, M. *et al.* True Nature of an Archetypal Self-Assembly System: Mobile Au-Thiolate Species on Au(111). *Phys. Rev. Lett.* 97, 166102 (2006).

43. Jin, R. Quantum sized, thiolate -protected gold nanoclusters. *Nanoscale* 2, 343–362 (2009).

44. Kumar, G. *et al.* Thermodynamics of Alkanethiol Self-Assembled Monolayer Assembly on Pd Surfaces. *Langmuir* 34, 6346–6357 (2018).

45. Mehring, P., Beimborn, A. & Westphal, C. The structural formation of methylthiolate SAMs on Au(111) for short deposition times from solution. *Appl. Surf. Sci.* 256, 7265–7269 (2010).

46. Zhang, X. *et al.* Two-Dimensional van der Waals Supramolecular Frameworks from Co-Hosted Molecular Assembly and C_{60} Dimerization. *J. Phys. Chem. C* 124, 12589–12595 (2020).

47. Zhang, X. *et al.* Complex supramolecular tessellations with on-surface self-synthesized C_{60} tiles through van der Waals interaction. *Nanoscale* 14, 1333–1339 (2022).

5. Two-dimensional C_{60}/Octanethiol van der Waals Supramolecular Framework

The results featured in this chapter extend from work previously published. This chapter includes text from publications, to which I have had the privilege of contributing in significant roles: as a co-author in the 2020 publication[1] and as the second author in the 2022 publication[2]. These foundational works include:

- Zhang, X.; Fan, X.; Zhu, G.; Wang, Y.; **Ding, H.**; Lin, H.; Li, Y.; Li, Q.; Gao, J.; Pan, M.; Guo, Q. Two-Dimensional van Der Waals Supramolecular Frameworks from Co-Hosted Molecular Assembly and C_{60} Dimerization. *J. Phys. Chem. C* 2020, 124 (23), 12589–12595. (Roles: Data curation, Formal analysis, Investigation, Methodology, Validation, Visualisation, Writing-original draft, and writing-review and editing.)
- Zhang, X.; **Ding, H.**; Chen, X.; Lin, H.; Li, Q.; Gao, J.; Pan, M.; Guo, Q. Complex Supramolecular Tessellations with On-Surface Self-Synthesized C_{60} Tiles through van Der Waals Interaction. *Nanoscale* 2022, 14 (4), 1333–1339. (Roles: Conceptualization, Data curation, Formal analysis, Investigation, Methodology, Resources, Software, Validation, Visualisation, Writing-original draft, and Writing-review and editing.)

5.1 Introduction

The successful isolation of graphene monolayers has led to rapid development in the study of two-dimensional materials[3–5]. The 2D materials can be broadly classified into two types. One is the 2D materials represented by graphene and transition metal dichalcogenide (TMDCs), characterised by strong planar covalent bonds between the constituent atoms. The other is the materials formed by stacking 2D molecular layers attracted by weak intermolecular

interactions, such as hydrogen bonds and vdW interactions[6–10]. Two-dimensional molecular materials can be formed on a solid substrate from simple structural molecules[6,11] or large molecules with complex structures[12]. Specifically, 2D molecular networks are a particular type of 2D molecular material, such as 2D metal-organic frameworks (MOFs), that have received great research attention[13]. The construction of molecular networks relies heavily on selecting molecules in specific coordination bonding and hydrogen bonding structures in metal-organic networks[10]. In the growth of these molecular networks, pairwise interactions between neighbouring molecules or atoms can be designed by selecting precursor molecules or atoms as the template[14]. In our case, the molecular networks are constructed entirely based on van der Waals interactions[15].

In this chapter, a weakly interacting binary molecular system consisting of C_{60} molecules and OT molecules was constructed on an Au(111) substrate[16,17]. Fermi-STM characterised the surface structure. Since neither the OT molecule nor the C_{60} molecule has specific functional groups, a system consisting of C_{60} molecules and OT molecules does not seem to be an apparent choice for creating a long-range ordered molecular network. Previous work on this system demonstrated phase-separated C_{60} and thiols on Au(111), suggesting that the thiols coverage is a significant parameter in the structural creation of these binary molecular networks. However, when a C_{60}/thiol ratio of 4:14 is applied, a regular porous structure with OT-filled nanopores can be produced. This ratio was determined through several trials, with experimental data indicating that the 4:14 ratio consistently produces a regular porous structure with OT-filled nanopores. The cooperative self-organisation with C60 molecules as cohosts emerged as the optimal condition from these experiments. Instead of constructing a porous framework from host molecules and then filling it with guest molecules, the porous framework in this system forms because of cooperative self-organisation with the C_{60} molecule and serves as cohost.

5.2 Experimental Procedure

The sample is created following the conventional procedure outlined in our earlier research[18,19], which involves depositing a single layer of OT molecules on an Au(111) substrate. After being blown dry with high-purity nitrogen, the immersed sample is moved to a UHV system equipped with an Omicron Fermi-STM. Electrochemically etched tungsten tips were used for imaging. After three hours of UHV heating to 120 °C for 3h, the sample organises into the striped δ phase[20] with a coverage of 0.23 ML. Therefore, thermal annealing at 120 °C has caused substantial desorption of OT molecules, with the surface coverage decreased from 0.33 ML to 0.23 ML[21]. Other thiols may also create comparable striped phases with varying conditions under the proper experimental treatment, such as an acceptable substrate temperature and thiol coverage in our previous studies[22]. Using the Createc evaporator source, C_{60} molecules are deposited onto the OT monolayer by sublimation at room temperature[23,24].

5.3 Results and Discussion

5.3.1 Formation of Porous C_{60}/Octanethiol Framework

Previous research on C_{60} deposition onto a saturated OT monolayer (0.33 ML) indicates that the OT monolayer with saturation coverage is not permitted for C_{60} incorporation[16]. Only a few C_{60} molecules were integrated into the OT monolayer through defect sites. C_{60} molecules easily mix with OT on Au(111) and form regular long-range ordered structures. These studies show that the formation and stability of the C_{60}/ OT framework are highly dependent on the precise coverage of C_{60}, as deviations can lead to incomplete or disordered structures and affect the framework's electronic properties. Controlling this coverage involves using a calibrated sublimation source to deposit C_{60} molecules at a controlled rate, maintaining specific substrate temperatures during deposition, starting with a well-defined initial OT coverage on the Au(111)

surface, and performing post-deposition annealing (50-60 °C) to achieve uniform distribution. These methods ensure the critical balance and cooperative interactions required for the desired phase and stability of the C_{60}/OT framework.

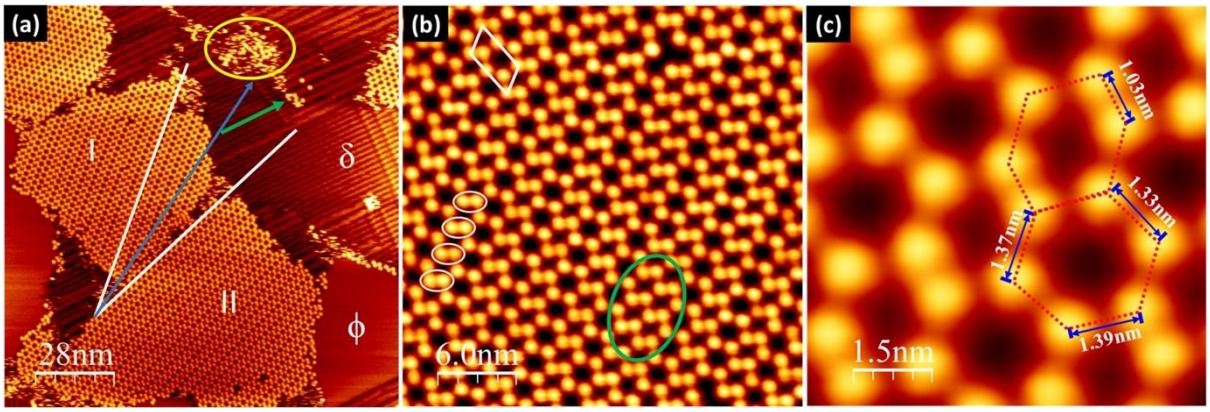

Figure 5.1 A porous framework nanostructure composed of C_{60} and OT. (a) It is observed that the porous framework coexists with both the striped δ phase and close-packed Φ phases of OT. The green arrow points towards the direction of $[11\bar{2}]$ and the direction of the δ phase's OT rows. Disordered C_{60} molecules that have not yet formed a regular structure can be highlighted with the yellow oval. (b) High-resolution STM image of C_{60} porous structure. Four white ovals emphasise the C_{60} pair rows. A unit cell composed of four C_{60} molecules is depicted. (c) The distances between C_{60} molecules that are adjacent, with the uncertainty of ±0.02 nm. STM imaging parameters: (a) 50 pA, -1.0 V; 150 nm, RT. (b) 50 pA, -1.3 V; 30 nm, RT. (b) 50 pA, -1.3 V; 10 nm, RT. Gaussian filter is applied to the original data. Figures are reproduced from Ref [1].

Figure 5.1 (a) shows that the Φ phase is defined as patches of densely packed OT with 0.33 ML coverage. The porous framework develops in places previously occupied by the striped δ phase. Since there are a lot of defects in the mismatch sites in the striped δ phase. The yellow ovals represent the C_{60} molecules that have not yet established the regular porous structure. The blue and green arrows in Figure 5.1 (a) indicate the $[0\bar{1}1]$ and $[11\bar{2}]$ directions in Au(111) surface. The δ phase's OT rows go parallel to the $[11\bar{2}]$ direction. The white lines indicate domains I and II's respective azimuthal orientations. The two domains are mirror-symmetric, with the mirror axis being the $[0\bar{1}1]$ crystal direction. Each domain is rotated 14 degrees from the $[0\bar{1}0]$ direction: +14 degrees clockwise for domain II and -14 degrees

counterclockwise for OT domain I. Figure 5.1 (b) shows a magnified STM image of the C_{60}/OT framework, which reveals that the framework is composed of C_{60} paired rows. White ovals denote four C_{60} pairs in a row. The C_{60} molecules are grouped differently in a small region within the green oval than the rest of the C_{60} molecules in the STM image.

Additionally, a unit cell composed of four C_{60} molecules is marked. Figure 5.1 (c) illustrates the critical spacing between C_{60} molecules inside the framework. These distances are crucial in constructing a framework's structural model in real space. The shortest distance between two C_{60} molecules is 1.03 ± 0.02 nm, the distance between the pairing C_{60} molecules. This distance is incredibly near to the shortest intermolecular distance seen in C_{60} crystals, which means the two C_{60} molecules are directly bonded together to form a pair.

5.3.2 Structural Model of Supramolecular Framework

The C_{60}/OT supramolecular structure is stable at room temperature under STM. This framework structure disintegrates when the sample is annealed to ~55 °C, creating close-packed C_{60} domains on the surface. We anticipate some degree of thermal desorption of OT molecules at this temperature. That will lead to a partial phase separation of C_{60} molecules from the framework.

In Figure 5.2 (a), the STM image depicts the coexistence of the C_{60}/OT framework and close-packed C_{60} domains. The close-packed C_{60} domain has a $\left(2\sqrt{3} \times 2\sqrt{3}\right) R30°$ lattice structure, which is well-characterised for C_{60} adsorbed on a pure Au(111) surface[25]. Moreover, C_{60} molecules are densely packed in the $\left(2\sqrt{3} \times 2\sqrt{3}\right) R30°$ phase along the $[11\bar{2}]$ directions. The C_{60} molecules included inside the framework are identical in the same height as the OT molecules contained within the densely packed domain. This demonstrates unequivocally that the C_{60} molecules in the framework absorbed directly on top of the Au(111) surface, not on top of the OT molecules. Using the close-packed C_{60} domain as the reference and the fact that C_{60}

sits atop the absorption site in the $\left(2\sqrt{3}\times 2\sqrt{3}\right)R30°$ phase, we can use the triangulation method to identify the adsorption locations for all C_{60} molecules in this framework[26]. In Figure 5.2 (b), C_{60} molecules occupy low symmetry positions within this binary molecular system. None of the molecules occupies an absorption site with a high degree of symmetry, such as atop, bridge, or the three-fold hollow. That may be due to the collective interaction between C_{60} and OT, which breaks the symmetry to place the molecules into the lowest energy sites.

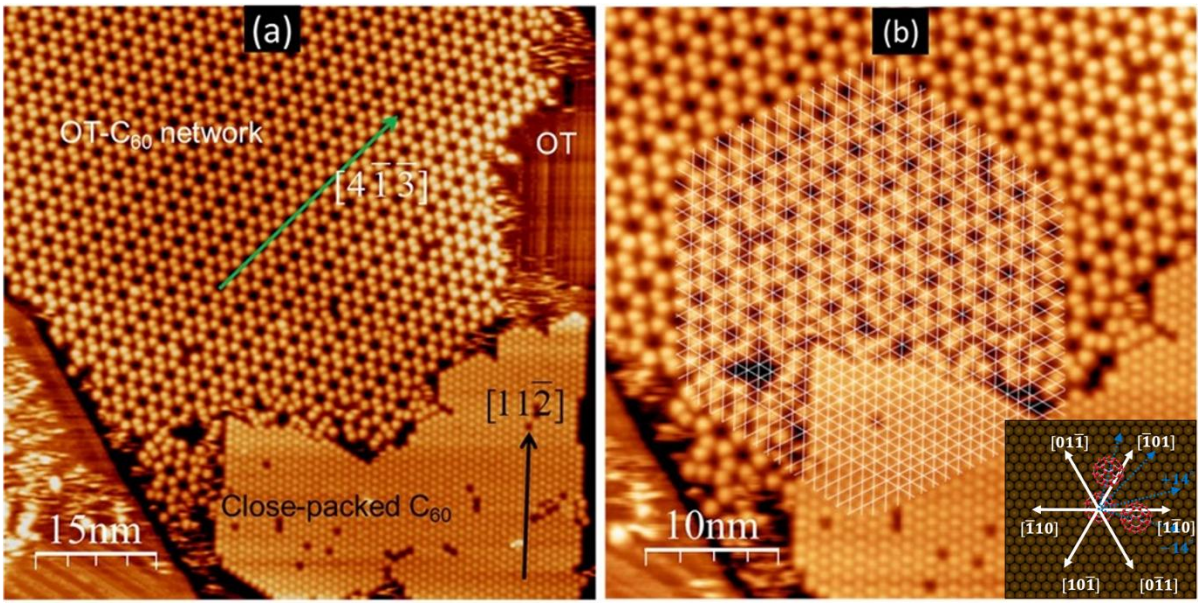

Figure 5.2 The C_{60} $\left(2\sqrt{3}\times 2\sqrt{3}\right)R30°$ densely packed phase coexists with the C_{60}/OT framework structure. (b) The absorbed positions of all C_{60} molecules in the porous framework are identified using the densely packed C_{60} as a calibration reference. The inset is a schematic diagram to show how C_{60} molecules are structurally related to Au(111) surface. STM imaging parameters: (a) 100 pA, -0.5 V; 70 nm, RT. (b) 100 pA, -0.5 V; 40 nm, RT. Gaussian filter is applied to the original data. Figures are reproduced from Ref [1].

Due to thermal drift and creep of the STM piezo scanner, the triangulation of the adsorption site is subject to a systematic error of ±0.01 nm. The random error, determined through multiple measurements, is ±0.02 nm. Therefore, the total uncertainty of the distance measurement is ±0.02 nm. Then, the proposed real space model can be fine-tuned throughout time to build an accurate structural representation of the framework.

Filling up the pores with a structural unit made of RS-Au-SR is the key. RS-Au-SR staple adsorbed on Au(111) has been extensively described[19,27]. The RS-Au-SR axis must be perpendicular to the bridge site when the pores are filled with OT[27]. Another requirement to be considered is keeping the alkane chains at an appropriate distance ($0.3 - 0.6$ nm) from the carbon atoms in the C_{60} cage to balance the van der Waals interaction. Many adjustments of lateral shifts for the framework unit on Au(111) are required to get the optimal fit positions. Thus, the most likely real space structure is derived without requiring comprehensive theoretical computations of the forcefield or the system's free energy.

The STM image reveals a high density of states inside the pore, indicating the presence of some thiol molecules within it (Figure 5.3 (c)). This occurs because the thiol molecules interact with the substrate and saturated molecules and contributing to the observed electronic density. A real space structural model in Figure 5.3 (a) has been optimised and agrees well with the STM image in Figure 5.3 (b) and (c). This model has two different pore sizes. Three RS-Au-SR structural units are found in each of the hexagonal pores, whereas four RS-Au-SR structural units are found in each of the linear pores. The local surface coverage of OT is ~0.33 ML, the maximum coverage for OT on Au(111) in each pore. As a result, the alkane chains in the pores are almost vertically aligned and perpendicular to the Au(111) surface, as seen in Figure 5.3 (a). Based on Figure 5.3 (a), the C_{60} molecular coverage in the framework has a C_{60}/OT ratio of 4:14, and the C_{60}/OT molecular coverage is ~0.04 ML. So the framework's composition is $(C_{60})_4$ $(OT)_{14}$. The initial coverage of OT in the δ phase is 0.23 ML, which should be considered. Following the C_{60}/OT formation, there has been a significant decrease in total OT molecular coverage. Partial desorption of OT probably occurred during the C_{60} deposition process. The diffusion of OT in the framework's vicinity has not been observed under STM.

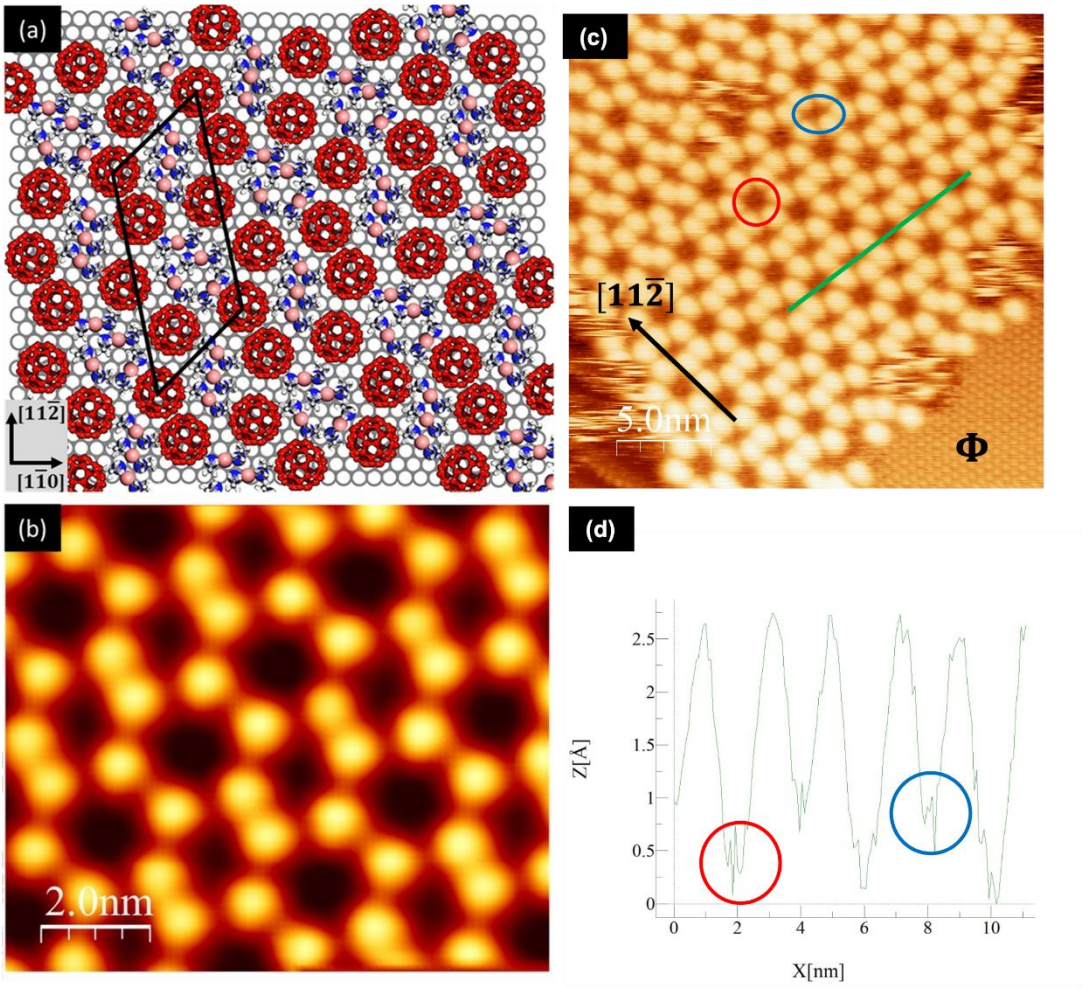

Figure 5.3 (a) Proposed ball model of the C_{60}/OT porous framework. Each yellow bar represents the S-Au-S axis of the RS-Au-SR staple. The alkyl chain is omitted for clarity. (b) High-resolution STM image from the C_{60}/OT framework for direct comparison with the structural model in real space. Gaussian filter is applied to the original data. (c) Original raw data. The $[11\bar{2}]$ direction can be seen by referencing the OT striped phase. The OT closed packed Φ phase ($(\sqrt{3} \times \sqrt{3})R30°$) can be used as the distance calibration reference. (d) Line profile of green line in (c). This shows there are two different pores in (c), and they are highlighted by red and blue ovals. The STM imaging parameters: (b) 50 pA, -1.3 V; 10 nm, RT. (c) 50 pA, -1.3 V; 25 nm, RT. Figures are reproduced from Ref [1].

The adsorption site of C_{60} can be finely tuned by applying several constraints. When measuring distances in an STM image, it is advisable to measure from the centre to the centre of the molecules rather than from edge to edge, as the edges are not well-defined. For instance, in a C_{60} molecule, the carbon-carbon covalent bond distance is approximately 0.15 nm. Since

there is no covalent bond between the thiol and C_{60} carbons, the distance should be greater than 0.15 nm. If the model shows the carbon from the thiol is 0.15 nm away from the carbon in C_{60}, then they are too close. Ideally, this distance should be around 0.20 nm or more, although the exact distance is not precisely known. This ensures that the atoms are not unrealistically close for non-bonded interactions. Introducing these thiol molecules raises the question of whether there is still room to add another AAD unit. If another unit is added, the carbon-carbon distance may become too short, which is a key factor in quantifying how many molecules fit into this region. If fewer molecules are fitted inside the pore, molecules in the middle may be too far from the surrounding C_{60} molecules, resulting in weak van der Waals interactions between the thiol and the surrounding C_{60} molecules. These parameters facilitate precise control over the positioning of C_{60} molecules, enhancing the reliability of the structural model. All possible alternatives to this model are still compatible with these assumptions.

Since the C_{60} molecules squeeze into the striped phase of OT, they cause the OT molecules to be displaced around them on the Au(111) surface. The densely packed structure of C_{60} is prevented from forming by the involvement of OT molecules. The cooperative interactions between the C_{60} and OT create the porous framework. The interaction between C_{60} molecules and OT in the C_{60}/OT framework is "cooperative" because it involves mutual stabilisation and collective vdW interactions among many molecules. OT molecules create a template that guides C_{60} organisation, resulting in a regular, ordered structure through combined vdW forces and spatial arrangement. This collective interaction leads to a more stable and ordered framework than either component could achieve alone.

The height profile in Figure 5.3 (d) indicates that the two types of pores have different measured heights. This discrepancy could be due to an actual difference in pore depth or the smaller pore appearing shallower as a result of tip convolution. There are some AAD units inside the pores. The varying depths of the pores suggest that the alkyl chains of the AAD units

may adjust their orientation, either standing perpendicular or lying flatter to optimise vdW interactions. This implies that the number of AAD units inside the pores may vary, as our proposed structural model assumes the alkyl chains are almost perpendicular to the surface. If the alkyl chains lie flat, the pores may contain fewer AAD units, resulting in a larger depth.

The other possibility may be caused by the STM tip. Tip convolution is an artifact that arises due to the finite size and shape of the STM tip used during imaging. The tip convolution can influence the appearance of features by making them seem larger or more rounded. The actual visibility inside the pore typically results from the spatial arrangement of the molecular framework, the size and structure of the pores, the electronic states of the framework, and the orientation of the C_{60} molecules. The difference in measured heights of the two kinds of pores might be due to this convolution effect, where the smaller pore appears shallower not because it is actually shallower, but because the STM tip cannot fully resolve its depth.

For example, we previously discovered a phase separation of C_{60} and propylthiolate on Au(111) in research using propanethiol SAMs, and there was no indication of C_{60}/propanethiol framework formation[17]. As a result, vdW interactions between the alkane chain and the C_{60} molecule are critical to the C_{60}/OT supramolecular structure. The S-Au bonding is insufficient to maintain stability and support the porous structure.

Consequently, the vdW interactions between the alkane chain and the C_{60} molecules should have the most impact on the forms of growing frameworks, leading to the development of irregularly shaped frameworks. The C_{60}/OT architecture has a unique feature in that it does not depend only on the interactions between neighbours. The sum of the interactions of many molecules on the surface determines the structure's long-range stability. A stark difference is a hydrogen-bonded framework or MOF, in which the bonding of closest neighbour molecules dictates the final molecular structure of the framework.

In previous studies, many compounds, including porphyrins[28], a-sexithiophene[29], and pentacene[30,31], may form 2D cocrystals with C_{60}. Researchers believe that the curved π C_{60} and porphyrin of the planar π surface play an important function[32]. Porous networks mediated by a 2D molecular gas are produced when C_{60} and pentacene are deposited on an Ag(111) substrate[31]. This illustrates how the two molecules generate the porous network on the surface cooperating interaction. There is a stable striped δ phase that is not a lattice gas for OT on the Au(111) surface. However, experimental data shows that the OT molecules as an integral molecular unit on Au(111) surface have some freedom of diffusion at RT. In response to the insertion of C_{60} molecules, the OT molecules may change their locations due to their restricted mobility. This may lead to a compression of the OT monolayer into a high-coverage phase that occurs within the pores on the surface.

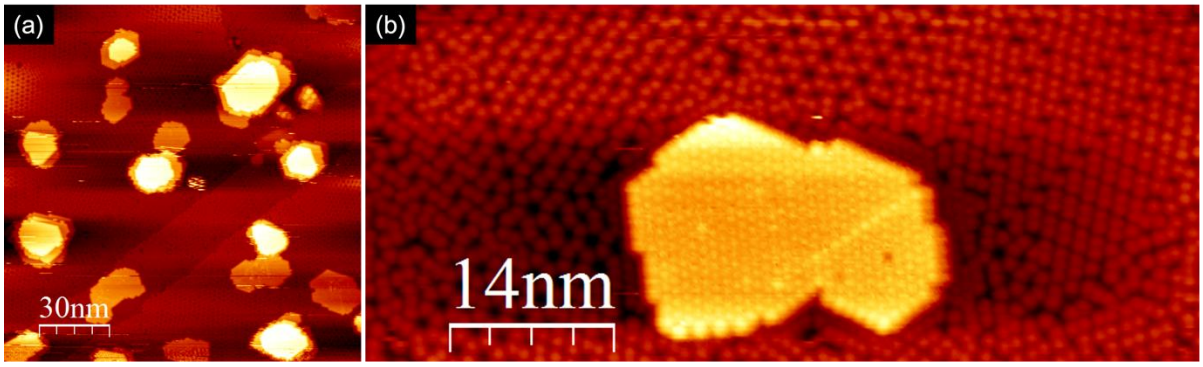

Figure 5.4 (a) STM image by further depositing C_{60} molecules onto the porous C_{60} framework. The preferential growth in the vertical direction contrasts the nearly layer-by-layer growth of C_{60} on the Au(111) surface. (b) Densely packed C_{60} molecules on a multilayer island can be seen in the high-resolution STM image, a porous C_{60} framework in the background. STM imaging parameters: (a) 300 pA, 1.5 V; 70 nm, RT. (b) 300 pA, 1.8 V; RT. Gaussian filter is applied to the original data. Figures are reproduced from Supporting Information of Ref [1].

Thus, the pores are prone to accepting various molecules as guests[33]. If these pores can accommodate more C_{60} molecules on the surface, we ran experiments by continuously depositing the C_{60} molecules onto the porous framework at RT. The experimental data shows that C_{60} has no affinity for the C_{60} /OT framework, with no extra ordered novel structure

emerging on top of the framework. The C_{60} molecules travel significant distances across the whole framework on the surface to find a limited number of C_{60} densely packed patches. An apparent vertical growth can be shown in Figure 5.4 (a).

Furthermore, Figure 5.4 (b) generates multilayers by adding a large amount of C_{60}. Densely packed C_{60} molecules comprise the two to three layers of C_{60} islands. That may be because a CH_3-terminated surface of densely packed OT molecules is not strong enough to bond C_{60} molecules within the pores of the framework.

5.3.3 Pairing C_{60} as Basic Structural Motif

Figures 5.1, 5.2, and 5.4 depict the C_{60}/OT structure characterised using STM imaging at RT. We deposited a small number of C_{60} molecules at RT to better understand how the 2D crystallisation of the compound began. We discovered that C_{60} molecules form in pairs of C_{60} in Figure 5.5.

By scanning at low temperatures, we can better understand this molecular framework's energy landscape. At 77 K, further STM studies show that the C_{60} pairs are formed. STM images in Figure 5.5 (a) and (b) were taken at a liquid nitrogen temperature. It is possible to gather more electronic information on the molecular orbitals and orientation of C_{60} molecules by scanning them at a low bias (0.1V) under LT. The C_{60} pairs illustrated in Figure 5.6 (b) are the bright round spot and the elongated and faint spot. The shape discrepancy of the C_{60} molecules on the Au(111) surface is caused by the varying orientations of the C_{60} cage. C_{60} molecules were discovered in five different orientations on an Au(111) surface, which were named a hexagon, pentagon, single bond, double bond, and edge atom prone to the surface by Lu *et al.*[34]

STM images of C_{60}'s LUMO orbital taken by Altman and Colton show a pentagon prone to the surface with five-fold symmetry[35]. Li *et al.* also discovered the hexagon facing the Ag(111) surface[36], while Hashizume *et al.* found the same arrangement on the Cu(111) surface

under STM at LT[37]. According to Silien *et al.*, a small part of C_{60} can form a pentagonal bonded with the Cu(111) surface[38]. Based on these previous studies, we may propose that the bright round spot of a C_{60} molecule in Figure 5.6 (d) is a pentagon pointing outwards to the surface. Based on our earlier observations. The longer bright spot is likely caused by an oriented C_{60} facing inwards to the Au(111) surface.

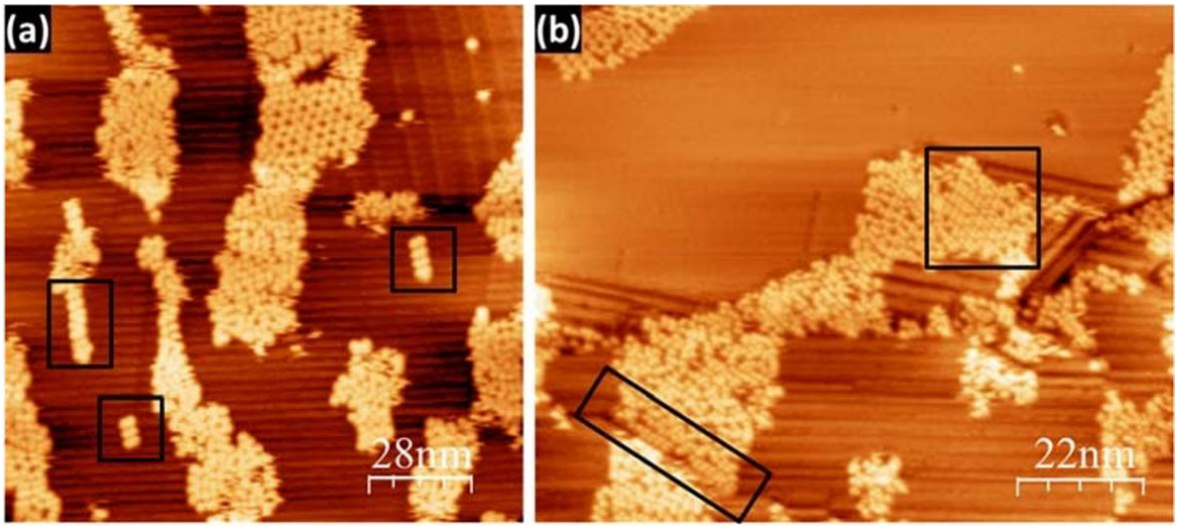

Figure 5.5 C_{60} 2D crystal formation at RT. Black rectangles indicate the presence of C_{60} in pairs. STM imaging parameters: (a) 300 pA, 1.2 V; 85 nm, RT. (b) 300 pA, 1.8 V; 90 nm×110 nm, RT. Gaussian filter is applied to the original data. Figures are reproduced from Supporting Information of Ref [1].

Two C_{60} molecules could potentially align into a paired configuration with their hexagonal facets directly facing one another, provided they are oriented accordingly (Figure 5.6 (b)). This arrangement entails an electron-rich face of one molecule aligning with an electron-deficient face of the other, facilitating a well-known interaction dynamic between the two. As shown in the upper line profile of Figure 5.6 (c), two adjacent C_{60} molecules are inside a pair with a distance of 0.98±0.02 nm, less than that between two C_{60} pairs at RT. However, the lower line profile measured the distance between two adjacent bright spots grows to 1.80± 0.02 nm.

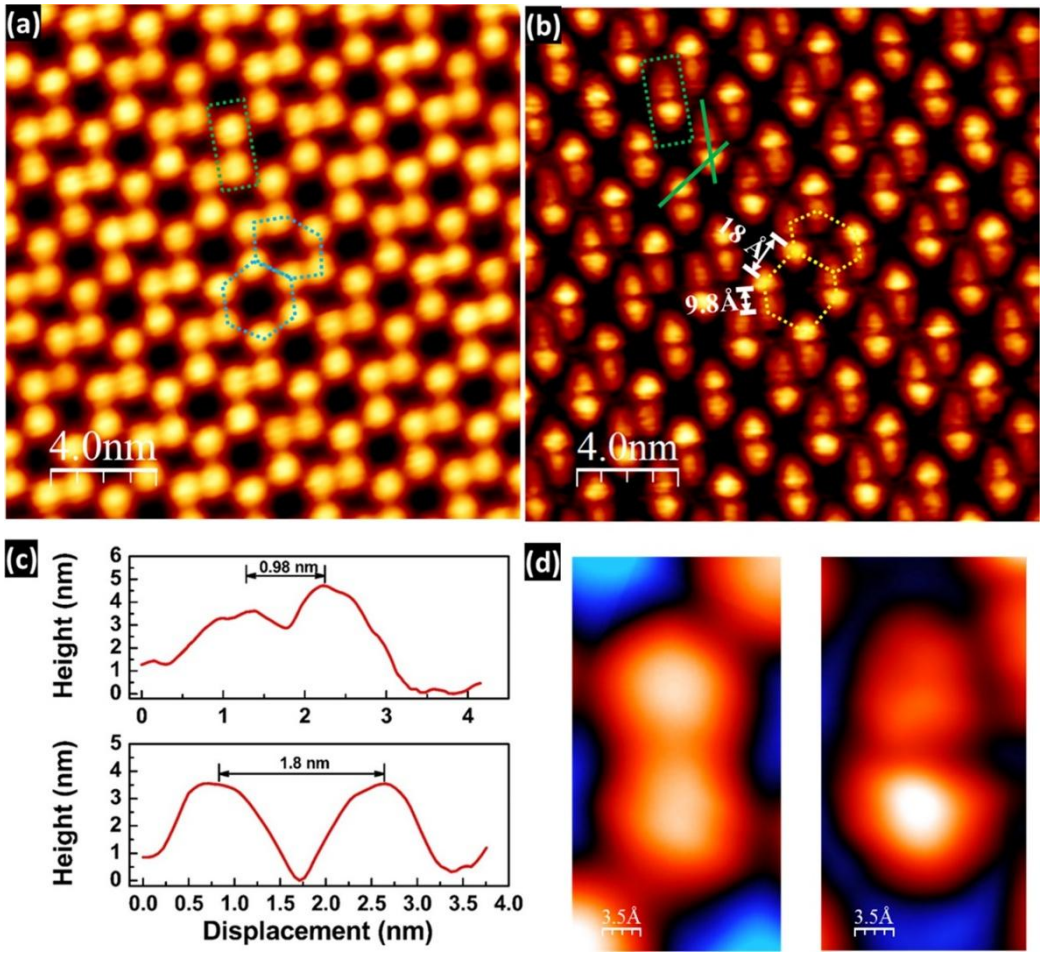

Figure 5.6 (a) & (b) These STM images were scanned at liquid nitrogen temperature (77 K) with biases of +1.5 V and +0.1 V, respectively. The distance between the C_{60} pair and neighbouring C_{60} molecules (along the green line) in a 2D C_{60} molecular framework is shown as line profiles in (c). As illustrated in (d), the strong contrast in a C_{60} pair. STM imaging parameters: (a) 200 pA, 1.5 V; 20 nm, LT. (b) 200 pA, 0.1 V; 20 nm, LT. Gaussian filter is applied to the original data. Figures are reproduced from Ref [1].

Two C_{60} molecules could potentially align into a paired configuration with their hexagonal facets directly facing one another, provided they are oriented accordingly (Figure 5.6 (b)). This arrangement entails an electron-rich face of one molecule aligning with an electron-deficient face of the other, facilitating a well-known interaction dynamic between the two. As shown in the upper line profile of Figure 5.6 (c), two adjacent C_{60} molecules are inside a pair with a distance of 0.98±0.02 nm, less than that between two C_{60} pairs at RT. However,

the lower line profile measured the distance between two adjacent bright spots grows to 1.80± 0.02 nm.

It suggests that the 2D C_{60} molecular framework undergoes a structural shift during cooling from RT to 77 K in the STM chamber. Two neighbouring C_{60} molecules may be forced to form a pair by the surrounding OT molecules because it is harder to push them together under LT. To explain this contrast, several possibilities exist, including charge shift. That means there are charge shifts from a charge-rich surface of a C_{60} to a charge-deficient of another C_{60}. Our collaborators conducted a DFT calculation and suggested there might be a charge transfer[1]. However, between two C_{60} molecules, significant charge transfer is unlikely because they are identical molecules, sharing electrons almost like a covalent bond[39]. The only possibility is a slight charge transfer from one side to the other[40]. Also, the C_{60} molecule might have a preferred orientation, which is possible at low temperatures. At room temperature, the molecules rotate freely and appear the same, but at low temperatures, they might adopt fixed orientations. Besides, the strong contrast in the C_{60} pair in the close-up STM images of a C_{60} pair was obtained with different biases (Figure 5.6 (d)). The possible reason is that C_{60} molecules rotate and flip at a rate faster than the imaging STM tip at RT. So, a time-averaged signal is obtained, and it shows a feature less rounded shape.

5.3.4 Manipulation of C_{60} Molecules by STM Tip

Beton *et al.* successfully employed the tip of STM to precisely position individual C_{60} molecules on a Si(111) surface[41]. This technique enables the formation of simple molecular patterns at room temperature, demonstrating a significant advancement in the manipulation of molecules for surface patterning[42,43].

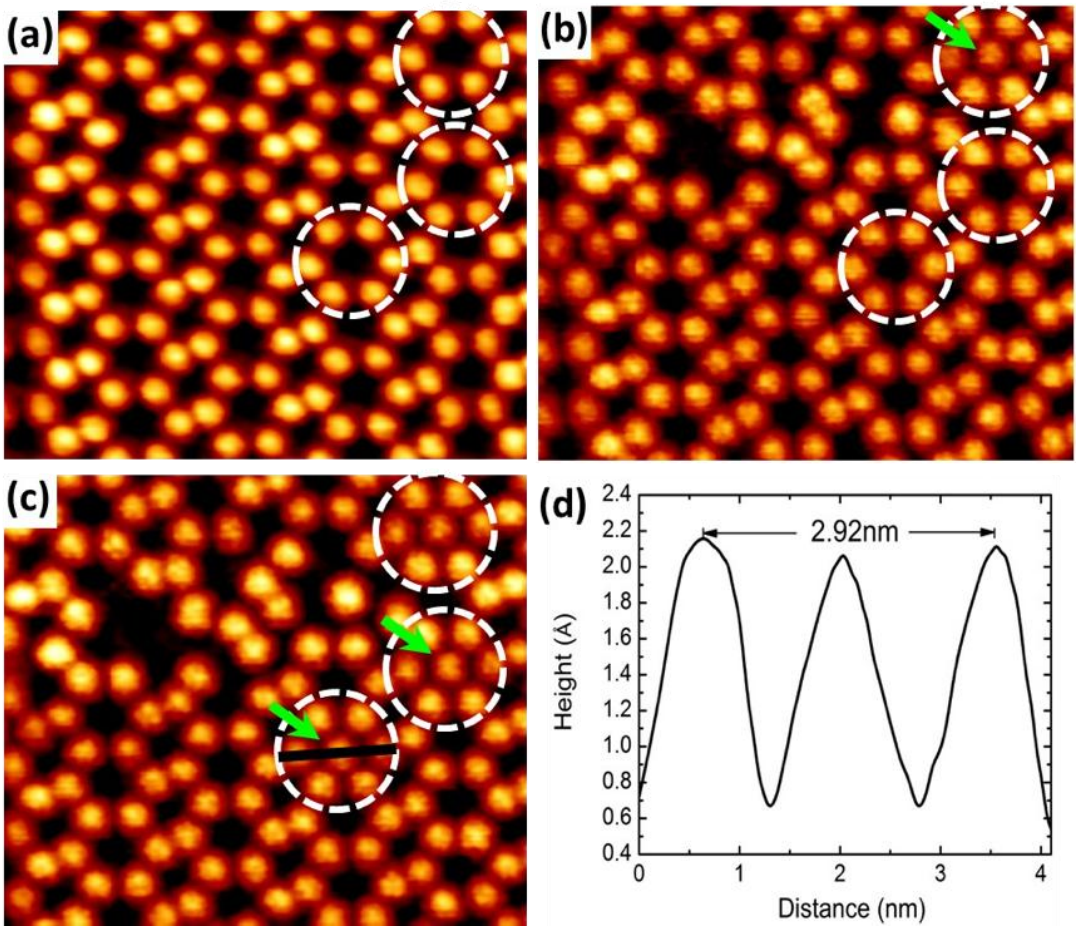

Figure 5.7 (a)-(c) Present a sequence of STM images that illustrate the process of molecular manipulation using an STM tip at LT. (d) Provides a line profile taken along the black line in the image (c), where all C_{60} molecules exhibit uniform brightness, with an approximate lateral separation of 1.46±0.02 nm between adjacent C_{60} molecules. Figures are reproduced from Supporting Information of Ref [2].

Figure 5.7 displays a porous C_{60}/OT network observed at room temperature (RT), revealing pores of two distinct sizes. The larger pores are spacious enough to accommodate an additional C_{60} molecule, with OT molecules filling the pores. In Figure 5.7 (b), a pore is depicted as occupied by a C_{60} molecule, which, as indicated by the line profile in Figure 5.7 (d), finds the pore slightly too large. Consequently, the C_{60} molecule positioned within the pore struggles to effectively interact with neighbouring molecules due to an excessive molecule-molecule distance. The cluster of seven C_{60} molecules within the dotted circle in Figure 5.7 (b) does not constitute a stable configuration at RT. Experimental observations show C_{60}

molecules continuously moving into and out of such pores. This may indicate there are no OT molecules inside the pore. Due to collective interaction between molecules, the C_{60} molecules can still maintain the hexagonal geometry.

This series of STM images, from Figure 5.7 (a) to (c), showcases a detailed procedure of molecular manipulation using the tip of an STM[43]. This technique highlights the precision with which individual molecules, in this case, C_{60} molecules, can be repositioned on a surface at the nanoscale. In Figure 5.7 (d), the line profile analysis, conducted along a specified black line in Figure 5.7 (c), offers quantitative insights into the spatial arrangement of the C_{60} molecules following manipulation. The consistent brightness across all C_{60} molecules in the line profile indicates uniform molecular orientation and similar electronic characteristics, suggesting that the manipulation process preserves the integrity of the molecular structure. The measured lateral distance of 1.46±0.02 nm between neighbouring C_{60} molecules confirms the precision of the manipulation and provides valuable information about the density and packing of the molecules on the surface.

This technique of molecular manipulation by STM tip opens avenues for constructing and studying nanostructures with defined geometries and properties[43]. By enabling the arrangement of molecules with such precision, researchers can probe the physical and chemical phenomena at the nanoscale in a controlled environment. This has implications for developing nanoelectronic devices, molecular sensors, and surface science, where understanding molecule-surface interactions is crucial[41]. Moreover, the ability to manipulate and analyse molecules at this level of detail contributes to the broader field of nanotechnology, paving the way for innovations in materials science, electronics, and beyond[44].

5.4 Summary

In summary, a $(C_{60})_4(OT)_{14}$ porous van der Waals supramolecular framework in two dimensions was synthesised on an Au(111) surface. Instead of relying only on pairwise interactions, the pairing C_{60} framework relies on the collective interactions of many molecules on the surface. Van der Waals supramolecular frameworks are challenging to build because they lack specific and directed bonding between molecules. It is projected to be a lot more common. Thus, it is essential to study these frameworks thoroughly. In the next step, a more detailed low-temperature characterisation of the C_{60}-OT framework structure will be carried out by LT-STM to obtain more evidence of the C_{60} molecular orientation of this binary molecular structure[26]. A dI/dV mapping can also be done to acquire the electron density of state distribution for the different molecular orientations[45].

References

1. Zhang, X. *et al.* Two-Dimensional van der Waals Supramolecular Frameworks from Co-Hosted Molecular Assembly and C_{60} Dimerization. *J. Phys. Chem. C* 124, 12589–12595 (2020).

2. Zhang, X. *et al.* Complex supramolecular tessellations with on-surface self-synthesized C_{60} tiles through van der Waals interaction. *Nanoscale* 14, 1333–1339 (2022).

3. Geim, A. K. & Novoselov, K. S. The rise of graphene. *Nat Mater* 6, 183–191 (2007).

4. Mounet, N. *et al.* Two-dimensional materials from high-throughput computational exfoliation of experimentally known compounds. *Nat Nanotechnol* 13, 246–252 (2018).

5. Lee, J. S. *et al.* Wafer-scale single-crystal hexagonal boron nitride film via self-collimated grain formation. *Science* 362, 817–821 (2018).

6. Cañas-Ventura, M. E. *et al.* Complex Interplay and Hierarchy of Interactions in Two-Dimensional Supramolecular Assemblies. *Acs Nano* 5, 457–469 (2011).

7. Ciesielski, A. *et al.* Concentration-Dependent Supramolecular Engineering of Hydrogen-Bonded Nanostructures at Surfaces: Predicting Self-Assembly in 2D. *J Am Chem Soc* 135, 6942–6950 (2013).

8. Elemans, J. A. A. W., Lei, S. & Feyter, S. D. Molecular and Supramolecular Networks on Surfaces: From Two-Dimensional Crystal Engineering to Reactivity. *Angew. Chem. Int. Ed.* 48, 7298–7332 (2009).

9. Zhang, Y.-Q. *et al.* Complex supramolecular interfacial tessellation through convergent multi-step reaction of a dissymmetric simple organic precursor. *Nat Chem* 10, 296–304 (2018).

10. Langner, A. *et al.* Self-recognition and self-selection in multicomponent supramolecular coordination networks on surfaces. *Proc National Acad Sci* 104, 17927–17930 (2007).

11. Stöhr, M. *et al.* Controlling Molecular Assembly in Two Dimensions: The Concentration Dependence of Thermally Induced 2D Aggregation of Molecules on a Metal Surface. *Angew. Chem. Int. Ed.* 44, 7394–7398 (2005).

12. Chen, J. *et al.* Building two-dimensional materials one row at a time: Avoiding the nucleation barrier. *Science* 362, 1135–1139 (2018).

13. Stepanow, S., Lin, N. & Barth, J. V. Modular assembly of low-dimensional coordination architectures on metal surfaces. *J Phys Condens Matter* 20, 184002 (2008).

14. Pivetta, M., Blüm, M., Patthey, F. & Schneider, W. Two-Dimensional Tiling by Rubrene Molecules Self-Assembled in Supramolecular Pentagons, Hexagons, and Heptagons on a Au(111) Surface. *Angew. Chem. Int. Ed.* 47, 1076–1079 (2008).

15. Zhong, D. *et al.* Multilevel Supramolecular Architectures Self-Assembled on Metal Surfaces. *Acs Nano* 4, 1997–2002 (2010).

16. Li, F., Tang, L., Zhou, W. & Guo, Q. Formation of Confined C_{60} Islands within Octanethiol Self-Assembled Monolayers on Au(111). *J. Phys. Chem. C* 113, 17899–17903 (2009).

17. Gao, J. *et al.* Growth of Two-Dimensional C_{60} Nanoclusters within a Propylthiolate Matrix. *J Phys Chem C* 120, 25481–25488 (2016).

18. Li, F., Tang, L., Zhou, W. & Guo, Q. Resolving the Au-Adatom-Alkanethiolate Bonding Site on Au(111) with Domain Boundary Imaging Using High-Resolution Scanning Tunneling Microscopy. *J. Am. Chem. Soc.* 132, 13059–13063 (2010).

19. Raigoza, A. F. *et al.* Coadsorption of Octanethiol and Dialkyldithiocarbamate on Au(111). *J Phys Chem C* 116, 1930–1934 (2012).

20. Poirier, G. E. Coverage-Dependent Phases and Phase Stability of Decanethiol on Au(111). *Langmuir* 15, 1167–1175 (1999).

21. Dubois, L. H., Zegarski, B. R. & Nuzzo, R. G. Molecular ordering of organosulfur compounds on Au(111) and Au(100): Adsorption from solution and in ultrahigh vacuum. *J Chem Phys* 98, 678–688 (1993).

22. Guo, Q. & Li, F. Self-assembled alkanethiol monolayers on gold surfaces: resolving the complex structure at the interface by STM. *Phys. Chem. Chem. Phys.* 16, 19074–19090 (2014).

23. Guo, L. *et al.* Orientational Epitaxy of van der Waals Molecular Heterostructures. *Nano Lett* 18, 5257–5261 (2018).

24. Xie, Y.-C., Tang, L. & Guo, Q. Cooperative Assembly of Magic Number C_{60}-Au Complexes. *Phys Rev Lett* 111, 186101 (2013).

25. Altman, E. I. & Colton, R. J. The interaction of C_{60} with noble metal surfaces. *Surf Sci* 295, 13–33 (1993).

26. Tang, L., Xie, Y. & Guo, Q. Complex orientational ordering of C_{60} molecules on Au(111). *J Chem Phys* 135, 114702 (2011).

27. Maksymovych, P., Voznyy, O., Dougherty, D. B., Sorescu, D. C. & Yates, J. T. Gold adatom as a key structural component in self-assembled monolayers of organosulfur molecules on Au(111). *Prog. Surf. Sci.* 85, 206–240 (2010).

28. Sedona, F., Marino, M. D., Basagni, A., Colazzo, L. & Sambi, M. Structurally Tunable Self-Assembled 2D Cocrystals of C_{60} and Porphyrins on the Ag (110) Surface. *J Phys Chem C* 118, 1587–1593 (2014).

29. Zhang, H. L. *et al.* C_{60} Molecular Chains on α-Sexithiophene Nanostripes. *Small* 3, 2015–2018 (2007).

30. Smerdon, J. A., Rankin, R. B., Greeley, J. P., Guisinger, N. P. & Guest, J. R. Chiral "Pinwheel" Heterojunctions Self-Assembled from C_{60} and Pentacene. *Acs Nano* 7, 3086–3094 (2013).

31. Jin, W., Dougherty, D. B., Cullen, W. G., Robey, S. & Reutt-Robey, J. E. C_{60}−Pentacene Network Formation by 2-D Co-Crystallization. *Langmuir* 25, 9857–9862 (2009).

32. Vijayaraghavan, S. *et al.* Selective Supramolecular Fullerene–Porphyrin Interactions and Switching in Surface-Confined C_{60}–Ce(TPP)2 Dyads. *Nano Lett* 12, 4077–4083 (2012).

33. Theobald, J. A., Oxtoby, N. S., Phillips, M. A., Champness, N. R. & Beton, P. H. Controlling molecular deposition and layer structure with supramolecular surface assemblies. *Nature* 424, 1029–1031 (2003).

34. Lu, X., Grobis, M., Khoo, K. H., Louie, S. G. & Crommie, M. F. Charge transfer and screening in individual C_{60} molecules on metal substrates: A scanning tunneling spectroscopy and theoretical study. *Phys Rev B* 70, 115418 (2004).

35. Altman, E. I. & Colton, R. J. Determination of the orientation of C_{60} adsorbed on Au(111) and Ag(111). *Phys Rev B* 48, 18244–18249 (1993).

36. Li, H. I. *et al.* Surface Geometry of C_{60} on Ag(111). *Phys Rev Lett* 103, 056101 (2009).

37. Hashizume, T. *et al.* Intramolecular structures of C_{60} molecules adsorbed on the Cu(111)-(1×1) surface. *Phys Rev Lett* 71, 2959–2962 (1993).

38. Silien, C., Pradhan, N. A., Ho, W. & Thiry, P. A. Influence of adsorbate-substrate interaction on the local electronic structure of C_{60} studied by low-temperature STM. *Phys Rev B* 69, 115434 (2004).

39. David, W. I. F., Ibberson, R. M., Dennis, T. J. S., Hare, J. P. & Prassides, K. Structural Phase Transitions in the Fullerene C_{60}. *Epl Europhys Lett* 18, 219–225 (1992).

40. Moriarty, P. *et al.* C_{60}-terminated Si surfaces: Charge transfer, bonding, and chemical passivation. *Phys. Rev. B* 57, 362–369 (1998).

41. Beton, P. H., Dunn, A. W. & Moriarty, P. Manipulation of C_{60} molecules on a Si surface. *Appl. Phys. Lett.* 67, 1075–1077 (1995).

42. Moriarty, P., Ma, Y. R., Upward, M. D. & Beton, P. H. Translation, rotation and removal of C_{60} on Si(100)-2 × 1 using anisotropic molecular manipulation. *Surf. Sci.* 407, 27–35 (1998).

43. Chiutu, C. *et al.* Precise Orientation of a Single C_{60} Molecule on the Tip of a Scanning Probe Microscope. *Phys. Rev. Lett.* 108, 268302 (2012).

44. Ding, H. *et al.* Perturbational Imaging of Molecules with the Scanning Tunneling Microscope. *J. Phys. Chem. C* 124, 25892–25897 (2020).

45. Pradhan, N. A., Liu, N. & Ho, W. Vibronic Spectroscopy of Single C_{60} Molecules and Monolayers with the STM. *J Phys Chem B* 109, 8513–8518 (2005).

6. Supramolecular Tessellations with Self-synthesised C_{60}/Octanethiol Tiles

The results presented in this chapter incorporate figures that are reformatted versions from a paper published in 2022[1], of which I am the second author. The reference for the paper is as follows:

- Zhang, X.; **Ding, H.**; Chen, X.; Lin, H.; Li, Q.; Gao, J.; Pan, M.; Guo, Q. Complex Supramolecular Tessellations with On-Surface Self-Synthesised C_{60} Tiles through van Der Waals Interaction. *Nanoscale* 2022, 14 (4), 1333–1339. (Roles: Conceptualization, Data curation, Formal analysis, Investigation, Methodology, Resources, Software, Validation, Visualisation, Writing-original draft, and Writing-review and editing.)

6.1 Introduction

Because of the variety of structural configurations, two-dimensional (2D) supramolecular structures have been the subject of extensive research in flexible production techniques and many applications in nanotechnology for many years[2–4]. Tiling a solid surface with molecules of specified geometric patterns[5,6] is an appealing technique for producing 2D molecular materials[7–9]. Two kinds of molecular tiles have been identified in the last several decades concerning the composition of tessellations. For example, there is a system consisting of a single component in which molecules with regular and semi-regular shapes and configurations are used as fundamental building blocks and linkers to accomplish polygonal tessellation. Flexible assembled systems of molecules with linear[10], triangular[11], rhombus[12], or other regular forms and configurations are also promoted[13].

When producing more sophisticated supramolecular tessellations, multicomponent systems are more flexible[14–17]. For molecules without specialised functional groups, the effects

of spatial confinement and molecular crowding may prohibit them from forming close-packed arrangements[18,19]. Consequently, the creation of supramolecular structures can be facilitated. On the other hand, novel tiles may be synthesised on the surface by taking advantage of aggregating various molecules into clusters[20]. Particular sorts of tiles can be created more easily by the advantages of the high selectivity of the preferred formation of magic number clusters[21].

The balance between intermolecular interactions and molecule-substrate interactions determines the architecture and characteristics of supramolecular tessellations. The pure van der Waals interaction occurs when interactions are so weak that tiling patterns are flexible on the surface. The vdW force can be used in non-planar and prolonged molecule assembly, but it lacks specific and directed molecule bonding[22,23]. In our previous work, we developed a hybrid $(C_{60})_7$-$(Au)_{19}$ cluster with the magic number that was driven by the vdW[24]. OT and C_{60} molecules form a binary system that we investigate, which will be introduced in detail in this chapter. Several molecules will be used to make C_{60} cluster tiles and bind the supramolecular tiles together. Tiles of $(C_{60})_7$ self-synthesis were used to tile the Au(111) surface, and OT was used as "grout". Also, the structure of the C_{60} chains as rectangular tiles is a comparable tessellation on the surface. A recent review paper has covered many examples of how to control the assembly of C_{60} molecules[25] with pre- or coadsorbed molecules[26].

6.2 Experimental Procedure

The experiments are carried out in an ultrahigh vacuum(UHV) chamber with a base pressure of 10^{-10} mbar utilising an Omicron Fermi-STM under room temperature (RT). In a UHV chamber, gold atoms are deposited on a HOPG substrate to create a 300 nm thickness Au(111) substrate. Several Ar^+ sputtering and annealing cycles were carried out to clean the surface. Ar^+ ions have a kinetic energy of 1 keV. Vacancy flaws of the Au(111) surface may be eliminated by annealing over 700 K after sputtering at RT. This kind of preparation can create

a clean and almost defect-free surface. The dimensions of Au steps and herringbone reconstruction surface unit cells are used as a reference to calibrate the STM scanning. Then immerse the sample in a 1 mM OT/ethanol solution for 24 hours, forming a self-assembled monolayer(SAMs) of OT on Au(111), which is in saturation coverage. A 3-hour thermal annealing process at 393 K is applied after placing the sample in the UHV system. The OT is partially desorbed during this annealing process, resulting in a striped phase. The striped phase of OT at RT is used to deposit C_{60} molecules onto the sample. Tungsten tips that have been electrochemically etched are used to gather STM images. Examining the periodic structure necessitates measuring a distance spanning many unit cell dimensions. We acquired lateral distance with an accuracy of 0.02 nm using several such measurements. However, experimental precision is not essential to establishing the structure of C_{60} tiles. The adsorption sites of individual C_{60} molecules are determined using the long-range ordered tiles and the measured values by STM.

6.3 Results and Discussion

6.3.1 $(C_{60})_7$ based Supramolecular Tiling

Porous C_{60} frameworks filled with OT are introduced in chapter 5. Heating the sample can alter the C_{60}/OT ratio. It is possible to minimise OT coverage by gently heating the sample while having minimal influence on C_{60} coverage. The desorption temperature of OT is 340 K~470 K, which is lower than that of C_{60}. A progressive shift from a porous C_{60} framework to C_{60} tiles occurs when the C_{60}/OT ratio rises. A mixed C_{60}/OT molecular layer is shown in Figure 6.1 (a). Three separate domains can be seen in this STM image. The C_{60}/OT structure occupies about 80% of the surface. Parallel rows of OT is the striped phase. The patch regions of $(C_{60})_7$ tiles are highlighted with purple undertones. The $(C_{60})_7$ tiles and porous framework are depicted

with a high-resolution STM image in Figure 6.1 (b), in which molecular tiles comprise seven C_{60} molecules. The hexagonal form of the $(C_{60})_7$ tile is due to the densely packed molecular arrangement. In the false-colour STM image, the molecule in the middle of the tile has a shorter apparent height. Aside from this middle C_{60}, all six C_{60} molecules are identically at the same height.

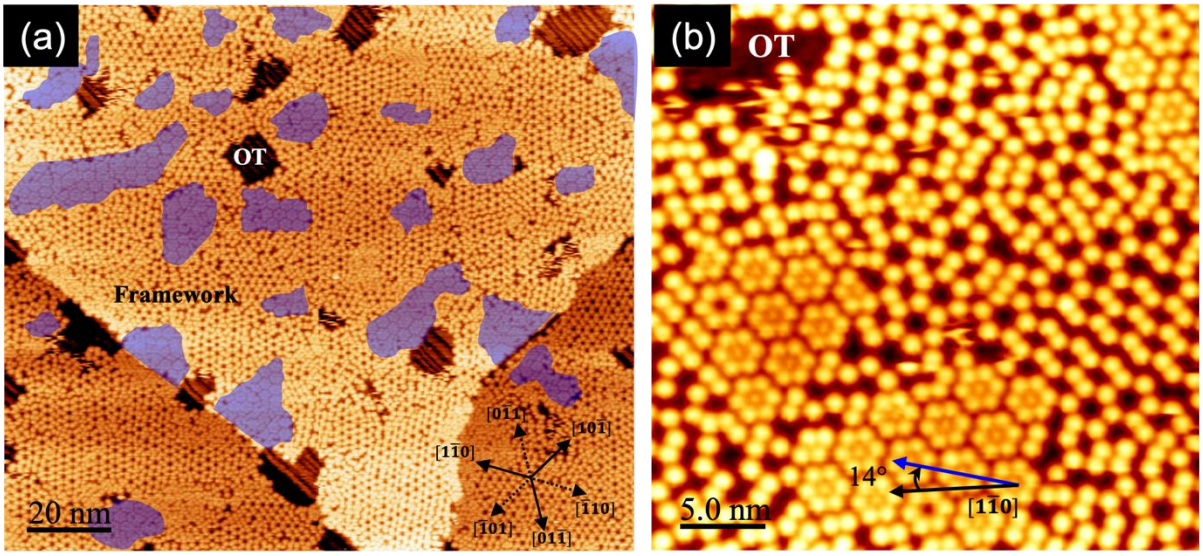

Figure 6.1 (a) A C_{60}/OT porous framework, OT striped phase, and $(C_{60})_7$ based supramolecular tessellations coexisting in a single large-scale STM image. (b) A close-up of a tiled area adjacent to a porous framework domain. It is 14 degrees clockwise from the $[1\bar{1}0]$ direction that the $(C_{60})_7$ tiles are aligned. STM imaging parameters: (a) 50 pA, 2.0 V; 150 nm × 128 nm, RT. (b) 50 pA, 1.5 V; 30 nm, RT.

This phenomenon of brightness contrast in C_{60}/Au(111) has been reported before[27–30]. This observed difference may be attributed to the presence of molecules with varying orientations or adatoms/interface restructuring. Moreover, two neighbouring $(C_{60})_7$ tiles are separated by ample space. The exact molecular structure of voids can not be resolved under STM. Since it is not stable at RT to have a gap between two $(C_{60})_7$ clusters, OT molecules must be used to fill it. The striped phase OT rows also tend to align in $[11\bar{2}]$ directions. The azimuth orientation of the $(C_{60})_7$ structure can be computed using the OT row as a reference. As illustrated in Figure 6.1 (b), the row of $(C_{60})_7$ tiles is oriented at an angle of 14 degrees from

the $[1\bar{1}0]$directions. A $(7 \times 7)R14°$ superstructure in which C_{60} molecules are densely packed on the surface has shown this azimuthal orientation (111)[27]. The C_{60} heptamer unit formation has been observed several times[29]. The centred C_{60} tends to settle in a fixed place on the Au(111) substrate through one of its hexagonal sides.

6.3.2 Bias-dependent STM Images

Figure 6.2 shows STM images of the $(C_{60})_7$ tile taken with positive and negative polarity bias voltages. We observed a bias polarity-dependent contrast in the $(C_{60})_7$ tile. The central C_{60} looks brighter in negative bias and darker in positive bias. This bias polarity dependency of the observed height implies the contribution of different LDOS. The core C_{60} molecule is thought to be resting on the substrate with its hexagonal face contacting the Au(111) surface.

In this scenario, we have a group of seven molecules, with one distinct molecule in the centre. The central molecule is unique due to its position, while the other six molecules are nearly identical and located symmetrically around it. This arrangement is unsurprising, as the six peripheral molecules are similar, and the central molecule stands out due to its unique positioning. The central molecule has six nearest neighbouring C_{60} molecules, whereas each peripheral C_{60} molecule has neighbouring thiol and C_{60} molecules. This difference means the central molecule can exhibit variations in appearance, such as appearing lower or higher, which can be attributed to its orientation within the C_{60} structure. Depending on its orientation, it may appear taller by 0.02 to 0.03 nm. Therefore, it is normal for one molecule to appear darker or brighter.

As a result, the STM image may reveal the time-averaged properties of the other six C_{60} molecules[27]. In this experiment, low-temperature imaging is not applied. Therefore, the orientation of the C_{60} molecules cannot be reliably established. A green circle emphasises the bright centre molecule scanned under positive sample bias. This shows that the STM tip

perturbed the centre C_{60} molecule in this tile. It will return to its original dim condition in Figure 6.2 (c).

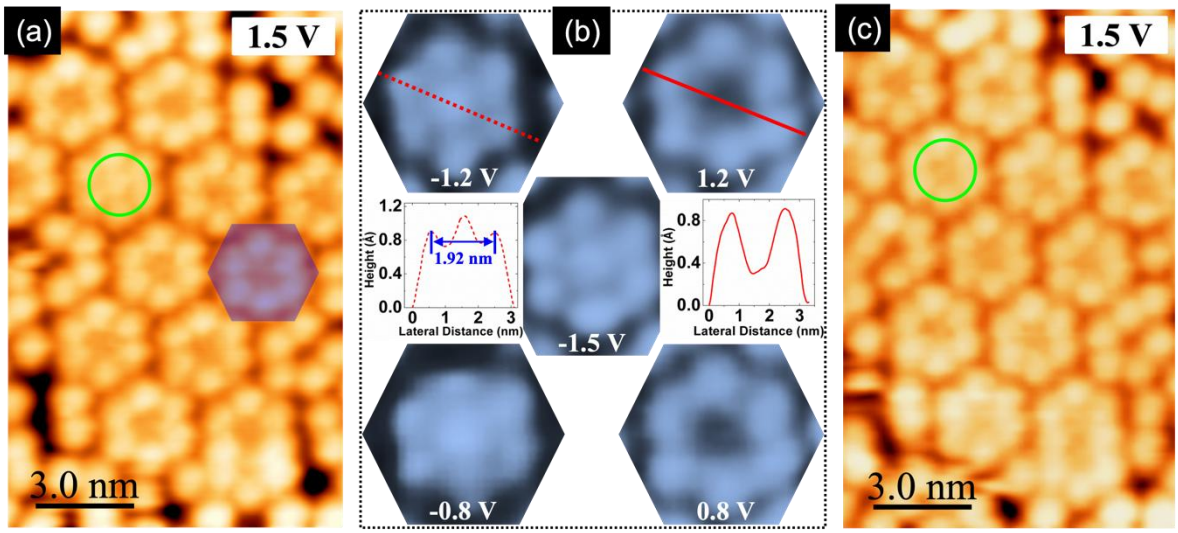

Figure 6.2 Bias dependency feature of $(C_{60})_7$ tiles. (a) (c) are the same region of the surface taken by STM with +1.5V bias. The green circles marked the flipping of the centre C_{60} under different scanning parameters. (b) A high-resolution STM image of a bias-dependent $(C_{60})_7$ unit is highlighted with the blue hexagon in (a). STM images are scanned under a certain tunnelling current of 50pA, and the bias voltage is $\pm$0.8V and $\pm$1.2V, respectively. The line profiles are measured along the red lines of the upper STM image.

According to the discussion presented above, regarding the different molecular adsorption characteristics in the $(C_{60})_7$ cluster, the central molecule can be an "anchor" fixed to the Au surface. Moreover, the other six C_{60} molecules are expected to be less strongly bonded to the Au(111) surface. The vdW interactions between all seven molecules benefit from maintaining the tiles together and increasing their stability[29]. It is not sufficient to maintain the structural integrity by only relying on the intermolecular interaction of the C_{60} molecules. Because these heptamer tiles do not form on the Au(111) surface with just C_{60} molecules. Pure C_{60} heptamers on the Au(111) surface at RT are unstable. However, molecular cavities[31] or metal coordination[24] can stabilise this arrangement. The presence of OT molecules assisted in the development of the heptamer tiles.

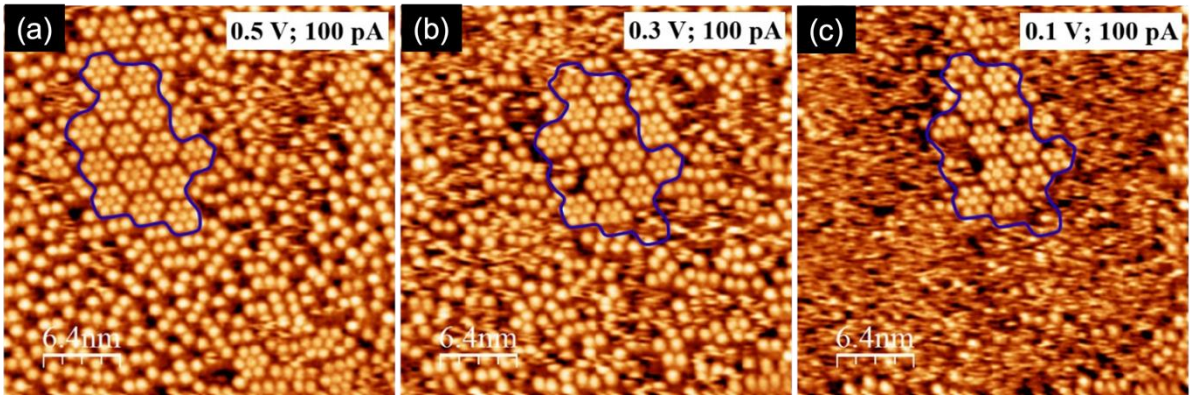

Figure 6.3 STM images with decreasing sample bias under the constant-current mode.

The domain inside the blue line exhibits higher stability than the surrounding areas. This intricate dynamic between the central C_{60} molecule and its six counterparts in the heptameric cluster underscores a nuanced interplay of forces at the nanoscale. The central molecule is in differential adsorption strengths. The weaker bonding of the peripheral C_{60} molecules to the Au(111) surface hints at a delicate balance between mobility and stability, allowing for potential reconfiguration under specific conditions[32].

The role of van der Waals (vdW) forces in this context is particularly noteworthy. Although weaker than covalent or ionic bonds, these interactions are fundamental in nanoscale assemblies, providing the cohesive force that binds the molecules into a stable configuration[33]. However, the reliance on vdW forces alone highlights a limitation in achieving stable, complex nanostructures solely through the inherent properties of the constituent molecules.

The instability of pure C_{60} heptamers at room temperature on the Au(111) surface reveals the challenges in maintaining ordered nanostructures without auxiliary stabilisation mechanisms[30]. This observation points to the necessity of external agents or conditions, such as molecular cavities, that can encapsulate and thus stabilise the C_{60} molecules or metal coordination, which introduces additional bonding interactions that can fortify the molecular structure[34,35].

6.3.3 Model of $(C_{60})_7$–$(OT)_6$ Bicomponent Tiling

The tiling mechanism of the individual $(C_{60})_7$ cluster is currently the focus of our investigation. Figure 6.4 (a) details the bicomponent tiling's molecular structure. The STM images reveal a periodic molecule arrangement with six-fold symmetry, corroborated by the inset's FFT image. The unit cell of the supramolecular tessellation shown by the blue rhombus has a hexagonal structure, where $c = 3.16\ \text{nm}, \alpha = 60°$. These well-defined lattice constants are essential to propose the optimal model in real space. Thermal drift and piezo scanner creep introduce uncertainty ±0.01 nm to the STM-measured lattice constant. The random error, determined through multiple measurements, is ±0.02 nm. Therefore, the total uncertainty of the distance measurement is ±0.02 nm. For the lattice arrangement in this system, the dim C_{60} molecule must occupy an identical position on Au(111). As a result, the proposed structure model is in Figure 6.4 (b). Our experimental result of 3.16 nm is highly similar to the distance between the two neighbouring tiles ($\sqrt{117}a, a = 2.889Å$) shown in the model in Figure 6.4 (b). The $\left(\sqrt{117}a \times \sqrt{117}a\right)R14°$ defines the unit cell of the C_{60} tiles.

Using the closed-packed C_{60} phase as a reference, the adsorption site in a C_{60} tile can be determined. The adsorption site for C_{60} molecules in extended domains of densely packed phase is atop[29]. Therefore, the middle C_{60} of the tile is located in the hollow site on the surface. The peripheral six C_{60} molecules do not occupy the same hollow site as the one in the centre. It seems they have all been shifted a little relative to the centre C_{60} molecule. The surrounding C_{60} molecules occupy a less favourable adsorption site regarding the C_{60}-Au(111) interaction to adjust the appreciable C_{60}-C_{60} distance. The best structural model we could develop is shown in Figure 6.4 (b). The distance between the central C_{60} molecule and each of the six surrounding C_{60} molecules is 0.96±0.02 nm, which is slightly smaller than the typical nearest neighbour

distance, 1.00±0.02 nm, within either C_{60} crystals or in the densely packed layer of C_{60} on Au(111) surface[36,37].

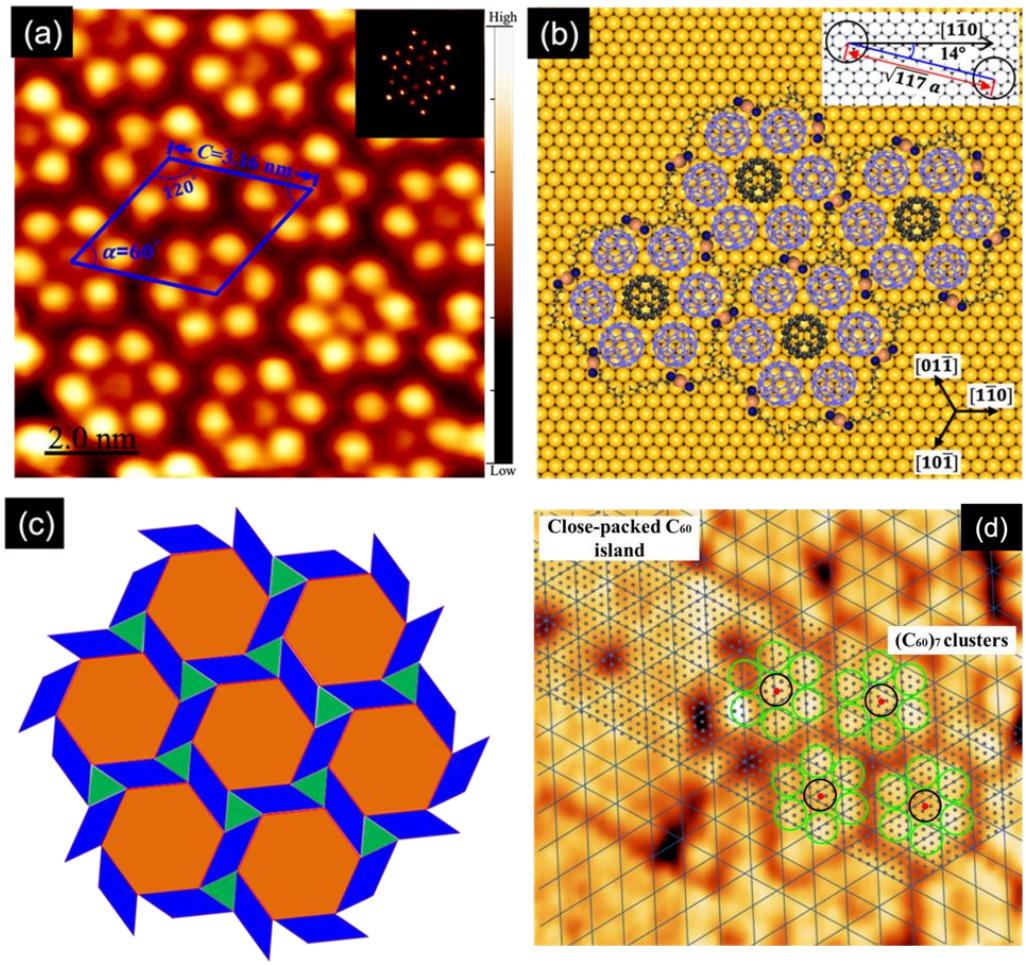

Figure 6.4 High-resolution STM image of the $(C_{60})_7$-based supramolecular structure is shown in (a). The FFT analysis is shown in the inset. Gaussian filter is applied to the original data. The uncertainty of distance measurement is ±0.02 nm. (b) The optimised ball model of the unit cell. The C_{60} cages in blue and black represent the centre and surrounding C_{60} molecules, respectively. RS-Au-SR structural unit surrounds the $(C_{60})_7$ in a ring formation. (c) Schematic diagram of the supramolecular tessellation based on $(C_{60})_7$ atoms. STM imaging parameters: (a) 100 pA, 0.5 V; 10 nm, RT. (d) The adsorption sites of C_{60} molecules within the $(C_{60})_7$ cluster are identified by referencing the arrangement of C_{60} in its close-packed phase.

We follow the same strategy in chapter 5 to build the structural model. Measuring and maintaining the proper distance between molecules ensures realistic vdW interactions and precise control over C_{60} positioning, enhancing model reliability and accommodating potential

alternative configurations. Figure 6.4 (d) shows that the densely packed C_{60} structure can be used as a calibration reference. Figure 6.4 (d) demonstrates the method used to identify the adsorption sites of C_{60} molecules within the $(C_{60})_7$ tiles, employing areas of close-packed C_{60} as a calibration reference. These close-packed C_{60} domains are typically located adjacent to the tiled areas. Prior research has established that C_{60} molecules are positioned atop the Au(111) surface. This knowledge enables us to superimpose the positions of the Au atoms (represented by grey dots in Figure 6.4 (d)) onto the image. Utilising this framework, we can accurately ascertain the locations of the C_{60} molecules within each tile. The closest neighbour distance of ~1 nm is set as a benchmark.

However, the C_{60} heptamer's centre molecule is closer to other C_{60} molecules than it should be. In this case, the short distance may be attributed to the number of coordinates used in the calculation rather than the uncertainty of the measurement. Previously, it was noted that C_{60} molecules on Au(111) tend to form heptamers[27]. The STM images taken at LT demonstrate that an extended 2D densely packed layer of C_{60} may occasionally include an ordered array of C_{60} heptamers[29]. The heptamers will lose their properties at RT due to surface molecules' random thermal flipping. Also, it has been shown that OT molecules may fill gaps between adjacent C_{60} tiles. The molecule in the middle of the tile has six closest neighbours. The six C_{60} molecules around it all have a coordination number of only three. Similar to the situation on a solid surface, where the distance between the first two atom layers is shortened, this under-coordination may result in the C_{60}-C_{60} gap relaxing.

For the tile, six C_{60} molecules nest around an "anchoring" molecule because the molecule in the centre tends to be fixed with higher stability. On the other hand, the heptamer's stability results from the seven molecules interacting collectively. The charge transfer from Au(111) to C_{60} is visible in bias-dependent imaging under STM, which indicates that the centre C_{60} molecule appears to be electron-rich. It has been found that the core C_{60} molecule can be

thermally flipped, which is assisted by the STM tip. The collective vdW interaction between OT and C_{60} molecules on the Au(111) surface stabilises the constructed supramolecular tessellation. OT molecules self-assembly on Au(111) has its fundamental structure, the RS-Au-SR ($R=CH_3(CH_2)_7S$) alkanethiol molecules, and this structural motif can be added in the gap between neighbouring $(C_{60})_7$ clusters. It has been widely accepted that a gold adatom must be absorbed on the bridge site of the surface. The axis of this structural motif must be perpendicular to the bridge[38]. Unit cells with OT molecules grouped around $(C_{60})_7$ clusters are illustrated in the optimal model in Figure. 6.4 (b). There are 0.058ML and 0.05 ML of molecular coverage in this proposed unit cell, respectively. A structural motif is made up of seven C_{60} and six OT molecules. In other words, $(C_{60})_7$-$(OT)_6$ is the formula for supramolecular tessellation based on $(C_{60})_7$.

The coloured tessellation of a partial two-dimensional periodic tile pattern is shown in Figure 6.4 (c). $(C_{60})_7$ clusters and RS-Au-SR structural unit are marked in the yellow and blue tiles, respectively. RS-Au-SR structural units separate each $(C_{60})_7$ cluster in a regular pattern to generate a periodic tile structure. This 2D supramolecular tessellation uses a "binder" (RS-Au-SR structural unit) to keep the C_{60} clusters together by rotating them through 60 degrees. The flexible alkyl chains in the regular tessellation are not always parallel to the substrate precisely at ambient temperature because of the high comparative coverage of OT molecules before C_{60} adsorption. The green triangular tiles represent the three alkyl chain end groups. As a result, the $(C_{60})_7$-based supramolecular structures seen in Figure 6.4 (c) can be described using the 2D tessellation without overlaps and gaps. This molecular self-assembly is based on the collective vdW interaction among molecules.

6.3.4 Tessellation Evolution Induced by Thermal Treatment

For the supramolecular tessellation based on the $(C_{60})_7$ cluster, the dim molecule with a hexagon attached to Au(111) is critical for building the supramolecular structure. In previous studies, thermal annealing treatment has been applied as an appropriate method for fine-tuning molecule adsorption patterns and assembly[39–43]. Therefore, it is possible to fabricate additional supramolecular tessellations by heat treatment in the UHV chamber.

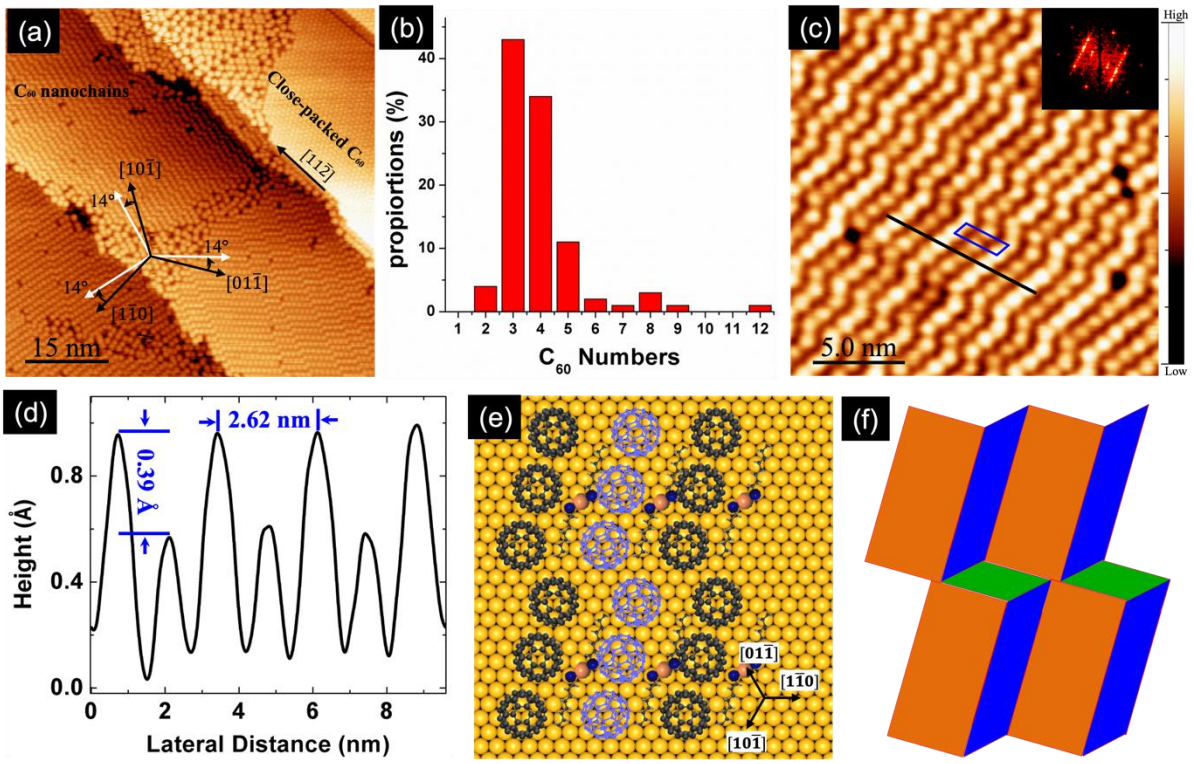

Figure 6.5 (a) STM image of nano chains coexisting with frameworks and close-packed C_{60} domain. (b) As can be seen in the histogram, the ratio of C_{60} numbers in different short segments of nanochains varies widely. (c) A closer look at nano chains with the accompanying FFT analysis in the inset (d) The line profile was measured with a straight black line in (b). (e) Diagram for C_{60}-OT nano chains in ball model, where the blue and dark C_{60} balls represent the bright and dim C_{60} molecules in the nano chains. (f) Schematic of the tessellation of $(C_{60})_n$-$(OT)_m$ nano chains. STM imaging parameters: (a) 300 pA, 1.8 V; 75 nm, RT. (b) 100 pA, 1.5 V; 25 nm, RT.

Due to its lower desorption temperature, the OT coverage is reduced preferentially when the sample is heated to higher temperatures. Figure 6.5 (a) shows the new tiling structure of C_{60} nano chains after thermal annealing at 120 degrees for 90 minutes. Densely packed C_{60}

domains are also formed at the same time. Contrary to expectations, we find that all of the segments in the C_{60} chains are staggered and rotated 14 degrees in either clockwise or counterclockwise orientations concerning the $[1\bar{1}0]$ axes of Au(111). The distributed number of C_{60} in $(C_{60})_n(OT)_m$ segments is shown in Figure 6.5 (b) as a histogram. Molecular C_{60} rows of three, four, or five molecules in each are the most frequent configurations. The regular nanochain tessellation is seen in the STM image in Figure 6.5 (c). According to the FFT analysis in Figure 6.5 (c), supramolecular structures will lose their three-fold symmetry and become two-fold symmetric when subjected to heat treatment. The unit cell is marked by using a blue quadrilateral. There is no intermolecular distance between neighbouring C_{60} molecules along the long-chain direction. With a period of 2.62 ± 0.02 nm, nanochains with bright and dull portions are placed at regular intervals along the direction of $[1\bar{1}0]$. The distance between them is perfectly matched with 9a. Because of the varying sub-molecular orientations of C_{60}, there is an apparent height difference (0.39Å) between bright and dim segments, which is consistent with the observation in clusters of $(C_{60})_7$ under the same bias[28]. The number of C_{60} molecules with lower LDOS has grown dramatically on the surface compared to the $(C_{60})_7$ based supramolecular tessellation.

We use the RS-Au-SR structural unit to fill in the gaps between the bright and dark chains, analogous to the previous modelling technique. Segments having a $(C_{60})_3$-$(OT)_2$ composition are shown in Figure 6.5 (e). The RS-Au-SR structural unit is almost parallel to the Au(111) surface with greater alkyl chain tilting angles in this proposed model. The length in this suggested arrangement is about 2.23 ± 0.02 nm for each structural motif. According to the histogram in Figure 6.5 (b), this length is critical for understanding the statistical findings. To begin with, the distance of 2.23 ± 0.02 nm is more than that of two C_{60} molecule segments. The long-chain growth orientation is preferred by C_{60} molecules instead of bending the alkyl

chain to alter molecular alignment along with the RS-Au-SR structural unit. It optimally aligns with three C_{60} molecules, considering the vdW interaction range. Nevertheless, alkyl chains should be tipped slightly to fill the gap between the adjacent two C_{60} segments. However, more significant tilting angles are easily achieved due to the reduced thiol coverage following thermal annealing[44]. In our experiment, just a few portions with two C_{60} molecules are observed under STM.

According to the ideal three-membered segment tiling, the substrate should be covered by many six-membered segments. However, the percentage of segments with six members is lower than those with four or five members. The adjacent RS-Au-SR structural motif is complicated to locate precisely due to the random diffusion of OT around the C_{60} molecules during annealing treatment. A modest distance between adjacent RS-Au-SR structural units may lead to a segment with four or five C_{60} molecules. In contrast, a significant distance may lead to two staggered three-membered segments rather than a six-membered segment. It is also necessary to use additional RS-Au-SR structural units oriented closely to link the adjacent C_{60} chains with longer segments. After thermal annealing, this is not realistic for OT molecules with limited coverage. The additional space is provided at each segment junction, which promotes the development of long-range order area nanochains. The tiling model shown in Figure 6.5 (f) is corresponded with $(C_{60})_3$-$(OT)_2$ nano chains in Figure 6.5 (e). The orange rectangular shape represents the C_{60} rows, the blue parallelogram indicates the AAD rows, and the green parallelogram denotes the gaps. This serves as a geometric representation of the structure. In geometric modelling, various shapes can be drawn using either space-filling or ball-and-stick models, providing numerous options for visualisation. This particular representation resembles a space-filling model, aiming to avoid empty spaces and create a seamless, continuous surface. The findings show that altering the thiol molecule's alkyl chain length can alter the supramolecular tessellation configurations.

Incorporating OT molecules is a critical factor in stabilising the molecular tiles, illustrating the concept of molecular synergy in supramolecular chemistry. OT, with its long alkyl chains, may provide additional vdW interactions or possibly form a coadsorbed layer that enhances the adhesion of C_{60} molecules to the surface, creating a more favourable environment for the formation and stability of supramolecular tessellation.

These results highlight the complexity of molecular interactions on surfaces and underscore the potential of combining different molecular species to achieve desired structural configurations and stability in nanotechnology applications. Such insights are invaluable for the design and synthesis of novel nanostructured materials, offering pathways to harness the unique properties of fullerenes and other molecular entities in advanced technologies, from electronics to catalysis and beyond.

6.4 Summary

A cooperative van der Waals interaction was the primary driving force behind our success in manufacturing C_{60}-based 2D supramolecular tessellations on Au(111) surfaces. This approach does not need functional groups for the explicit purpose of 'glueing' adjacent tiles together. The binder molecule OT fills the gaps between the $(C_{60})_n$ tiles and self-assembly on the surface. The importance of the vdW interaction in supramolecular tessellations is well demonstrated in this study. Supramolecular tessellations are more stable because the anchoring C_{60} molecule is in the centre of the $(C_{60})_7$ cluster. Following heat treatment, the regular change in the C_{60} molecular adsorption configuration may serve as a case study for C_{60} molecular orbital tuning. The C_{60}-OT supramolecular tiles described here are essential to synthesise and control complicated bicomponent supramolecular tessellations. The involvement of the vdW interaction opens more research pathways for less firmly bound but more versatile molecular tessellations.

References

1. Zhang, X. *et al.* Complex supramolecular tessellations with on-surface self-synthesized C_{60} tiles through van der Waals interaction. *Nanoscale* 14, 1333–1339 (2022).

2. Li, G. *et al.* Epitaxial growth and physical properties of 2D materials beyond graphene: from monatomic materials to binary compounds. *Chem. Soc. Rev.* 47, 6073–6100 (2018).

3. Goronzy, D. P. *et al.* Supramolecular Assemblies on Surfaces: Nanopatterning, Functionality, and Reactivity. *ACS Nano* 12, 7445–7481 (2018).

4. Wang, Z. *et al.* Two-dimensional light-emitting materials: preparation, properties and applications. *Chem. Soc. Rev.* 47, 6128–6174 (2018).

5. Cheng, F. *et al.* Two-dimensional tessellation by molecular tiles constructed from halogen–halogen and halogen–metal networks. *Nat. Commun.* 9, 4871 (2018).

6. Liu, M. *et al.* Two-Dimensional (2D) or Quasi-2D Superstructures from DNA-Coated Colloidal Particles. *Angew. Chem. Int. Ed.* 60, 5744–5748 (2021).

7. Liu, G., Zhen, C., Kang, Y., Wang, L. & Cheng, H.-M. Unique physicochemical properties of two-dimensional light absorbers facilitating photocatalysis. *Chem. Soc. Rev.* 47, 6410–6444 (2018).

8. Liu, Y., Duan, X., Huang, Y. & Duan, X. Two-dimensional transistors beyond graphene and TMDCs. *Chem. Soc. Rev.* 47, 6388–6409 (2018).

9. Wang, F. *et al.* 2D library beyond graphene and transition metal dichalcogenides: a focus on photodetection. *Chem. Soc. Rev.* 47, 6296–6341 (2018).

10. Jing, C. *et al.* Snapshots of Dynamic Adaptation: Two-Dimensional Molecular Architectonics with Linear Bis-Hydroxamic Acid Modules. *Angew. Chem. Int. Ed.* 58, 18948–18956 (2019).

11. Shen, Y. *et al.* Triangular-shaped molecular random tiling and molecular rotation in two-dimensional glassy networks. *Nanoscale* 6, 7221–7225 (2014).

12. Blunt, M. O. *et al.* Random Tiling and Topological Defects in a Two-Dimensional Molecular Network. *Science* 322, 1077–1081 (2008).

13. Millan, J. A., Ortiz, D., Anders, G. van & Glotzer, S. C. Self-Assembly of Archimedean Tilings with Enthalpically and Entropically Patchy Polygons. *ACS Nano* 8, 2918–2928 (2014).

14. Cui, D., Ebrahimi, M., Macleod, J. M. & Rosei, F. Template-Driven Dense Packing of Pentagonal Molecules in Monolayer Films. *Nano Lett.* 18, 7570–7575 (2018).

15. Wang, T. *et al.* Chiral Kagome Lattices from On-Surface Synthesized Molecules. *ChemPhysChem* 18, 3329–3333 (2017).

16. Song, Z., Sun, X. & Wang, L. Switchable Asymmetric Moiré Patterns with Strongly Localized States. *J. Phys. Chem. Lett.* 11, 9224–9229 (2020).

17. Wang, R., He, C., Chen, W., Zhao, C. & Huo, J. Rich B active centers in Penta-B2C as high-performance photocatalyst for nitrogen reduction. *Chin. Chem. Lett.* 32, 3821–3824 (2021).

18. Zhang, X. *et al.* Two-Dimensional van der Waals Supramolecular Frameworks from Co-Hosted Molecular Assembly and C_{60} Dimerization. *J Phys Chem C* 124, 12589–12595 (2020).

19. Fan, Q., Gottfried, J. M. & Zhu, J. Surface-Catalyzed C–C Covalent Coupling Strategies toward the Synthesis of Low-Dimensional Carbon-Based Nanostructures. *Acc. Chem. Res.* 48, 2484–2494 (2015).

20. Bouju, X., Mattioli, C., Franc, G., Pujol, A. & Gourdon, A. Bicomponent Supramolecular Architectures at the Vacuum–Solid Interface. *Chem. Rev.* 117, 1407–1444 (2017).

21. Pinkard, A., Champsaur, A. M. & Roy, X. Molecular Clusters: Nanoscale Building Blocks for Solid-State Materials. *Acc. Chem. Res.* 51, 919–929 (2018).

22. MacLeod, J. Design and construction of on-surface molecular nanoarchitectures: lessons and trends from trimesic acid and other small carboxlyated building blocks. *J. Phys. D: Appl. Phys.* 53, 043002 (2019).

23. Zhang, Y.-Q. *et al.* Complex supramolecular interfacial tessellation through convergent multi-step reaction of a dissymmetric simple organic precursor. *Nat Chem* 10, 296–304 (2018).

24. Xie, Y.-C., Tang, L. & Guo, Q. Cooperative Assembly of Magic Number C_{60}-Au Complexes. *Phys Rev Lett* 111, 186101 (2013).

25. Marino, M. D. *et al.* STM Investigation of Temperature-Dependent Two-Dimensional Supramolecular Architectures of C_{60} and Amino-tetraphenylporphyrin on Ag(110). *Langmuir* 26, 2466–2472 (2010).

26. Geng, Y., Zeng, Q. & Wang, C. Dependence of the surface-assisted fullerene-based complex structure on the template molecule design. *Nano Res* 12, 1509–1537 (2019).

27. Schull, G. & Berndt, R. Orientationally Ordered (7×7) Superstructure of C_{60} on Au(111). *Phys Rev Lett* 99, 226105 (2007).

28. Gardener, J. A., Briggs, G. A. D. & Castell, M. R. Scanning tunneling microscopy studies of C_{60} monolayers on Au(111). *Phys. Rev. B* 80, 235434 (2009).

29. Tang, L., Xie, Y. & Guo, Q. Complex orientational ordering of C_{60} molecules on Au(111). *J Chem Phys* 135, 114702 (2011).

30. Shin, H. *et al.* Structure and dynamics of C_{60} molecules on Au(111). *Phys. Rev. B* 89, 245428 (2014).

31. Theobald, J. A., Oxtoby, N. S., Phillips, M. A., Champness, N. R. & Beton, P. H. Controlling molecular deposition and layer structure with supramolecular surface assemblies. *Nature* 424, 1029–1031 (2003).

32. Moriarty, P., Ma, Y. R., Upward, M. D. & Beton, P. H. Translation, rotation and removal of C_{60} on Si(100)-2 × 1 using anisotropic molecular manipulation. *Surf. Sci.* 407, 27–35 (1998).

33. Chiutu, C. *et al.* Precise Orientation of a Single C_{60} Molecule on the Tip of a Scanning Probe Microscope. *Phys. Rev. Lett.* 108, 268302 (2012).

34. Moriarty, P. *et al.* C_{60}-terminated Si surfaces: Charge transfer, bonding, and chemical passivation. *Phys. Rev. B* 57, 362–369 (1998).

35. Beton, P. H., Dunn, A. W. & Moriarty, P. Manipulation of C_{60} molecules on a Si surface. *Appl. Phys. Lett.* 67, 1075–1077 (1995).

36. Wilson, R. J. *et al.* Imaging C_{60} clusters on a surface using a scanning tunnelling microscope. *Nature* 348, 621–622 (1990).

37. Wragg, J. L., Chamberlain, J. E., White, H. W., Krätschmer, W. & Huffman, D. R. Scanning tunnelling microscopy of solid C_{60}/C_{70}. *Nature* 348, 623–624 (1990).

38. Guo, Q. & Li, F. Self-assembled alkanethiol monolayers on gold surfaces: resolving the complex structure at the interface by STM. *Phys. Chem. Chem. Phys.* 16, 19074–19090 (2014).

39. Li, C. *et al.* Evidence of a Thermal Annealing Effect on Organic Molecular Assembly. *ChemPhysChem* 4, 857–859 (2003).

40. Huang, Y. L. *et al.* Tunable Two-Dimensional Binary Molecular Networks. *Small* 6, 70–75 (2010).

41. Feng, L. *et al.* Supramolecular Tessellations at Surfaces by Vertex Design. *ACS nano* 13, 10603–10611 (2019).

42. Pinardi, A. L. *et al.* Vacancy formation on C_{60}/Pt (111): unraveling the complex atomistic mechanism. *Nanotechnology* 25, 385602 (2014).

43. Liu, C. *et al.* Molecular orientations and interfacial structure of C_{60} on Pt(111). *J. Chem. Phys.* 134, 044707 (2011).

44. Delamarche, E., Michel, B., Kang, H. & Gerber, C. Thermal Stability of Self-Assembled Monolayers. *Langmuir* 10, 4103–4108 (1994).

7. Orientational Growth of Flexible van der Waals C_{60}/Decanethiol Co-assembly

The entirety of the results and discussions in this chapter are sourced from a paper published in 2024[1], for which I serve as the first author. This includes not only the figures but also the textual content and analytical discussions, all of which have been adapted to fit the context and flow of this chapter. The original paper is cited as follows:

- **Ding, H.**; Zhang, X.; Li, B.; Wang, Y.; Xia, C.; Zhao, H.; Yang, H.; Gao, Y.; Chen, X.; Gao, J.; Pan, M.; Guo, Q. Orientational Growth of Flexible van Der Waals Supramolecular Networks. *Small Struct.* 2024, 5. (Roles: Conceptualisation, Data curation, Formal analysis, Investigation, Methodology, Resources, Software, Validation, Visualisation, Writing-original draft, and Writing-review and editing.)

7.1 Introduction

Supramolecular self-assembly provides an efficient mechanism for creating complex systems maintained through non-covalent bonds[2,3]. This phenomenon entails spontaneous, self-organised aggregation of discrete or interconnected components[4,5]. Although the methodology is relatively straightforward, self-assembly predominantly relies on a heuristic approach with an element of trial and error[6]. Nevertheless, a growing interest is being observed in designing bicomponent self-assembled networks, which precisely orchestrate chemically diverse molecular building blocks within a regular matrix[7,8]. Such bicomponent structures are anticipated to manifest functions unattainable from their single-component counterparts[9].

Additionally, supramolecular self-assembly is increasingly recognised as an efficient approach for examining the interplay between fullerene derivatives and substrates[10]. A ubiquitous example is bicomponent systems embodying host-guest architectures, where one

component constitutes the host framework and the other assumes the guest role, filling spaces within the host framework[11]. In specific scenarios, intrinsically porous building blocks are utilised to generate the host network[12]. These building blocks exhibit covalent cavities, a property intrinsic to their chemical structure[13].

A distinct subclass of host networks with covalent cavities includes 2D-sCOFs[14], recently deployed for trapping guest C_{60} molecules[15]. Alternatively, when forming the host network, the precursor molecule can construct a porous framework through self-assembly on the surface, facilitated by strategically placed C_{60} molecules into the molecular framework, such as hydrogen bonding functional groups[16] or elongated alkyl chains[17].

Nonetheless, certain complex molecular networks comprising binary components cannot be easily classified as host-guest networks, primarily because neither of the two assembling components forms a host network. However, these two components can form a co-hosted network through distinct intermolecular interactions, resulting in a co-crystalline arrangement[18,19] dictated by a defined unit cell[15] or a random mixture[20]. These non-host-guest bicomponent networks on surfaces are widely studied in UHV[21] and under ambient conditions[22]. They can be categorised according to dominant intermolecular interactions in the stabilisation of self-assembly on surfaces, such as hydrogen bonding[23], halogen bonding[24], or metal-ligand coordination[25]. C_{60} does not have functional groups. Hence, its interaction with other molecules relies on cooperative interactions where the stability of 2D assemblies depends on the simultaneous interaction among many molecules instead of that of the nearest neighbour molecules[26–29].

This chapter investigates the formation of 2D vdW supramolecular structures through the self-assembled co-crystallisation of DT and C_{60} molecules on an Au(111) surface at RT. Given the absence of specialised functional groups on either the DT or the C_{60} molecules, the coexistence of such conformers allows for the creation of complex supramolecular

architectures. However, the practical control of supramolecular nanostructures presents significant challenges. Using STM, We explored the C_{60}/DT co-assembly with flexible phase transition on Au(111) substrate.

7.2 Experimental Procedure

The experiments were conducted at RT utilising an Omicron VT-STM in a UHV environment, maintaining a base pressure on the order of 10^{-10} mbar. A self-assembled DT monolayer was formed on Au(111) by submerging the sample in a 1 mM DT/ethanol solution for 24 hours. The sample was subsequently placed into the UHV chamber, which underwent thermal annealing at 393 K for 2 hours. This annealing process triggered partial desorption of the DT, forming a striped δ phase. C_{60} molecules were then deposited onto the sample featuring the striped phase of DT at RT. The C_{60} and DT molecules mixed through molecular diffusion, resulting in the emergence of an array of bicomponent structures.

STM images were obtained using electrochemically polished tungsten tips. The lateral distance measured was subject to an uncertainty of ±0.05 nm. However, this does not imply that features separated by 0.05 nm could be readily determined from a single measurement. Given the structure's periodic nature, distances spanning multiple unit cell dimensions were measured. Due to the thermal drift and creep of the STM piezo scanner, the triangulation of the adsorption site is subject to a systematic error of ±0.03 nm. The random error, determined through multiple measurements, is ±0.04 nm. Therefore, the total uncertainty of the distance measurement is ±0.05 nm. The long-range order of the DT striped phase, C_{60} closed-packed structures, and $(C_{60})_7$ clusters, in conjunction with the measured distance and lattice direction, were used in determining the adsorption sites of individual C_{60} molecules. STM images were recorded in a constant current mode under RT and analysed with WSxM software[30].

7.3 Results and Discussion

7.3.1 C_{60} Dimerisation within Decanethiol/Au(111) Matrix

Prior research examining the deposition of C_{60} onto saturated OT (OT) monolayers (0.33 ML) has shown that the full coverage OT monolayer exhibits limited receptivity to C_{60}[31], with C_{60} molecules being incorporated into the OT monolayer through a small number of defect sites[31]. (Figure 7.1) In the current investigation, we remove a fraction of thiol molecules via thermal desorption. The remaining thiols are re-organised into a striped structure. The striped structure consisting of staggered AAD rows offers regular docking sites for C_{60}. An STM image in Figure 7.1 (a) shows the formation of many C_{60} islands after the deposition of C_{60} onto DT/Au(111), which is kept at RT[32]. Contrary to observations of C_{60} adsorption on bare Au(111)[33], it is rare to observe close-packed C_{60} molecules in this stage.

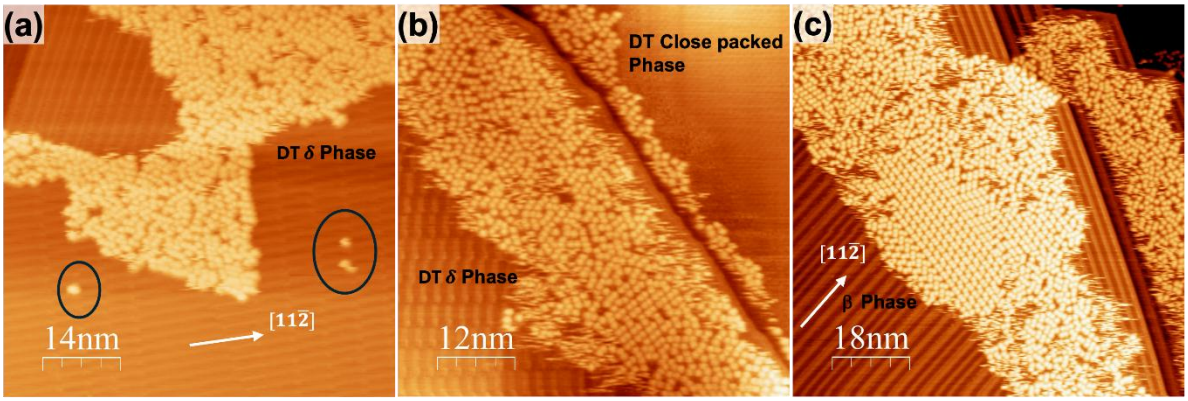

Figure 7.1 STM images of initial growth of C_{60} on templated DT striped δ phase at room temperature (RT). (a) Coexistence of closed-packed C_{60} island and disordered C_{60}/DT domains (70 nm × 70 nm; Vb = 2.0 V; It = 0.3 nA). Some C_{60} monomers and dimers are absorbed on the defects of segmented DT rows (marked by blue ovals). (b) The C_{60} molecules are difficult to absorb on the top of close-packed DT, which has been squeezed around the step edge (60 nm × 60 nm; Vb = 1.8 V; It = 0.3 nA). (c) STM image of large surface area after annealing sample at 323 K for 30 min, some regular domains are formed by C_{60} dimer (90 nm × 90 nm; Vb = 1.5 V; It = 0.3 nA).

Figure 7.1 (a) suggests that the C_{60} islands nucleate at some particular sites, presumably defects within the DT layer. Once a nucleus is formed, it expands by capturing more C_{60} molecules. In contrast to the formation of close-packed C_{60} islands on bare Au(111), hardly

any C_{60} islands are formed from step edges on the DT/Au(111) surface. This is either due to the steps being heavily passivated by thiols or the diffusion of C_{60} towards the steps hindered by the AAD rows. Our observations indicate that C_{60} molecules form C_{60} dimers and initiate growth from defects within segmented DT rows (Figure 7.1 (a)).

These are not true dimers due to the absence of a covalent carbon-carbon bond. They are pairs of molecules interacting via vdW forces. When we refer to them as "dimers," we do not imply the presence of a covalent bond but rather that the two molecules appear to behave as a single unit on the surface. Therefore, using the term "dimer" in this context is appropriate. The C_{60} molecules are observed to be 0.43 nm taller than the baseline level established by the DT striped phase. DT has an apparent height of 0.18 nm when measured using STM from bare Au(111) substrate. Thus, C_{60} appears 0.61 nm taller than the Au(111) substrate. This height is consistent with C_{60} molecules embedded within the DT SAMs and directly bonded to the gold substrate[34,35], analogous to golf balls in a patch of grass. Upon landing, C_{60} molecules diffuse over DT until they find a docking site, usually a defect within the DT layer (Figure 7.1 (b)).

The C_{60} molecule moves downwards at the docking site and becomes directly attached to Au(111). As more and more C_{60} molecules are added, DT molecules need to give up some of their territory. This is achieved by moving the alkyl chain from a nearly flat-lying configuration towards the surface normal in junction with the lateral movement of DT molecules. Figure 7.1 (b) shows that DT molecules occupy a smaller area on Au(111) after C_{60} are incorporated. This is equivalent to the compression of the DT layer into a higher-density phase[36]. There is also the possibility that the alkyl chains change from a nearly flat-lying configuration to a standing-up configuration, hence making space for C_{60}. The long striped β phase is along $[11\bar{2}]$ direction(Figure 7.1 (c)).

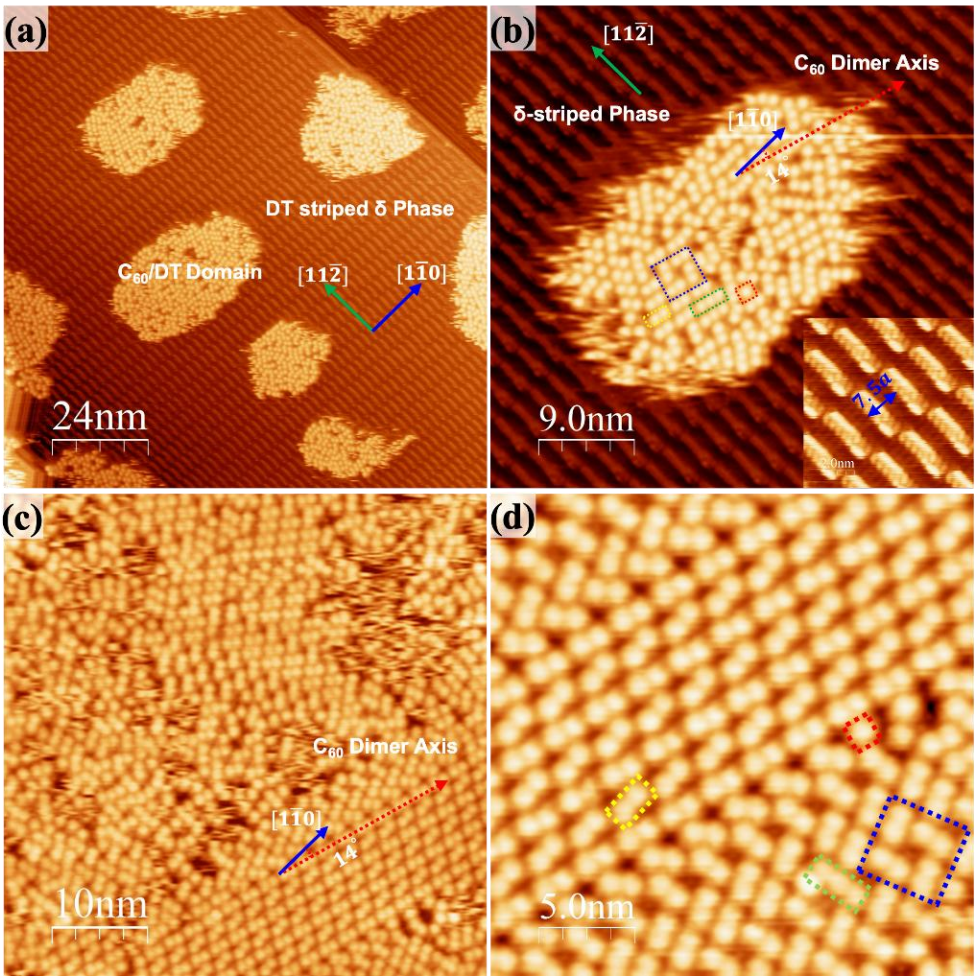

Figure 7.2 The initial growth of mixed C_{60}/DT islands at RT. (a) STM image (120 nm × 120 nm) shows domains of C_{60}/DT coexisting with DT striped δ phase on the Au(111) surface. The green arrow denotes the [11$\bar{2}$] direction, which also aligns with the DT rows in the δ phase. The blue arrow signifies the [1$\bar{1}$0] direction, and the angle between the C_{60} dimer axis and [1$\bar{1}$0] direction is 14 degrees (Vb = 1.5 V; It = 0.3 nA). (b) High-resolution STM image (45 nm × 45 nm; Vb = 1.5 V; It = 0.3 nA) of the top left domain of (a). Red, yellow, and green rectangles delineate the C_{60} groups. A blue rectangle marks the metastable C_{60} square pore. The inset (10 nm × 10 nm; Vb = 1.8 V; It = 0.3 nA) provides a magnified view of the DT striped δ phase. (c) STM image of (50 nm × 50 nm; Vb = -1.8 V; It = 0.3 nA) C_{60} dimer rows are formed after annealing at 323 K for 30min. (d) High-resolution STM image (25 nm × 25 nm; Vb = -1.5 V; It = 0.3 nA) of the bottom right domain of (c). A coexistence of C_{60} monomer, dimer, trimer, and square porous are marked.

Figure 7.2 (a) & (b) illustrate the C_{60} islands on DT δ phase, the [1$\bar{1}$0] and [11$\bar{2}$] directions of Au(111) as indicated by the blue and green arrows, respectively. The DT rows in the δ phase are found to be parallel to the [11$\bar{2}$] direction[37]. Notably, in Figure 7.2 (c)

& (d), the C_{60} molecules tend to pair up after the sample was annealed at 323 K for 30 min. The dimer axis is 14 degrees on either side of the $[1\bar{1}0]$ crystal direction.

Each C_{60} island in Figure 7.2 (a) & (c) is a mixture of C_{60} and DT. Without DT being involved, C_{60} would simply form close-packed domains. The high-resolution STM images of C_{60}/DT domains, as shown in Figure 7.2 (b) & (d), reveal the presence of dimers, trimers, and monomers, with dimers the dominant species. DT fills the gaps between the C_{60} molecules, although the STM cannot locate these DT molecules. This is due to different tunnelling conductance, which will be discussed later. One can see that two or more dimers align themselves to form short dimer rows in Figure 7.2 (c). However, we only observe short-range order here as the growth process is significantly hindered by kinetics. In an earlier study with C_{60} and OT, long-range order appears at RT[38]. In order to form a long-range ordered C_{60}/thiol mixture, the initial striped structure of thiol must be broken first. The alkyl chain of DT is longer than that of OT, and thus, it presents a higher energy barrier for re-organisation. The inset image illustrates the period of the DT striped phase as 7.5a, where 'a' represents the nearest neighbour distance for Au atoms. Each striped phase comprises regularly spaced AAD rows, with the distance between two neighbouring rows dependent on the coverage[37,39].

We can see the locations of individual C_{60} molecules in Figure 7.2 (d). However, we cannot experimentally identify the locations of the DT molecules within the C_{60}/DT mixture. This is most likely due to the significant difference in tunnelling conductance[40]. C_{60} measures ~0.6 nm (apparent height measured with the STM) from the Au(111) substrate. Standing up DT molecules measure <0.2 nm from Au(111). When C_{60} and DT sit next to each other, the contribution of C_{60} towards the overall tunnel current overshadows that of DT. This is partly due to the finite size of the STM tip. An infinitely narrow STM tip would be required to resolve the DT molecules. The individual C_{60} molecules are somewhat unstable and are observed to

shift under normal scanning conditions, as indicated by horizontal streaks surrounding the molecules.

For C_{60}/DT co-assembly, the primary building blocks can be categorised into Monomer, Dimer, and Trimer (observable in Figure 7.2 (b) & (d)), which are highlighted by red, green, and yellow dot frames, respectively. Although dimers are the preferred structure, the existence of monomers is a direct consequence of kinetic constraint. In Figure 7.2 (b) & (d), one can also see four dimers enclosing a space that DT occupies. This is a primitive porous structure. More porous structures are observed upon thermal annealing and will be presented in the next section.

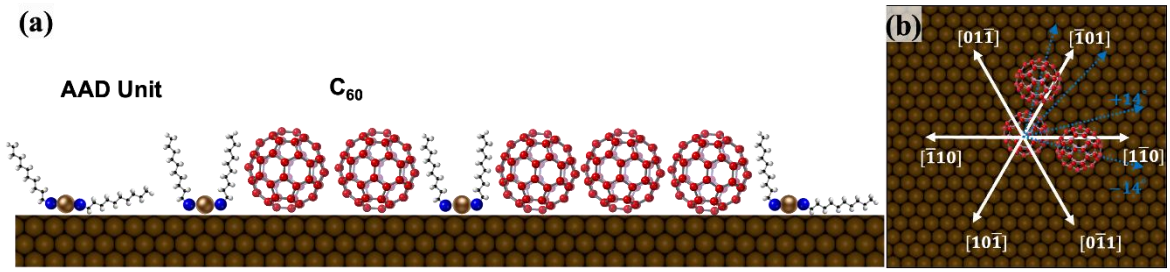

Figure 7.3 (a) A schematic diagram illustrates the relationship between C_{60} molecules and the AAD units in various locations on Au(111). (b) The dimer axis is 14 degrees on either side of the close-packed direction of Au(111). Hence, there are six possible directions. Four of the six possible directions for the C_{60} dimer axis are illustrated.

Figure 7.3 (a) shows a schematic diagram illustrating the relationship between C_{60} molecules and AAD units in various locations. On the bare Au(111) surface, C_{60} can form more than three close-packed phases[41]. One of the close-packed phases is known as the R14 phase. The dimer axis is aligned along the same direction as the close packing direction of C_{60} molecules in the R14 phase[33,34]. The distance between the two C_{60} molecules in each dimer is 1.00 ± 0.05 nm, using the typical distance between DT molecules as the reference[42]. This measured distance is the same as the nearest neighbour distance of C_{60} molecules associated with the R14 phase. That indicates close-packed alignment along the dimer or trimer axis. Apart from molecules in the dimer, other C_{60}-C_{60} distances are significantly greater than 1.00 nm. In Figure 7.3 (b), multiple possibilities for the dimer or trimer axis can be observed, each

axis being rotated from the [1$\bar{1}$0] direction by 14 degrees. All six possible directions of the dimer axis have been observed in C_{60}/DT system.

7.3.2 Formation of C_{60}/DT Porous Framework

The diversity of achievable structures can be relatively constrained in molecular systems where van der Waals (vdW) forces constitute the dominant bonding mechanism. This is due to the tendency of vdW forces to guide the molecules toward a close-packed arrangement at the nanoscale[36]. Hence, control over a binary molecular self-assembly system, solely reliant on vdW forces [43], presents significant challenges[44].

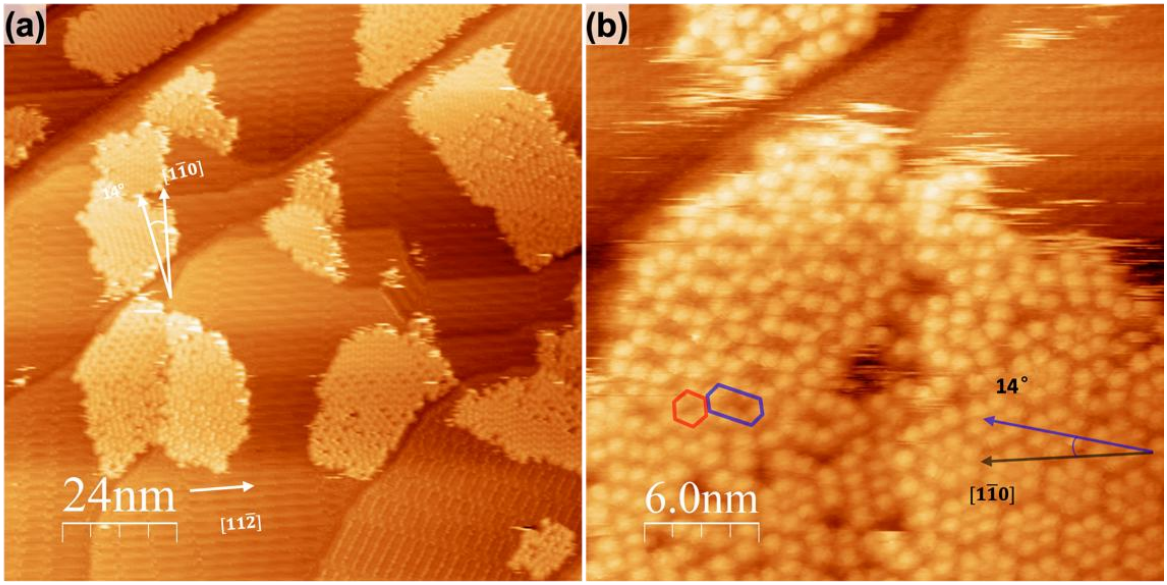

Figure 7.4 STM images of C_{60}/DT after annealing at 343 K for 30 min. (a) A large area of surface topography with four distinct structures: (i) porous C_{60}/DT frameworks in different hexagon shapes; (ii) a pure striped phase of DT exhibiting parallel rows; (iii) patches of $(C_{60})_7$clusters; and (iv) staggered C_{60} nanochains domains (120 nm × 120 nm; Vb = 2 V; It = 0.15nA). (b) High-resolution STM image shows C_{60} frameworks and $(C_{60})_7$ clusters are co-exist on Au(111) surface under RT (30 nm × 30 nm; Vb = 2 V; It = 0.15 nA).

In an earlier study, when C_{60} was deposited onto OT/Au(111), spontaneous formation of porous frameworks was observed at RT[38]. We also observe the formation of porous frameworks when C_{60} is added to DT/Au(111). However, long-range order is poor with DT, and the C_{60}/DT mixture usually exists in a rather disordered state, as shown in Figure 7.1 and

Figure 7.2. The order of mixture depends on several parameters, including sample temperature, C_{60}/thiol ratio, and the quality of the pre-prepared thiol/Au(111) sample. To demonstrate the effect of temperature, we show STM images in Figure 7.4, obtained after thermal annealing a C_{60}/DT mixture to 343 K for 30 min.

Figure 7.4 (a), an STM image of a mixed C_{60}/DT layer, displays four distinct structures: (i) porous C_{60}/DT frameworks in varying hexagonal shapes, (ii) a pure striped phase of DT forming parallel rows, (iii) patches of $(C_{60})_7$ clusters, and (iv) staggered domains of C_{60} nano chains.

Figure 7.4 (b) shows the magnified image of the $(C_{60})_7$ cluster domain in Figure 7.4 (a). The growth direction of the $(C_{60})_7$ cluster is 14 degrees relative to $[1\bar{1}0]$, which is the C_{60} closed-packed direction. This angle can be referenced for determining C_{60} porous structure growth direction. Also, the unit cell of $(C_{60})_7$ is already determined in chapter 6, which means this known structure can calibrate the distance measurement of C_{60} porous structures. Figure 7.5 (a) & (b) shows the method to determine the adsorption site of C_{60} in $(C_{60})_7$ clusters, which is precisely the same as the case in C_{60}/OT system in chapter 6. Unlike the C_{60}/OT system, forming $(C_{60})_7$ cluster-based molecular tessellation appears more challenging in the C_{60}/DT case. However, these $(C_{60})_7$ clusters can be used as calibration references because they always appear near other novel structure domains.

These $(C_{60})_7$ clusters have the same structure compared with the $(C_{60})_7$ tiles in C_{60}/OT supramolecular tessellation in chapter 6. It can be further referenced to determine the unit cell of C_{60} porous framework and nanochain structure[38,45].

Comparing Figure 7.2 with Figure 7.6, one can see clearly that the overall order of the C_{60}/DT mixture improved after annealing. There are still many C_{60} dimers in Figure 7.6 (a), but the dominant structure is now the porous framework. Six, eight, or ten C_{60} molecules can form the pore, leading directly to different pore sizes. The number of AAD inside the pore

depends on the pore size. We have not been able to produce a porous framework with a single structure, which indicates that the energy difference between the coexisting structures is relatively small.

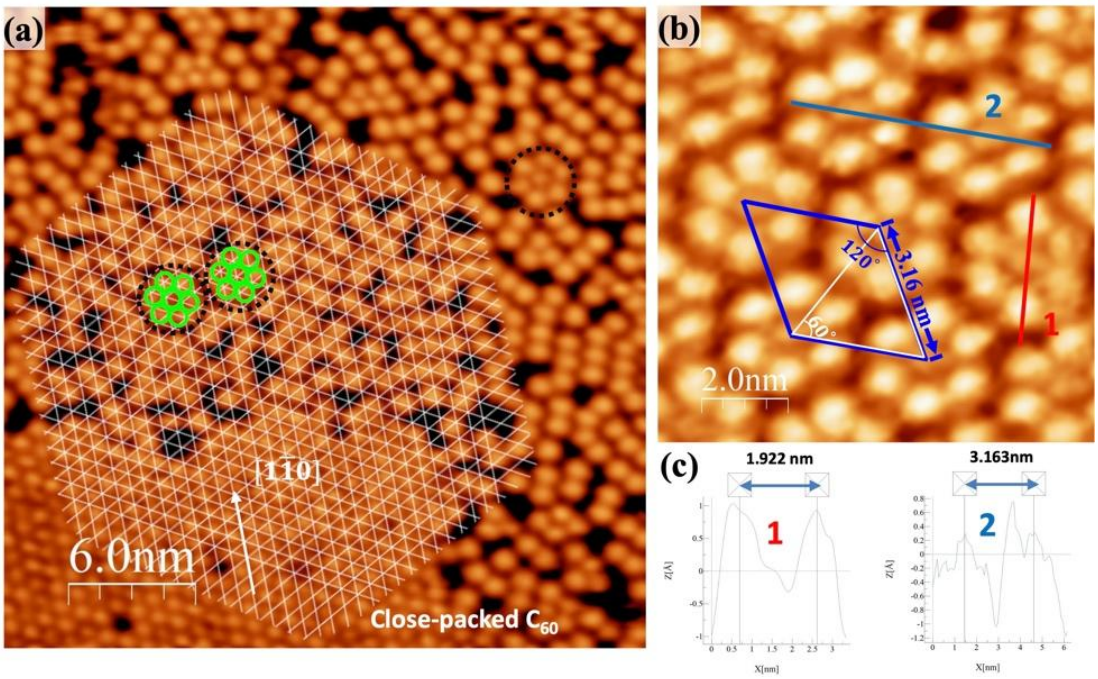

Figure 7.5 STM images of $(C_{60})_7$ cluster of C_{60}/DT bicomponent system. (a) The adsorption sites of the C_{60} molecules within the $(C_{60})_7$ cluster are determined via triangulation. Gaussian filter is applied to the original data. The closed-packed C_{60} is used as the reference. Such $(C_{60})_7$ can be found next to the C_{60} porous framework and nanochain regions (30 nm × 30 nm; Vb = 1.0 V; It = 0.5 nA). (b) High-resolution STM images of $(C_{60})_7$ cluster (10 nm × 10 nm; Vb = 2 V; It = 0.15 nA). Based on previous studies, C_{60} molecules occupy the top site of Au(111). (c) Distance profiles of lines A and B.

Some C_{60} rows can be seen in Figure 7.6 (a). This transition to C_{60} rows is associated with an increased C_{60}/thiol ratio as thiol becomes thermally desorbed. Figure 7.6 (a) presents an STM image illustrating the coexistence of hexagonal C_{60} frameworks and C_{60} nanochain structures on the Au(111) surface. White lines outline the relative azimuthal orientations of framework domains I and II. All the C_{60} rows within the C_{60}/DT frameworks are staggered and segmented, with a further 14 degree clockwise or counterclockwise rotation relative to the [1$\bar{1}$0] directions of Au(111) (see Figure 7.4 (b)), aligning with the close-packing direction of C_{60} in the R14 phase[33].

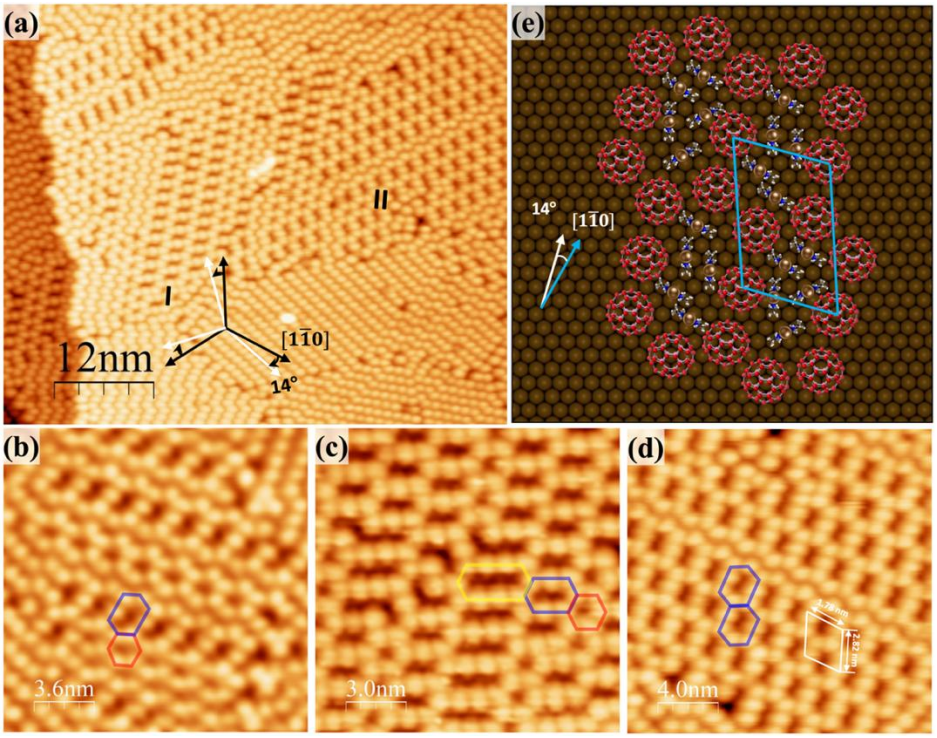

Figure 7.6 Formation of C_{60}/DT porous frameworks after thermal annealing at 343 K for 30min. (a) An STM image (60 nm × 50 nm; Vb = 1.5 V; It = 0.3 nA) illustrating the concurrent existence of the C_{60}/DT frameworks and the zig-zag C_{60} nano chains at RT. Notably, all the segmented C_{60} rows conform to one of the C_{60} closed-packed directions. (b), (c) & (d) High-resolution STM images depict three distinct arrangements of C_{60}/DT hexagonal frameworks, marked by red, blue, and yellow hexagons. Tunnelling parameters are Vb = 1.4 V and It = 0.1 nA for all STM images. The image sizes are (18 nm × 18 nm) for (b), (15 nm × 15 nm) for (c), and (25 nm × 25 nm) for (d). (e) A ball model of the $(C_{60})_8$ porous framework. Each pore is large enough to accommodate five AAD units, although the exact configuration of the five AAD is not yet clear. It visually represents the unit cell illustrated in image (d).

The high-resolution STM images in Figure 7.6 (b), (c), and (d) display a $(C_{60})_8$ framework (highlighted by a blue hexagon) accompanied by two distinct pore structures: $(C_{60})_6$ (in a red hexagon) and $(C_{60})_{10}$ (in a yellow hexagon). $(C_{60})_8$ is the most abundant on the surface. The coexistence of pores of various sizes indicates that these different sized pores have similar stability. How to achieve a single-sized pore structure for C_{60}/DT is not yet understood. In our earlier investigation with C_{60}/OT, the self-assembly process seems to be able to self-select pores consisting of six C_{60} molecules.

To create a structural model of the framework, we embarked on a progressive fine-tuning of the model. Beginning with an initial model derived purely from triangulation, we filled the RS-Au-SR staples into the pores. The adsorption of the RS-Au-SR alkanethiol staples on Au(111) is well-documented[46]. Filling the pores with DT must conform to the established principle that the Au adatom occupies the bridge site with the RS-Au-SR axis perpendicular to the bridge. The shortest distance between two alkyl chains is around 0.5 nm[42]. It is also vital that the alkyl chains maintain a reasonable distance from the carbon atoms within the C_{60} cage. The framework is laterally shifted above Au(111) multiple times until the optimal fit is achieved.

Figure 7.6 (e) presents an optimised structural model for the $(C_{60})_8$ framework. The arrangement of C_{60} molecules in the model matches quite well with what is observed in STM images. We have no reliable information about the locations of the AAD from STM. A trial and error approach is taken. The thiol molecules inside the pore interact with each other and with C_{60}. Thiol molecules inside the pore are not in an equivalent bonding environment. However, to optimise the thiol-C_{60} interaction, the alkyl chains need to be oriented nearly perpendicular to the substrate. According to the structural model of Figure 7.6 (e), each pore contains five AAD units. According to the model in Figure 7.6 (e), if we place five AAD units inside the pore, the C_{60} coverage in framework is 0.045 ML, and the DT coverage is 0.15 ML, resulting in a C_{60}/DT ratio of 3:10. Both the coverages for C_{60} and DT are scaled to the atomic density of surface Au atoms.

Consequently, the framework composition is $(C_{60})_3(DT)_{10}$. Also, the molar ratio of C_{60}/OT frameworks is 4:14 in our previous study[38]. When compared to 4:14 and 3:10, they exhibit comparable magnitudes. This correspondence proves that our proposed model aligns effectively with the appropriate level. Additionally, the initial coverage of DT in the δ phase also stands at 0.23 ML[32], reaffirming a reduction in the overall thiol coverage. During the

deposition of C_{60} or the subsequent thermal annealing process, some thiol molecules may have desorbed, as we do not observe mass migration of DT to areas surrounding the framework.

A noteworthy attribute of the C_{60}/DT framework is that its structure does not solely rely on nearest neighbor interactions. Instead, collective interactions among many molecules dictate the stable structure transition. This is a marked deviation from hydrogen-bonded frameworks[8] or MOFs[47], where nearest neighbour bonding predominantly determines the final structure of the framework.

7.3.3 Evolution of C_{60}/DT Nanochains

Following prior research, thermal annealing has been recognised as an effective method to modulate molecular adsorption configurations and assembly processes[48–50]. For the C_{60}/DT system, thermal treatment causes preferential removal of DT through thermal desorption. This then changes the C_{60}/DT ratio, resulting in the change of structures. Notably, the desorption temperature of C_{60} exceeds that of DT by more than 200 K. Upon annealing the sample at 363K for 30 min, we observed C_{60} zig-zag nano chains, as depicted in Figure 7.7 (a). The formation of the C_{60} rows results from further reduction of the thiol coverage due to thermal desorption. Based on previous studies in chapter 6, C_{60} molecules favour self-assembly as a zig-zag chain arrangement via thiol molecules based molecular template after thermal treatment. However, for C_{60}/DT system, the C_{60} rows will expand longer without mismatch after annealing.

The formation of the C_{60} rows results from further reduction of the thiol coverage due to thermal desorption. C_{60} molecules are close-packed along the row. There is a space between two neighbouring rows, and DT occupies this space. This C_{60}/DT row phase is similar to the C_{60}/OT rows formed under similar experimental conditions[45]. However, it is interesting to note that the C_{60}/DT nano chains are considerably longer than the C_{60} rows formed with OT after thermal treatment (Figure 7.7 (b)). The direction of the C_{60} chains is plus or minus 14 degrees from the $[1\bar{1}0]$ directions of Au(111), the same as the direction of the dimer axis.

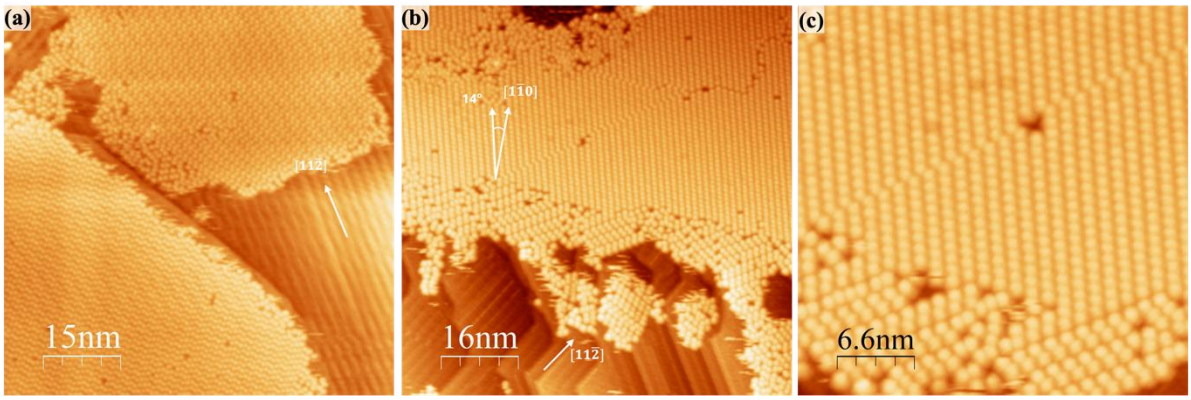

Figure 7.7 C_{60} zig-zag nanochains. (a) STM image (75 nm × 75 nm; Vb = -1.6 V; It = 0.15 nA) depicts zig-zag C_{60} rows after annealing at 363 K for 30 min. (b) STM image of staggered C_{60} nano chains after annealing at 363 K for 60 min. The direction of C_{60} rows can be determined by reference to the direction of the DT striped phase (80 nm × 80 nm; Vb = 1.8 V; It = 0.1 nA). (b) High-resolution STM image of staggered C_{60} chains (33 nm × 33 nm; Vb = 1.5 V; It = 0.1 nA).

Upon further heating the sample to 363 K for 1 hour, STM images, as presented in Figure 7.8 (b), reveal the disappearance of the staggered C_{60} rows. Now, long-range ordered C_{60} nano chains emerge, following the growth direction of closely packed C_{60}. However, they are not "chains" as they have no chemical interaction beyond dispersion forces. From these observations, we deduce that the shape of individual building blocks plays a pivotal role in the bottom-up self-assembly of nanostructured materials[51]. Even a simple change in shapes from OT to DT can significantly influence the assembly process due to the modified length of the orientational alkyl chains.

The symmetry of the C_{60} nanochain structure is reduced to two-fold symmetry[45]. A white quadrilateral highlights the unit cell in a high-resolution STM image (Figure 7.8 (c)). Employing a modelling approach similar to the previously mentioned, we can propose the structural model of segments with a C_{60}–$(DT)_2$ composition, as illustrated in Figure 7.8 (d). The respective coverages of C_{60} and DT molecules are 0.045ML and 0.09ML. In the long-chain direction, there is no spacing between adjacent molecules, allowing RS-Au-SR staples to fill the space between two C_{60} chains.

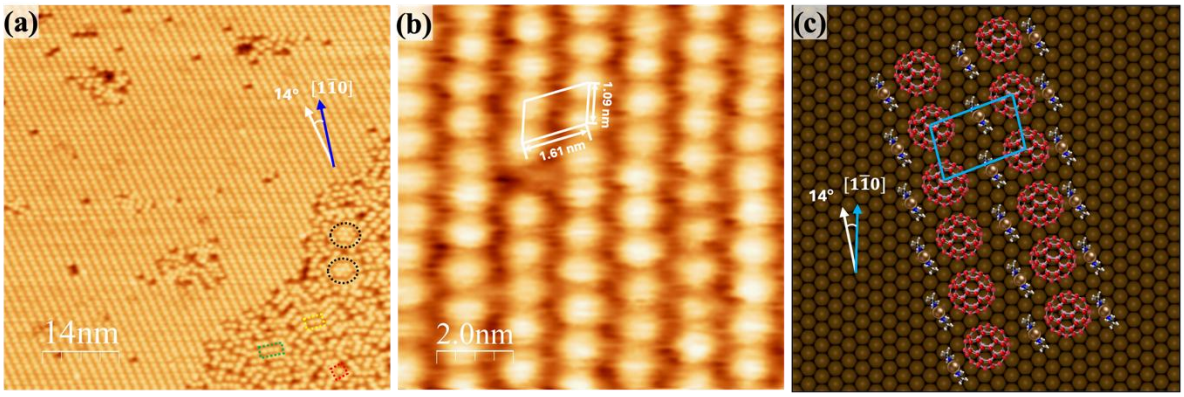

Figure 7.8 Long-range ordered C_{60} nanochain structure. (a) STM image (70 nm × 70 nm; Vb = -1.0 V; It = 0.2 nA) shows the long C_{60} nano chains after 90 min annealing. The lower right corner shows C_{60} molecules that have not yet formed regular rows. (b) A high-resolution STM image (10 nm × 10 nm; Vb = 1.0 V; It = 0.3 nA) illustrating a C_{60} nanochain with a unit cell. (c) The optimised ball model provides a visual representation of the unit cell.

Similar to the forming process of the C_{60} framework, starting with the square pore structure, the local coverage of DT can be reduced by gently heating the sample. This will keep the local coverage of C_{60} constant and only change the molar ratio between DT and C_{60}. As the C_{60}/DT ratio increases, we observe a gradual transition from a porous C_{60} network to C_{60} chains. All the structures in this system follow an orientational growth along the direction 14 degrees from [1$\bar{1}$0] direction.

Subsequent thermal annealing prompts a transition from a staggered C_{60} nanochain to a straight one. The re-arrangement of molecules during the annealing process signifies the importance of thermodynamics in shaping the final nanostructure. The final C_{60} nanochain is characterised by a higher level of order and reduced molecular freedom, indicative of a lower total energy state. This suggests that the straight C_{60} nanochain is thermodynamically more stable than the staggered arrangement.

7.3.4 Design Principle of C_{60}/DT Co-assembly

As illustrated in Figure 7.9, the DT/Au(111) SAMs serve as the molecular template. The adsorption of DT on Au(111) results in the formation the AAD unit[52]. The AAD unit can be

represented as RS-Au-SR ($R=CH_3(CH_2)_9$)[32,42]. The RS-Au-SR staples form long-range ordered crystalline domains at saturation coverage with a nearest neighbour distance of 0.5 nm. A combined sulfur-gold interaction and the vdW interaction between the alkyl chains stabilise the ordered thiol monolayer. The alkyl chains tilt 30 degrees from the surface, which is normal at high coverage. Also, they lie nearly flat on the surface at low coverages[37].

Earlier studies on this system unveiled phase-separated C_{60} and thiols on Au(111) with no signs of a regular mixture[31,36,38]. A saturated OT monolayer[31] can prevent C_{60} molecules from reaching the Au(111) substrate except at locations of defects. On a propylthiol monolayer, C_{60} forms close-packed domains even at 100 K with clear phase-separated domains of C_{60} and thiol at RT. The relatively short propyl chains do not offer strong enough interactions with C_{60}. Hence, no ordered C_{60}-thiol mixture is observed at any coverage of propylthiol[36]. Here, we take a different approach, preparing the DT layer with less than the saturation coverage. This approach effectively promotes the trapping of C_{60} molecules and opens the path to forming cocrystals of C_{60} and DT. The DT/Au(111) SAMs sample is heated in a UHV chamber to 393 K for 2 hours, leading to partial desorption of DT and the emergence of the striped δ phase with a coverage of 0.23 ML(One monolayer is defined as one DT molecule per surface Au atom), wherein each segment comprises a small number of AAD units, as depicted in Figure 7.9 (a) and chapter 4. Subsequently, around 0.045 ML of C_{60} molecules are deposited onto the DT striped phase monolayer and incorporated into the AAD units via defect sites between staggered DT segments. Due to the favourable C_{60}-C_{60} and C_{60}-thiol interaction directed self-assembly, the supramolecular C_{60} framework manifests with thiol-filled pores in Figure 7.9 (b). The porous structure transforms into C_{60} nano chains upon annealing with thiols occupying the space between neighbouring C_{60} chains, as shown in Figure 7.9 (c). This research elucidates the competition between equilibrium and metastable phases steered by molecular coverage, molar ratios, and annealing temperature.

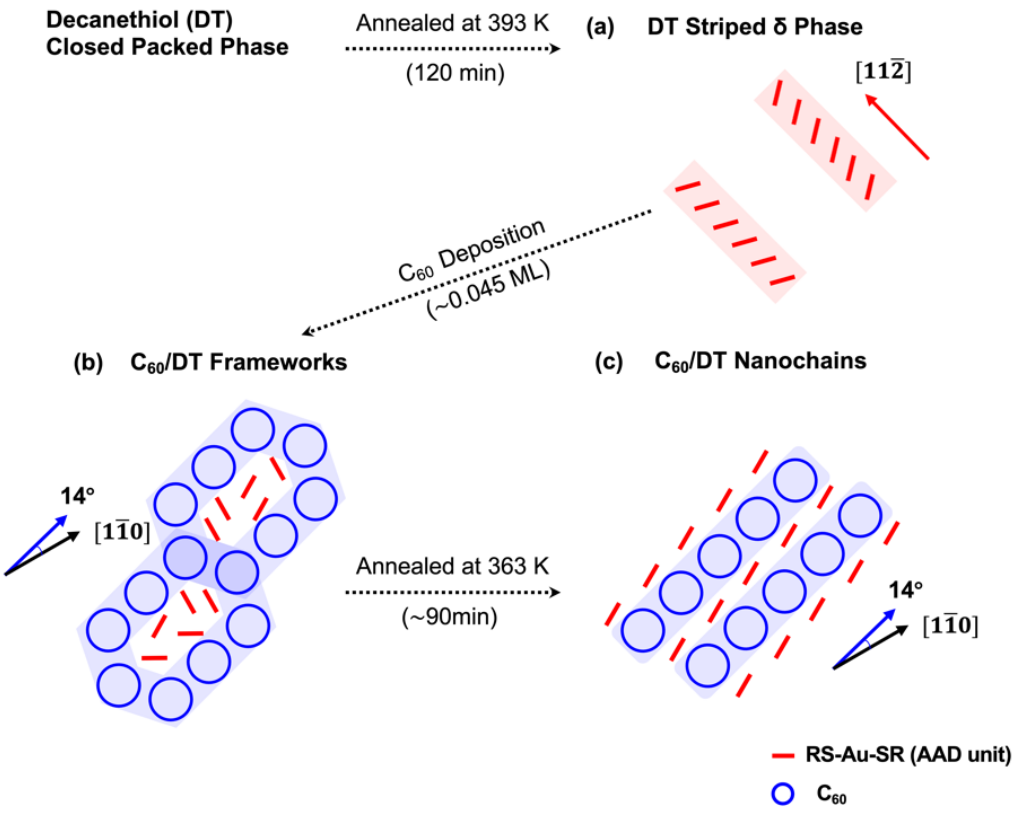

Figure 7.9 Schematic illustration of the C_{60}/DT co-assembly design principle on the surface. (a) Schematic of the striped phase consisting of rows of AAD. Each red bar represents the S-Au-S axis, with the alkyl chains not shown for clarity. (b) Porous C_{60} framework with pores filled with AAD. C_{60} molecules are shown according to the observed STM images, but AAD is shown for illustrative purposes only, as the exact locations of AAD have not been accurately determined. (c) C_{60} nanochain array confined by the aligned AAD units.

The C_{60}/DT and C_{60}/OT systems exemplify the innovative use of supramolecular self-assembly for creating intricate molecular patterns, leveraging the strength of van der Waals (vdW) interactions to organise molecules on gold substrates. A key similarity between the two systems is their reliance on vdW interactions rather than specific functional groups for the organisation and stabilisation of the molecular structures. Both systems achieve control and precision in patterning by manipulating variables such as molecular coverage and annealing temperatures. However, the C_{60}/DT system primarily focuses on forming porous networks and nano chains by combining C_{60} with DT, highlighting the adaptability of vdW bonds in creating varied stable phases at room temperature. In contrast, the C_{60}/OT system advances the concept further by facilitating the self-synthesis of $(C_{60})_7$ tiles in a tessellation pattern using OT as a

binder, emphasising simultaneous tile synthesis and self-organised tiling. The C_{60}/OT system's ability to generate complex 2D tessellations showcases a more intricate application of vdW supramolecular frameworks compared to the simpler structures produced in the C_{60}/DT system, indicating a potential for technological applications.

7.4 Summary

In conclusion, we have successfully engineered a two-dimensional C_{60}/DT porous molecular framework and extensive nanochain structures on the Au(111) surface at room temperature. This bicomponent molecular self-assembly is primarily governed by a cooperative van der Waals interaction, eliminating the need for specific bonding via functional groups among neighbouring molecules. We can synthesise flexible bicomponent molecular structures by controlling the molecular coverage and annealing temperature, leading to orientational growth[51]. This approach enriches our understanding of van der Waals co-assembly on surfaces and offers a promising strategy for creating complex functional nanostructures[53,54]. This work will likely significantly impact the future design and synthesis of molecular nanostructures/nanomaterials, offering enhanced control over their structures and properties.

References

1. Ding, H. *et al.* Orientational Growth of Flexible van der Waals Supramolecular Networks. *Small Struct.* 5, (2024).

2. Champness, N. *Supramolecular Chemistry on Surfaces: 2D Networks and 2D Structures*. (Wiley-VCH, 2022). doi:10.1002/9783527816699.

3. Kuhnke, K., Große, C., Merino, P. & Kern, K. Atomic-Scale Imaging and Spectroscopy of Electroluminescence at Molecular Interfaces. *Chem. Rev.* 117, 5174–5222 (2017).

4. Verstraete, L. & Feyter, S. D. 2D Self-assembled molecular networks and on-surface reactivity under nanoscale lateral confinement. *Chem. Soc. Rev.* 50, 5884–5897 (2021).

5. Barth, J. V. Molecular Architectonic on Metal Surfaces. *Annu. Rev. Phys. Chem.* 58, 375–407 (2007).

6. Geagea, E., Palmino, F. & Cherioux, F. On-Surface Chemistry on Low-Reactive Surfaces. *Chemistry* 4, 796–810 (2022).

7. Staniec, P. A., Perdigão, L. M. A., Saywell, A., Champness, N. R. & Beton, P. H. Hierarchical Organisation on a Two-Dimensional Supramolecular Network. *ChemPhysChem* 8, 2177–2181 (2007).

8. Theobald, J. A., Oxtoby, N. S., Phillips, M. A., Champness, N. R. & Beton, P. H. Controlling molecular deposition and layer structure with supramolecular surface assemblies. *Nature* 424, 1029–1031 (2003).

9. Okesola, B. O. & Mata, A. Multicomponent self-assembly as a tool to harness new properties from peptides and proteins in material design. *Chem. Soc. Rev.* 47, 3721–3736 (2018).

10. Geng, Y., Zeng, Q. & Wang, C. Dependence of the surface-assisted fullerene-based complex structure on the template molecule design. *Nano Res* 12, 1509–1537 (2019).

11. Teyssandier, J., Feyter, S. D. & Mali, K. S. Host–guest chemistry in two-dimensional supramolecular networks. *Chem. Commun.* 52, 11465–11487 (2016).

12. Mena-Osteritz, E. & Bäuerle, P. Complexation of C_{60} on a Cyclothiophene Monolayer Template. *Adv. Mater.* 18, 447–451 (2006).

13. Pan, G. *et al.* Configurations of a Calix[8]arene and a C_{60}/Calix[8]arene Complex on a Au(111) Surface. *Angew. Chem.* 115, 2853–2857 (2003).

14. Blunt, M. O., Russell, J. C., Champness, N. R. & Beton, P. H. Templating molecular adsorption using a covalent organic framework. *Chem. Commun.* 46, 7157–7159 (2010).

15. Cui, D., Ebrahimi, M., Rosei, F. & Macleod, J. M. Control of Fullerene Crystallization from 2D to 3D through Combined Solvent and Template Effects. *J. Am. Chem. Soc.* 139, 16732–16740 (2017).

16. Blunt, M. O. *et al.* Guest-induced growth of a surface-based supramolecular bilayer. *Nat. Chem.* 3, 74–78 (2011).

17. Pan, G.-B., Cheng, X.-H., Höger, S. & Freyland, W. 2D Supramolecular Structures of a Shape-Persistent Macrocycle and Co-deposition with Fullerene on HOPG. *J. Am. Chem. Soc.* 128, 4218–4219 (2006).

18. Pivetta, M., Blüm, M., Patthey, F. & Schneider, W. Two-Dimensional Tiling by Rubrene Molecules Self-Assembled in Supramolecular Pentagons, Hexagons, and Heptagons on a Au(111) Surface. *Angew. Chem. Int. Ed.* 47, 1076–1079 (2008).

19. Copie, G. *et al.* Surface-Induced Optimal Packing of Two-Dimensional Molecular Networks. *Phys. Rev. Lett.* 114, 066101 (2014).

20. Zhang, Y. *et al.* Construction of single-crystalline supramolecular networks of perchlorinated hexa-peri-hexabenzocoronene on Au(111). *J. Chem. Phys.* 142, 101911 (2015).

21. Xiao, W. *et al.* C_{60}/Corannulene on Cu(110): A Surface-Supported Bistable Buckybowl−Buckyball Host−Guest System. *J. Am. Chem. Soc.* 130, 4767–4771 (2008).

22. Qiu, X. *et al.* Alkane-Assisted Adsorption and Assembly of Phthalocyanines and Porphyrins. *J. Am. Chem. Soc.* 122, 5550–5556 (2000).

23. Zhang, X. *et al.* Kinetic Controlled Chirality Transfer and Induction in 2D Hydrogen-Bonding Assemblies of Glycylglycine on Au(111). *Small* 19, e2207111 (2023).

24. Zheng, Q.-N. *et al.* Formation of Halogen Bond-Based 2D Supramolecular Assemblies by Electric Manipulation. *J. Am. Chem. Soc.* 137, 6128–6131 (2015).

25. Écija, D. *et al.* Five-vertex Archimedean surface tessellation by lanthanide-directed molecular self-assembly. *Proc. Natl. Acad. Sci.* 110, 6678–6681 (2013).

26. Sedona, F., Marino, M. D., Basagni, A., Colazzo, L. & Sambi, M. Structurally Tunable Self-Assembled 2D Cocrystals of C_{60} and Porphyrins on the Ag (110) Surface. *J Phys Chem C* 118, 1587–1593 (2014).

27. Zhang, H. L. *et al.* C_{60} Molecular Chains on α-Sexithiophene Nanostripes. *Small* 3, 2015–2018 (2007).

28. Smerdon, J. A., Rankin, R. B., Greeley, J. P., Guisinger, N. P. & Guest, J. R. Chiral "Pinwheel" Heterojunctions Self-Assembled from C_{60} and Pentacene. *Acs Nano* 7, 3086–3094 (2013).

29. Jin, W., Dougherty, D. B., Cullen, W. G., Robey, S. & Reutt-Robey, J. E. C_{60}−Pentacene Network Formation by 2-D Co-Crystallization. *Langmuir* 25, 9857–9862 (2009).

30. Horcas, I. *et al.* WSXM: A software for scanning probe microscopy and a tool for nanotechnology. *Rev. Sci. Instrum.* 78, 013705 (2007).

31. Li, F., Tang, L., Zhou, W. & Guo, Q. Formation of Confined C_{60} Islands within Octanethiol Self-Assembled Monolayers on Au(111). *J. Phys. Chem. C* 113, 17899–17903 (2009).

32. Poirier, G. E. Coverage-Dependent Phases and Phase Stability of Decanethiol on Au(111). *Langmuir* 15, 1167–1175 (1999).

33. Schull, G. & Berndt, R. Orientationally Ordered (7×7) Superstructure of C_{60} on Au(111). *Phys Rev Lett* 99, 226105 (2007).

34. Tang, L., Xie, Y. & Guo, Q. Complex orientational ordering of C_{60} molecules on Au(111). *J Chem Phys* 135, 114702 (2011).

35. Tang, L. & Guo, Q. Orientational ordering of the second layer of C_{60} molecules on Au(111). *Phys Chem Chem Phys* 14, 3323–3328 (2012).

36. Gao, J. *et al.* Growth of Two-Dimensional C_{60} Nanoclusters within a Propylthiolate Matrix. *J Phys Chem C* 120, 25481–25488 (2016).

37. Guo, Q. & Li, F. Self-assembled alkanethiol monolayers on gold surfaces: resolving the complex structure at the interface by STM. *Phys. Chem. Chem. Phys.* 16, 19074–19090 (2014).

38. Zhang, X. *et al.* Two-Dimensional van der Waals Supramolecular Frameworks from Co-Hosted Molecular Assembly and C_{60} Dimerization. *J. Phys. Chem. C* 124, 12589–12595 (2020).

39. Zhang, X. *et al.* Orientation-Selective Growth of Single-Atomic-Layer Gold Nanosheets via van der Waals Interlocking and Octanethiolate-Confined Molecular Channels. *J. Phys. Chem. C* 123, 25228–25235 (2019).

40. Ding, H. *et al.* Perturbational Imaging of Molecules with the Scanning Tunneling Microscope. *J. Phys. Chem. C* 124, 25892–25897 (2020).

41. Gardener, J. A., Briggs, G. A. D. & Castell, M. R. Scanning tunneling microscopy studies of C_{60} monolayers on Au(111). *Phys Rev B* 80, 235434 (2009).

42. Li, F., Tang, L., Zhou, W. & Guo, Q. Resolving the Au-Adatom-Alkanethiolate Bonding Site on Au(111) with Domain Boundary Imaging Using High-Resolution Scanning Tunneling Microscopy. *J. Am. Chem. Soc.* 132, 13059–13063 (2010).

43. Lei, S. B., Yin, S. X., Wang, C., Wan, L. J. & Bai, C. L. Modular Assembly of Alkyl-Substituted Phthalocyanines with 1-Iodooctadecane. *Chem. Mater.* 14, 2837–2838 (2002).

44. Lei, S. B., Wang, C., Yin, S. X. & Bai, C. L. Single Molecular Arrays of Phthalocyanine Assembled with Nanometer Sized Alkane Templates. *J. Phys. Chem. B* 105, 12272–12277 (2001).

45. Maksymovych, P., Voznyy, O., Dougherty, D. B., Sorescu, D. C. & Yates, J. T. Gold adatom as a key structural component in self-assembled monolayers of organosulfur molecules on Au(111). *Prog. Surf. Sci.* 85, 206–240 (2010).

46. Lin, N. *et al.* Template-directed supramolecular self-assembly of coordination dumbbells at surfaces. *Chem. Commun.* 0, 4860–4862 (2007).

47. Huang, Y. L. *et al.* Tunable Two-Dimensional Binary Molecular Networks. *Small* 6, 70–75 (2010).

48. Feng, L. *et al.* Supramolecular Tessellations at Surfaces by Vertex Design. *ACS nano* 13, 10603–10611 (2019).

49. Li, C. *et al.* Evidence of a Thermal Annealing Effect on Organic Molecular Assembly. *ChemPhysChem* 4, 857–859 (2003).

50. Zhang, X. *et al.* Complex supramolecular tessellations with on-surface self-synthesized C_{60} tiles through van der Waals interaction. *Nanoscale* 14, 1333–1339 (2022).

51. Guo, L. *et al.* Orientational Epitaxy of van der Waals Molecular Heterostructures. *Nano Lett* 18, 5257–5261 (2018).

52. Maksymovych, P., Sorescu, D. C. & Yates, J. T. Gold-Adatom-Mediated Bonding in Self-Assembled Short-Chain Alkanethiolate Species on the Au(111) Surface. *Phys. Rev. Lett.* 97, 146103 (2006).

53. Guo, L. *et al.* Self-build of C_{60}-C_{70} molecular heterojunctions on highly oriented pyrolytic graphite. *Appl Surf Sci* 538, 148142 (2021).

54. Wang, Y., Guo, L. & Guo, Q. Two-Component Fullerene Molecular Layers Assembled on the Au(111) Substrate. *J Phys Chem C* 123, 7776–7785 (2019).

8 Summary and Future Work

The preparation of 2D nanostructures on metal surfaces is of great importance in surface science. In this thesis, the growth mechanism and structural models of various 2D nanostructures such as OT and DT SAMs, C_{60} nanopores framework, $(C_{60})_7$ clusters and nanochains based on Au(111) surface were investigated in details by using UHV-STM. The main contents and novel results are as follows:

1. Low-coverage striped phases of OT and DT on Au(111) surface.

The self-assembled structure of OT on Au(111) is highly dependent on the molecular coverage of OT. The different striped phases can be transformed from each one to another. At saturation coverage, the OT molecules are arranged in a $\left(3 \times 2\sqrt{3}\right)$ densely packed phase on the surface of Au(111). After controlled annealing treatment, the OT molecules on Au(111) are partially desorbed, reducing molecular coverage and forming various forms of striped phase structures on the surface. The existence of striped phases $p\left(6.5 \times \sqrt{3}\right)$ and $p\left(11.5 \times \sqrt{3}\right)$ was confirmed with STM. Some of the molecular chains in the striped phase are periodically dislocated due to the release of surface stress. The DT rows in the $p(7.5 \times \sqrt{3})$ striped phase are misplaced periodically along $[11\bar{2}]$directions. In addition, the striped phases and the mesh-like structures of the OT SAMs consisted of short-chain molecules, and they were prepared under precisely controlled annealing conditions.

2. Two-dimensional van der Waals C_{60}/OT supramolecular framework.

A supramolecular framework is created by self-assembled crystallisation of C_{60} and OT molecules on the Au(111) surfaces via van der Waals (vdW) interaction. Binary molecular nanostructures, including C_{60} and OT, are prepared after depositing C_{60} molecules with different surface coverage on the OT/Au(111) template. The C_{60} was deposited on the surface with an OT striped phase structure. The surface molecular coverage of OT molecules is

0.23ML. The binary molecular two-dimensional nanostructures with C_{60}-OT molecule ratios of 1:4 and 4:14 were obtained at different deposition rates. Similarly, a nanochain structure with a ratio of 1:2 is obtained, further reducing the OT molecular coverage by controlling the annealing temperature of the sample. Nevertheless, the low-temperature (80K) STM characterisation of these two-dimensional porous nanostructures revealed that the C_{60} molecules converge regularly to form C_{60} pairs. These frameworks are likely widespread, making them worthy of further studies.

3. Supramolecular tessellations with on-surface self-synthesised C_{60}/OT tiles.

Supramolecular tessellation with self-synthesised $(C_{60})_7$ tiles are created based on cooperative interaction between co-adsorbed C_{60} and OT molecules on the Au(111) surface. A C_{60}-OT molecule ratio of 7:12 ratio is achieved by heating the sample. Similarly, a nanochain structure with a ratio of 1:2 is obtained, further reducing the OT molecular coverage by controlling the annealing temperature of the sample. Also, a gradual transition from a porous C_{60} framework to $(C_{60})_7$ tiles and nanochain structure is observed under STM. This analysis shows that although there is an absence of specific functional groups in this system, the collective vdW interaction among many molecules is the key to ordered supramolecular tiling. This bi-component system offers a new pathway for the synthesis of 2D complex vdW supramolecular tessellations.

4. Orientational growth of flexible van der Waals C_{60}/DT networks.

The formation of molecular frameworks entirely dependent on van der Waals (vdW) interactions has been infrequently explored. Herein, we synthesise two-dimensional (2D) vdW supramolecular structures through the self-assembled co-crystallisation of C_{60} and DT (DT) molecules on the Au(111) surface. Notably, the system eliminates the need for functional groups for specific bonding between adjacent units. The conformation C_{60}/DT was delicately manipulated by adjusting molecular coverage and annealing temperature. The absence of

directional bonding between C_{60} and DT molecules facilitated the formation of a variety of stable phases at room temperature (RT), such as i) porous C_{60} networks with thiol-filled pores and ii) self-synthesised $(C_{60})_n$ nano chains with thiol spacers interspersed between the chains are achieved and visualised by STM imaging under RT. This innovative integration of the vdW interaction unveils new avenues for developing supramolecular patterns characterised by their comparatively weak but exceptionally adaptable bonding.

The examination of OT SAMs, C_{60} nanoporous frameworks, $(C_{60})_7$ clusters, and nano chains on Au(111) surfaces has illuminated the critical role of molecular coverage, annealing processes, and van der Waals interactions in dictating the formation, structure, and stability of these complex nano assemblies. The findings underscore the nuanced interplay between molecular species and their substrate, revealing how subtle variations in experimental conditions can significantly influence the self-assembly process. This delicate balance between intermolecular forces and surface interactions opens up many opportunities for engineering nanostructures with specific characteristics and functionalities.

Furthermore, the potential to investigate the electronic properties of these structures through advanced techniques such as STS and NC-AFM promises to deepen our understanding of the quantum mechanical phenomena at play within these self-assemblies. Such investigations could shed light on the charge transport mechanisms, electronic density states, and quantum confinement effects within these materials.

In conclusion, this thesis presents a study on the role of vdW interaction in molecular assembly, exploring how this non-directional and relatively weak force influences molecular self-assembly. The journey from understanding to application is fraught with challenges, yet it is rich with the potential for ground-breaking discoveries that could revolutionise our technological landscape.

Appendix

Quantum Mechanical Tunnelling

Quantum mechanical tunnelling is a phenomenon where particles pass through a potential energy barrier that they classically shouldn't be able to cross due to insufficient energy, stemming from the wave-like nature of particles in quantum mechanics. This effect is crucial in various applications: it is fundamental in semiconductor devices like tunnel diodes and field-effect transistors, enabling modern electronics; it underlies the operation of STM, which images surfaces at the atomic level by measuring tunnelling currents; it facilitates nuclear fusion in stars, including the sun, by allowing protons to overcome the Coulomb barrier; it is exploited in quantum computing components such as Josephson junctions in superconducting qubits; and it influences certain chemical reactions, especially those involving light atoms like hydrogen, by affecting reaction rates and mechanisms beyond classical predictions.

The basic model of the quantum tunnelling effect in one dimension is depicted in Figure 8.1 (a). Two electrodes are separated in the one-dimensional model by a finite energy barrier, the potential of which is U. If the electrodes were made of two different metals. The tunnelling characteristics, such as the tunnelling current and the conductance, would be affected by the differences in the electronic properties of the two metals. The asymmetry introduced by using different metals must be considered when analysing the tunnelling process and interpreting the I-V characteristics. For simplicity, we will suppose that the two electrodes are constructed of the same material. Φ denotes the electrode's work function. Solid black lines denote the tip and sample Fermi levels, whereas the potential barrier has a width of z.

The Fermi level is the highest energy level occupied by electrons in a material at absolute zero temperature. It represents the chemical potential for electrons and determines the distribution of electrons in the energy states of the material. when the two electrodes are made

of the same material and no bias voltage is applied, the Fermi levels of the two electrodes are equal because the system is in thermal equilibrium. In this state, the chemical potential for electrons is the same across both electrodes, and the electrons are distributed such that they occupy energy states up to the Fermi level, with no net flow of electrons between the electrodes. Electrons exhibit wave-like qualities in quantum physics and can thus be characterised by wave functions $\Psi(z)$.

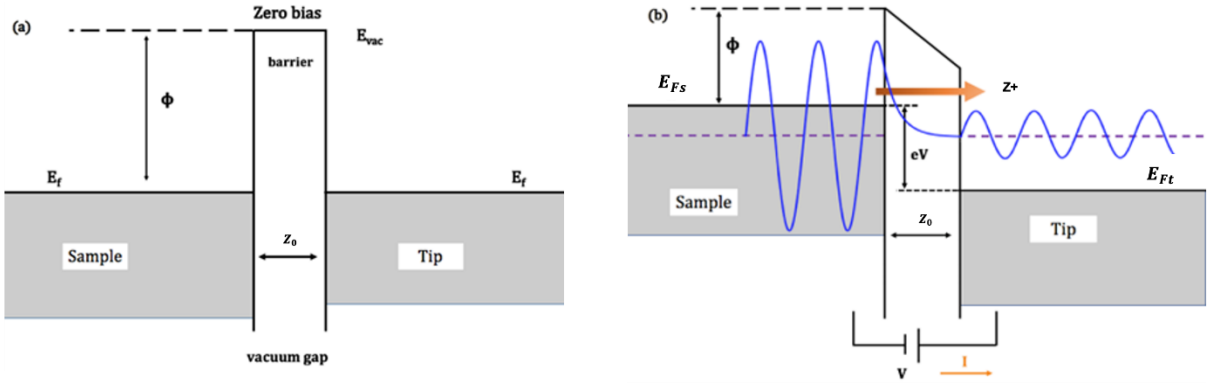

Figure 8.1 Schematic representation of the tip-barrier-sample junction's one-dimensional energy model. (a) If the tip and sample are constructed of the same material, their Fermi levels are equal when no bias voltage is supplied, and all electrons in the sample and tip are contained inside their Fermi levels. The energy barrier has no tunnelling current. (b) When a bias voltage is applied, the sample's Fermi level increases by eV. Electrons with energies between the two Fermi levels can propagate and generate a stable tunnelling current.

When the two electrodes are close together, a tiny number of electrons will tunnel through the energy barrier. The Schrödinger equation, representing one of the basic principles in quantum mechanics, predicts the states of particles. When an electron with energy E propagates in the +z direction toward the energy barrier:

$$-\frac{\hbar^2}{2m}\frac{d^2}{dz^2}\Psi(z) + U(z)\Psi(z) = E\Psi(z) \tag{2.1}$$

Assuming that the potential is zero outside of the barrier region. As a result, outside the barrier region, the Schrödinger equation is:

$$-\frac{\hbar^2}{2m}\frac{d^2}{dz^2}\Psi(z) = E\Psi(z) \tag{2.2}$$

Electrons' wave function $\Psi(z)$ is denoted as:

$$\Psi_1(\mathrm{z}) = \mathrm{Ae}^{+\mathrm{ikz}} + \mathrm{Be}^{-\mathrm{ikz}} \tag{2.3}$$

where k is the wave vector and is defined as follows:

$$\mathrm{k} = \frac{\sqrt{2mE}}{\hbar} \tag{2.4}$$

Within the barrier, $U \neq 0$ and $U > E$ exist. The equation can be written as:

$$-\frac{\hbar^2}{2m}\frac{d^2}{dz^2}\Psi(z) = (E-U)\Psi(z) \tag{2.5}$$

and electrons have the following wave function:

$$\Psi_2(\mathrm{z}) = \mathrm{Ce}^{\kappa\mathrm{z}} + \mathrm{De}^{-\kappa\mathrm{z}} \tag{2.6}$$

which κ is the decay constant and denoted by:

$$\kappa = \frac{\sqrt{2m(U-E)}}{\hbar} \tag{2.7}$$

On the right side of $U < E$ potential barrier in Figure 1 (b). Electrons have a wave function identical to that on the left side of the potential barrier. That region only transmitted waves can propagate. Thus, the wave function $\Psi(z)$ is expressed as:

$$\Psi_3(\mathrm{z}) = \mathrm{Fe}^{\mathrm{ikz}} \tag{2.8}$$

The coefficients A, B, C, D and F are replaced in terms of k and κ. The wave functions and their first order derivative are continuous when electrons propagate through the barrier.

When $x = 0$,

$\Psi_1(0) = \Psi_2(0)$

$$\left.\frac{d\Psi_1(x)}{dx}\right|_{x=0} = \left.\frac{d\Psi_2(x)}{dx}\right|_{x=0} \tag{2.9}$$

besides, $x = z_0$,

$\Psi_2(\mathrm{z}_0) = \Psi_3(z_0)$

$$\left.\frac{d\Psi_2(x)}{dx}\right|_{x=z_0} = \left.\frac{d\Psi_3(x)}{dx}\right|_{x=z_0} \tag{3.0}$$

Which means,

$$A + B = C + D \tag{3.1}$$

$$A - B = \frac{\kappa}{ik}(C - D) \tag{3.2}$$

$$\mathrm{C}e^{\kappa z_0} + D\mathrm{e}^{-\kappa z_0} = \mathrm{F}e^{\mathrm{i}kz_0} \tag{3.3}$$

$$\mathrm{C}e^{\kappa z_0} - D\mathrm{e}^{-\kappa z_0} = \frac{\kappa}{ik}\mathrm{F}e^{\mathrm{i}kz_0} \tag{3.4}$$

That gives

$$2A = \left(1 + \frac{\kappa}{ik}\right)C + \left(1 - \frac{\kappa}{ik}\right)D \tag{3.5}$$

$$2C\mathrm{e}^{\kappa z_0} = \left(1 + \frac{ik}{\kappa}\right)\mathrm{F}e^{\mathrm{i}kz_0} \tag{3.6}$$

$$2D\mathrm{e}^{-\kappa z_0} = \left(1 - \frac{ik}{\kappa}\right)\mathrm{F}e^{\mathrm{i}kz_0} \tag{3.7}$$

We can combine these to express F in terms of A

$$\frac{F}{A} = \frac{4i\kappa k}{(2i\kappa k+\kappa^2-k^2)\mathrm{e}^{-\kappa z_0}+(2i\kappa k-\kappa^2+k^2)\mathrm{e}^{\kappa z_0}}\mathrm{e}^{-\mathrm{i}kz_0} \tag{3.8}$$

The fraction of particles transmitted is just the ratio of the probabilities of the particles being in the transmitted and incident beams, which is just $|F|^2/|FA|^2$ and can be evaluated directly from equation (2.8). In many practical cases, the tunnelling probability is quite small, so we can ignore the term in $\mathrm{e}^{-\kappa z_0}$ in the denominator of equation (2.8). In this case the tunnelling probability becomes

$$\frac{|F|^2}{|A|^2} = \frac{16\kappa^2k^2}{(\kappa^2+k^2)^2}\mathrm{e}^{-2\kappa z_0} \tag{3.9}$$

then the transmission coefficient T is derived in the following equation:

$$T = \frac{(\Psi_3)^2}{(\Psi_1)^2} = \frac{FF^*}{AA^*} = \left[1 + \frac{(e^{\kappa z_0}+e^{-\kappa z_0})}{16\left(1-\frac{E}{U}\right)\frac{E}{U}}\right] \tag{4.0}$$

As for $\kappa z_0 \gg 1$, the equation can be derived as:

$$T \approx 16\left(1 - \frac{E}{U}\right)\frac{E}{U}e^{-\kappa z_0} \tag{4.1}$$

This indicates that as the barrier width z_0 grows, the probability of transmitted elections diminishes exponentially. When no bias voltage is applied, electrons with energies between the two Fermi levels have the same probability of tunnelling into the vacuum, so no net tunnelling current is produced.